From Vlasov to STEREO: nonlinear coupling in the solar wind

Pierre Henri

PhD Thesis in co-supervision between

Université Pierre et Marie Curie
École Doctorale "Astronomie et Astrophysique d'Île de France"

Università degli Studi di Pisa
Scuola di Dottorato di ricerca in Fisica Applicata

Pierre HENRI

From Vlasov to STEREO: nonlinear coupling in the solar wind

Discussed July 8, 2010

Jury :

- Laurence REZEAU, Université Pierre et Marie Curie, France *(President of the jury)*
- Robert MACDOWALL, NASA Goddard Space Flight Center, USA *(Referee)*
- Thierry PASSOT, Observatoire de la Côte d'Azur, France *(Referee)*
- Pierluigi VELTRI, Università della Calabria, Italy, *(Examiner)*
- Steve SHORE, Università di Pisa, Italy, *(Examiner)*
- Giovanni LAPENTA, KU Leuven, Belgium, *(Examiner)*
- Carine BRIAND, LESIA, Observatoire de Paris, France *(Supervisor)*
- Francesco CALIFANO, Università di Pisa, Italy *(Supervisor)*

Acknowledgments

I would like to express my sincere gratitude to all the people that have contributed in different ways to the work presented in this Ph.D. thesis. I will never be able to provide an exhaustive list, I would like, however, to emphasize some of them.

- My deepest gratitude is to my two supervisors, Carine Briand and Francesco Califano, who have made such work possible thanks to their constant patience, support and advice. I am grateful to them for having taught me how to do research.
- I am also deeply grateful to André Mangeney for his continuous encouragement and guidance all along this trip through the meanders of space plasma physics. This work owes him much.
- I am very grateful to Nicole Meyer-Vernet for her help and guidance that helped me understand the basics of the behavior of a spacecraft embedded in the solar wind.
- I would also like to thank Francesco Pegoraro and Steve Shore for useful and always pleasant discussions.
- Part of this co-supervised Ph.D. was financed by a Programme Vinci 2008 Grant from the Université Franco-Italienne (Projet n°5, VINCI 2008 chapitre 2).
- I am grateful to the Italian super-computing center CINECA (Bologna, Italy) where part of the calculations where performed. I also acknowledge Dr. C. Cavazzoni for useful discussion on code performance and the basics of HPC.
- Part of this thesis has been performed under the Project HPC-EUROPA2 (Project number 228398), with the support of the European Community - under the FP7 "Research Infrastructures".
- I am grateful to the members of the jury for having accepted to evaluate this work, and especially the referees for their interest and useful comments.
- Last, but not least, the biggest personal thanks goes to my family and my friends for their presence and their confidence in me.

Abstract

Many astrophysical plasmas, among them the solar wind, are collisionless. The typical frequencies of the system dynamics are indeed much higher than the collision frequency, so that the solar wind cannot be considered at local thermodynamic equilibrium. In this context, kinetic and/or nonlinear processes (wave-particle and wave-wave interactions) are of primary importance for the redistribution of the energy in the plasma. Kinetic processes and nonlinear plasma theory have been extensively studied since the 1960s, but observational evidence for such processes is still lacking.
In the particular case of electron and ion electrostatic coupling and in the context of space plasma, the main goals of this thesis are (i) to understand the physics of kinetic and/or nonlinear processes and (ii) to provide observational evidence of such processes.
The study is based on electric field observations and kinetic plasma simulations. In-situ waveform measurements are provided by the TDS observing mode of the WAVES instrument onboard the STEREO mission. The kinetic simulations were performed using a 1D-1V Vlasov-Poisson code in the electrostatic approximation.
The results of this thesis are the following. (1) A method has been developed to measure and to calibrate in-situ small scale density fluctuations, through the quasistatic fluctuations of the spacecraft floating potential. (2) The first observational evidence for ponderomotive effects (which nonlinearly couples solar wind ion dynamics to high-amplitude Langmuir waves) is obtained by analyzing a data set of density and electric field measurements over more than three years. (3) This work also provides the first direct, complete set of evidence for Langmuir electrostatic decay (an archetype of wave-wave interaction) associated to a Type III burst. The resonant character of the interaction is shown in the observations, by verifying the conservation of momentum and energy during the interaction (relation of resonance), as well as the phase coherence through a bicoherence analysis. A new expression for the Langmuir decay threshold is computed from the simulations, taking into account the dynamics of the process, and is shown to be in agreement with the observations. (4) Finally, the long time evolution of weak Langmuir turbulence (in the Langmuir electrostatic decay regime) is shown to asymptotically end up with strong turbulence and the formation of Langmuir cavitons, through the Vlasov-Poisson system. This thesis shows the importance of a complementary approach between observations and simulations.

Résumé

De nombreux plasmas astrophysiques, dont le vent solaire, sont non-collisionels. Les fréquences typiques des processus dynamiques sont grandes devant la fréquence de collision, de sorte que le vent solaire est hors équilibre thermodynamique local. Dans ce contexte, les processus cinétiques et/ou non-linéaires (interactions ondes-particules et ondes-ondes) permettent de redistribuer l'énergie dans le plasma. Si les processus cinétiques et la théorie non-linéaire des plasmas ont été intensivement étudiés depuis les années 1960, des preuves observationnelles concluantes manquent encore.
L'objectif de cette thèse est double : d'une part comprendre les effets cinétiques et/ou non-linéaires (en particulier dans le cas des couplages electrostatiques ions-electrons) et d'autre part fournir des preuves observationnelles de leur existence dans les plasmas spatiaux.
Cette étude se fonde sur des observations in-situ et des simulations numériques. Les mesures de formes d'onde de champ électrique sont fournies par l'instrument radio WAVES embarqué sur les sondes STEREO. Les simulations numériques sont réalisées en utilisant un code cinétique Vlasov-Poisson unidimensionel dans l'approximation électrostatique.
Les résultats de cette thèse sont les suivants. (1) Une méthode de mesure et d'étalonnage in-situ des fluctuations de densité haute fréquence (0.1 - 1kHz donc dans un domaine non accessible par les instruments particulaires) a été développée en utilisant les variations quasi-statiques du potentiel flottant des sondes. (2) Des mesures simultanées de champ électrique et de densité sur plus de trois ans de données fournissent la première preuve observationnelle d'effets pondéromoteurs dans le vent solaire, permettant de coupler la densité du plasma aux ondes de Langmuir de grande amplitude. (3) Ce travail fournit également la première preuve observationnelle directe de l'instabilité de décroissance des ondes de Langmuir, un archétype d'interaction onde-onde, associé à un sursaut de type III. Le caractère résonant de l'interaction est validé grâce aux observations de forme d'ondes, en vérifiant la conservation de l'impulsion et de l'énergie (relations de résonances), ainsi que la résonance de phase à travers une analyse de bicohérence. Les simulations fournissent une nouvelle expression du seuil d'instabilité de décroissance des ondes de Langmuir, en accord avec les niveaux d'énergie observés. (4) Enfin, les simulations Vlasov-Poisson montrent que l'évolution de la turbulence faible de Langmuir sur des temps longs tend vers un régime de turbulence forte via la formation de structures cohérentes électrostatiques (cavitons).
Cette thèse illustre l'importance d'une approche complémentaire observations-simulations pour l'étude des plasmas spatiaux, ainsi que le rôle fondamental joué par les processus cinétiques.

Riassunto

Gran parte dei plasmi astrofisici, tra cui il vento solare, sono non-collisionali. In questi sistemi infatti le frequenze tipiche della dinamica del sistema sono grandi in confronto alla frequenza di collisione, e quindi questi sistemi non possono essere considerati all'equilibrio termodinamico locale. In questo contesto, i processi cinetici e/o nonlineari (interazione onda-particella e onda-onda) permettono una ridistribuzione dell'energia nel plasma. Nonostante che sia i processi cinetici che la teoria nonlineare del plasma siano stati intensivamente studiati a partire dagli anni sessanta, mancano ancora prove osservative precise che tali processi abbiano effettivamente luogo nei plasmi spaziali.
Nell'ambito dei plasmi spaziali e più in particolare per quanto riguarda la dinamica elettrostatica ionica ed elettronica, questa tesi di dottorato si pone un obiettivo duplice: (i) comprendere la fisica relativa ai processi cinetici e/o nonlineari e (ii) dare prove osservative di quest'ultimi.
Lo studio si basa sia su osservazioni spaziali in-situ che su simulazioni numeriche. Misure di forme d'onda del campo elettrico provengono dello strumento radio WAVES sulle sonde STEREO. Le simulazioni numeriche sono state effetuate usando un codice cinetico Vlasov-Poisson unidimensionale nel limite elettrostatico.
I risultati sono i seguenti. (1) È stato sviluppato un metodo di misura e di calibrazione in-situ di fluttuazioni di densità a piccola scala, usando le variazioni quasistatiche del potenziale della sonda. (2) Si è ottenuta la prima prova osservativa di effetti ponderomotrici nel vento solare (accopiando nonlinearmente la densità del plasma alle onde plasma elettroniche, dette Langmuir, di grande ampiezza), analizzando più di tre anni di osservazioni in-situ del campo elettrico e di densità. (3) La prima prova diretta del decadimento Langmuir elettrostatico (un archetipo di interazione onda-onda) è stata ottenuta associando osservazioni e simulazioni. Le forme d'onde in-situ, associate ad un evento di tipo III, permettono di osservare il carattere risonante dell'interazione sia attraverso la conservazione del momento e dell'energia, che attraverso la coerenza di fase, per mezzo di un'analisi detta di bicoerenza. Una nuova soglia per il decadimento Langmuir elettrostatico è ricavata dalle simulazioni tenendo conto della dinamica dell'interazione, convalidata dalle osservazioni. (4) Infine, le simulazioni Vlasov-Poisson mostrano che l'evoluzione della turbolenza Langmuir debole su tempi lunghi tende asintotticamente verso un regime di turbolenza forte tramite la formazione di cavitoni Langmuir.
Questa tesi illustra l'importanza strategica di un approccio basato sia sulle osservazioni sia sulle simulazioni numeriche.

Contents

Chapter 1

Introduction

1.1 Studying nonlinear space plasma dynamics... What for?

One of the main difficulty in describing space plasmas dynamics is that the systems are often out of equilibrium since collisions are infrequent. Indeed, for most astrophysical plasma the mean free path is much larger than the other typical scale lengths that characterize the plasma dynamics (gyration radii, skin depth, Debye length). In the absence of collisions, what are the processes responsible for the relaxation of the system?

In a collisionless plasma, the particle velocity distribution function is not bound to be Maxwellian, but may exhibit strong distortions. The distribution function distortions may be source of free energy that feeds the development of different kinds of kinetic instabilities. Temperature anisotropies are the source of several electromagnetic instabilities (e.g. the firehose, mirror and ion-cyclotron instabilities for proton temperature anisotropies, Weibel and whistler instabilities for electron temperature anisotropies, etc.), while beams of charged particles are the source of electrostatic instabilities (e.g. Buneman and bump-on-tail instabilities) or electromagnetic instabilities (current filamentation instability). Different kinds of waves are thus generated that extract energy from the unstable particle distribution function.
These waves can in turn interact with the particles and modify the distribution function. *Wave-particle interaction* is a nonlinear process that, in the absence of collisions, "thermalizes" the plasma through energy exchange between the waves and the particles. The collisionless plasma certainly does not finally reach a Maxwellian equilibrium, but at least the unstable irregularities of the distribution functions are smoothed through wave-particle interactions.
A second kind of nonlinear process, namely *wave-wave interaction*, describes the interaction between different plasma oscillations. The energy exchanged between different waves

enables to redistribute the energy at different time and/or spatial scales. In the context of the relaxation of a collisionless plasma, wave-wave interactions are a way to transfer energy from oscillations for which wave-particle interactions would be inefficient to other oscillations where coupling with particles is this time efficient.

To put it in a nutshell, wave-wave interactions enable the circulation of the energy between different plasma waves while wave-particle interactions finally give the energy back the distribution function. Nonlinear plasma processes are the channels that enable, in the absence of collisions, to redistribute the energy at scales much smaller than the particle mean free path. Nonlinear plasma processes has been extensively studied from the 70s [*Sagdeev and Galeev*, 1969; *Davidson*, 1972; *Hasegawa*, 1975]. The key problem is to identify, for a given set of parameters and among the wide range of possible nonlinear plasma processes, the efficient ones. To answer this question, we need both to (i) understand the nonlinear processes, to this end numerical experiments are of great help, (ii) afford observational evidence of nonlinear processes in space plasma.

We address this problem in the case of weakly magnetized plasmas, for electrostatic waves. This work focuses on the *wave-wave interactions* that couple the plasma dynamics at the electron scales, namely Langmuir waves, with the dynamics at ion scales, namely ion acoustic waves. The nonlinear behavior of Langmuir waves is an archetype of nonlinear effects in plasma physics. Such a study is interesting for two reasons: (a) because Langmuir waves are ubiquitous in space plasma and (b) because the nonlinear behavior simplified in the case of Langmuir waves since they are linearly polarized, electrostatic oscillations. They can thus be described in the electrostatic approximation using a one dimensional description. This aspect considerably simplifies the geometry of the problem and hence the understanding of both observations and numerical investigations.

Such work is made possible owing to the presence of three complementary aspects: (i) a typical example of out of equilibrium and weakly magnetized astrophysical plasma accessible for in-situ measurements, namely the solar wind, (ii) a space instrumentation that enables to resolve the electrostatic scales, in our case the WAVES experiment on board of STEREO spacecraft, (iii) and the nowadays computational capabilities which enable accurate and almost noiseless numerical investigations of nonlinear kinetic plasma dynamics.
Throughout this Ph.D. thesis, I present observational results and numerical studies that prove the occurrence of nonlinear processes in the interplanetary medium. In particular, I focus my attention on the mechanism that enables to couple high frequency **electron** plasma disturbances (Langmuir waves) to low frequency **ion** dynamics.

1.2 Modeling collisionless space plasma: the Vlasov equation

As discussed above the solar wind is a collisionless medium. This means that usually the phenomena of interest have time (and space) scales short with respect to collision time (and space) scales; in this sense, the absence of collisions is a general feature of space plasma. On these time scales, of the order or smaller than the ballistic transit time of the particles, the motion of charged particles is dominated by the interaction with the waves that are created by the deformation of the distribution functions induced by these motions. This enables to describe the plasma dynamics by a mean field approximation. The kinetic model of a weakly coupled plasma, which allows to take into account departures from equilibrium, is the Vlasov equation, also called collisionless Boltzmann equation [*Vlasov*, 1938, 1968].

The Vlasov equation is obtained from the Liouville equation for the n-particles distribution function, reordered in term of the reduced distribution functions through the so-called BBGKY hierarchy. The absence of collisions enable to truncate the BBGKY chain by neglecting the two-particle correlation function, leading to the Vlasov equation for the one-particle distribution function[1]. The Vlasov equation describes, in the collisionless regime, the evolution of the plasma species distribution function:

$$\frac{\partial f_\alpha}{\partial t} + \left(\vec{v}.\vec{\nabla}_x\right)\ f_\alpha + \left(\frac{\vec{F}}{m_\alpha}.\vec{\nabla}_v\right)\ f_\alpha = 0 \tag{1.1}$$

The α-th plasma species, composed by particles of mass m_α, is characterized by the distribution function $f_\alpha(\vec{x},\vec{v},t)$ defined so that $f_\alpha(\vec{x},\vec{v},t)\ \vec{dx}\vec{dv}$ is the number of particles located in a phase space volume element $\vec{dx}\vec{dv}$ centered on $(\vec{x},\vec{v})$ at time t. $\vec{F}$ is the force exerted on the α-th species particles, given by the Lorentz force due to the electromagnetic field self-consistently generated by the plasma charge distributions and motions and all other external forces.

In the following, the discussion is restricted to weakly magnetized plasma, i.e. to plasma such that the plasma frequency is much higher than the electron cyclotron frequency. We thus neglect the influence of the magnetic field at small scales and limit ourselves to the electrostatic approximation. The force $\vec{F}$ is then associated with the self-consistent electric field $\vec{E}$:

$$\vec{F} = q_\alpha \vec{E} = -q_\alpha \vec{\nabla}\Phi \tag{1.2}$$

where q_α is the electric charge associated with the α-th plasma species and Φ is the electric potential expressed in terms of the distribution functions through Poisson equation:

$$\Delta\Phi = \frac{1}{\epsilon_0}\ \sum_\alpha \left(\int_v f_\alpha dv\right) \tag{1.3}$$

[1]The derivation of the Vlasov equation is found in most textbooks on kinetic plasma physics or statistical physics [*Krall and Trivelpiece*, 1973; *Diu et al.*, 2001]

with ϵ_0 the vacuum permittivity.
The nonlinearities of the Vlasov-Poisson system arise from the last term $\left(\frac{\vec{F}}{m_\alpha}.\vec{\nabla}_v\right) f_\alpha$ of Vlasov equation 1.1, because the force $\vec{F}$ is a function of the distribution functions f_α. We will come back on that point in the next section, when describing some nonlinearities of the Vlasov-Poisson system. Let us first recall some classic linear results.

An important physical mechanism associated with the kinetic description of plasmas is the so-called Landau damping [*Landau*, 1946]. It is a linear process leading to the decrease of the wave amplitude when the distribution function locally varies monotonically, in velocity space, at velocity close to the wave phase velocity v_{ph} such that $\left(v\frac{\partial f}{\partial v}\right)|_{v_{ph}} < 0$. In the case of a monotonically decreasing distribution function, Landau damping is efficient since there are more particles able to extract energy from the wave than particles transferring energy to it. This case is illustrated in the top panel of Fig. 1.1 where the distribution function is locally decreasing at the phase velocity of the wave. Particles traveling faster (resp. slower) than the wave release (resp. extract) energy to (resp. from) the wave.

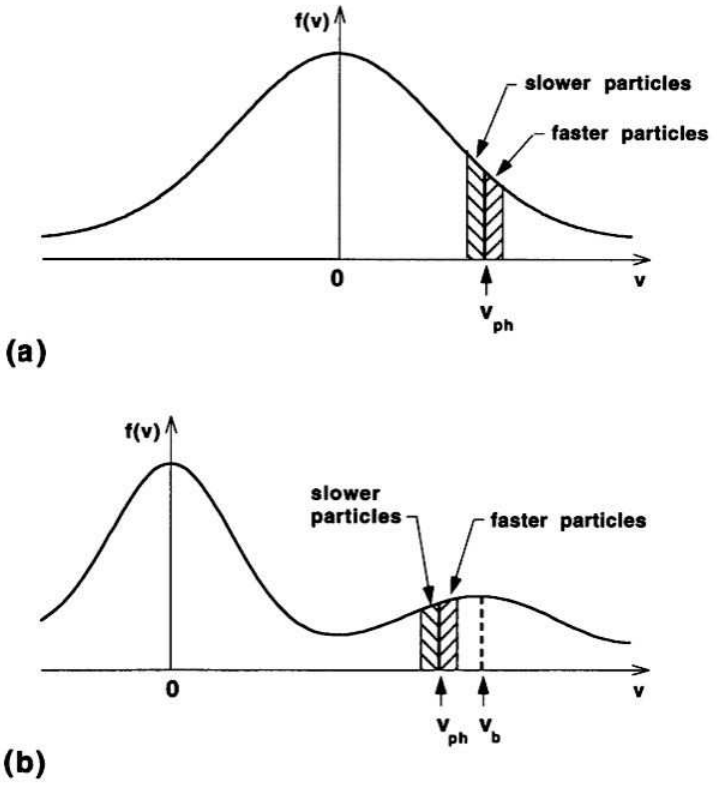

Figure 1.1: Schematic representation of a distribution function for which the wave at phase velocity v_{ph} is kinetically damped by Landau damping (a) or excited by bump-on-tail instability (b). In case (a) (resp. (b)), the energy gained from the waves by the slower particles is more (resp. less) than the energy given to the waves by the faster particles. [Adapted from *Tsurutani and Lakhina*, 1997]

As already mentioned before, in a non-uniform and non-stationary situation, even an initially Maxwellian plasma can be severely distorted from this Maxwellian state. In particular, it is possible for a plasma to exhibit a beam in velocity space. Around a given velocity, the particle distribution contains more fast particles than slow ones, as shown is the bottom panel of Fig. 1.1. Such configuration is an example of unstable distribution function, source for free energy for the development of the so-called bump-on-tail instability, or inverse Landau damping, for configurations such that $\left(v\frac{\partial f}{\partial v}\right)|_{v_{ph}} > 0$. There is a net injection of particle energy into a resonant wave traveling with a phase velocity v_{ph} slightly inferior to the beam velocity v_b.
In the electrostatic case, described by the Vlasov-Poisson system, this kind of deformation of the distribution functions may generate either Langmuir waves and ion acoustic waves[2]. In the following, we will be interested in the weak nonlinearities that couple together this two modes. Let us briefly describe these linear modes.

Ion acoustic waves are compressible oscillations of the plasma density (both ions and electrons). The pressure force is coupled to a restoring electric field generated by a (small) charge separation between ions and electrons. The dispersion relation of ion acoustic waves, in the limit where the electron temperature is much larger than the proton temperature, reads:

$$\omega_{_S} = \frac{k_{_S} c_s}{(1 + k_{_S}^2 \lambda_{_D}^2)^{1/2}}$$

where $k_{_S}$ is the ion acoustic wave vector, $c_s = \sqrt{T_e/m_i}$ is the ion sound speed and $\lambda_{_D}$ the Debye length, the screening length scale of a particle of charged e, defined by

$$\lambda_{_D} \equiv \sqrt{\frac{\epsilon_0 k_{_B} T_e}{n_e e^2}} = v_{th,e}/\omega_{pe}$$

with T_e the electron temperature, m_i the ion mass and $k_{_B}$ the Boltzmann constant.
When the electron and ion temperature are close, ion sound speed get close to the ion thermal speed. This situation corresponds to case illustrated in the top panel of Fig. 1.1, for which much more resonant particles travel slower than the wave, extracting energy from it. Ion acoustic waves are thus highly damped by Landau damping when electron and ion temperatures are close.
For ion acoustic wavelengths much larger than the Debye length, the dispersion relation reduces to $\omega_{_S} = kc_s$. This wave is equivalent to a sound wave for which the ions would have the temperature of the electrons.

Langmuir waves, also called electron plasma waves, are high frequency oscillations of the electron density over a fixed ion background. The frequency is high enough for the ions not to have time to respond because of their higher inertia. The charge separation

[2]The wave vector associated with Langmuir waves and ion acoustic waves is parallel to the oscillating electric field associated with the wave. In this case, Faraday law shows that no magnetic field is associated with the oscillation of the electric field, this is the origin of the term "electrostatic" waves. The "electrostatic world" modeled by the Vlasov-Poisson system actually corresponds to the frequency domain between the electron cyclotron frequency f_{ce} and the plasma frequency f_{pe}.

generates an electric force acting as the restoring force. In the cold plasma approximation, i.e. when the thermal velocity of the plasma is much smaller than the phase velocity of the wave, the Langmuir waves oscillate at the plasma frequency $f_{pe} = \omega_{pe}/2\pi$. We recall the expression of the (angular) plasma frequency:

$$\omega_{pe} = \sqrt{\frac{n_e e^2}{\epsilon_0 m_e}}$$

with n_e the electron density, m_e the electron mass and e the elementary charge. When taking into account the finite temperature of the electrons, a (small) frequency correction appears, leading to the following dispersion relation:

$$\omega_{_L}^2 = \omega_{pe}^2 + 3k_{_L}^2 v_{th,e}^2 = \omega_{pe}^2(1 + 3k_{_L}^2 \lambda_{_D}^2)$$

where $k_{_L}$ is the wave vector, $v_{th,e}$ the electron thermal velocity. The Langmuir waves propagate at the group velocity $v_g = 3v_{th,e}^2/v_\phi$, with $v_\phi = \omega_{_L}/k_{_L}$ the phase velocity.
Langmuir waves are found in space plasma wherever there are electrons beams propagating parallel to the magnetic field. These electrons then radiate Langmuir waves through the bump-on-tail instability (bottom panel of Fig. 1.1).
Plasma kinetic theory shows that unless the phase velocity is much greater than the electron thermal velocity ($\omega_{_L}/k_{_L} >> v_{th,e}$, equivalent to $k_{_L}\lambda_{_D} << 1$), the Langmuir wave is damped by the already mentioned Landau damping (top panel of Fig. 1.1).

The Landau damping is a linear phenomenon that describes the local effect (in velocity space) of the distribution function on the waves. However, it does not describe the feedback of the same wave on the resonant particles at $v \simeq v_{ph}$. The self-consistent picture requires to take into account the nonlinearities of the Vlasov equation, contained in the term $\left(\frac{\vec{F}}{m_\alpha}.\vec{\nabla}_v\right) f_\alpha$.

1.3 Nonlinear evolution of Langmuir waves

Landau damping (resp. inverse Landau damping) describes how a local monotonic variation of the distribution function close to the wave phase velocity affects the wave amplitude. In return, the wave also modifies the distribution function by transferring (resp. extracting) energy to (resp. from) the distribution function. In the absence of binary collisions, this nonlinear feedback of the waves on the particles is the mechanism that lead to the relaxation of the distribution function.
The nonlinear Landau damping described the trapping of resonant particles in the potential well of the wave. Quasilinear diffusion of the distribution function in velocity space then leads to the local flattening of the distribution function at velocities close to the wave phase velocity ($(\frac{\partial f}{\partial v})|_{v\simeq v_{ph}} = 0$), which eventually stops the energy exchange between the wave and the distribution function. Other kind of wave-particle interactions can compete with the quasilinear diffusion of the distribution function. For instance, for large enough Langmuir waves, trapped particles may in turn interact with the Langmuir wave oscillation and generate coupled sideband oscillations (sideband instability).
However, wave-particle interactions are efficient in extracting energy from the waves only when there are enough resonant particles traveling at the wave phase velocity $v \simeq v_{ph}$. In the particular case of Langmuir waves, this means that the wave phase velocity is of the order or a few times greater than the electron thermal velocity, corresponding to the wavevector domain $k_L \lambda_D > 0.1$. This condition is not, however, valid in the solar wind. Electron beams have typical beam velocities $v_b \simeq 10 - 50\ v_{th,e}$ that generate Langmuir waves with phase velocities $v_{ph} \simeq v_b$ much greater than the electron thermal velocity. This corresponds to wavevectors $k_L \lambda_D \sim 10^{-2} - 10^{-1}$.

In the following I will consider the evolution of these small k_L Langmuir waves. The nonlinear evolution of Langmuir waves is a broad topic. I hereafter limit the discussion to the electrostatic case and focus on the nonlinear feedback of Langmuir waves on the ion background density.

Ponderomotive effects

Coupling between electrons and ions dynamics enable to transfer the energy from electron time scales to ion time scales. Such nonlinear instabilities are described in the framework of the Zakharov model [*Zakharov*, 1972]. The derivation of the Zakharov equations is based on a simplified model[3] involving fluid concepts. The model leads to two equations coupling the high frequency dynamics of the electric field to the low frequency dynamics of the plasma density. One of these equations describes the evolution of the electric field envelop, including the nonlinearity through a term involving a density fluctuation, and the other describes the evolution of the density fluctuation due to the ponderomotive force (Eq. 1.4) exerted by the Langmuir waves electric field.

[3]The Vlasov description includes the Zakharov equations.

The origin of the ponderomotive force is the following. Oscillations of a wave induces an energy density proportional to the square of its amplitude, equivalent to a pressure. When this energy density varies in space, a force proportional to its gradient is exerted on the plasma. It is defined as

$$F_{pond} = -\frac{e^2}{4m_i\omega_L^2}\frac{\partial E_0^2}{\partial x} \tag{1.4}$$

where $E_0(x)$ is the slowly varying electric field amplitude in space. The ponderomotive effect is an essential nonlinear ingredient for the description of modulated, or localized, large-amplitude high-frequency oscillations of the electric field. Localized Langmuir wavepackets with large enough amplitude can for instance dig ion cavities through this ponderomotive force.

In the framework of the Zakharov model, Langmuir waves evolve through different kinds of wave-wave instabilities (decay instabilities, modulational instabilities) depending on the wavelength and amplitude. Figure 1.2, extracted from *Zakharov et al.* [1985], summarizes the electrostatic instabilities of interest in the case of the nonlinear evolution of a monochromatic Langmuir wave (seen in the energy-wavelength space). Typical parameters in the solar wind, my plasma laboratory, range in region (I) that corresponds to a maximum growth rate for the Langmuir decay instability, a resonant three-wave interaction coupling electron plasma waves (Langmuir waves) with ion density waves (ion acoustic waves).

Three-wave coupling

Wave-wave interactions[4] describe the nonlinear interactions between the (linear) eigenmodes of the system. At least three waves are needed to describe nonlinear wave-wave interactions. The electrostatic decay instability (Fig. 1.2, region I) is a three-wave mechanism, while the modulational instability (region II) is a four-wave coupling.

Let me introduce the basics of three-wave coupling with a simple model. I consider three harmonic oscillators $y_i(t)$ with respective natural frequencies ω_i $(i = 1, 2, 3)$, interacting through a weak quadratic nonlinear coupling via the coupling constant K. This would represent the first order corrections to the linear theory.

$$\begin{aligned}
\frac{\partial^2}{\partial t^2}y_1(t) + \omega_1^2 y_1(t) &= K y_2(t) y_3(t) \\
\frac{\partial^2}{\partial t^2}y_2(t) + \omega_2^2 y_2(t) &= K y_1(t) y_3(t) \\
\frac{\partial^2}{\partial t^2}y_3(t) + \omega_3^2 y_3(t) &= K y_1(t) y_2(t)
\end{aligned}$$

[4]Introductions on wave-wave interactions can be found in most nonlinear plasma physics textbooks [*Sagdeev and Galeev*, 1969; *Bellan*, 2006].

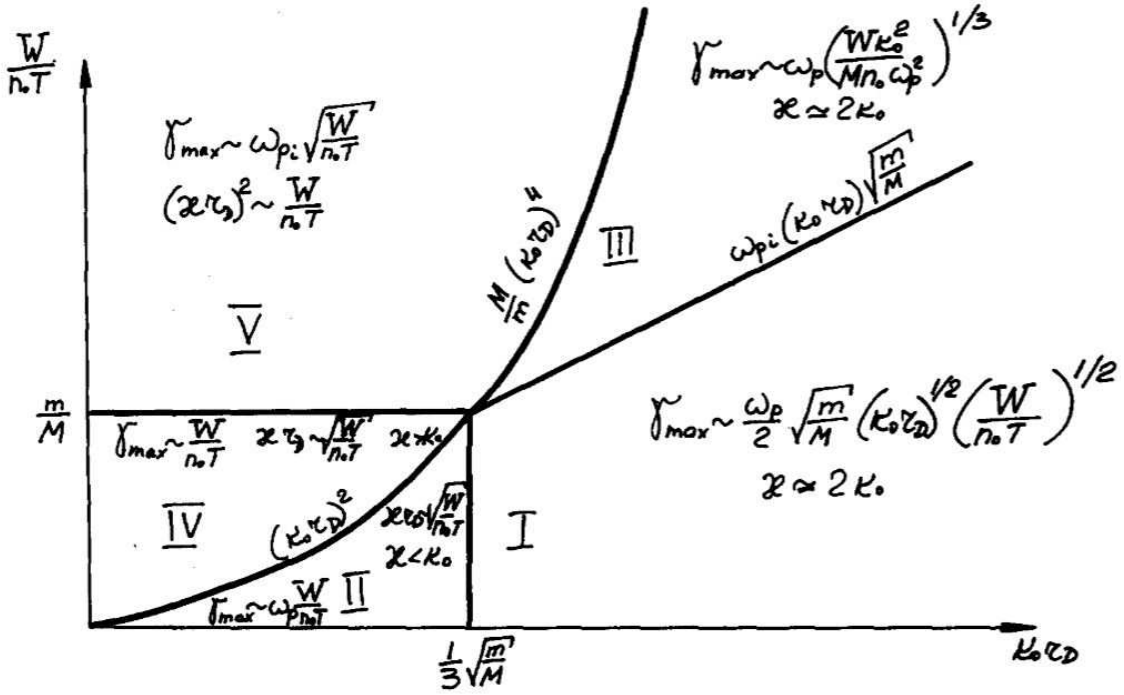

Figure 1.2: Location in the energy-wavelength space of different electrostatic instabilities for a monochromatic Langmuir wave in an isotropic plasma. W/n_0T is the Langmuir electric energy normalized with the thermal energy, $k\lambda_D$ is the wavevector, normalized with the Debye length, corresponding to maximum growth rate. Approximate boundaries are as labeled: **(I) electrostatic decay instability**; (II) modulational instability; (III) modified decay instability; (IV) subsonic modulational instability; (V) supersonic modulational instability. [Source: *Zakharov et al.*, 1985]

Let us express each oscillator in term of a slowly varying amplitude in time $Y_i(t)$ and a rapidly varying phase $(\omega_i t + \phi_i)$ such that $y_i(t) = Y_i(t)\ cos(\omega_i t + \phi_i)$. The right-hand products $KY_i(t)Y_j(t)\ cos(\omega_i t + \phi_i)\ cos(\omega_j t + \phi_j)$ are seen for each oscillator as the sum of two "external" oscillators at frequencies $\omega_i + \omega_j$ and $\omega_i - \omega_j$:

$$\frac{1}{2}KY_i(t)Y_j(t)\ \Big[cos\big((\omega_i + \omega_j)t + (\phi_i + \phi_j)\big) + cos\big((\omega_i - \omega_j)t + (\phi_i - \phi_j)\big)\Big].$$

If the beat due to one of this two "external" oscillators is close to the natural frequency of the left-hand side oscillator

$$\omega_i \pm \omega_j \simeq \omega_k$$

then the forcing is resonant and energy is exchanged between the oscillators.
This picture is easily extended to a propagating wave by adding its wavevector k_i in the phase $(\omega_i t + k_i x + \phi_i)$. It leads to a second equivalent resonant relation on the wavevectors:

$$k_i \pm k_j = k_k.$$

Finally, in order for three-wave coherent interaction to remain efficient, the phase difference between the three waves should not vary much. This is the origin of a third resonant relation that characterizes the phase locking between the waves:

$$\phi_i - \phi_j = \phi_k.$$

A powerful test of this last conservation law is the bicoherence test, described in Appendix D. The three-wave coupling is thus a **resonant** nonlinear interaction.

I now consider two different initial conditions on the relative amplitude between the three waves. First, consider two finite-amplitude oscillations much larger than the third one. This last one grows from the nonlinear coherent interaction of the two preexisting oscillations. This is equivalent to inelastic *scattering*.

Table 1.1: Different possibilities for electromagnetic (e.m.) and electrostatic (e.s.) nonlinear three-wave interactions between electromagnetic waves, Langmuir waves and ion acoustic waves. The last two processes, in bold, were studied in this Ph.D. work.

Mother wave	High frequency daughter wave	Low frequency daughter wave	Common name
e.m.	e.m.	Langmuir	stimulated Raman instability
e.m.	e.m.	acoustic	stimulated Brillouin instability
e.m.	e.m.	zero frequency	self-focusing (e.m. caviton)
e.m.	Langmuir	Langmuir	two-plasmon decay
e.m.	Langmuir	ion acoustic	e.m. parametric decay instability
Langmuir	e.m.	ion acoustic	Langmuir e.m. decay instability
Langmuir	Langmuir	ion acoustic	**Langmuir e.s. decay instability**
Langmuir	Langmuir	zero frequency	**Langmuir caviton**

Now consider a single finite-amplitude oscillation much larger than the two others. Then the large amplitude oscillation feeds the two other oscillations. The initially large amplitude oscillation is called *mother*, while the two others are called *daughters*. This process decreasing the amplitude of the mother oscillation through the resonant amplitude increase of the daughters is called *parametric decay*. Damping effects may eventually be added to this description, introducing a threshold on the mother wave amplitude to trigger its decay.
Some possibilities for three-wave interactions between electromagnetic waves, Langmuir waves and ion acoustic waves are shown in Table 1.1. We now concentrate on a particular case of three-wave coupling between Langmuir waves and ion acoustic waves: the Langmuir electrostatic decay.

Langmuir electrostatic decay

Langmuir electrostatic decay (hereafter LED) – also called Langmuir decay instability or parametric decay instability – is an archetype of wave-wave interaction in an unmagnetized plasma. It is a resonant parametric instability that transfers energy from a finite amplitude Langmuir wave L toward a second Langmuir wave L' and an ion acoustic wave S through a three-wave resonant interaction:

$$L \rightarrow L' + S$$

From a quantum point of view, each Langmuir plasmon decays into a secondary Langmuir plasmon and an ion acoustic phonon as illustrated in Figure 1.3.

An efficient three-wave coupling requires the fundamental equations of energy and momentum conservation to be satisfied:

$$\omega_L = \omega_{L'} + \omega_S \tag{1.5}$$
$$\vec{k}_L = \vec{k}_{L'} + \vec{k}_S \tag{1.6}$$

where ω and $\vec{k}$ are the frequency and wavenumber of the waves, as well as the phase

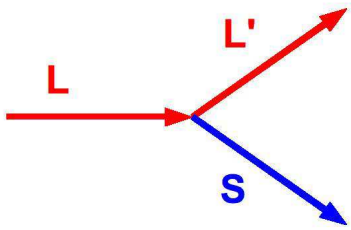

Figure 1.3: Schematic representation of Langmuir electrostatic decay: a Langmuir plasmon decaying into a daughter Langmuir plasmon and an ion acoustic phonon.

locking of the waves:

$$\phi_L = \phi_{L'} + \phi_S \tag{1.7}$$

where ϕ is the phase lag of each wave.

The conservation of momentum and energy during the Langmuir electrostatic decay process is illustrated in Figure 1.4. Combining the respective dispersion relations and the relation of resonance 1.5 and 1.6, we obtain the frequencies and wavenumbers of the daughter Langmuir wave **L'** and ion acoustic wave **S** from a given mother Langmuir wave **L** at frequency ω_L and wavevector k_L. Wavenumbers are of the same order, so that the momentum is well distributed between the product waves, but since the frequency of the ion acoustic wave is much smaller than the frequency of the daughter Langmuir, the energy carried out by the phonon is small compared to the energy carried out by the daughter plasmon, so that almost all the initial energy eventually goes to the daughter Langmuir wave.

When observed on board of a spacecraft, equations 1.5 and 1.6 reduce to a single relation for the Doppler shifted frequencies $f^{Doppler} = \omega^{Doppler}/2\pi$:

$$\begin{aligned} f_1^{Doppler} &= f_1 + \frac{\vec{k}_1}{2\pi}.\vec{V}_{SW} \\ &= (f_2 + f_3) + \frac{(\vec{k}_2 + \vec{k}_3)}{2\pi}.\vec{V}_{SW} \end{aligned}$$

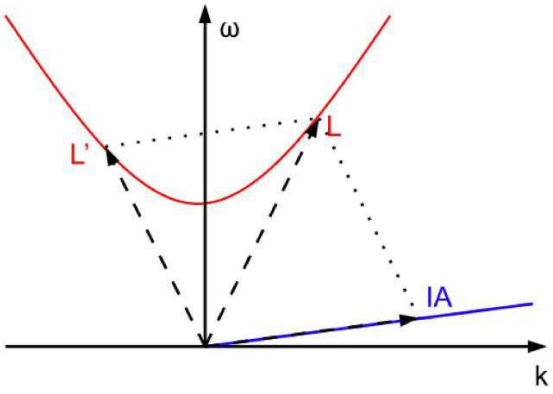

Figure 1.4: Relation dispersion of Langmuir waves (red line) and ion acoustic waves (blue line). The curvature of the Langmuir waves dispersion relation has been voluntarily exaggerated for illustrative purposes. This graphic illustrates the conservation of momentum and energy during the electrostatic decay of the Langmuir wave **L** into the backscattered Langmuir wave **L'** and the ion acoustic wave **S**:

$$\begin{pmatrix} \omega_L \\ \vec{k}_L \end{pmatrix} = \begin{pmatrix} \omega_{L'} + \omega_S \\ \vec{k}_{L'} + \vec{k}_S \end{pmatrix}$$

leading to the following equation for resonance:

$$f_1^{Doppler} = f_2^{Doppler} + f_3^{Doppler} \tag{1.8}$$

Equation 1.8 can be directly tested from *in situ* measurements which combine high spectral and temporal resolution, as well as phase information. Only waveform measurements can provide the required information. Such observations are available with the waveform analyzer of the WAVES instrument on board the STEREO mission that will be discussed in section 2.2.

Moreover, for the LED to develop, the electric field of the mother Langmuir wave has to reach a critical value. The analytical calculation of this threshold has been discussed in *Nishikawa* [1968]; *Sagdeev and Galeev* [1969]; *Dysthe and Franklin* [1970]; *Bardwell and Goldman* [1976]; *Robinson et al.* [1993b] by considering three **monochromatic** waves. The underlying idea is that for the instability to develop, the growth rate γ_{LED} of the two daughter waves must be higher than their own linear Landau damping rates $\gamma_{L'}$ and γ_S:

$$\gamma_{LED} > \sqrt{\gamma_{L'}\gamma_S}$$

The threshold for the parametric decay of a monochromatic mother Langmuir wave can be expressed in term of the electric energy of the mother Langmuir wave, normalized to the kinetic energy [*Bardwell and Goldman*, 1976]:

$$\frac{\epsilon_0 E_L^2}{nk_BT} > 8\frac{\gamma_{L'}}{\omega_{L'}}\frac{\gamma_S}{\omega_S}$$

with $\omega_{L'}$, ω_S the angular frequency of the daughter waves. The threshold for electrostatic decay has been estimated for typical solar wind parameters to be $(\epsilon_0 E^2)/(nk_BT) \geq 2.5 \times 10^{-5}$ [*Lin et al.*, 1986b]. However, Langmuir waves above this threshold are observed without any signature of electrostatic decay.

If the theory relative to Langmuir electrostatic decay is well established since the 60s, first observations of the ion acoustic decay product in laboratory experiments is astonishingly recent [*Depierreux et al.*, 2000], while no such ion acoustic decay product had yet been found in space observations. We show the first observation of this nonlinear process in space plasma in *Henri et al.* [2009]. Also, the threshold for Langmuir electrostatic decay to occur has been revisited in *Henri et al.* [2010b] to consider the most realistic case of **localized, propagating Langmuir wavepackets** in solar wind temperature conditions. These two new results are discussed in section 3.2.

Transition toward strong Langmuir turbulence

Until now, I have discussed wave-wave interactions in term of the interactions between linear modes. This describes *weak* nonlinearities, i.e. corresponding to electric fields large enough for the nonlinearities to affect the dynamics of the system, but however not too

high so that the description in terms of linear modes is still valid. In other terms, the nonlinearities do not strongly modified the dielectric response of the plasma. This is the framework of *weak turbulence*, in opposition to the so-called *strong turbulence*, when the amplitude is so large that the linear dielectric response does not apply anymore. The transition between weak and strong turbulence is generally described in term of (i) the energy and (ii) the spectral width of the waves. For an initial Langmuir wave of high enough energy (and/or large enough spectrum), the nonlinear dynamics is govern by strong turbulence effects [*Robinson*, 1997; *Goldman*, 1984].

It is known that the modulational instability, found for $k_L \lambda_D < 10^{-3}$ (see Fig. 1.2, p. 9), can evolve toward strong turbulence through the collapse of modulated Langmuir wave packets that eventually form Langmuir cavitons [*Thornhill and ter Haar*, 1978]. When the Langmuir amplitude is high enough and/or its spectrum is large enough, the Langmuir pump wave beats with itself (modulational instability) and modifies the equilibrium via the ponderomotive pressure which acts to expel the plasma. The Langmuir wave may then dig a hole in the plasma density which can in return focus and even trap the pump wave. This is the origin of the so-called Langmuir *caviton*. It is a non propagating coherent structure characteristic of strong Langmuir turbulence, formed by a localized electric field oscillating at the plasma frequency self-consistently associated with density cavities *Zakharov* [1972]. By "self-consistently" we mean that the localized oscillating electric field is an eigenmode of the ion density cavity, while the ion density cavity is itself sustained by the ponderomotive force generated by the high frequency electric field oscillation.
In this picture the transition from weak to strong turbulence seems to be controlled by the amplitude of the initial wave.

I report in *Henri et al.* [2010d], described in section 3.3, that the Langmuir electrostatic decay can also evolve toward the formation of cavitons. I show that the transition from weak to strong Langmuir turbulence is not only determined by an initial Langmuir wave with strong amplitude and/or large spectral width, but that it also occurs for the long-time weak-turbulent evolution of a monochromatic wave at moderate amplitude. It illustrates the breakdown of long time evolution Langmuir weak turbulence, already discussed by other authors for the general description of wave turbulence [*Biven et al.*, 2001, 2003]. Conceptually, such transition occurs when the time evolutions have reached the time scale of strong turbulence effects.

Contents

This thesis is organized as follow. I first describe in chapter 2 the tools I used for my study: STEREO observations in the solar wind (section 2.1) of both electric field (section 2.2) and density fluctuations (section 2.3) and numerical kinetic simulations (section 2.4) to interpret the observed data (section 2.5). To ease the reading, the details are given in the appendices.
The chapter 3 is devoted to the comments on the main results. I first show observational evidence of Langmuir ponderomotive effects (section 3.1), then evidence of Langmuir electrostatic decay is provided by complementary observations and numerical simulations (section 3.2). I finally discuss the long time evolution of weak Langmuir turbulence (section 3.3). The published papers can be found there (section 5).
The last chapter discusses the consequences of this work and provide new perspectives for future developments.

Chapter 2

The complementary tools: from in-situ observations to kinetic simulations.

Studies of space plasma nonlinear dynamics become possible owing to the favorable conjunction of three different factors.

(i) We have a direct access to a *natural plasma laboratory*. Near-Earth space plasmas: the ionosphere, the magnetosphere and, in the particular context of this thesis, the solar wind are examples of collisionless plasma that are accessible for in-situ plasma experiments. One could argue that plasma experiments may be enough to study the wide range of plasma nonlinearties. If major advances have indeed been made through the interrelationship between laboratory and space plasma experiments, "it is unrealistic to expect the dimensional parameters corresponding to space plasma to be matchable in the laboratory" [*Koepke*, 2008].

(ii) Space instrumentation, through *in-situ* measurements, gives access to the processes at the kinetic scales. In particular, the electromagnetic fields are observed through high cadence waveform measurements which enable observations of wave-wave interactions[1].

(iii) Last but not least, we can accurately model kinetic plasma. Modern computers start to reach the necessary computing power to investigate the nonlinear dynamics of plasmas through noiseless simulations. The joint investigation of numerical experiments and space plasma observations is essential to reveal the efficient nonlinear mechanisms taking place in astrophysical plasma to redistribute free energy at small scales.

[1]Unfortunately, up to now, space instrumentation relative to particle experiments does not enable to sample the distribution functions at high enough rate, at least in the solar wind, to directly observe wave-particle interactions, which are the processes that finally thermalize, in some way, the plasma.

2.1 The solar wind: a natural laboratory for nonlinear plasma dynamics

The solar wind is the expansion of the solar corona outward into the solar system. It is a stream of fully ionized atomic particles, mostly composed of electrons and protons[2] emitted outward from the sun, with a density of a few particles per cubic centimeter. The solar wind has two components distinguished by their average speed.Representative properties of the solar wind, as observed in the ecliptic plane at the heliocentric distance of one astronomical unit, are summarized in table 2.1. Let us now give a quantitative perspective on some typical plasma parameters.

Table 2.1: Representative Solar Wind Properties (Ecliptic Plane, 1 AU). The solar wind velocity, density, etc. are highly variable; the quantities represented in the table are illustrative only. The temperatures given are kinetic temperatures.

Property	Typical Value
Slow solar wind mean velocity	400 km.s^{-1}
Fast solar wind mean velocity	800 km.s^{-1}
Density n	1-10 cm^{-3}
Proton temperature T_p	1-2 10^5 K
Electron temperature T_e	1-5 10^5 K
Magnetic field	5 10^5 gauss (5 nT)
Composition	electron, ions: 96% protons, 4% He^{++}

The solar wind is an archetype of collisionless and weakly magnetized plasma flow. First, the solar wind flow is collisionless. The typical Debye length is typically $\lambda_D \simeq 10$ m at 1 AU, so that the plasma parameter $g = n\lambda_D^3$, which represents the number of particles in a Debye sphere, is $g \simeq 10^9$, equivalent to a Coulomb logarithm $\log g \sim 20$. In other words, the solar wind plasma is weakly coupled. An equivalent point of view consist in realizing that at 1 Astronomical Unit (hereafter AU), the solar wind mean free path is about $\lambda_{mfp} \sim 10^{11}$ at 1 AU, i.e. of the order of the length scale of the system itself. The collision frequency is then typically $\nu \sim 10^{-5}$ Hz, much smaller that the other typical frequencies. Since collisions are very unlikely on the typical length scale and time scales of interest, the plasma components depart from Maxwellian equilibrium, exhibiting different anisotropies and suprathermal components, confirmed by in-situ observations of electron [*Montgomery et al.*, 1968; *Pilipp et al.*, 1987; *Maksimovic et al.*, 2005] and proton [*Hundhausen et al.*, 1970; *Marsch et al.*, 1982; *Hammond et al.*, 1996] distribution functions. The particle distribution function is usually described with a Maxwellian core of thermal particles, a halo of superthermal particles and a strahl of magnetic field-aligned high energy particles directed in the anti-sunward direction. On top of that, local disturbances may lead to

[2]The ion part of the solar wind is composed of 96% of protons (hydrogen nuclei) and 4% of α particles (helium nuclei), with a trace of heavier nuclei.

the appearance of beam, or anisotropies. That is why studying the solar wind requires a kinetic approach to explain the observed deformations of the distribution functions that a fluid approach is enable to describe.
The solar wind can be considered weakly magnetized because the plasma frequency is much larger than the gyrofrequencies. At 1 AU, the plasma frequency is about $f_{pe} \sim 10$ kHz, while the electron gyrofrequency is $f_{ce} \sim 100$ Hz. The electrostatic domain thus ranges from 100 Hz to a few kHz at the Earth radii. This is the range of frequency where ion acoustic and Langmuir waves are found.

High energy electron beams propagating parallel to the ambient magnetic field are formed by several electron acceleration mechanisms such as in shocks and magnetic reconnection regions. These deformations of the distribution function then radiate Langmuir waves. In this thesis I have illustrated the nonlinear evolution of beam-driven Langmuir waves in two regions: in the Earth foreshock and during Type III bursts.

The solar wind flow is supersonic and superalfvenic; for example, in the ecliptic plane at 1 AU the flow velocity is typically 300 to 800 km.s^{-1}, whereas typical sound and Alfvén

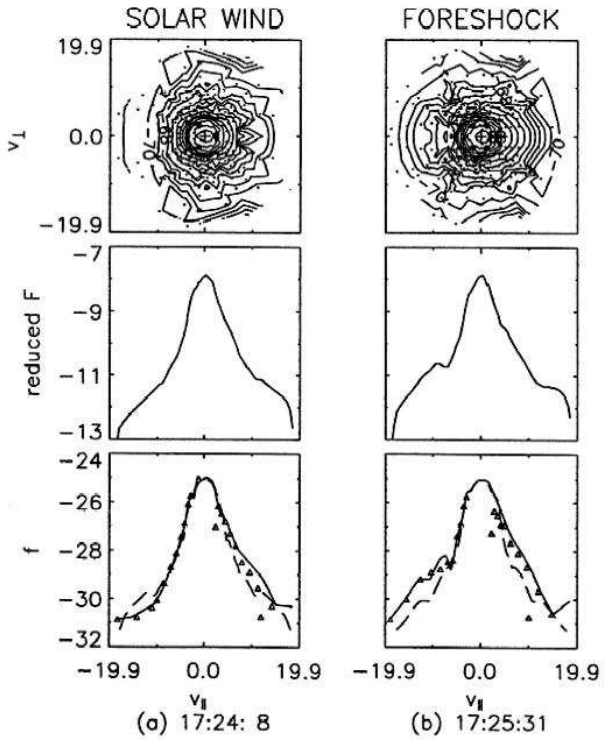

Figure 2.1: Observations of the electron distribution function with SWE instrument onboard WIND spacecraft in a) the undisturbed solar wind and b) the Earth electron foreshock. Upper panels: iso-contours of the electron distribution function f($v_\parallel, v_\perp$), with $v_\parallel$ (resp. $v_\perp$) the velocity parallel (resp. perpendicular) to the ambient magnetic field. Middle panels: reduced distribution functions f($v_\parallel$). Bottom panels: parallel cut (solid curve) and perpendicular cur (dashed line) through f($v_\parallel, v_\perp$). [Source: *Fitzenreiter et al.*, 1996]

speeds are of order 50 km.s^{-1}. Since the flow is supersonic, collisionless shocks are formed. Shock waves travelling outwards the Sun in the solar wind are formed when the fast solar wind flow encounters the slow solar wind flow, or when plasma is ejected from the solar corona after filament disruptions (CMEs). Standing bow shocks are also formed when the solar wind is deflected by planetary obstacles. In the absence of collisions, the main process that dissipates the energy at the shock is the reflection of particles upstream the shock, forming electron and ion beams. Langmuir waves are observed where the electron beams are formed in front of these shocks. This is for instance the case of the Earth's electron foreshock. It is the region upstream from the bow shock that is downstream of the magnetic field lines tangent to the shock. The foreshock plasma includes convected solar wind plasma as well as electrons reflected by the bow shock. The Earth's electron foreshock is easily accessible for in-situ space plasma experiments that detect the reflected electron beams, as shown in Fig. 2.1. The apparition of the electron beam at negative velocity is observed when the WIND spacecraft enters the electron foreshock.

A second example of process that leads to the generation of Langmuir waves in the solar wind are the Type III bursts. During the violent reorganizations of intense magnetic fields in and above the solar photosphere called solar flares, usually occurring in active regions on the sun, a large amount of energy is release through radiation (especially UV and X-rays) and acceleration of particles in the solar corona. High energy electrons (1-100 keV) are expelled from the solar corona and travel along the interplanetary magnetic field lines, producing a bump on the local electron distribution function. Fig. 2.2 shows an

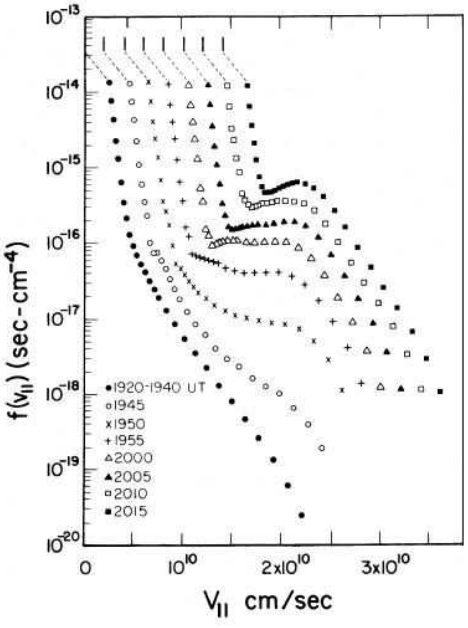

Figure 2.2: Electron distribution function, in the velocity direction parallel to the ambient magnetic field, measured by ISEE 3 during the onset of a Type III burst at different times. [Adapted from *Lin et al.*, 1981]

observational example of such deformation of the electron distribution function, when the electrons coming from the solar corona crosses the spacecraft. Note the apparition of the electron beam at $v_b = 2\ 10^{10}$ cm.sec^{-1}. Due to this unstable configuration of the electron distribution function, Langmuir waves resonantly grow via bump-on-tail instability such that $\omega_{_L}/k_{_L} \simeq v_b$.

During Type III events as well as in the electron foreshock, the beam-driven Langmuir waves somehow convert to electromagnetic waves at the *local* electron plasma frequency f_{pe} (fundamental emission) or twice this value $2f_{pe}$ (harmonic emission). I recall that the plasma frequency scales as the square root of the plasma density n ($\omega_{pe}^2 = ne^2/\epsilon_0 m_e$) and the plasma density decreases with the heliocentric distance r because of the spherical expansion of the solar wind ($n \propto r^{-2}$). In the case of Type III bursts, electron beams are observed to travel for long distances (several astronomical units, across the solar wind). As the high energy electrons, expelled during a flare, ballistically travel from the Solar corona across the solar wind, Type III radio emissions simultaneously show a pronounced time drift towards lower frequencies, as shown in Fig. 2.3. This is the main signature of Type III radio bursts.

The physical mechanism that leads to the generation of these radio emissions has however not yet been identified. Different models have been developed to explain the origin of the

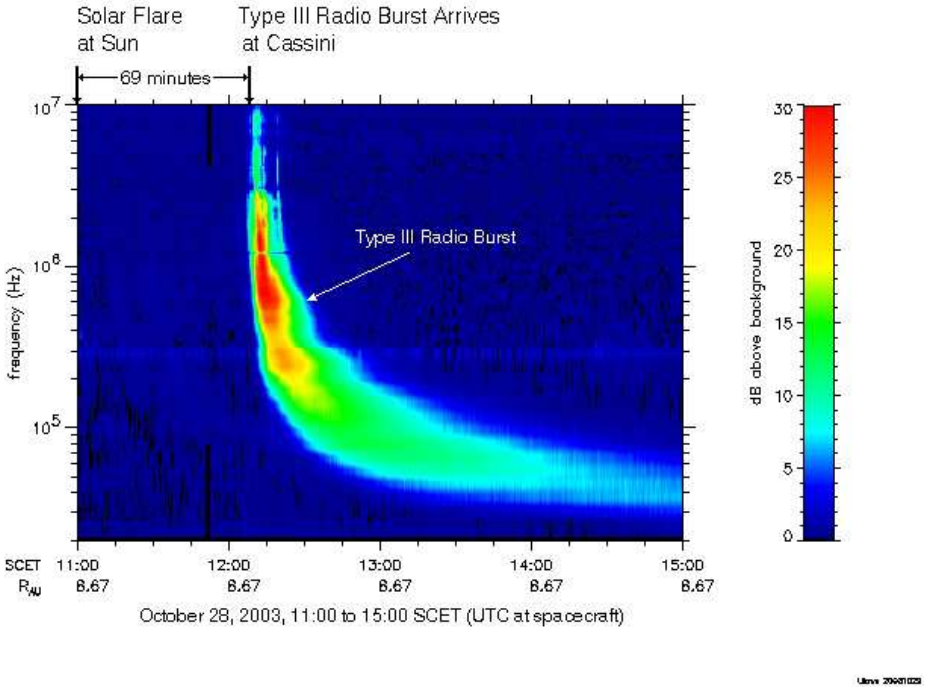

Figure 2.3: Typical "dynamic diagram" of a Type III radio burst. The dynamic diagram shows the time-frequency evolution of the radio emission (Type III observation from Cassini spacecraft, image courtesy: Ron Gurnett, University of Iowa).

radio emissions found at the local plasma frequency and its harmonic.
A common point of these different models in explaining why the radio waves are emitted at the plasma frequency, or its harmonic, is that the beam-driven Langmuir waves convert to electromagnetic waves. This conversion can be linear or nonlinear.
Among the linear models, the origin of electromagnetic waves may be explained by linear mode conversion of Langmuir to electromagnetic waves induced by density inhomogeneities [*Sakai et al.*, 2005; *Kim et al.*, 2008]. An alternative approach considers the electromagnetic radiation of trapped Langmuir waves in density holes [*Malaspina et al.*, 2010].
On the other part, nonlinear models start with the fact that the beam-driven Langmuir waves are observed in-situ at amplitude large enough ($\epsilon_0 E^2/nk_BT_e \simeq 10^{-3} - 10^{-4}$) to further evolve through nonlinear processes. Different nonlinear conversion processes based on wave-wave interactions has been proposed to generate the radio waves. In particular, parametric instabilities provide an effective channel for nonlinear mode conversion starting with the nonlinear evolution of large amplitude Langmuir waves. Some authors proposed mechanisms based on four-wave interactions [*Alves et al.*, 2002], but most involve three-wave interactions, through the coupling of Langmuir waves with lower frequency waves, such as whistler waves [*Kennel et al.*, 1980; *Kellogg et al.*, 1992a; *Moullard et al.*, 1998; *Abalde et al.*, 2001] or ion acoustic waves [*Wild*, 1950; *Ginzburg and Zheleznyakov*, 1958; *Lin et al.*, 1986a; *Hospodarsky and Gurnett*, 1995]. Three-wave interactions that could lead to the emission of radio waves are the following. Through electromagnetic coupling, a mother Langmuir wave L decays into a low frequency wave LF and a transverse electromagnetic wave $T_{f_{pe}}$ at the local plasma frequency, observed as Type III fundamental emission:

$$L \rightarrow T_{f_{pe}} + LF \tag{2.1}$$

Through a two-step coupling process, the mother Langmuir wave L decays into an ion acoustic wave S and a daughter Langmuir wave L', which further couples with the mother wave to generate a transverse electromagnetic wave $T_{2f_{pe}}$ at twice the local plasma frequency, observed as Type III harmonic emission:

$$\begin{aligned} L &\rightarrow L' + LF \\ L' + L &\rightarrow T_{2f_{pe}} \end{aligned}$$

Different observations have favored this channel to convert Langmuir waves toward electromagnetic radio waves.
A number of authors have claimed that the spectral analyses of the electric field in the solar wind provides some support in favor of the electrostatic decay process [*Lin et al.*, 1986b; *Kellogg et al.*, 1992b; *Gurnett et al.*, 1993; *Thejappa et al.*, 1993, 1995; *Thejappa and MacDowall*, 1998; *Thejappa et al.*, 2003]. They based their conclusions on some characteristics signatures like the simultaneous occurrence of Langmuir and low frequency waves (like ion acoustic, whistlers or lower hybrid waves), or the comparison between theoretical thresholds and the observed energy in the waves. However, as already pointed out by *Kennel et al.* [1980] and *Thejappa et al.* [1995], the simultaneous occurrence of two

waves in the spectrum doesn't necessarily mean wave coupling. Indeed, the waves can be generated by particles of different energy present in a same electron cloud. It is necessary to check the resonance interaction between the waves in order to conclude in favor of the three-wave coupling process.
Waveform observations of beat-like Langmuir wave packets had also been observed during Type III bursts [*Cairns and Robinson*, 1992; *Hospodarsky and Gurnett*, 1995; *Li et al.*, 2003] and in the Earth foreshock [*Bale et al.*, 1996; *Soucek et al.*, 2005] and interpreted as a signature of the Langmuir decay. However, no signature of the daughter low frequency wave was found. The exact mechanism was still unclear and different interpretations remained open for the identity of the low frequency wave: ion-acoustic, electron acoustic, whistler.

To summarize, Langmuir electrostatic decay is of particular importance concerning the generation of solar wind type III radio emission since it could be the first step of the nonlinear conversion of Langmuir oscillations to the electromagnetic radiation at twice the plasma frequency ($T_{2f_{pe}}$). If some observations of beam-driven Langmuir waves in Type III events and in the Earth electron foreshock tend to favor the occurrence of electrostatic decay, there is still no direct observational evidence of such coupling.
Without a **simultaneous waveform observation** of the three waves involved in the coupling, it is impossible to verify the direct signature of the resonance interaction through the resonant relations (Eqs. 1.5 and 1.6 p. 11) and in particular the phase-locking (Eq. 1.7), a direct signature of the phase resonance between the waves.

This is a main topic addressed in this thesis, tackled by using both in-situ observations of Langmuir waves and kinetic simulations of their nonlinear evolution. I describe in the two following sections the waveform provided by the STEREO/WAVES experiment that I used to simultaneously (i) observe the three waves involved in Langmuir electrostatic decay in the solar wind and (ii) directly confirm the resonant interaction [*Henri et al.*, 2009, 2010b].

2.2 Observations of the electric field: STEREO/WAVES experiment

The Solar TErrestrial RElations Observatory (STEREO) mission was launched on October 26, 2006. It is composed of two identical spacecraft, described in Appendix A. Both spacecraft have an heliocentric orbit in the ecliptic plane at nearly 1 Astronomical Unit (AU) [*Kaiser et al.*, 2007]. The "ahead" spacecraft (hereafter STEREO A) being slightly closer from the sun, it has a shorter orbital period than the Earth and hence drifts ahead of the Earth (at an average rate of approximately 22° per year), while the "behind" spacecraft (hereafter STEREO B) is in a slightly larger orbit. As a result, STEREO A travels faster than STEREO B so that, viewed from the Sun, the two spacecraft separates at an average of 45° per year.

The STEREO observatory carries four complementary scientific instruments, described in Appendix A. Among them, STEREO/WAVES (S/WAVES) experiment, build by a team led by the Observatoire de Paris and the University of Minnesota, consists of (i) three radio receivers (fixed, high and low frequency receivers) that track electromagnetic disturbances through the heliosphere and (ii) a time domain sampler that measures in-situ electric waveforms [*Bougeret et al.*, 2008]. S/WAVES use three mutually orthogonal wire antenna, each 6 meters long, with an effective length of about 1 meter, to measure the electric field. Details on the electric antenna system of the S/WAVES instrument can be found in *Bale et al.* [2008]. S/WAVES has inherited from the experience gain from WIND/WAVES, a previous similar instrument mounted on the WIND spacecraft (1994). Among the questions regarding Type III radio emission listed in *Bougeret et al.* [2008] at the beginning of the STEREO mission, I will discuss the following ones:

- What is the mechanism of coupling between Langmuir waves and radio waves?
- What are the roles of linear and nonlinear processes in the evolution of Langmuir waves and the production of Type III radiation?

To investigate these questions, two modes of observation are thus available: (i) remote observation of radio waves, through three spectral radio receivers, which enables to follow the propagation of the Type III radiosources, as a tracer for electron beams in the heliosphere and (ii) *in situ* measurement of electric waveforms with the Time Domain Sampler mode (hereafter TDS).

This last mode produces rapid samples of electric field waveforms and is primarily intended for the study of Langmuir waves. Practically, the TDS samples the voltage on the S/WAVES antennas continuously. When the sampled amplitude exceeds a comandable threshold, a triggering system takes a snapshot with the largest part of the signal at the center of the time series. A typical event from one channel is shown in Fig.2.5. The TDS gathers events on four channels simultaneously: three orthogonal antennas

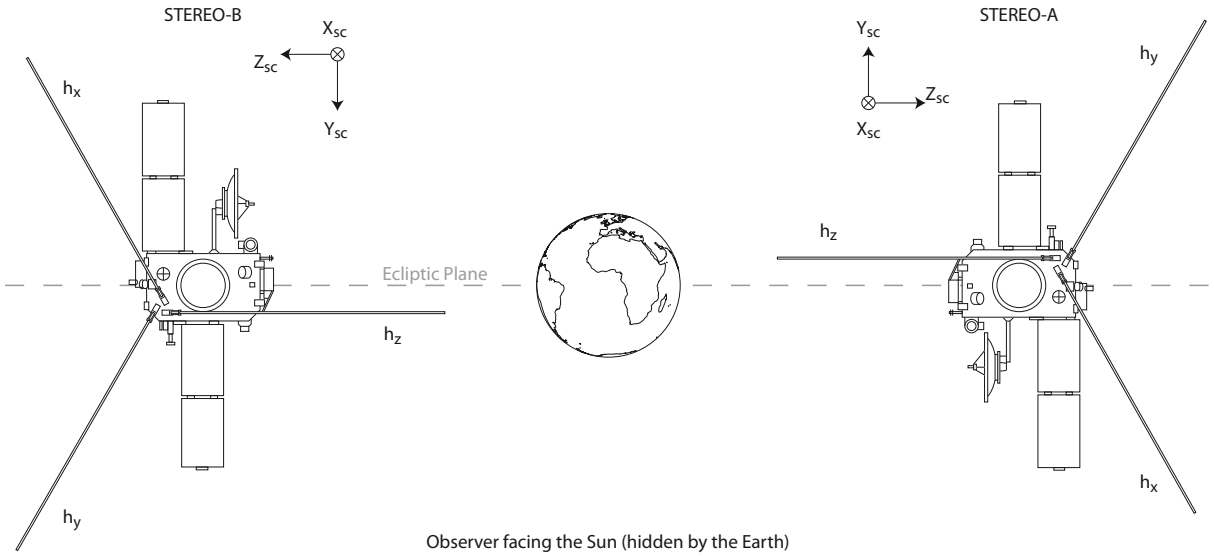

Figure 2.4: Orientation of STEREO spacecrafts and definition of the spacecraft coordinates (courtesy: Baptiste Cecconi).

monopole channels as well as a pseudo-dipole channel obtained by taking the difference of two monopoles. By monopole, we mean that the measured voltage is the difference between the antenna potential and the spacecraft potential that is usually considered constant. The analog voltage signal is then filtered, the frequency gain being flat from $\sim$ 100 Hz to about the sampling rate. After filtering, the analog signals are digitized, the S/WAVES A/D converter is accurately linear. This point is particularly important for our study: it ensures that spurious nonlinear artifacts are not introduced, and make possible the studies of nonlinear wave interactions. The largest signal obtained before saturation is about 125 mV RMS. The sensitivity of the TDS depends on frequency, but in practice the noise level for each channel is less than 10 μV RMS (at about 10 kHz) at the input to the preamplifier. Events can be as long as 16,384 samples. For this kind of long events, the memory provides storage for about 40 full events a day, each of which has 4 channels. More events may be stored by defining shorter events.

Practically, the voltage measured on the three antennas is converted into an electric field, and projected in the spacecraft coordinates, using the set of parameters called *w/base caps (Graz)* by *Bale et al.* [2008, Table 13], in order to take into account the effective length and direction of the STEREO antennas. In its final orbit the spacecraft coordinates (X,Y,Z) are defined as follows: the X-component is sunward along the radial direction, the Z-component is normal to the ecliptic plane, southward for STEREO A and northward for STEREO B, and the Y-component complete the direct orthogonal frame as shown in Fig. 2.4.

The available sampling times are listed in Table 2.2. Signatures of Langmuir waves are accessible through configurations A and B, which resolve the plasma frequency (typically 10 to 30 kHz). An example of TDS Langmuir waveform is shown in Fig. 2.5. The results

Table 2.2: Different available configurations on TDS.

	Sample speed (sample per sec)	Corresponding time resolution (μsec)	Pass band filter (kHz)	Maximum duration (msec)
A	250,000	4	0.1 – 108	66
B	125,000	8	0.1 – 54	131
C	31,250	32	0.1 – 13.5	524
D	7,812	128	0.1 – 3.38	2,097

shown in section 3.1 are based on waveforms from both configurations, whereas results from section 3.2 where obtained while the TDS was in the "B" configuration only. This last configuration is of particular importance for our study. Waveforms are composed of $N = 16,384$ samples with an acquisition rate of 125,000 samples per second, i.e. a time step of $\delta t = 8$ μsec for a total duration of 130 msec per event. In terms of frequencies, those electric field waveforms enable to cover a range from 10 Hz to 60 kHz. Thus, signatures from below the electron cyclotron frequency (typically 100 Hz in the solar wind) to the plasma frequency are available. Moreover, the *long total duration* of each waveform allows both to capture entire Langmuir wave packets and to *access low frequency signals*. This key-point is essential for my observational investigation of wave-wave interactions that couple high frequency Langmuir oscillations to much lower frequency waves, in particular the ion acoustic waves.

Spacecraft dedicated to space plasma only are usually spinning spacecraft (e.g. Ulysses and WIND), while they are three-axis stabilized when imaging instruments are carried

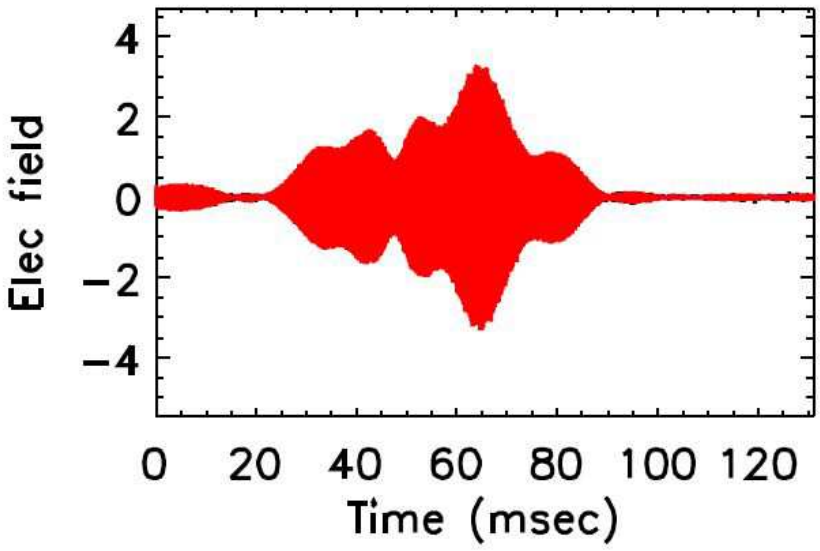

Figure 2.5: Example of TDS Langmuir waveform. The electric field is expressed in mV.m^{-1}.

on board (e.g. CASSINI and STEREO). In the case of spinning spacecraft, it is easier to deploy wire-like or ribbon-like long (several tens of meters) and thin (a few millimeters) antennas, while three-axis stabilized spacecraft can only carry smaller (a few meters) and thicker (a few centimeters) rigid antennas. The longer the antenna, the more current is integrated along the antenna axis, the larger the signal-to-noise ratio. An electric impulse is associated with each particle impacting the surface, producing an antenna shot noise. The larger is the total antenna surface, the more impacted charged particles are collected increasing the shot noise and limiting the signal-to-noise ratio. That is one of the reasons why long and thin antenna are preferred.
There are two different passive ways to measure a voltage with electric antennas. The voltage measured by an antenna used in *monopole* mode is the difference between the antenna potential and the spacecraft potential that is usually considered constant. The voltage measured by an antenna used in *dipole* mode is the difference between two antenna potentials; this kind of measure is thus independent from the spacecraft potential. The shot noise is obviously even greater when the antenna is used in monopole mode. Since this is the case of S/WAVES, the electron plasma noise at the plasma frequency is hidden and cannot be used to deduce temperature and density from the quasi thermal noise spectroscopy [*Meyer-Vernet and Perche*, 1989].

The TDS noise level in space condition is thus dominated by the shot noise resulting from impacting charged particle on both the antennas and the spacecraft. It is typically about 0.1 mV. On the S/WAVES 1-meters equivalent length antennas, this noise level enable to observe electric field signals with an amplitude larger than $\gtrsim 0.1$ mV.m^{-1}. Typical Type III and foreshock Langmuir waves are observed above this value. But what for the ion acoustic waves?

The electric field fluctuation $\delta E_{_S}$ associated to an ion acoustic-like density fluctuation $\delta n/n$ is evaluated to $\delta E_{_S} = (k_B T_e/e) k_{_S}\ \delta n/n$ by considering a Boltzmanian equilibrium of the electrons. Small scale ($k_{_S} \sim 0.1\ \lambda_D^{-1}$) ion acoustic waves with $\delta n/n \sim 10^{-3}$ have an associated electric field $\delta E_{_S} \simeq 10^{-4}$ V.m^{-1}. Such electric field fluctuation would produce a voltage $\delta V \simeq 0.1$ mV on the S/WAVES 1-meters equivalent length antennas. This voltage is comparable to the level of noise. The electric field associated to the ion acoustic mode is thus too low to be observed by S/WAVES. Instead, the density fluctuations themselves have to be observed.

In order to study the coupling of Langmuir waves oscillations with the ion density background through solar wind observations, simultaneous observations of both the electric field and the density fluctuations are required. We have described so far how the electric field is measured in the solar wind, enabling to observe the Langmuir waves advected by the solar wind. But how can we observe the ion acoustic waves, and more generally the density fluctuations that nonlinearly couple with the large amplitude Langmuir waves?
A solution has been found using the fact that the spacecraft potential is affected by the density fluctuations associated to the waves and crossing the spacecraft. Spacecraft-plasma interaction is the key to directly observe the density fluctuations.

2.3 Observations of density fluctuations, a new approach

Compared to former "time domain samplers", the TDS observation mode of the S/WAVES experiment provides long time series. It therefore gives access to low frequency signals. The low frequency signal recorded by the TDS is often identical on the three monopole antenna channels. An example is shown in Fig. 2.6 where we plot the voltage measured by the three monopole antennas, each plotted in a different color. This might be interpreted as the signature of a longitudinally polarized wave along the bisectrix of the three antennas. However, since this direction is related to the spacecraft geometry and is usually different from any solar wind speed or magnetic field directions, such an explanation is very unlikely.
More likely, as previously pointed out [*Kellogg et al.*, 2009], at low frequencies the signal can be dominated by local density fluctuations in which the spacecraft is embedded, inducing quasistatic changes in the spacecraft charging. In this case, the response is expected to be identical on the three antennas.

I hereafter discuss the origin of this low frequency signal in the context of spacecraft-plasma interactions and show how I have calibrated the measured spacecraft voltage in function of density fluctuations crossing the spacecraft. I also discuss the validity range of calibration. Detailed calculations for this calibration are given in Appendix B, a letter has also been submitted [*Henri et al.*, 2010c].

The body of a spacecraft embedded in a plasma emits and collects charged particles, and its electric potential permanently adjusts to the variations of the ambient plasma,

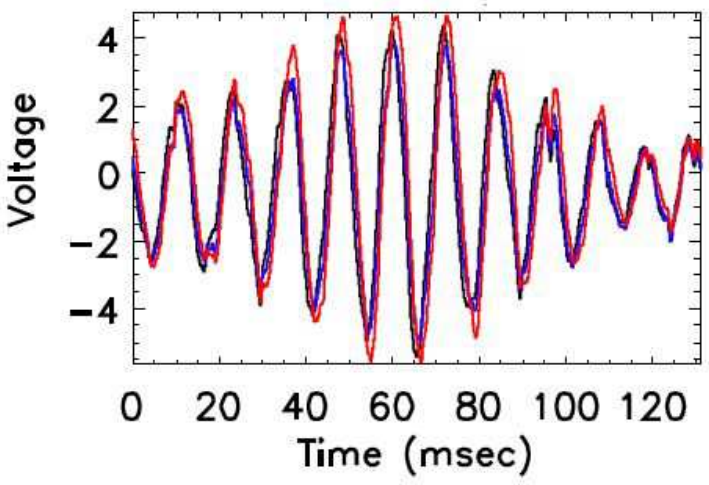

Figure 2.6: Example of TDS waveform, expressed in antenna voltage in mV, with an identical signal at about 100 Hz on all three monopole antenna channels, each plotted in a different color. This signal is identified as a variation of the spacecraft potential, and interpreted in term of a density wave crossing the spacecraft.

in order to ensure that the currents balance is satisfied [*Pedersen*, 1995]. In the solar wind, the spacecraft charging is mainly determined by the balance between the emission of photoelectrons, due to ionizing photons from the sun, and the collection of ambient solar wind electrons. I neglect the much smaller collection of solar wind protons and the secondary emission of electrons. The balance between the outgoing photoelectron current and the incoming solar wind electron current gives the equilibrium spacecraft potential Φ_{SC}, which is typically a few volts positive.
Quasi-neutrality holds at the considered frequencies (100 Hz to 1 KHz), so that the electron density is here a tracer for the plasma density. Since the incoming solar wind electron flux depends on the plasma density, a small variation in the plasma density δn produces a change in spacecraft potential $\delta\Phi_{SC}$ that is well approximated in quasistatic equilibrium by:

$$\delta n/n = -\left(\frac{e}{k_B T_{ph}} + \frac{e}{k_B T_e}\frac{1}{1+\frac{e\Phi_{SC}}{k_B T_e}}\right)\delta\Phi_{SC} \tag{2.2}$$

where T_{ph} is the temperature of the photoelectrons escaping the spacecraft and T_e the solar wind electron temperature (see Appendix for derivation of Eq. B.5). This expression contains an implicit dependance on both the plasma density and the spacecraft collecting surfaces through Φ_{SC}.

Several values of the photoelectron temperature T_{ph} can be found in the literature [*Pedersen*, 1995; *Escoubet et al.*, 1997; *Scudder et al.*, 2000; *Pedersen et al.*, 2008]. They span in the range in the range $T_{ph} \simeq [1-4]\times 10^4$ K for different spacecraft covers material and at different phases of the solar cycle. Since the photoelectron temperature is smaller than the electron temperature ($T_e \simeq [1-2]\times 10^5$ K), $\delta n/n$ is dominated by the first term in Eq. B.5, so that it is roughly proportional to $\delta\Phi_{SC}$. Finally, density fluctuations crossing the spacecraft can be retrieved from the observed fluctuations of spacecraft potential, measured on monopole antenna simultaneously to the electric field, using:

$$\boxed{\delta\Phi_{SC} \simeq -(k_B T_{ph}/e)\ (\delta n/n)} \tag{2.3}$$

If density fluctuations can be measured this way, then we should be able to observe a strong correlation between the level of density fluctuations and the level of Langmuir electric energy (for large enough Langmuir wave amplitude) due to ponderomotive effects: $\delta n/n \simeq W_L$. I will describe such observations in section 3.1. I discuss in Appendix B how this result constraint the photoelectron temperature to $T_{ph} \simeq 3$ eV for the STEREO spacecraft.

I have assumed quasistatic equilibrium to deduce the variations of spacecraft potential due to fluctuations of the incoming plasma density. It holds as long as the solar wind density fluctuates with frequencies lower than the typical charging frequency of the spacecraft $f_{SC} \simeq 1$ KHz. Conversely, density fluctuations at frequencies higher than f_{SC} will scarcely modify the spacecraft potential.
The same discussion holds for the antenna: (i) its equilibrium potential depends on the density of the surrounding plasma and (ii) a fluctuation of the density may modify its equilibrium potential. However, the antenna collecting surface is much smaller and so is

its charge frequency $f_{_A} \simeq 100$ Hz.
For $\delta n/n$ to produce a signal on a monopole antenna voltage, the density fluctuation must modify the spacecraft potential *without modifying the antenna potential*. This means that observable density fluctuations have frequencies $f_{\delta n}$ such that

$$f_{_A} < f_{\delta n} < f_{_{SC}}$$

The typical noise level on S/WAVES monopole antenna is about 0.1 mV, which means that density fluctuation $\delta n/n > 10^{-4}$ are observable. However, the selection criteria which controls the choice of telemetered events favors the highest voltage events, high amplitude signal will thus be preferentially telemetered. I will show in section 3.1 that signature of density fluctuations are observed in TDS waveforms in the range $10^{-4} < \delta n/n < 10^{-2}$.

To summarize, I have provided a calibration of the relative density fluctuations modifying the spacecraft floating potential (Eq. B.6). This method gives access to the level of relative density fluctuations from long time series waveform observations on a monopole antenna. This calibration has been applied to the STEREO spacecraft, showing that density fluctuations $\delta n/n > 10^{-4}$ in the frequency range[3] [100 Hz – 1 KHz] leave identical signatures on the different TDS waveforms.
At these scales, density fluctuations propagate in the solar wind at the ion sound speed ($c_s \simeq 30$ km.s^{-1} at 1 AU). Since it is much smaller than the solar wind speed, the observed frequencies are dominated by Doppler effect[4]. When accounting this Doppler shift, the frequency range of observation corresponds to solar wind density fluctuations with wavelengths $\lambda \sim [500 - 5000\ m]$, i.e. $[50 - 500\ \lambda_{_D}]$.

This discussion holds for signals (i) observed on a monopole antenna and (ii) created by density fluctuations only[5]. The signal is then carried by the spacecraft potential and the antenna acts as a ground. Measuring the electric field oscillations is basically the opposite: the spacecraft potential acts as a ground and the potential antenna oscillate with the electric field.
STEREO/WAVES antennas thus enable to measure simultaneously both (a) the Langmuir electric field, via high frequency variations of the antenna potential $\Phi_{_A}$, and (b) density fluctuations, via low frequency oscillations of the spacecraft potential $\Phi_{_{SC}}$ that give identical signals on the different antennas.
Measures of the solar wind density through the spacecraft floating potential has already been done by other authors on other spacecraft by using Langmuir probes. The new and

[3]Note that the TDS pass-band filter has its own low frequency cut-off at ~ 100 Hz so that *any* signals of lower frequency should be considered with caution.

[4]The (group and phase) velocity of ion acoustic waves, c_s, being much smaller than $V_{_{SW}}$, the observed frequency of ion acoustic waves are dominated by Doppler effect and reads:

$$\omega_{_S}^{obs} = \omega_{_S} + \vec{k}_{_S}.\vec{V}_{_{SW}} \simeq k_{_S}(c_s + V_{_{SW}} \cos\theta_{\vec{B},\vec{V}_{_{SW}}}) \simeq k_{_S} V_{_{SW}} \cos\theta_{\vec{B},\vec{V}_{_{SW}}}$$

[5]If a large electric field is associated with the density fluctuation, then the measured signal on a monopole antenna would be much more complex to analyze.

important aspect of this work is that we measure density fluctuations at much smaller spatial scales, simultaneously to electric field measurements. This provides the first occasion to directly observe the ponderomotive effects of finite-amplitude Langmuir waves on the density background. I discuss such observations in the next chapter.

In-situ spacecraft observations in a moving plasma, as the solar wind, have two intrinsic limitations. First, measures are performed at a single spatial point, where the spacecraft is located. Second, the plasma moves in the spacecraft frame. This introduces a Doppler effect that mixes up the time and spatial evolutions. A numerical model is a strong support to in-situ observations, as it enables to investigate the nonlinear dynamics in space and time, without these intrinsic limitations of in-situ spacecraft observations. I discuss in the next section how the collisionless solar wind plasma is modeled numerically through the Vlasov-Poisson system of equations. I then show in section 2.5 how such simulations enable to understand the signal that would be recorded on the STEREO antenna when a decaying Langmuir wave crosses the spacecraft. In particular, I show how the density fluctuations associated with the daughter ion acoustic waves would affect the voltage signal.

2.4 Numerical model for the Vlasov-Poisson system

The Vlasov-Poisson model, previously described in section 1.2, is used for the simulations described in sections 3.2 and 3.3.
The numerical scheme that solves these equations uses a partially eulerian approach. The distribution function f at a given time t is known on a space velocity grid (x_i, v_j). Then a Lagrangian step is used to follow f along the characteristics which at $t + \Delta t$ ends up at (x_i, v_j). This characteristics started at time t at a phase space point $(x_i^\star, v_j^\star)$ which usually is not a grid point, so that some interpolation is needed to calculate $f(x_i^\star, v_j^\star, t) = f(x_i, v_j, t + \Delta t)$. The numerical model uses a III order Van-Leer interpolation scheme.

The code integrates the Vlasov equation by means of the so-called "splitting scheme" (i.e. it splits the Vlasov equation in several advection equations). The main points of the numerical scheme can be described as follows. It uses a fundamental property of the Vlasov equation is the Liouville theorem, which states that the phase-space distribution function is conserved along trajectories of matter elements (the characteristics curves) in phase space:

$$f\big(x(t), v(t), t\big) = constant$$

The numerical treatment for solving the Vlasov equation uses this property to advance with time the distribution function in the (x,v) phase space. The numerical scheme of the electrostatic version of the Vlasov code is based on the splitting scheme [*Cheng and Knorr*, 1976]. It consists in exploiting the Liouville theorem in two steps, while evolving the system during a time step Δt, where the space and velocity advection terms are advanced separately:

$$\begin{aligned} f^{sp}(x, v) &= f(x - v\Delta t/2, v, t) \\ f^{v}(x, v) &= f^{sp}(x, v - \frac{\partial^2 \phi}{\partial x^2}\Delta t) \\ f(x, v, t + \Delta t) &= f^{v}(x - v\Delta t/2, v) \end{aligned}$$

The distribution function $f(t)$ is first spatially advected to f^{sp} over half a time step, then f^{sp} is advected in the velocity space to f^v over an entire time step, finally f^v is spatially advected to $f(t + \Delta t)$ over a second half time step. Such mapping of the distribution function conserves the volume element in phase space $\delta x \delta v$, a property characterizing symplectic transformations. This enables to conserve the Hamiltonian character of the Vlasov equation. However, the projection of the distribution function on the grid points at each time step breaks the symplectness of the numerical scheme by including some dissipation at the spatial and velocity grid scales. In order to know the level of numerical dissipation after each run, different invariants of the Vlasov-Poisson system are checked to remain constant during the run.

The Eulerian approach is complementary to the Particle in Cell Lagrangian (PIC) one that consists in approximating the plasma by a finite number of macro-particles. Both approaches are based on the mean field approximation of plasma dynamics. The main

advantage of the Eulerian approach is that it enables a direct and almost noise-free (even in the nonlinear regime) investigation of the evolution of the electron and ion distribution function.

The Vlasov-Poisson system is solved for the electron and ion distribution function, $f_e(x, v, t)$ and $f_i(x, u, t)$. I here limit the discussion to the 1D-1V case that concerns the results shown in sections 3.2 and 3.3. The equations are normalized with the following characteristic electron quantities: the charge e, the electron mass m_e, the electron density n_e, the plasma (angular) frequency ω_{pe}, and the Debye length λ_D, the electron thermal velocity $v_{th,e} = \lambda_D \omega_{pe} = \sqrt{T_e/m_e}$ and an electric field $\bar{E} = m_e v_{th,e} \omega_{pe}/e$. Then, the dimensionless equations for each species read:

$$\frac{\partial f_e}{\partial t} + v\frac{\partial f_e}{\partial x} - (E + E_{ext}^{init})\frac{\partial f_e}{\partial v} = 0 \tag{2.4}$$

$$\frac{\partial f_i}{\partial t} + u\frac{\partial f_i}{\partial x} + \frac{1}{\mu}(E + E_{ext}^{noise})\frac{\partial f_i}{\partial u} = 0 \tag{2.5}$$

Since I concentrate on mechanisms taking place in the frequency range $f_{ce} < f < f_{pe}$, I can neglect the influence of the magnetic field. The set of equation 2.4 and 2.5 is closed with the Poisson equation where the charge density is computed from the distribution functions.

$$\frac{\partial^2 \phi}{\partial x^2} = \int f_e dv - \int f_i du \; ; \; E = -\frac{\partial \phi}{\partial x} \tag{2.6}$$

where v (resp. u) is the electron (resp. ion) velocity normalized to the electron thermal velocity. In all the simulations presented hereafter $\mu = m_i/m_e = 1836$ is the ion-to-electron mass ratio. ϕ and E are the self-consistent electric potential and electric field generated by the plasma charge density fluctuations according to Poisson equation (Eq. 2.6). E_{ext}^{init} and E_{ext}^{noise} are 'external' drivers, added to the Vlasov equation that can be switched on or off during the run. E_{ext}^{init} is an external forcing that enable to resonantly generates a monochromatic wave or a wave packet propagating in a given direction. I decided to generate the Langmuir waves with an external forcing instead of the classic bump-on-tail instability in order to control the initial shape and amplitude of the wavepackets. E_{ext}^{noise} is an external forcing that can generate ion density noise during the runs. Details on both 'external' drivers E_{ext}^{init} and E_{ext}^{noise} are given in Appendix E.

The electron (resp. ion) distribution function is discretized in space for $0 \leq x < L_x$, with L_x the total box length. The electron velocity grid ranges over $-v^{max} \leq v \leq +v^{max}$ (resp. $-u^{max} \leq u \leq +u^{max}$ for the ion velocity grid). Finally, periodic boundary conditions are used in the spatial direction.

In all the runs the following initial conditions have been taken: electron and ion distributions functions are initially Maxwellian with respect to velocity, with a random noise in density:

$$f_e(x,v) = \frac{e^{-v^2}}{\sqrt{2\pi}}[1 + \epsilon \sum_k cos(kx + \psi_k)] \tag{2.7}$$

$$f_i(x,u) = \frac{\sqrt{\frac{\Theta}{\mu}} e^{-\frac{\Theta}{\mu}u^2}}{\sqrt{2\pi}}[1 + \epsilon' \sum_k cos(kx + \psi'_k)] \tag{2.8}$$

where $\Theta = T_i/T_e$ is the ion-to-electron temperature ratio set to $\Theta = 0.1$ or 1 in the different runs. Those values correspond to typical temperature ratios in the solar wind. ψ_k and ψ'_k are random phases with a uniform distribution. A (small) initial Langmuir random noise is needed for the parametric instability to develop. The parameter ϵ (resp. ϵ') is the amplitude of the initial electron (resp. ion) density level of noise. The parameters (ϵ,ϵ') are chosen so that the development of the instability occurs relatively rapidly, as Vlasov codes have a very low level of numerical noise. When imposing such a random density in the initial condition for the distribution functions, a charge separation is generated and rapidly self-organise into a large spectrum of Langmuir noise. A "sea" of Langmuir waves then fills the simulation box.

The code used in this work has been developed by A. Mangeney, F. Califano. A multidimensional version of the code has been parallelized by C. Cavazzoni (CINECA, Bologna, Italy). The numerical scheme as well as the parallelization strategy is described in *Mangeney et al.* [2002]. To properly study the nonlinear interaction of Langmuir waves with density fluctuations, I had to face several difficulties, some of them inherent to kinetic simulations. In particular:

- Observed Langmuir waves generated in the solar wind have a phase velocity much larger than the electron thermal velocity. They are thus not directly affected by Landau damping. Since kinetic damping effects are not dominant in this case and in order for us to better control the shape and amplitude of the waves, I decided to generate such waves with an external forcing instead of the classic bump-on-tail instability. I thus implemented such an external forcing that resonantly generates a monochromatic wave or a wave packet propagating in a given direction.

- Conversely, solar wind ion acoustic fluctuations are expected to be kinetically damped by Landau damping because $T_e \sim T_i$. They are nonetheless observed [*Gurnett and Frank*, 1978; *Kurth et al.*, 1979]. To generate such density noise during the whole runs, I have implemented an external forcing that continuously inject a low level of density fluctuations.

The simulations discussed in this thesis are 1D and start with an homogeneous medium that include the previously discussed random noise. However, some preliminary simulations have been performed (i) with considering an initially inhomogeneous plasma, (ii) in 2D configurations. I did the following complementary investigations to prepare this new step.

- In order to start the simulation with a macroscopic density fluctuation that does not reorganize itself into Langmuir oscillations, a Maxwellian equilibrium in the initial electron distribution function must be imposed.
- In order to control the isotropy of an initial 2D density fluctuation spectrum, the rotational component of the random noise must be filtered out. I define a controlled initial irrotational electric noise generated by an isotropic spectrum of density random noise.
- In order to run bidimensional Vlasov simulations, much heavier because the distribution function need to be advanced in time is 4D (2 dimensions in space, but also 2 dimensions in velocity), I did a six-week visit at the High Performance Computing group at the Italian supercomputer center CINECA, to optimize the performance 2D-2V electrostatic Vlasov code. New simulations with this optimized version are in preparation, but will not be discussed here.

In appendix E, I discuss the methods and schemes I have developed to overcome these questions.

A kinetic model is a strong support to in-situ observations. It enables to investigate the nonlinear dynamics in space and time, without the intrinsic limitations of observations obtained in a moving frame, such as the solar wind, which measures are performed at a single spatial point and mix the time and spatial evolutions.

2.5 Example of interpretation of in-situ observations through Vlasov simulations

Henri et al., Solar Wind 12 Proceedings, 2010

I now show an example of how the Vlasov simulation can be used to produce the expected signal that STEREO/WAVES would record when crossing a decaying Langmuir wave packet.

An initial Langmuir wave packet, generated by the "external" electric field E_{ext}, propagate in the simulation box and self-consistently evolves through the Vlasov-Poisson model. At some point, the mother Langmuir wave decays into a daughter Langmuir wave and an ion acoustic wave. Details on the simulation setup are given in *Henri et al.* [2010a]. I concentrate here on explaining the observed voltage between the antenna used in monopole mode and the spacecraft. The different kind of noise that affect the observations (shot noise on the spacecraft and on the antennas, thermal noise, etc) will not be discussed, the observed signal being here much higher than the noise level.

In order to compare the simulation results with in-situ waveform observations, we mimic the conditions of observation onboard a spacecraft that would record, on monopole antennas, a decaying Langmuir wave. We thus hereafter introduce in the presentation of simulation results both (i) a spacecraft floating potential effect and (ii) a Doppler-shift effect.
As previously developed in section 2.3, the antenna voltage in monopole mode is a combination of an electric field signal, affecting the antenna potential, and a density fluctuation signal, affecting the spacecraft potential. To reproduce this effect in the simulation, we consider an "equivalent signal" $s(x,t)$, that mimic the voltage measured between the antenna and the spacecraft, defined by $s(x,t) = \alpha\ E(x,t) + \beta\ n_p(x,t)$, with α the equivalent in the simulation of a calibration parameter that gives the antenna potential variations due to fluctuations of the electric field, and β the equivalent in the simulation of a calibration parameter that gives the spacecraft potential variations due to fluctuations of the density.
In-situ observed waveforms are Doppler-shifted because the plasma is moving in the spacecraft frame. A Doppler-shift effect is introduced in the simulation by considering a virtual spacecraft moving in the simulation box measuring the "equivalent signal" $s\big(x(t),t\big)$ at position $x(t) = x_0 + V_s t$ where V_s is a constant velocity. We choose here $V_s = v_{th,e}$ for convenience.
This "equivalent signal" $s\big(x(t),t\big)$, obtained from the simulations, represents the voltage signal that would be recorded by an antenna in monopole mode, such as the ones on STEREO, when the spacecraft crosses a decaying Langmuir wavepacket advected in the solar wind.

For an easy confrontation with observed waveforms, simulation results are presented in Fig. 2.7 as the will be presented when describing the observations in section 3.2. The

top left panel shows the electric field (grey) and proton density (black line) waveforms from the simulation. Both are plotted in normalized units, as described in the simulation model. The left bottom panel shows the wavelet transform of the "equivalent signal" $s(x(t), t)$.

The simulations show (i) a beat-like modulation of the Langmuir electric field at the plasma frequency corresponding to the mother and daughter Langmuir waves, (ii) an ion acoustic signal detected at lower frequency and centered where the maximum of the beat-like Langmuir signal is observed.

The Fourier spectrum of $s(x(t), t)$ is shown in the right top panel, with a zoom at the plasma frequency in the right bottom panel. The frequency of the ion acoustic density fluctuations as well as the separation between the frequency peaks of the two Langmuir waves are essentially a Doppler-shift effect. The full line represents the total Fourier spectrum. Dashed and dotted lines distinguish the contribution of the ion density fluctuations and electric field respectively. I will show that this is in full agreement with the observations.

The simulation thus shows how the high frequency part of the observed spectrum is dominated by the response of the antenna to the fluctuations of the electric field, whereas the low frequency part is dominated by the response of the spacecraft potential to density fluctuations. This analysis and the results have been published in *Henri et al.* [2010a].

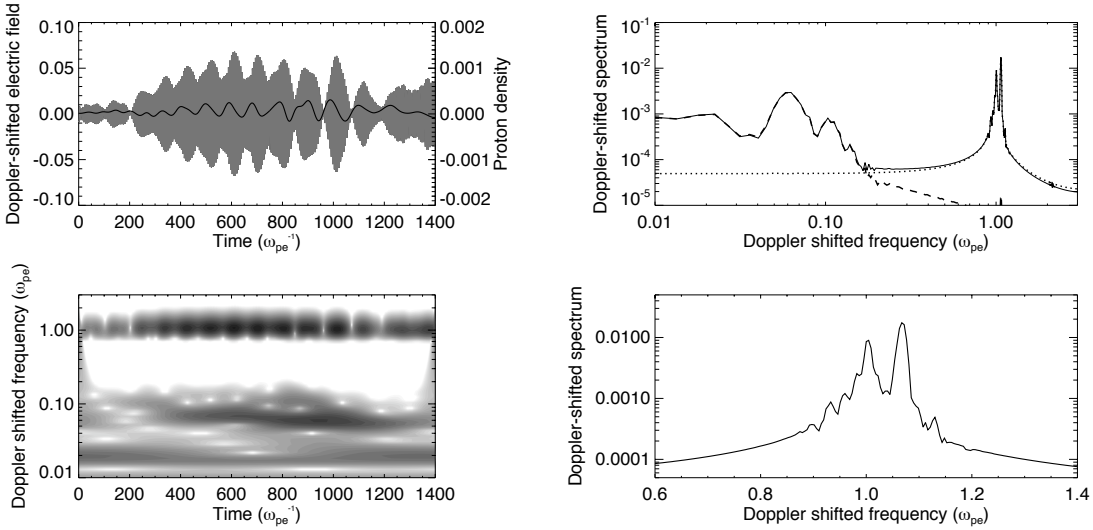

Figure 2.7: Waveform, spectrum and wavelet transform from simulation results, as they would appear when observed by spacecraft instruments when crossing a decaying Langmuir wave packet. Top left panel: waveform in a moving frame: electric field (grey) and proton density (black). Bottom left panel: Morlet wavelet transform of signal $s(x(t), t)$. Top right panel: corresponding Fourier spectrum (full line) with respective contribution of the density fluctuations (dashed line) and electric field (dotted line). Bottom right panel: zoom on the double peak at the plasma frequency. (Source: *Henri et al.* [2010a])

Chapter 3

Results

In section 1 I have presented some arguments in favor of studies of nonlinear plasma processes. As presented in section 2, my laboratory of investigation is the solar wind and the methods are based on analysis of observations from STEREO and kinetic simulations. I now present in this section the results of my work.

3.1 Observational evidence for Langmuir ponderomotive effects

First observations of Langmuir ponderomotive effects using the STEREO spacecraft as a density probe.
Henri et al. (2010), *submitted to GRL*

In this section, I give observational evidence for Langmuir ponderomotive effects in the solar wind. I use simultaneous observations of the electric field and density fluctuations through the method described in section 2.3.

We first isolate in the TDS data from November 2006 to December 2009, the waveforms that contain both Langmuir oscillations and density fluctuations signals. TDS events that contain Langmuir oscillations are selected by considering the waveforms with a localized frequency peak between 5 kHz and 50 kHz. Waveforms with identical signal on the three monopole antennas at low frequency (f$<$ 5kHz) are identified as showing density fluctuations. Details on this selection are given in Appendix C.

For each selected event, the high frequency part of the voltage fluctuations, associated to Langmuir waves, is converted into electric field. The associated Langmuir electric energy is normalized to the electron kinetic energy $W_{_L} = (\epsilon_0 E_{_L}^2)/(2 n_e k_B T_e)$, where $E_{_L}$ is

the modulus of the observed Langmuir electric field, n_e is the electron density deduced from the Langmuir frequency and T_e is the solar wind electron temperature. In the absence of in-situ measurement, we use the typical value in the solar wind $T_e \simeq 10^5$ K. The low frequency part of the voltage fluctuations, identified as a fluctuation of the spacecraft potential Φ_{SC}, is converted into relative density fluctuations $\delta n/n$ via Eq. B.6, assuming a photoelectron temperature $T_{ph} = 3$ eV. The determination of the photoelectron temperature is discussed in Appendix B.

Fig. 3.1 shows an example of TDS event where both density fluctuations (blue) and Langmuir oscillations, plotted in term of the associated electric energy (black), are observed. In this waveform, the Langmuir energy is large enough ($W_L \simeq 10^{-2}$) to generate density fluctuations by ponderomotive effects. As expected by the nonlinear theory, the level of density fluctuations is of the order of the electric-to-thermal energy ratio (the normalized Langmuir energy). Note also that the steeper the Langmuir envelop, the deeper the generated density fluctuations, as expected from ponderomotive theory described in section 1.3.

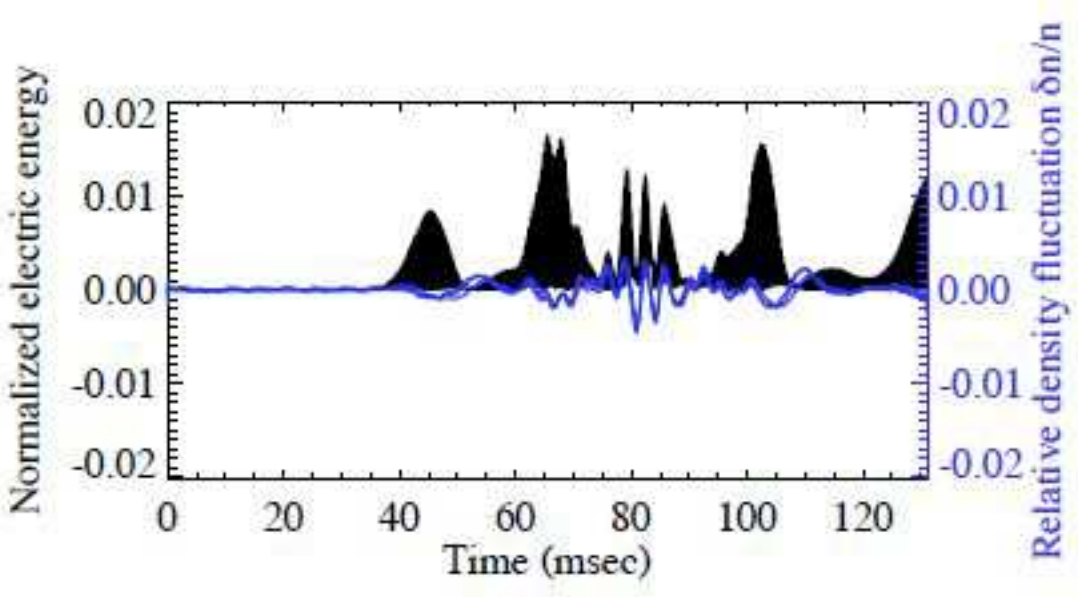

Figure 3.1: Example of TDS waveform for which both Langmuir waves, plotted here in term of the Langmuir normalized electric energy $W_L(t)$ (black line), and density fluctuations $\delta n/n(t)$ (blue line) are observed.

For each waveform, we plot the maximum density fluctuation and the maximum Langmuir electric energy normalized to the electron thermal energy W_L. Following the energy of the Langmuir waves, two different behaviors are observed (Fig 3.2).
For low energy Langmuir waves ($W_L < 10^{-4}$), the level of density fluctuations is independent of the level of Langmuir oscillations. In other words, Density fluctuations are not affected by the propagation of Langmuir waves. It corresponds to the linear regime of Langmuir waves.

At higher energies, the non-linear evolution of Langmuir waves affects the density background until it reaches at saturation a level of density fluctuations $\delta n/n \simeq W_L$. The red dashed line is the expected saturation level of density fluctuations forced by Langmuir ponderomotive effects. The transition between the linear and nonlinear domain is observed for a normalized Langmuir electric energy $W_L \sim 10^{-4}$.
The blue dotted lines show the 3σ detection level for both electric energy and density fluctuations. Density fluctuations associated to high amplitude Langmuir waves are well above the noise level.

The waveforms are separated between those observed between November 2006 and February 2007, while the two STEREO spacecraft were still in the Earth environment (black) and those observed between March 2007 and December 2009, when the two probes were in their final orbit in the free solar wind (red). Most of the nonlinear Langmuir waves are found at the beginning of the mission, while the spacecraft performed several crossings of the Earth electron foreshock, a region where Langmuir waves are known to be intense.

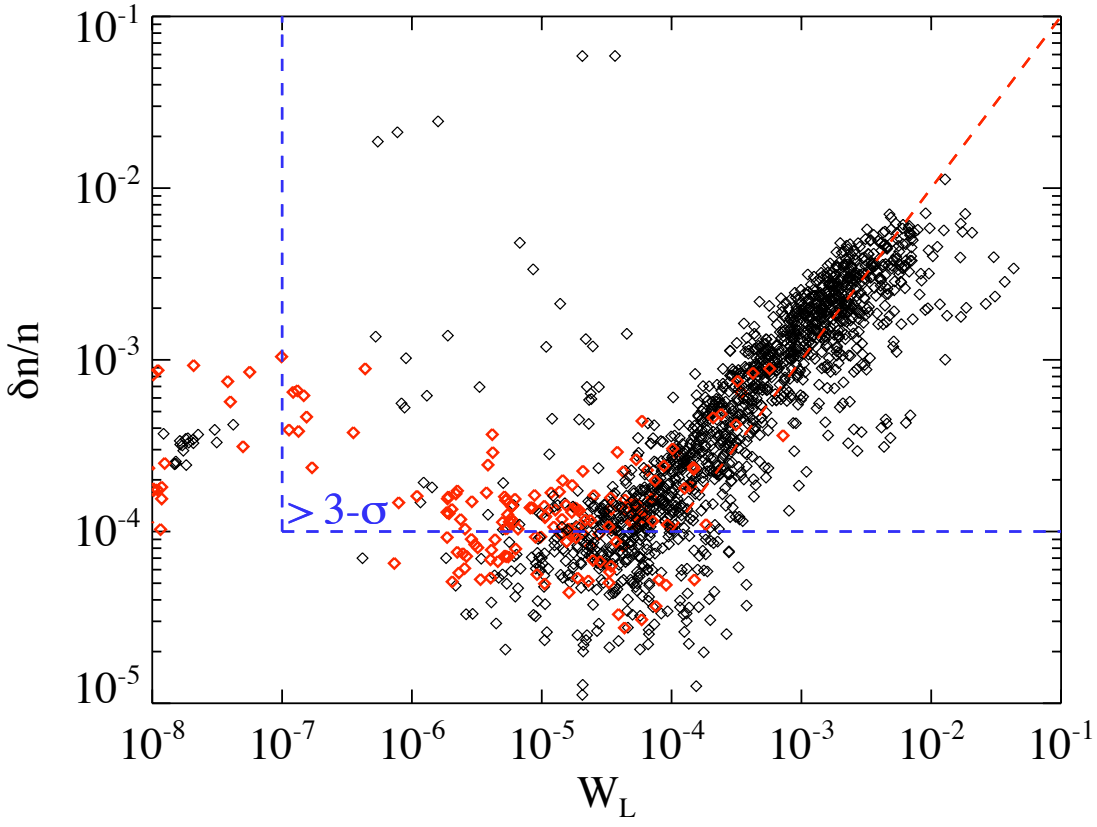

Figure 3.2: Level of density fluctuations vs Langmuir energy in the Earth electron foreshock (black diamond) and in the quiet free solar wind (red diamond). The red dotted line shows the expected saturation level of density fluctuations generated by Langmuir ponderomotive effects. The blue dotted line shows the 3σ detection level for both electric energy and density fluctuations.

This analysis confirms the interpretation of the low frequency voltage signals as a signature of solar wind density fluctuations (section 2.3). Details can be found in a submitted paper [*Henri et al.*, 2010c] reproduced at the end of the thesis.

I have here shown how simultaneous in-situ observations of electric field and density fluctuations give observational evidence for non-linear coupling between Langmuir oscillations and density fluctuations. It is the first time that ponderomotive effects in space physics, out of ionospheric experiments, are directly observed. It illustrates the energy transfer between different time scales in space plasma and shows that the coupling between high frequency oscillations of the electric field and low frequency variations of density is efficient. In the following I will concentrate on a particular case of resonant ponderomotive effect: the three-wave interaction between Langmuir and ion acoustic waves.

3.2 Evidence for Langmuir electrostatic decay

The electrostatic decay of Langmuir waves, described in section 1.3, is a resonant version of Langmuir ponderomotive effects. As explained in section 2.1, three-wave coupling in general and Langmuir electrostatic decay in particular may explain the physical mechanism at the origin of radio emissions associated with Type III bursts.
I use (i) in-situ observations from the STEREO mission to show that three-wave coupling between Langmuir and ion acoustic waves indeed occur during Type III events, (ii) Vlasov simulations to compute the threshold for Langmuir electrostatic decay in typical solar wind conditions. By coupling in-situ observation and kinetic simulations, we show that the observed level of Langmuir energy matches the computed threshold for the decay process, confirming that Langmuir electrostatic decay is indeed observed during Type III bursts.

Evidence for wave coupling associated with Type III bursts
Henri et al. (2009), JGR (Space Physics), 114, 3103

Based on data obtained in 2007-01-14 by the two STEREO spacecraft, we give the first direct observation of nonlinear three-wave interaction between Langmuir waves associated with a Type III event, observed at ≈ 20 kHz, and ion acoustic waves, observed at $\approx 80 - 250$ Hz. Three complementary methods are employed: spectral, wavelet and bicoherence analyses.

During the period of strong Langmuir activity associated with the Type III electron beam crossing both spacecraft, a total of 37 TDS waveforms (19 from STEREO A and 18 from B) were transmitted from the two spacecraft. A spectral analyses shows that among the 37 waveforms, 14 (10 on STEREO A and 4 on B) show two distinguishable Langmuir wave peaks together with an ion acoustic wave[1]. An example of such waveform is shown in Fig. 3.3 (top left panel) with the associated Fourier spectrum (top and bottom right panels). For these waveforms, the frequency of the waves verifies the doppler-shifted frequency relation expected in case of three-wave coupling:

$$f_{L}^{Doppler} = f_{L'}^{Doppler} + f_{S}^{Doppler}$$

which is a combination of both the conservation of energy and momentum:

$$\begin{aligned} \omega_{L} &= \omega_{L'} + \omega_{S} \\ \vec{k}_{L} &= \vec{k}_{L'} + \vec{k}_{S} \end{aligned}$$

A wavelet analyses verifies the simultaneous time occurrence of the waves, and gives the average scale length of the coupling estimated to 18 ± 5 km, corresponding to about 2000 Debye lengths (example shown in the bottom left panel of Fig. 3.3).

[1] The others show one Langmuir wave.

However, observing simultaneous waves is not enough to conclude that they are resonantly coupled. The resonant interaction is effective if the relative phases is such that the waves remain in phase for long enough during the coupling mechanism:

$$\phi_{_L} \quad = \quad \phi_{_{L'}} + \phi_{_S} \tag{3.1}$$

This concept is sometimes called *phase locking* in the literature. In the opposite, if the relative dephasing of the waves changes in time to much, the energy exchange becomes highly inefficient and the three-wave coupling does not occur. The bicoherence is a powerful statistical estimator of quadratic phase coupling, characteristic of three-wave coherent interactions. Detailed on the bicoherence are given in Appendix D. A bicoherence analysis is used to statistically test Eq. 3.1 on the whole series of data. It shows that the relative phase remains constant from one event to another, thus confirming the phase resonance between the three waves.

In the specific context of Type III burst, we also show that the ion acoustic waves coupled to the Langmuir waves show a frequency drift with time consistent with the ballistic evolution of the Type III-associated electron beam that crosses the spacecraft, as suggested by *Cairns and Robinson* [1995].

This analysis and the results have been published in *Henri et al.* [2009], reproduced at the end of this thesis.

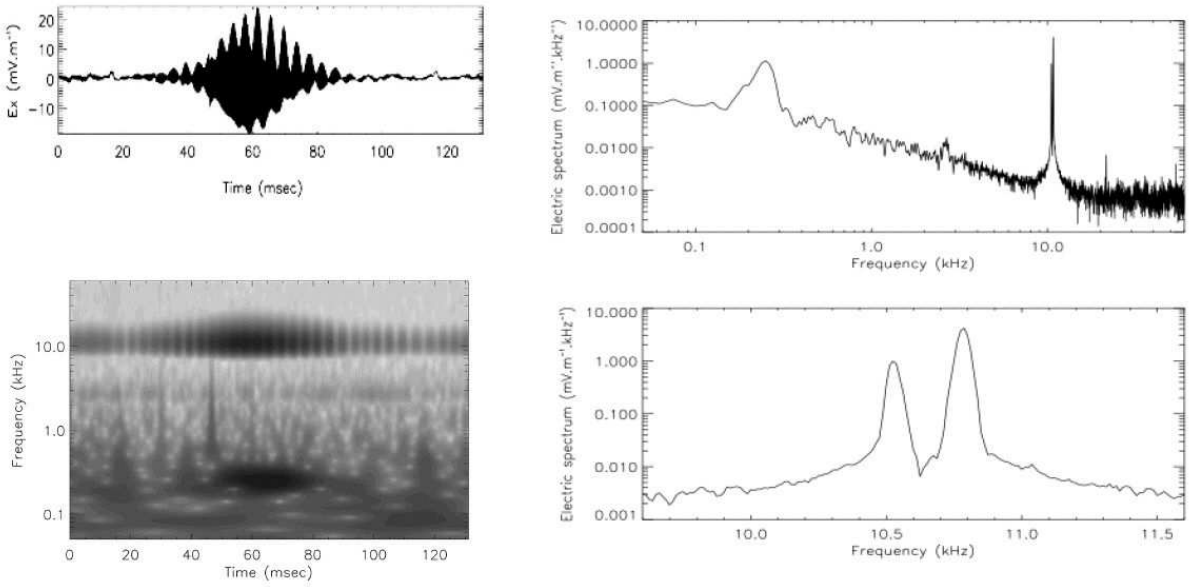

Figure 3.3: S/WAVES observations of Langmuir electrostatic decay. Top left panel: typical antenna voltage waveform. Bottom left panel: corresponding Morlet wavelet transform. Top right panel: corresponding Fourier spectrum. Bottom right panel: zoom on the double peak at the plasma frequency. (Adapted form *Henri et al.* [2009])

Vlasov simulations of Langmuir Electrostatic Decay and consequences for Type III observations
Henri et al., (2010) JGR (Space Physics), 115, 6106

In the previous work, I have provided observational evidence for three-wave coupling between Langmuir waves and ion acoustic density fluctuations during a Type III burst. However, these observations give no indication concerning the *direction* of the energy transfer between the coupled waves. Such three-wave coupling could indeed be either the signature of the scattering of the beam-driven Langmuir waves L by preexisting ion acoustic waves S:

$$L + S \rightarrow L'$$

or the decay of the mother beam-driven Langmuir waves:

$$L \rightarrow S + L'.$$

The decay process being a parametric instability, it is necessary to compare the energy of the wave to the instability threshold in order to discriminate between these two mechanisms.

Solar wind observations show that (i) Langmuir waves are localized wavepackets and (ii) that the electron and the proton temperature are of the same order.
Since the electron temperature is close to the proton temperature, the phase velocity of ion acoustic waves get close to the ion thermal velocity, so that Landau damping becomes very efficient. The parametric instability threshold is determined by the fact that the daughter waves growth rate $\gamma_{_{LED}}$ should be greater than the Landau damping rates ($\gamma_{_{LED}} > \sqrt{\gamma_{_{L'}}\gamma_{_S}}$). The high Landau damping of ion acoustic waves could limit or prohibit the development of the ion acoustic waves and thus the initialization of the decay. This decay, which is conceptually a fluid process, is thus regulated by *kinetic* processes.
Moreover, observed Langmuir waves are localized. This induces two other limitations for the decay to occur. First, it decreases the resonance between the waves, by generating multiple k-channels for the decay. Second, since the mother and daughter waves propagate at different group velocities, the wavepackets are expected to separate at some point. This *dynamic* process means that only a finite interaction time is available to transfer energy from the mother wave to the two daughter waves, which may reduce the efficiency of the decay process.

The evaluation of the parametric instability threshold have to take into account both *kinetic* and *dynamic* effects. Unfortunately, analytical estimations of this threshold (see section 1.3) hold for (i) monochromatic waves[2], without considering the dynamics of the wavepackets in physical space, and (ii) idealized temperature ratios: $T_e/T_p >> 1$. Unfortunately, the ion acoustic Landau damping rate in realistic temperature condition, $T_e \simeq T_p$, cannot be solved analytically. A Vlasov-Poisson approach has thus been used

[2] *Tsytovich* [1970] gives a comprehensive discussion of the Langmuir decay starting from a broad Langmuir $k_{_L}$-spectrum, but without considering the dynamics of the wavepackets in physical space.

to study the decay dynamics. It allows to consider self-consistently the decay of the Langmuir wave together with damping effect on the product waves.

Langmuir decay is studied numerically, at temperature ratios $T_e/T_p = 1$ and $T_e/T_p = 10$, starting both from a monochromatic Langmuir wave and a Langmuir wavepacket. Even for an initial monochromatic Langmuir wave, the product waves are resonantly generated over a broad range of wavenumbers, naturally producing narrow daughter wavepackets. Saturation levels for the ion acoustic relative density fluctuations are of the order of the ratio of Langmuir electric energy to the total kinetic energy, as expected, but growth rates are observed one to two orders of magnitude lower than the analytical values deduced from the analytical purely monochromatic case. The growth rate for Langmuir decay products γ_{LED} is obtained from simulations for different initial Langmuir amplitude E_L and wavevector k_L in the parameter range of observations:

$$\gamma_{LED} = \Gamma \; E_L^{\alpha} k_L^{\beta} \tag{3.2}$$

The fitting parameters Γ, α and β are given in *Henri et al.* [2010b] and reproduced in table 3.1 for the two temperature ratios considered.

	Γ	α	β
$T_p/T_e = 0.1$	0.026	1.11	0.59
$T_p/T_e = 1$	0.025	1.82	0.30

Table 3.1: Numerical values for the fit for the growth rate of LED driven density fluctuations in expression 3.2. [Source: *Henri et al.*, 2010b]

Then this growth rate is used to interpret and deduce a threshold for localized wavepackets in dynamical conditions. During the decay process, the mother wavepacket generates a daughter wavepacket traveling at a different group velocity. Eventually the two wavepackets separate after a time interval τ_{int} thus stopping the decay process. τ_{int} is evaluated from the initial Langmuir packet width and wavevector. Therefore, Langmuir decay is efficient only if the interaction time between the two wavepackets before they separate, τ_{int}, is larger than the growth time for the daughter waves, γ_{LED}^{-1}. The effective threshold for the electrostatic decay of a **propagating Langmuir wavepacket** with wavevector k_L and a packet width Δ can be estimated by imposing $\tau_{int} = \gamma_{LED}^{-1}$:

$$\boxed{E_{LED}^{threshold} = \left(\frac{6\; k_L^{1-\beta}}{\Gamma\Delta}\right)^{1/\alpha}} \tag{3.3}$$

A series of simulations of the decay of an initial Langmuir wavepacket has been performed that validate Eq. 3.3.

The threshold I obtain from Vlasov simulations of the electrostatic decay is well above the threshold usually found in the literature (estimated for (i) monochromatic Langmuir waves, (ii) considering an infinite available coherent interaction time) which is an unreasonable low value ($\epsilon_0 E^2/nk_BT \geq 2.5 \times 10^{-5}$). With such a low value, most Langmuir waves would decay, which is not observed.

Finally, we go back to S/WAVES observations to check if the observed level of Langmuir energy is large enough to trigger the electrostatic decay. The threshold expressed in Eq. 3.3 is compared to the amplitude of Langmuir waves S/WAVES observations from *Henri et al.* [2009].
Figure 3.4 displays the amplitude and wavelength of the Type III beam driven Langmuir wave. Each square, together with error bars, represents a single waveform where electrostatic three-wave coupling is observed.
Decay threshold from Eq. 3.3 is overplotted for temperature ratios $T_p/T_e = 1$ and 0.1. The observed Langmuir electric field during Type III perfectly span in the range of electrostatic decay effective threshold computed from Vlasov simulations.

This analysis and the results have been published in *Henri et al.* [2010b], reproduced at the end of this thesis.

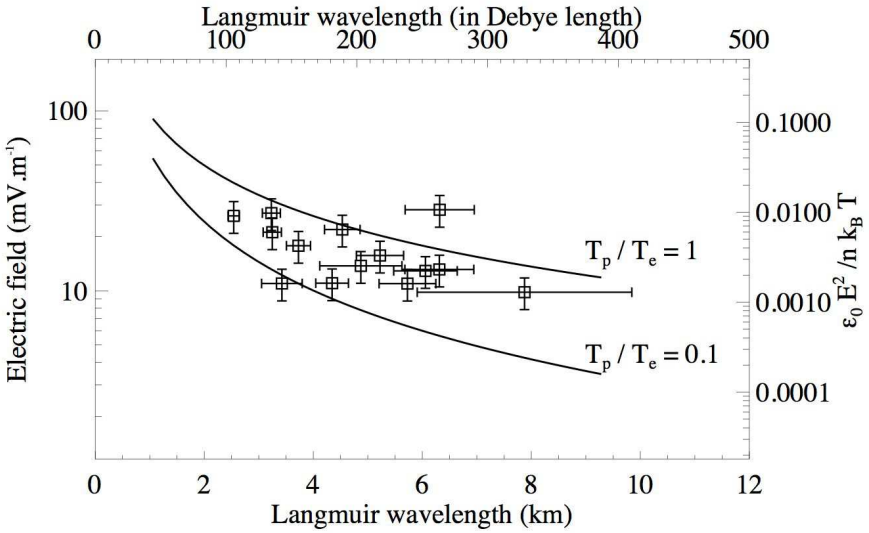

Figure 3.4: Observed Langmuir electric field amplitude vs. wavelength. The threshold for Langmuir electrostatic decay computed from Vlasov simulations is overplotted for two values of the temperature ratio $T_p/T_e = 0.1$ and 1. (Adapted from *Henri et al.* [2010b])

3.3 Low energy Langmuir cavitons, the breakdown of weak turbulence

Henri et al., submitted to PRL (2010)

I now concentrate on the long-time evolution[3] of the Vlasov-Poisson system for moderately high initial amplitude, still corresponding to the weak turbulence domain $\epsilon_0 E_L^2/nk_BT_e \sim 10^{-3}$.

Though 1D-1V Vlasov-Poisson simulations, the long time evolution of Langmuir weak turbulence self-consistently generates ion cavitons. Langmuir cavitons are coherent structures in equilibrium between the total kinetic pressure force and the ponderomotive force created by the high frequency Langmuir oscillations. They are characteristic of strong Langmuir turbulence and are widely thought to be generated at high energy and to saturate when the Langmuir energy is of the order of the background plasma thermal energy. Langmuir cavitons observed for long-time evolution of Langmuir waves saturate at low energy (with an electric to kinetic energy ratio as low as three orders of magnitude), unlike the widespread belief that such structures saturate at higher energy ratios.

Electrostatic coherent structures of typical dimension much greater that a few Debye length are produced by the long time evolution of an initial relatively moderate amplitude turbulence. In particular, it gives evidence that "large" and "shallow" stable cavitons also exist, which could give new insight in the interpretation of space plasma observations of localized Langmuir waves. This result can have an important impact on the interpretation of space plasma spacecraft data and encourage the space physics community to revisit the admitted conclusion that strong turbulent Langmuir structures are formed at too high energy to be relevant in space plasma environments. This analysis and the results have been submitted [*Henri et al.*, 2010d], the submitted version in reproduced at the end of this thesis.

Henri et al. [2010d] shows how the Langmuir electrostatic decay can also evolve toward the formation of cavitons. It illustrates the breakdown of long time evolution Langmuir weak turbulence, previously described for general wave turbulence in *Biven et al.* [2001]. The point there is that the system can fully evolve through weak turbulence effects, until the time scale for strong turbulence is reached. At this point the system dynamics is completely modified and govern by the evolution of spatially coherent structures, the same as the one described by strong turbulence. The main difference is that the observed cavitons saturate at much smaller energy and remain stable until the end of simulation.

[3]Note that long time simulations may lead to numerical artifacts generated by the accumulation of numerical error during the run. In order to validate the numerical experiment, the conservation of Vlasov invariants during the whole runs is always checked.

Chapter 4

Conclusions and Perspective

Nonlinear plasma processes are the mechanisms that enable, in the absence of collisions, to redistribute the energy at scales much smaller than the particle mean free path. Wave-particle interactions in some way "thermalize" the plasma, while wave-wave interactions redistribute the energy at different time and spatial scale between the different plasma modes.
The main goals of this thesis were namely (a) to infer observational evidence of such nonlinear process, in particular of electrostatic wave-wave interactions, and (b) to understand the full coupling dynamics by modeling realistic propagating localized wavepackets which limit the coherence of the interaction, These goals have been reached by using a complementary approach based on (i) instrumentation considerations in the context of spacecraft-plasma interactions, (ii) in-situ observations of simultaneous electric field and density fluctuations waveforms and (iii) kinetic simulations.

Langmuir electrostatic decay: a common process in the solar wind

I concentrated in this thesis on observations associated to one Type III burst (2007-01-14 observed with both STEREO spacecraft). Since the beginning of the STEREO mission, several Type III bursts have been observed by the STEREO/WAVES remote radio receivers. However, only a few bursts were associated with electron beams that actually crossed the STEREO spacecraft. From November 2006 to December 2010, only three Type III bursts have been observed with an unambiguous associated Langmuir activity recorded by the in-situ measurements, as a signature of electrons crossing the spacecraft. Similar waveforms and associated spectrum are also found in the TDS waveforms associated to the two others Type III bursts which electron beams crossed one of the STEREO spacecraft (in 2009-07-18 for STEREO A, in 2010-03-06 for STEREO B), indicating that the same process occur and confirming the interpretation of the first observation.

Evidence of electrostatic three-wave coupling is also found in TDS Langmuir waveforms

associated to the Earth foreshock. An example of waveform showing Langmuir electrostatic decay, observed in the Earth foreshock at the begin of the STEREO mission, is shown in Fig. 4.1 (top panel).
Since foreshock electron beams have smaller velocities than those associated to Type III, the foreshock beam-driven Langmuir waves have smaller wavelengths. Theory for electrostatic wave coupling shows that the observed frequency of the daughter ion acoustic wave is larger in this case (typically about 1 kHz). The higher frequency of the daughter ion acoustic signal gives a more dynamical picture of the coupling process. The bottom panels of Fig. 4.1 show the spectrum computed in three different time intervals of the waveform. The mother Langmuir wave at $f_{_L} \simeq 20$ kHz is observed during the whole duration of observation, while the daughter Langmuir wave $f_{_{L'}} \simeq 21$ KHz and the ion acoustic wave (at $f_{_S} \simeq 0.9$ kHz) appear simultaneously for times $30 < t < 85$ msec. This example illustrates how the electron foreshock could represent an ideal plasma laboratory for dynamical observations of Langmuir electrostatic decay.
Contrary to what was observed during the Type III burst, the mother Langmuir wave is this time Doppler-shifted toward lower frequency. This simply indicates that the mother Langmuir wave propagate sunward, as expected since foreshock electron beams are composed of reflected electrons accelerated at the Earth bowshock.

These different observational pieces of evidence of the same process in various regions of the solar wind strongly suggest that the electrostatic decay of Langmuir waves is a general feature of the nonlinear evolution of small k_L Langmuir waves in space physics.

Origin of radio emissions at the plasma frequency

Langmuir electrostatic decay may be an essential ingredient in the mechanism that leads to radio emission at the harmonic of the plasma frequency, observed during Type II and Type III radio bursts as well as in the electron foreshocks. This mechanism, described by *Ginzburg and Zheleznyakov* [1958], has remained so far a theoretical model to explain the origin of these kinds of radio emission, but was poorly supported by observational evidence so far. We recall that it is a two step mechanism, starting with Langmuir electrostatic decay. The second part of this mechanism, namely the coalescence of the mother and daughter Langmuir waves that generate a transverse electromagnetic wave $T_{2f_p^-}$ at twice the local plasma frequency has not been directly observed. This would represent a further step in order to conclude for the complete physical mechanism leading to radio emissions at the harmonic of the plasma frequency. The efficiency of this electromagnetic wave-coupling is also to be confirmed. It is necessary to develop electromagnetic kinetic models to give a final answer to the question of the origin of radio emissions at twice the plasma frequency. Such kinetic simulations of this electromagnetic coupling implies a multidimensional model that would require huge computational capabilities.
Such computation is, however, not only a question of computer resources. Wave-wave interactions are processes taking place over frequencies and scales covering several orders of magnitude. A kinetic description may not be needed at every scale of the simulation.

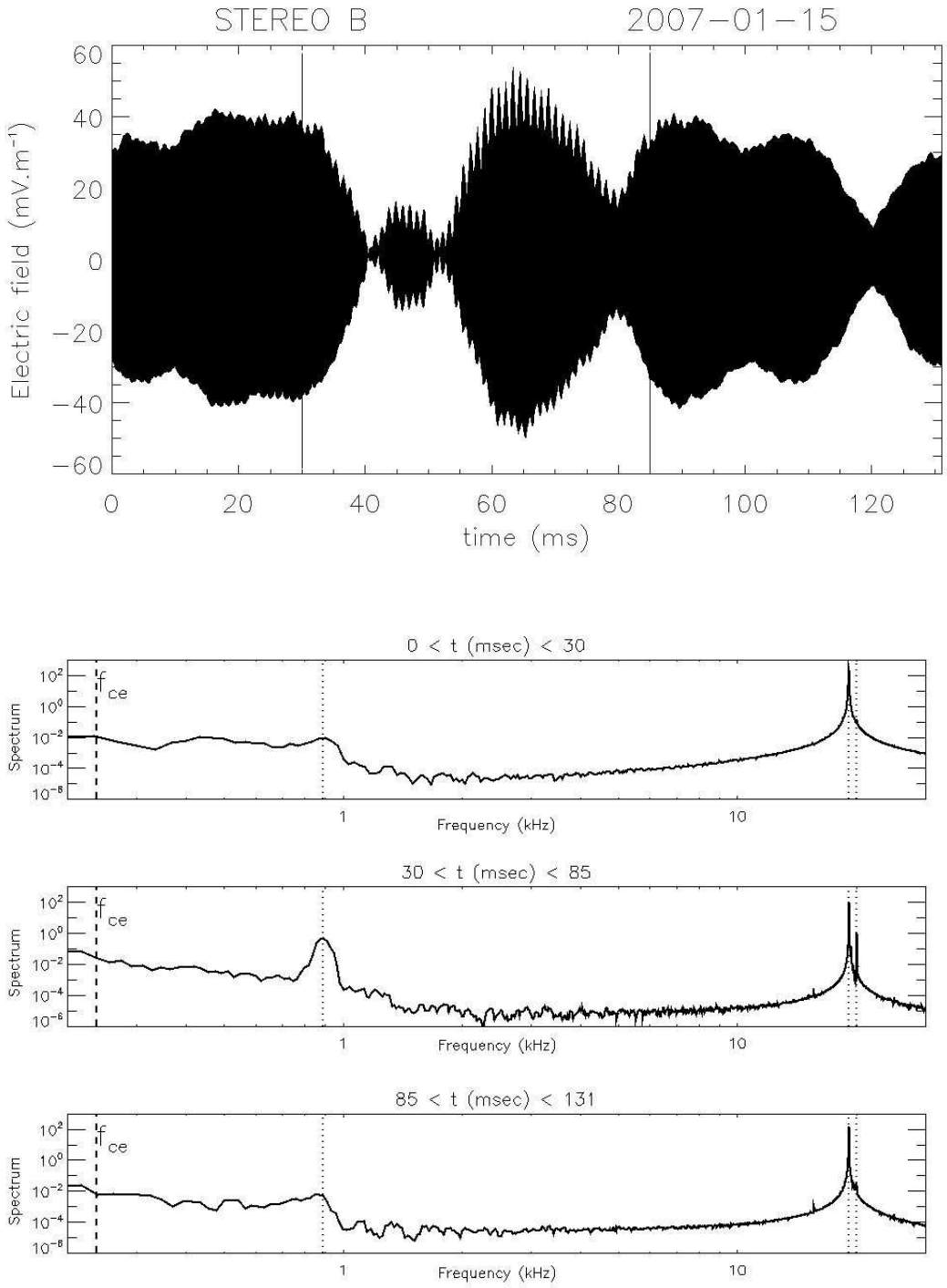

Figure 4.1: Signature of Langmuir electrostatic decay in the Earth foreshock. Top panel: electric field waveform. Bottom panels: corresponding fourier spectrum at three different time interval: [0–30], [30–85] and [85–131] msec, indicated by vertical lines in the waveform. The faint dotted lines show the frequency of the three coupled waves. The electron cyclotron frequency at the time of observation $f_{ce} \simeq 100Hz$ is indicated by the thicker dotted line. Note the simultaneous appearance of the two daughter waves in the time interval [30–85] msec.

Some coupling interface between fluid and kinetic description of the plasma could provide an efficient approach to numerically model such processes. New computational scheme to define this interface are thus to be developed.

A second direction of research concerns the origin of the fundamental radio emission $T_{f_p^-}$ at the plasma frequency. The "classical" theoretical mechanism is the electromagnetic decay, through which a mother Langmuir wave decays into a backscattered ion acoustic wave and a transverse radio wave. This mechanism has not been tested, in part because no fundamental emission was associated with the Type III burst I studied. The two other Type III observed by STEREO with in-situ associated Langmuir waves could enable to study this other coherent wave-wave process. Methods similar to those described in this work could be used.

Limits of the model

The nonlinear interaction of Langmuir waves with the ion density background through the ponderomotive force have been studied through a (i) 1D model (ii) in the electrostatic approximation, and (iii) by considering an initially homogeneous medium.

A multidimensional model of wave-wave interactions would open other energy transfer channels. The conservation of momentum, leading to the resonant relation on wavevectors $\vec{k}_1 = \vec{k}_2 + \vec{k}_3$, indeed provides different directions for the energy redistribution of the mother wave.

When introducing the presence of a weak magnetic field (so that $\omega_{ce} << \omega_{pe}$), the physics for electrostatic decay is barely modified. But it opens, again, a wide range of possible wave-wave interaction channels for the evolution of Langmuir waves. It is for instance possible for the Langmuir wave to couple with much lower frequency waves, such as whistler waves, shear Alfven waves, fast magnetosonic waves, and kinetic Alfven waves [*Luo et al.*, 1999; *Abalde et al.*, 2001; *Chian et al.*, 2002; *Voitenko et al.*, 2003].

In my work, I have studied the reaction of the ion density background to the high amplitude electric field due to ponderomotive effects, considering an initially homogeneous plasma. However, the solar wind plasma is known to be inhomogeneous. How would these initial density fluctuations modify the dynamic of Langmuir waves?
First, it introduces the scattering of the Langmuir waves propagating on an inhomogeneous background. In addition, it also modifies the generation of the beam-driven by Langmuir wave. This question is linked to an unanswered question concerning Type III bursts electron beams generated in the solar corona is the so-called "Sturrock paradox" [*Sturrock*, 1964]: why does the electron beam remain "unstable" over 1 AU of transit? The behavior of Langmuir waves in an inhomogeneous medium is of particular interest, in particular in the growth stage of the beam-driven Langmuir wave. As pointed out by several authors density fluctuations can put the beam out of resonance with the generated

Langmuir waves and enable its propagation over long distances. A statistical approach of this effect has been developed in the framework of the stochastic growth theory [*Robinson*, 1993; *Robinson et al.*, 1993a]. Numerical kinetic investigations of the bump-on-tail instability for an inhomogeneous medium could provide direct tests on the stochastic growth theory.

Studying wave-wave interactions with future space experiments

Future space plasma experiments are already in preparation. Space missions such as Solar Orbiter, Solar Probe, etc, have been proposed to further investigate space plasma. What would be the ideal spacecraft for the investigations of coherent nonlinear wave-wave interactions?

First of all, three-wave couplings are resonant coherent processes. I stress that the phase coherence is the signature that enables to identify coherent wave-wave interactions. Testing the phase coherence requires that the data conserves the information on the phase of the signal. Waveform measurements are the only way to identify the phase coherence during the coupling process. It is thus mandatory to keep such measurements capabilities in future missions.

Second, to study nonlinear physics by means of observations, it is necessary to make sure that the observed nonlinearities are parts of the physical mechanisms, and have not been introduced by the instrument itself. Electronic should be free of spurious nonlinear behavior that would contaminate the data, in particular through the A/D converter. This is one of the improvements made from WIND/WAVE/TDS to STEREO/WAVE/TDS, that should be kept in mind in future similar space plasma experiments.

Wave-wave interactions couple oscillations at different frequencies. The frequencies of the different coupled waves can span over several order of frequencies. It is thus necessary to have long time series, associated with wide filters, to be able to compare the dynamics at high and low frequencies. Ideally the frequency range [1 Hz – 50 kHz] would cover signals from below the electron cyclotron frequency ($\sim$ 100 Hz) to above the plasma frequency ($\sim$ 10 kHz). This could enable to address the question of the possible coupling between electrostatic waves and electromagnetic waves (such as the Langmuir – whistler coupling).

The compressible oscillation of a weakly magnetized plasma in the frequency range $f_{ce} < f < f_{pe}$ are the ion acoustic waves. They are associated oscillations of the ion (and electron) density and the electric field. How to observe ion acoustic signals? This depends on the context of the mission. If the spacecraft is spinning, then long electric antennas can be incorporated. The ion acoustic oscillations will be detectable through their associated electric field for antenna length $l \gtrsim 100$ m (see discussion p. 27). If the spacecraft is three-axes stabilized, as it is requires when imaging experiments are parts of the space mission, shorter and more rigid electric antennas must be used. The electric field associated to ion

acoustic waves is then no more detectable. However, as shown in *Henri et al.* [2010c] and discussed in section 2.3, ion acoustic oscillations are detectable through their associated density fluctuations that affect the equilibrium electric potential of the spacecraft. Electric antennas in monopole mode conserve the information on the spacecraft potential, but antennas in dipole mode cancel it. That is why it would be interesting to keep the monopole antenna voltage if using short antennas, in order to be able to observe the ion acoustic density fluctuations.

The new possibility to directly observe density fluctuations (section 2.3) has enabled to study some nonlinear interactions between Langmuir oscillations and the density background. Those density fluctuations are observed at small scales, in the range $\lambda_S \sim [50, 500]\ \lambda_D$, close to the dissipation scales of turbulence. This new way to observe small scale density fluctuations could give new insight into solar wind turbulence dissipation processes.

I have here concentrated on the observation of wave-wave interactions through observations of the electric field and the ion density. Considering these two observables is pertinent for frequencies larger than the cyclotron frequencies. To extend wave-wave studies at smaller frequencies, observations of the magnetic field would be needed. All development of high frequency, until a few 100 Hz, magnetic field waveform instrument is thus to be supported.

Chapter 5

List of Papers

This thesis is based on the hereafter papers, reproduced in the following pages:

- Henri, P. et al., Evidence for wave coupling in type III emissions, *Journal of Geophysical Research (Space Physics)*, **114**, 3103 (2009)

- Henri, P., F. Califano, C. Briand, A. Mangeney, Vlasov simulations of Langmuir Electrostatic Decay and consequences for type III observations, *Solar Wind 12 proceedings*, AIP, 288, 1216 (2010)

- Henri, P., F. Califano, C. Briand, A. Mangeney, Vlasov-Poisson simulations of electrostatic parametric instability for localized Langmuir wave packets in the solar wind, *Journal of Geophysical Research (Space Physics)*, **115**, 6106 (2010)

- Henri, P., F. Califano, C. Briand, A. Mangeney, Low energy Langmuir cavitons or the asymptotic limit of weak turbulence, *submitted to PRL*

- Henri, P., Meyer, N., Briand, C., Donato, S., Observations of Langmuir ponderomotive effects using the STEREO spacecraft as a density probe, *submitted to GRL*

Papers not included in the thesis:

- Balbus, S. A. & Henri, P., On the Magnetic Prandtl Number Behavior of Accretion Disks, *ApJ*, **674**, 408 (2008)

- Opitz, A. et al. Temporal evolution of the solar wind electron core density at solar minimum by correlating the STEREO A and B SWEA measurements, *submitted to Solar Physics*

- Briand, C., Soucek, I, Henri, P., Mangeney, A. Waves at the plasma frequency in solar wind magnetic holes, *submitted to JGR*

Henri et al. (2010)
Submitted to Geophysical Research Letters

Observations of Langmuir ponderomotive effects using the STEREO spacecraft as a density probe.

P. Henri[1,2], N. Meyer-Vernet[1], C. Briand[1], S. Donato[3]

[1] LESIA, Observatoire de Paris, CNRS, UPMC, Univ. Paris Diderot; 5 Place J. Janssen, 92190 Meudon, France

[2] Dip. Fisica, Università di Pisa; Largo Pontecorvo 3, 56127 Pisa, Italy

[3] Dip. Fisica, Universit della Calabria, Via P. Bucci, 87036 Arcavacata di Rende (CS), Italy

Density fluctuations, nonlinearly coupled by ponderomotive effects to Langmuir waves with energy $(\epsilon_0 E^2)/(nk_B T) > 10^{-4}$, are directly measured in the solar wind for the first time. High frequency density fluctuations in the solar wind are measured using the observed quasistatic fluctuations of the STEREO spacecraft floating potential in the frequency range where the spacecraft floating potential is in quasistatic equilibrium between photoionization and electron attachment, whereas the potential of the antenna, of much longer equilibrium time scale, is blind to the density fluctuations.

Nonlinear coupling between electron and ion dynamics enable to transfer the energy from electron to ion time scales. In the electrostatic case, such nonlinearities are described by the Zakharov model [*Zakharov*, 1972] which shows that high amplitude Langmuir wave packets can generate density fluctuations through a ponderomotive force. If such processes have been extensively studied from the 70's, observational evidence in space plasma is still lacking. The main reason is the difficulty to simultaneously observe electric field and plasma density variations at comparable spatial scales. We describe in this letter a method that allows such simultaneous observations. To our knowledge, this is the first direct quantitative study of density fluctuations nonlinearly coupled to finite amplitude Langmuir waves in space, based on simultaneous observations of electric field and density fluctuations.

The voltage measured on an electric antenna used in monopole mode is the difference between the antenna potential and the spacecraft floating potential. The spacecraft floating potential is usually considered as a ground to study electric field oscillations measured on the antenna. Compared to previous time domain samplers, the TDS observation mode of the SWAVES experiment on board the STEREO mission gives access to long time series (until 131 msec of total duration with a time step $\delta t = 8\ \mu sec$) [*Bougeret et al.*, 2008], thus giving access to in-situ electric field in a large frequency range [10 Hz to 60 kHz].

The low frequency component of these waveforms is often identical on the three monopole antenna channels. This might be interpreted as the signature of a longitudinally polarized wave along the bisectrix of the three antennas, but since this direction is related to the spacecraft geometry and is generally different from any physical directions, such an explanation is very unlikely. More likely, as previously pointed out [*Kellogg et al.*, 2009], at low frequencies the signal can be dominated by local density fluctuations in which the spacecraft is embedded, inducing quasistatic changes in the spacecraft charging. In this case, the response is expected to be identical on the three antennas. The goal of this paper is (i) to give a calibration of this density fluctuation signal $\delta n/n$ as a function of the measured spacecraft potential variations, (ii) to discuss the frequency range in which this calibration holds, and (iii) to use this method in order to observe the density fluctuations forced by Langmuir ponderomotive effects in the solar wind.

0094-8276/10/$5.00

Floating potential of spacecraft and antennas

The spacecraft body emits and collects charged particles, and its electric potential permanently adjusts to the change in parameters of the ambient plasma, in order to ensure that the currents balance. In the solar wind, the main charging currents are due to the emission of photoelectrons I_{ph}, and to the collection of ambient plasma electrons, I_e. We neglect here the smaller proton current and the secondary emission of electrons. On a surface at zero potential, the photoemission flux j_{ph} due to solar ultraviolet radiation depends on the average surface photoemission efficiency:

$$j_{ph} \simeq \delta\ 10^{14}\ m^{-2} sec^{-1}$$

per unit of projected sunlit surface, with $\delta \sim 1-4$ for typical spacecraft covers [*Pedersen*, 1995; *Escoubet et al.*, 1997; *Scudder et al.*, 2000; *Pedersen et al.*, 2008]. On the other hand, since solar wind electrons have a thermal velocity much larger than the solar wind speed, they are collected on the total surface and the incoming electron flux on a surface of zero potential is the ambient electron random flux:

$$j_e \simeq n\sqrt{kT_e/2\pi m_e} < 10^{13} m^{-2} sec^{-1}$$

where m_e, n and T_e are respectively the electron mass, electron density (equal to the ion density) and temperature. Since $j_{ph} S_\perp >> j_e S$, where $S_\perp$ and S are respectively the sunlit projected surface and the total surface, the surface charges positively, until its positive electric potential Φ binds sufficiently the photoelectrons to make their net outward flux balance the inward flux of solar wind electrons. The potential must thus provide the photoelectrons with a potential energy that outweighs their typical kinetic energy of a few eV. Hence the equilibrium potential is a few volts positive. By making the simplifying assumption that both solar wind electrons and photoelectrons populations are Maxwellians

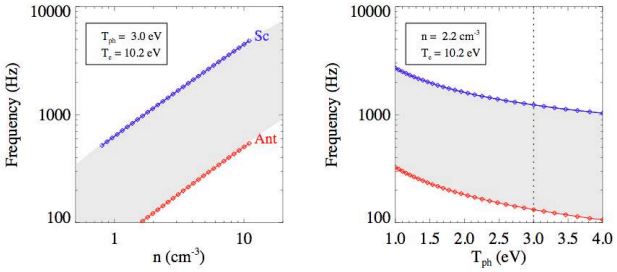

Figure 1. Frequency range of detection of density fluctuations (in grey) between the spacecraft (blue line) and antenna (red line) charging frequencies as a function of n (left panel) and T_{ph} (right panel).

with respective temperature T_e and T_{ph}, an approximation that will be discussed below, the ejected photoelectron current I_{ph} and the incoming plasma electron current I_e on a surface at positive potential Φ are respectively given by [*Meyer-Vernet*, 2007, pp. 352-355]:

$$I_{ph} \simeq j_{ph}\ eS_{\perp}\ \left(1+\frac{e\Phi}{k_B T_{ph}}\right)^{\alpha}\ \exp\left(\frac{-e\Phi}{k_B T_{ph}}\right) \qquad (1)$$

$$I_e \simeq n\left(\frac{k_B T_e}{2\pi m_e}\right)^{1/2}\ eS\ \left(1+\frac{e\Phi}{k_B T_e}\right)^{\beta} \qquad (2)$$

where e is the electron charge, α and β both equal to 0, 1/2 and 1 for respectively plane, cylindrical and spherical geometry of the considered charging process.

Let us first evaluate the spacecraft equilibrium potential. Since the scale length of the spacecraft body L_{sc} is larger than the photoelectrons Debye length, the photoemission takes place in plane geometry so that $\alpha_{sc} = 0$. On the other hand, since L_{sc} is smaller than the solar wind electron Debye length, plasma electrons are collected in 3D so that $\beta_{sc} = 1$. The current balance condition $I_{ph} = I_e$ applied to Eqs.(1)-(2) for the spacecraft body then gives its equilibrium potential Φ_{sc}:

$$-e\Phi_{sc}/k_B T_{ph} = log\left[(n/N_0)\ (1+e\Phi_{sc}/k_B T_e)\right] \qquad (3)$$

where $N_0 = j_{ph}\ (k_B T_e/2\pi m_e)^{-1/2}\ S_{\perp}^{sc}/S^{sc}$.

The above calculations also hold for the equilibrium potential of the antenna Φ_A in cylindrical geometry so that $\alpha_A = \beta_A = 0.5$ in Eqs.(1)-(2), which gives:

$$-e\Phi_A/k_B T_{ph} \simeq log\left[\frac{n}{N_0^A}\left(\frac{1+e\Phi_A/k_B T_e}{1+e\Phi_A/k_B T_{ph}}\right)^{1/2}\right] \qquad (4)$$

where $N_0^A = j_{ph}\ (k_B T_e/2\pi m_e)^{-1/2}\ S_{\perp}^{A}/S^{A}$.

Equations (3) and (4) are solved using the STEREO spacecraft parameters. The spacecraft body has the dimensions $L_1 \times L_2 \times L_3 = 1.14 \times 1.22 \times 2.03$ meters [*Kaiser et al.*, 2007], with a sunlit surface $S_{\perp}^{sc} = L_2 \times L_3 \simeq 2.5\ m^{-2}$. The solar wind electrons are collected from all the spacecraft surface, except the face located in the wake, so that the surface $S^{sc} \simeq 9.9\ m^{-2}$. The S/WAVES antennas are 6 m long, with an average diameter of 23.6 mm, inclined by 125^o to the sun-spacecraft direction [*Bale et al.*, 2008]. This gives a sunlit projected surface of about $S_{\perp}^{A} = 0.12\ m^{-2}$ and a total surface area of about $S_{tot}^{A} = 0.45\ m^{-2}$ per boom. Note that equation (4) is a rough approximation in the STEREO case since the antenna length is not greater than the plasma Debye length, but this does not affect significantly the final result.

The solutions of Eqs. (3) and (4) depends mainly on the value of the photoelectron temperature. Various authors have evaluated it in the range $T_{ph} \simeq [1-4] \times 10^4$ K for different spacecraft covers and phases of the solar cycle [*Pedersen*, 1995; *Escoubet et al.*, 1997; *Scudder et al.*, 2000; *Pedersen et al.*, 2008]. We will show later that by applying this calibration to density fluctuations generated by the nonlinear evolution of Langmuir wave in the solar wind, we constrain the temperature of photoelectrons emitted by STEREO at $T_{ph} \simeq 3 \pm 1$ eV. We will assume the same value for the photoelectrons emitted by the antennas since this does not affect significantly our results.

For $T_{ph} = 3$ eV, Eqs. (3) and (4) yield, for typical solar wind densities $n = [1-10]\ cm^{-3}$ and temperature $T_e = 10$ eV, $\Phi_{sc} = [3-8]$ Volts and $\Phi_A = [5-10]$ Volts. With these values, the suprathermal components of photoelectrons and ambient electrons which play an important role in the magnetosphere [*Escoubet et al.*, 1997] do not afffect our results.

These calculations hold as long as the solar wind density fluctuates with frequencies lower than the typical charging frequency of the considered object, so that the equilibrium remains quasistatic. Conversely, density fluctuations with frequencies higher than the charging frequency of the object will scarcely modify the potential. In other words, we concentrate on density fluctuations with frequencies $f_{\delta n}$ lower than the charging frequency of the spacecraft f_{sc}, but larger than the charging frequency of the antenna f_A, able to change the spacecraft floating potential without changing significantly the antenna potential. We now evaluate these two frequencies by considering the respective charging e-folding times $\tau = RC$, with C the capacitance and R the resistance evaluated as follows.

Since the dimension of the spacecraft L_{sc} and the antenna radius a are both much smaller than the ambient Debye length λ_D, the electric field surrounding them can be considered as a Coulomb field locally, vanishing at distance λ_D. The spacecraft capacitance C_{sc} is evaluated as the capacitance of a spherical conductor of radius $L_{sc} \simeq 1$ m:

$$C_{sc} \simeq 4\pi\epsilon_0 L_{sc} \simeq 110\ \text{pF}$$

and the antenna capacitance C_A is evaluated as the low frequency capacitance of a cylindrical conductor of length L and radius a in a plasma of Debye length λ_D [*Meyer-Vernet and Perche*, 1989]. In the limit $L >> \lambda_D$ the antenna capacitance is:

$$C_A \simeq \frac{2\pi\epsilon_0\ L}{ln(\lambda_D/a)} \simeq 47\ \text{pF}$$

whereas for $L << \lambda_D$ it reduces to the capacitance in vacuum:

$$C_A \simeq \frac{2\pi\epsilon_0\ L}{ln(L/a)-1} \simeq 64\ \text{pF}$$

The STEREO antenna length is of the same order as the Debye length and the low frequency antenna capacitance is between those two values, i.e. $C_A \simeq 60$ pF.

The resistance $R = 1/|dI/d\Phi|$ simplifies to $R \simeq 1/|dI_{ph}/d\Phi|$, since the photoelectron current is the fastest charging process [*Meyer-Vernet*, 2007]. Using $dI_{ph}/d\Phi \simeq (e/k_B T_{ph})\ I_{ph}$ and $I_{ph} = I_e$, the resistances read:

$$R_i^{-1} \simeq eS^i\ \frac{e}{k_B T_{ph}}\ n\left(\frac{k_B T_e}{2\pi m_e}\right)^{1/2}\left(1+\frac{e\Phi_i}{k_B T_e}\right)^{\beta_i}$$

with $i = sc$ or A, $\beta_{sc} = 1$, $\beta_A = 1/2$ for respectively the spacecraft and the antenna.

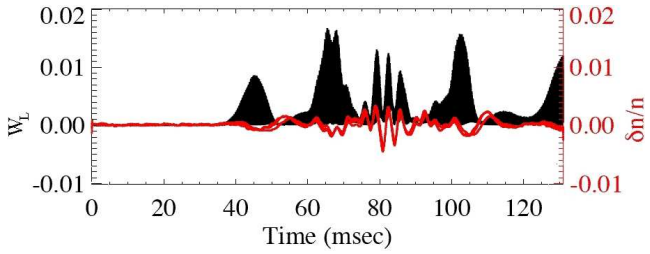

Figure 2. Example of TDS waveform for which both Langmuir waves, plotted here in term of the Langmuir normalized electric energy $W_L(t)$ (black), and density fluctuations $\delta n/n(t)$ (red) are observed.

The charging frequencies $f_i = 1/(2\pi R_i C_i)$ are solved numerically and shown in Fig.1 as a function of the plasma density and the photoelectrons temperature. They are nearly independent to the electron temperature in the range of solar wind parameters. Therefore, density fluctuations with frequencies between $\sim$ 100 Hz and a few kHz will produce a change in spacecraft potential but no change in antenna potential. Signals of much higher frequency vary too fast for changing the floating potential of the spacecraft and antennas. Signals of much smaller frequency change similarly the floating potentials of the spacecraft and antennas, so that the difference barely changes and should not be observed on the monopole antennas.

Note that (i) the previous discussion holds for signals observed on a monopole antenna and produced by density fluctuations, whereas electric field oscillations behave just opposite since the spacecraft potential is a ground and the antenna potential oscillates with the electric field; (ii) the TDS pass-band filter has its own low frequency cut-off at $\sim$ 100 Hz so that signals of lower frequency should be considered with caution.

A small variation δn of the plasma density in this frequency range produces a change in spacecraft potential $\delta\Phi_{sc}$ obtained by differentiating Eq. 3

$$\delta n/n = -\left(\frac{e}{k_B T_{ph}} + \frac{e}{k_B T_e}\frac{1}{1+\frac{e\Phi_{sc}}{k_B T_e}}\right)\delta\Phi_{sc} \qquad (5)$$

Since $T_{ph} << T_e$, $\delta n/n$ is mainly determined by the first term in Eq.(5) so that it is roughly proportional to $\delta\Phi_{sc}$ with a proportionality factor determined by T_{ph}. This is confirmed by solving numerically Eq.(5) in a typical range of solar wind plasma parameters. A relative variation in plasma density $\delta n/n$ thus produces a voltage $\delta\Phi \simeq -\delta\Phi_{sc}$ detected on all monopole antenna channels:

$$\delta n/n \simeq \frac{1}{T_{ph}[eV]}\,\delta\Phi[Volt] \qquad (6)$$

Evidence for Langmuir ponderomotive effects

According to the previous discussion, S/WAVES antennas enable to measure both the Langmuir electric field, via high frequency variations of the antenna potential Φ_A, and density fluctuations, via low frequency oscillations of the spacecraft potential Φ_{sc} seen on the three booms in monopole mode. We now check the validity of this analysis and calibrate Eq. 6 by studying the ponderomotive effects of finite-amplitude Langmuir waves on the density background.

We isolate in the TDS data from 10/2006 to 12/2009, the waveforms that contain both Langmuir oscillations and density fluctuations signals. TDS events that contain Langmuir oscillations are selected by considering the waveforms with a localized frequency peak above 5 kHz, while those that contain density fluctuations signals are isolated by considering waveforms whose low frequency part ($<$ 5 kHz) is identical on the three monopole antennas.

For each event, the high frequency part of the voltage fluctuations, associated to Langmuir waves, is converted into electric field E_L. The electric energy is normalized to the electron kinetic energy $W_L = (\epsilon_0 E_L^2)/(2nk_B T_e)$, with n estimated from the Langmuir frequency. In the absence of accurate in-situ measurement, we use a typical solar wind temperature $T_e \simeq 10^5$ K. The low frequency part of the voltage fluctuations observed on the three monopoles is converted into relative density fluctuations $\delta n/n$ via Eq. 6, assuming a photoelectron temperature $T_{ph} = 3$ eV.

Figure 2 shows such an example where the Langmuir energy is large enough ($W_L \simeq 10^{-2}$) to generate density fluctuations by ponderomotive effects. As expected by nonlinear theory, the level of density fluctuations is of the order of the electric-to-thermal energy ratio (the normalized Langmuir energy W_L). Note also that the steeper the Langmuir envelop, the deeper the generated density fluctuations, as expected in the case of ponderomotive effects.

For each event, we compare the maximum density fluctuation to the maximum normalized Langmuir electric energy W_L. Depending on the energy of the Langmuir waves, two different behaviors are observed (Fig. 3). (i) For low energy Langmuir waves ($W_L < 10^{-4}$), the level of density fluctuations is independent on the level of Langmuir oscillations. In other words, density fluctuations are not affected by the propagation of Langmuir waves, which corresponds to the linear regime of Langmuir waves. (ii) At higher energies, the nonlinear evolution of Langmuir waves affects the density background until it reaches at saturation a level of density fluctuations $\delta n/n \simeq W_L$. The red dashed line is the expected saturation level of density fluctuations forced by Langmuir ponderomotive effects. The transition between the linear and nonlinear domain is observed for a normalized Langmuir electric energy $W_L \sim 10^{-4}$.

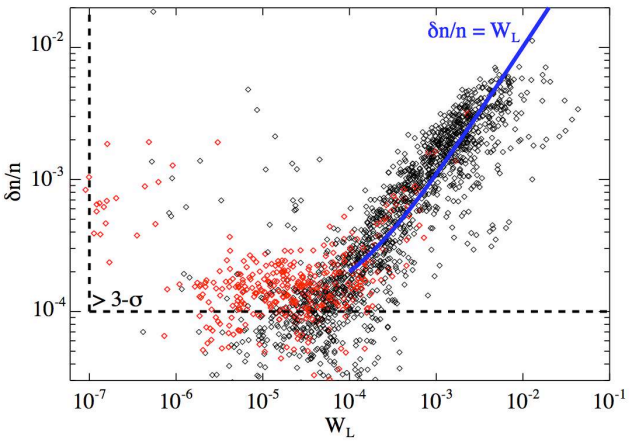

Figure 3. Density fluctuations vs Langmuir energy in the Earth electron foreshock (black diamonds) and in the quiet free solar wind (red diamonds). The blue line shows the expected saturation level of density fluctuations generated by Langmuir ponderomotive effects. The black dotted lines are the 3σ detection level.

Between 11/2006 and 02/2007, the two STEREO spacecraft were still in the Earth environment (black labels in Fig. 3), whereas between 03/2007 and 12/2009, the two probes were in their final orbit in the free solar wind (red labels). Most of the nonlinear Langmuir waves are found at the beginning of the mission, while the spacecraft performed several crossings of the Earth electron foreshock, a region where Langmuir waves are known to be intense.

The typical noise level on S/WAVES monopole antenna channel is about 0.1 mV, which means that both Langmuir waves with electric energy $W_L > 10^{-7}$ and density fluctuation with $\delta n/n > 10^{-4}$ can be observed (3σ above noise). The black dotted lines in Fig. 3 show the 3σ detection level for both electric energy and density fluctuations. One sees that density fluctuations associated to high amplitude Langmuir waves are well above the noise level. The selection criteria that controls the choice of events sent by the telemetry favors the highest voltage events, so that higher amplitude Langmuir waves are preferentially observed. The blue line $\delta n/n = W_L + 3\sigma$ also takes into account the 3σ detection level on density.

We hereafter justify the choice of the photoelectron temperature $T_{ph} = 3\ eV$. The maximum level of spacecraft potential fluctuations $\delta\Phi_{sc}$ and the maximum Langmuir energy are plotted for each waveform in Fig. 4. We recall that the expected saturation level of density fluctuations generated by nonlinear Langmuir evolution is $\delta n/n = W_L$ [*Sagdeev and Galeev*, 1969]. The dotted lines shows the level of $\delta\Phi_{sc}$ corresponding to $\delta n/n = W_L$ by using Eq. 6 with different values of $T_{ph} = 1$, 3 and 5 eV, taking into account the 3σ noise level of spacecraft potential. The observed level of spacecraft potential fluctuations is consistent with $T_{ph} = 3 \pm 1$ eV. This value is consistent with previously published values, whereas, as we explained, the linear slope is consistent with the expected saturation level of density fluctuations generated by nonlinear Langmuir evolution.

Conclusion

In this letter, we have shown that the voltage observed identically on the three booms of the STEREO antennas at frequencies 10^2 - 10^3 Hz are consistent with variations in spacecraft potential due to small scale solar wind density fluctuations. We also provided a calibration for such signals. This frequency range corresponds to solar wind density fluctuations with wavelengths $\lambda \sim [500 - 5000\ m]$, i.e. $[50 - 500\ \lambda_D]$, when taking into account the Doppler effect. To our knowledge it is the first time one directly observes and measures small-scale density fluctuations in the solar wind, in such a wavelength range.

Using simultaneous in-situ observations of electric field and density fluctuations, we gave direct observational evidence for ponderomotive coupling between solar wind density fluctuations and high-frequency Langmuir oscillations with electric-to-kinetic energy ratio $W_L > 10^{-4}$. It is the first time that ponderomotive effects are directly observed in natural space plasma, out of ionospheric experiments.

The authors are confident that this new oportunity to observe contemporaneously finite amplitude Langmuir oscillations and associated density fluctuations will give new insights in nonlinear Langmuir processes occurring in the solar wind. These small scale density measurements provide a new opportunity to directly observe the physical processes occurring close to the dissipation range of solar wind turbulence.

References

Bale, S. D., et al., The Electric Antennas for the STEREO/WAVES Experiment, *Space Sci. Rev.*, *136*, 529, 2008.

Bougeret, J. L., et al., S/WAVES: The Radio and Plasma Wave Investigation on the STEREO Mission, *Space Sci. Rev.*, *136*, 487, 2008.

Escoubet, C. P., A. Pedersen, R. Schmidt, and P. A. Lindqvist, Density in the magnetosphere inferred from ISEE 1 spacecraft potential, *J. Geophys. Res.*, *102*, 17,595, 1997.

Kaiser, M. L., T. A. Kucera, J. M. Davila, O. C. St. Cyr, M. Guhathakurta, and E. Christian, The STEREO Mission: An Introduction, *Space Sci. Rev.*, p. 198, 2007.

Kellogg, P. J., K. Goetz, S. J. Monson, S. D. Bale, M. J. Reiner, and M. Maksimovic, Plasma wave measurements with STEREO S/WAVES: Calibration, potential model, and preliminary results, *J. Geophys. Res.*, *114*, 2107, 2009.

Meyer-Vernet, N., *Basics of the Solar Wind*, Cambridge University Press, 2007.

Meyer-Vernet, N., and C. Perche, Tool kit for antennae and thermal noise near the plasma frequency, *J. Geophys. Res.*, *94*, 2405, 1989.

Pedersen, A., Solar wind and magnetosphere plasma diagnostics by spacecraft electrostatic potential measurements, *Annales Geophysicae*, *13*, 118, 1995.

Pedersen, A., et al., Electron density estimations derived from spacecraft potential measurements on Cluster in tenuous plasma regions, *Journal of Geophysical Research (Space Physics)*, *113*, 7, 2008.

Sagdeev, R. Z., and A. A. Galeev, *nonlinear Plasma Theory*, Benjamin, 1969.

Scudder, J. D., X. Cao, and F. S. Mozer, Photoemission current-spacecraft voltage relation: Key to routine, quantitative low-energy plasma measurements, *J. Geophys. Res.*, *105*, 21, 281, 2000.

Zakharov, V. E., Collapse of Langmuir Waves, *Soviet Journal of Experimental and Theoretical Physics*, *35*, 908, 1972.

LESIA, Observatoire de Paris, CNRS, UPMC, Université Paris Diderot; 5 Place Jules Janssen, 92190 Meudon, France

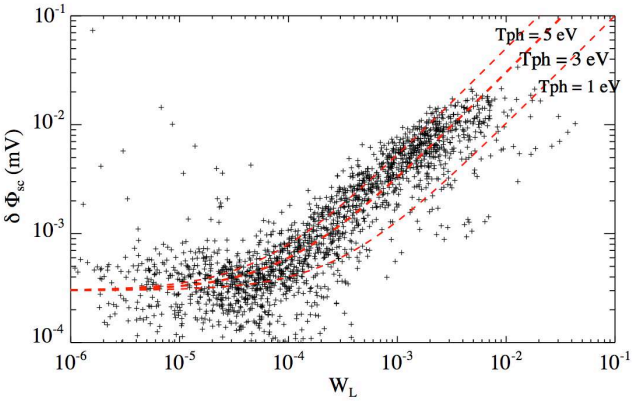

Figure 4. Fluctuations of potential $\delta\Phi_{sc}$ simultaneous to Langmuir oscillations of normalized energies W_L. The dotted lines show the expected level of density fluctuations generated by Langmuir ponderomotive effects, associated to $\delta\Phi_{sc}$ via Eq. 6, for different T_{ph}.

Henri et al. (2009)
JGR-Space Physics, 114, A03103

JOURNAL OF GEOPHYSICAL RESEARCH, VOL. 114, A03103, doi:10.1029/2008JA013738, 2009

Evidence for wave coupling in type III emissions

P. Henri,[1,2] C. Briand,[1] A. Mangeney,[1] S. D. Bale,[3] F. Califano,[1,2] K. Goetz,[4] and M. Kaiser[5]

Received 8 September 2008; revised 5 December 2008; accepted 23 December 2008; published 5 March 2009.

[1] Using new capabilities of waveform analyses provided by the S/WAVES instruments onboard the two STEREO spacecraft, we present for the first time a complete set of direct evidence for three-wave coupling occurring during a type III emission and involving two Langmuir waves and an ion acoustic wave. Information on the Doppler-shifted frequencies and especially the phases of the waves are used in order to check first the conservation of momentum and energy, through Fourier analyses, and second the phase locking between the waves, through bicoherence analyses. Wavelet analyses allow us to resolve for the first time the coupling regions, in which spatial length is estimated to be 18 ± 5 km. The wave packets travel at comparable speed, and the characteristic available interaction time is about 1 s. Interpretations of the phase coupling and evaluation of the growth rate of the waves tend to favor the parametric decay, at least in the observational events considered in this work.

Citation: Henri, P., C. Briand, A. Mangeney, S. D. Bale, F. Califano, K. Goetz, and M. Kaiser (2009), Evidence for wave coupling in type III emissions, *J. Geophys. Res.*, *114*, A03103, doi:10.1029/2008JA013738.

1. Introduction

[2] Solar type III radio emissions are one of the most prominent features of the meter-decameter ranges of frequency. The emissions show a pronounced drift with time toward lower frequencies (an example is shown on Figure 2). Since the early work of *Wild* [1950] and *Ginzburg and Zheleznyakov* [1958], the generally accepted model for such emission is as summarized below. During a flare, high-energy electrons (1–100 keV) are expelled from the solar corona and travel along the interplanetary magnetic field lines. They produce a bump on the local electron distribution function generating Langmuir waves via the so-called "bump-on-tail instability." Then, nonlinear wave couplings generate electromagnetic waves at f_p^- (the local electron plasma frequency) or $2f_p^-$. The plasma frequency decreases with the heliocentric distance owing to the decrease of the electron density: this is the origin of the time frequency drift characteristic of the type III emissions.

[3] However, as noted by *Sturrock* [1964], such a mechanism should deplete all the energy of the beam on a very short time scale, which would not be able to travel long distances as observed. Since then, many studies have been devoted to validate the general model and to identify the processes able to remove the particles out of resonance with the waves and that stopping the growth of the waves and allowing the beam to survive long distances.

[4] Different lines of research were developed. The first one, within the frame of the quasi-linear theory, takes advantage of the turbulent state of the solar corona and solar wind: the fast particles are moved out of resonance with the waves through scattering of the unstable waves on density fluctuations covering a wide spectrum (from a few hundred of meters to several hundred of kilometers) [*Smith*, 1970; *Li et al.*, 2006]. However, *Lin et al.* [1981, 1986] provided observational evidence that quasi-linear relaxation alone cannot explained the evolution of the beam (at least for the events they studied). First, they showed that the electric field intensity computed from the theoretical growth rate, extrapolated using the observed positive slope of the electron distribution function, would be too large. The amplitude of the waves would grow out of the framework of quasi-linear theory. Second, quasi-linear models predicts a plateauing of the bump of the distribution function which is not observed.

[5] A second line of research takes into account inhomogeneities in the solar wind density [*Budden*, 1985] through linear mode conversion and scattering of Langmuir waves on density gradients. *Willes and Cairns* [2001] and *Willes et al.* [2002] explained how Langmuir waves propagating along the density gradients can be mode converted, which could remove the beam particles out of resonance with the waves. In the Stochastic Growth Theory framework [*Robinson*, 1993], the beam driven Langmuir growth rate is treated as a random variable that depends on random density inhomogeneities, thus allowing the beam to propagate long distances.

[6] Type III electromagnetic emissions are thought to be produced via two different nonlinear wave-wave couplings.

[1]LESIA, Observatoire de Paris, Université Paris Diderot, CNRS, UPMC, Meudon, France.
[2]Dipartimento di Fisica, Università di Pisa, Pisa, Italy.
[3]Physics Department and Space Sciences Laboratory, University of California, Berkeley, California, USA.
[4]School of Physics and Astronomy, University of Minnesota, Minneapolis, Minnesota, USA.
[5]NASA Goddard Space Flight Center, Code 674, Greenbelt, Maryland, USA.

0148-0227/09/2008JA013738$09.00

Through electromagnetic coupling, a pump Langmuir wave L decays into a low-frequency LF waves and a transverse electromagnetic wave T_{fp-} at the local plasma frequency, observed as type III fundamental emission:

$$L \rightarrow T_{f_p^-} + LF \tag{1}$$

Through electrostatic coupling, the pump Langmuir wave L decays into a low-frequency LF and a daughter Langmuir wave L', which can further couple with the pump wave to generate a transverse electromagnetic wave T_{2fp-} at twice the local plasma frequency, observed as type III harmonic emission:

$$L \rightarrow L' + LF \qquad L' + L \rightarrow T_{2f_p^-} \tag{2}$$

[7] This paper focuses on the electrostatic coupling. A number of authors have claimed that the spectral analyses of the electric field in the solar wind provides some support in favor of the electrostatic decay process [e.g., *Lin et al.*, 1986; *Kellogg et al.*, 1992; *Gurnett et al.*, 1993; *Thejappa et al.*, 1993, 1995, 2003; *Thejappa and MacDowall*, 1998]. They based their conclusions on some characteristics signatures like the simultaneous occurrence of Langmuir and low-frequency waves (like ion acoustic, whistlers or lower hybrid waves), or the comparison between theoretical thresholds and the observed energy in the waves. However, as already pointed out by *Kennel et al.* [1980] and *Thejappa et al.* [1995], the simultaneous occurrence of two waves in the spectrum doesn't necessarily mean wave coupling. Indeed, the waves can be generated by particles of different energy present in a same electron cloud; an efficient three-wave coupling requires the fundamental equations of energy and momentum conservation to be satisfied:

$$\omega_1 = \omega_2 + \omega_3 \tag{3}$$

$$\vec{k_1} = \vec{k_2} + \vec{k_3} \tag{4}$$

where ω and $\vec{k}$ refer to the pulsation and wave number of the waves. When observed onboard only one spacecraft, equations (3) and (4) reduce to a single relation for the Doppler-shifted frequencies $f^{Doppler} = \omega^{Doppler}/2\pi$:

$$\begin{aligned} f_1^{Doppler} &= f_1 + \frac{\vec{k}_1}{2\pi}.\vec{V}_{SW} \\ &= (f_2 + f_3) + \frac{(\vec{k}_2 + \vec{k}_3)}{2\pi}.\vec{V}_{SW} \end{aligned}$$

leading to the following equation for resonance:

$$f_1^{Doppler} = f_2^{Doppler} + f_3^{Doppler} \tag{5}$$

Equation (5) can be directly tested from in situ measurements which combine high spectral and temporal resolution, as well as phase information. Only waveforms measurements can provide the required information. Such observations are available with the S/WAVES investigation on the STEREO mission [*Bougeret et al.*, 2007].

[8] On the basis of data obtained on 14 January 2007 by the waveform analyzer of the S/WAVES instrument onboard STEREO, evidence for nonlinear coupling between Langmuir and ion acoustic waves (also known as ion sound waves in the literature), at ≈80–250 Hz, occurring during a type III event are presented. Three complementary methods are employed: (1) a spectral analyses that checks the frequency correlation, (2) a wavelet analyses that verifies the time occurrence of the waves, and (3) a bicoherence analyses that checks the phase correlation between the waves. The validity of equations (3) and (4) on observed data is thus directly tested (through equation (5)). The phase relation was already studied in the Earth bow shock [*Dudok de Wit and Krasnosel'Skikh*, 1995] and the foreshock [*Bale et al.*, 1996] environments, but, to our knowledge, it is the first time it is used on data related to type III event. This paper focuses on the parametric instability version of the electrostatic decay, through direct tests on the phase resonance, rather than its weak turbulence version [*Robinson et al.*, 1993]. This will be justified by the bicoherence analysis of the electric waveforms.

[9] Details on the instrument, the data and the solar wind conditions are presented in section 2. After identification of the low-frequency mode, three independent analyses for the three-wave coupling are presented in section 3. Section 4 discusses details on the coupling and describes it in the context of the type III.

2. Observations and Data

[10] S/WAVES is composed of three 6 m monopole antennas, orthogonal to each other, with an effective length of about 1 m [*Bougeret et al.*, 2007; *Bale et al.*, 2008]. Two modes of observation are available: remote sensing to follow the propagation of the radiosources in the solar wind with spectral radio receivers and *in situ* measurement of electric waveforms along the three antennas with the Time Domain Sampler mode (TDS).

[11] The TDS data reported in this paper are composed of N = 16384 samples with an acquisition rate of 125,000 samples per second (a time step of δt = 8 μs for a total duration of 130 ms per event). This long total duration allows us to capture entire Langmuir wave packets. In terms of frequencies, those electric field waveforms enable to cover a range from 10 Hz to 60 kHz. Thus, signatures from below the electron cyclotron frequency (typically 100 Hz in the solar wind) to above the plasma frequency (typically 10 to 20 kHz) are accessible. The frequency gain is flat in the frequency range of interest here (100 Hz to 20 kHz). Finally, the S/WAVES A/D converter is accurately linear. Thus spurious nonlinear artifacts are not introduced, so that studies of nonlinear wave interactions are possible.

[12] The voltage measured on the three antennas is then converted into an electric field, and projected in the spacecraft coordinates, using the set of parameters called w/base caps (Graz) by *Bale et al.* [2008, Table 13] in order to take into account the effective length and direction of the STEREO antennas.

[13] In its final orbit the spacecraft coordinates (X, Y, and Z) are defined as follows: the x component is sunward along the radial direction, the Z component is normal to the ecliptic plane, southward for STEREO A and northward

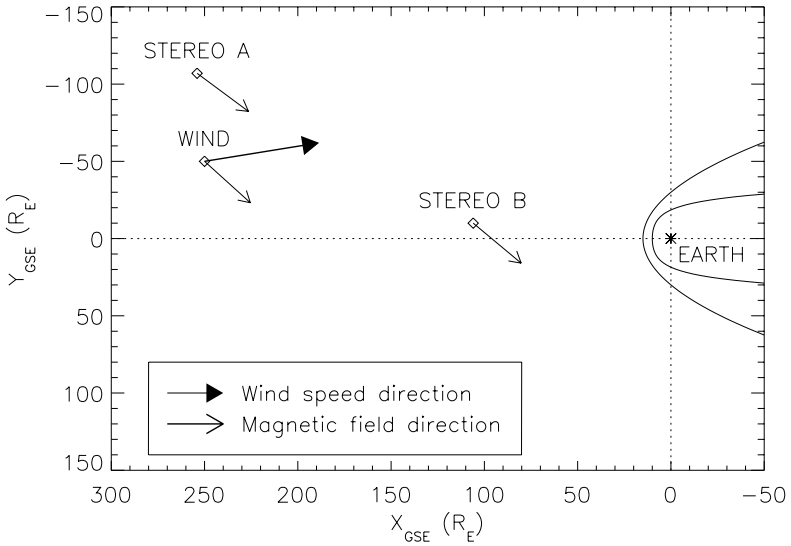

Figure 1. Position of WIND and STEREO A and B projected on the ecliptic plane in GSE coordinates on 14 January 2007 when the type III solar burst reaches the spacecraft. Distances are expressed in Earth radii (R_E) units. The solar wind speed and the magnetic field direction recorded by the spacecraft are displayed. The values of the magnetic field magnitude and angle with the solar wind direction are discussed in the text.

for STEREO B, and the Y component complete the direct orthogonal frame. But by the day considered in this study, both STEREO spacecraft were not yet in their final orbit. They were slowly rotating around the radial direction, to reach their final configuration. Thus, the spacecraft coordinates are corrected as follows: the x component is indeed sunward in the radial direction, but the Y and Z components are rotated by an angle of about $-90°$ compared to the previous definition on STEREO A and 180° on STEREO B. In the following, the electric field measurements are expressed in the corrected spacecraft coordinates.

[14] Figure 1 displays the position of WIND, STEREO A and STEREO B on 14 January 2007, together with magnetic field and wind speed directions. The spacecraft are separated by less than 200 Earth radii, so that plasma measurements from WIND are used when those from STEREO are not available (wind speed, temperatures). The 1 h average wind speed from WIND/3-DP [*Lin et al.*, 1995] is about $V_{SW} = 315$ km s^{-1}. The magnetic fields are recorded by IMPACT [*Acuña et al.*, 2007] at 8 samples s^{-1} onboard both STEREO and by MFI [*Lepping et al.*, 1995] onboard WIND with 3 s resolution. The amplitude of the magnetic field is 7.4 nT at STEREO A, 7.3 nT at STEREO B, and 7.4 nT at WIND with maximal fluctuations below 0.2 nT during the period of interest. The magnetic field and wind speed directions, obtained from WIND data with 92 s resolution values, make an angle $\theta = 60°$ with maximal fluctuations below 9 during this period. The magnetic field direction is almost identical at the three spacecraft positions and remains constant within a few degrees during the whole period of interest.

[15] The electron temperature observed by WIND/3DP is $T \simeq 10^5$ K, and the electron density in the solar wind, estimated from the plasma frequency, is about $n \simeq 10^6$ m^{-3}. From the electron density and temperature, the Debye length is $\lambda_D \simeq 10$ m.

[16] Figure 2 displays the time-frequency spectrum (the so-called dynamic spectrum) recorded by WIND/WAVES (WIND has higher sensitivity than STEREO for distinguishing the plasma line) between 0700 and 1500. Type III is observed from 1040 to 1150 (UT). The drift of the fundamental (full line) and the harmonic (dashed line) radio emissions are estimated from the onset time of the type III and the Parker spiral (Estimation courtesy of S. Hoang following *Hoang et al.* [1994]). The radio emission in this event is dominated by the harmonic while the fundamental is very weak. An enhanced level of Langmuir wave activity appears when the extrapolated fundamental of the type III intersects the local (satellite position) plasma frequency line (at about 1110 (UT) on WIND). Assuming that the beam travels along the Parker spiral, the estimation of the onset time of the type III, together with the observed onset time of Langmuir wave activity, leads to an estimation of the electron beam speed associated with the type III of about $V_b \simeq 0.21c$. The Langmuir activity was also recorded by the in situ measurements of S/WAVES/TDS, as a signature of the type III electrons passing the spacecraft. Note that owing to ballistic effects, the type III electrons should cross the three spacecraft at different times. In the following, we concentrate on the TDS Langmuir events associated with this type III on STEREO A between 1125 and 1205 UT, and on STEREO B between 1150 and 1215 UT. Nineteen such events have been measured by STEREO A and 26 events by STEREO B.

[17] Other type III bursts are recorded by WIND/WAVES before and after the one we study. No TDS electric field waveforms associated with these bursts have been telemetered, possibly because of criteria selection from the TDS or because the electron beams associated with these bursts may not have crossed the STEREO spacecraft. Thus, they are not described in the present paper.

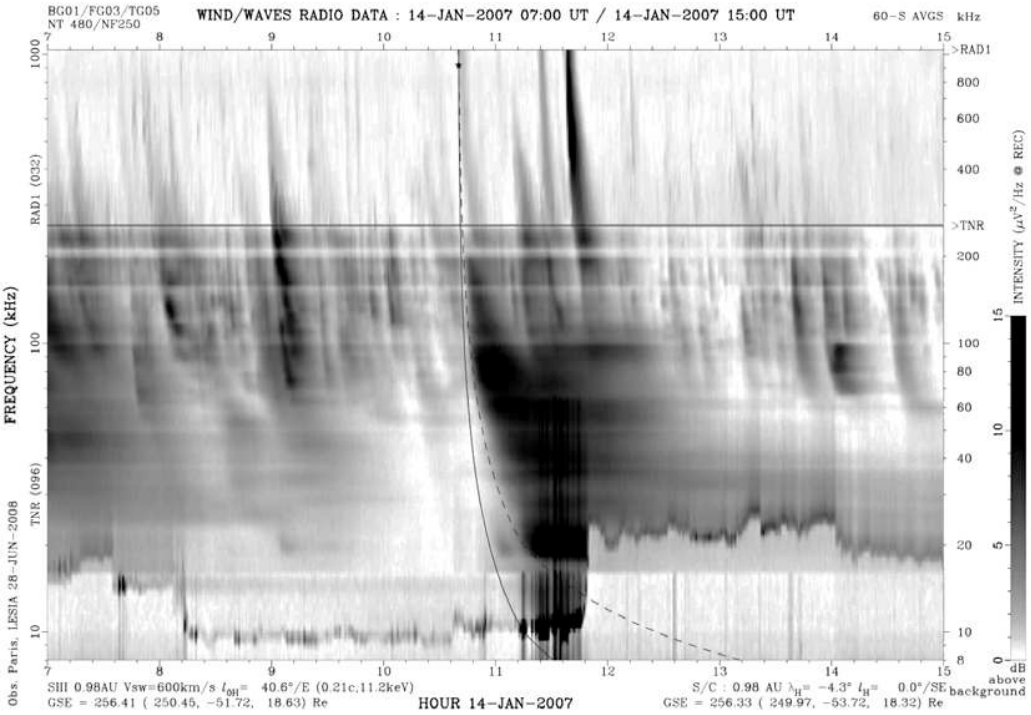

Figure 2. Time frequency spectrum from WIND/WAVES on 14 January 2007. A type III burst is observed from 1040–1150 (UT). The full line shows the leading edge of the fundamental emission. The dashed line corresponds to the leading edge of the harmonic emission. Courtesy of S. Hoang.

[18] Moreover, since the fundamental electromagnetic emission was not observed in this type III burst, the electromagnetic coupling mechanism, see equation 1, for generating the fundamental radio emissions at the plasma frequency is out of the scope of this paper.

3. Evidence for Wave Coupling

[19] Figure 3 shows the three components of the electric field of a typical event. An entire beat-like wave packet is captured, lasting 50 ms. The maximal intensity of the electric field is of the order of 10 mV m^{-1}, the amplitude along the X direction being larger than the two other components.

3.1. Spectral Analyses

[20] Figure 4 displays the Fourier spectrum of the x component of the electric field for the event shown on Figure 3. Three main features appear: a low-frequency peak at 0.25 kHz, an small intermediate frequency peak at 3 kHz, and a high-frequency peak at 10 kHz. This last frequency is identified from the dynamic spectrum (Figure 2) as the local plasma frequency f_p, and corresponds to the Langmuir waves. A closer view on the high-frequency signal (Figure 4, bottom) shows that it is actually composed of two peaks separated by 0.25 kHz. The difference between the frequency of the two Langmuir waves matches the lower frequency. We now focus on the identification of the low-frequency wave.

[21] The electron cyclotron frequency is about 0.2 kHz, i.e., in the frequency range where the LF signal is observed. The LF wave could be electromagnetic waves, such as whistler and lower hybrid waves, or electrostatic waves such as electron Bernstein mode or ion acoustic waves.

[22] When filtering out the high-frequency component, the LF signal appears as a modulated sine-like function identical on the three antennas. This could be interpreted as the signature of a longitudinally polarized wave along the bisectrix of the three antennas (the X direction), but since this direction is related to the spacecraft geometry and is usually different from the solar wind speed or the magnetic field directions, such an explanation is very unlikely. However, as pointed out by *Kellogg et al.* [2007], the signal can be dominated at low frequencies by local density fluctuations in which the spacecraft is embedded (through quasi-static modifications of the spacecraft charging). In this case, the response is expected to be identical on the three antennas and the signal would appear only on the x component, when "projected" in the spacecraft coordinates.

[23] The LF signal is thus identified as density perturbations associated with a LF wave. Among the candidates in this range of frequency, the only wave mode associated with density fluctuations is the ion acoustic wave (IAW). Indeed, when observing the other waves, which density fluctuations are negligible, the recorded signal should be dominated by the electric field, rather than by density fluctuations, thus showing different signals on the three antennas, which is not observed. We thus identify the low-frequency signature as an IAW.

[24] Let us stress that we observe the IAW density fluctuation in terms of an "equivalent" electrical field. The true IAW electric field is proportional to and in phase quadrature with the observed potential generated by the

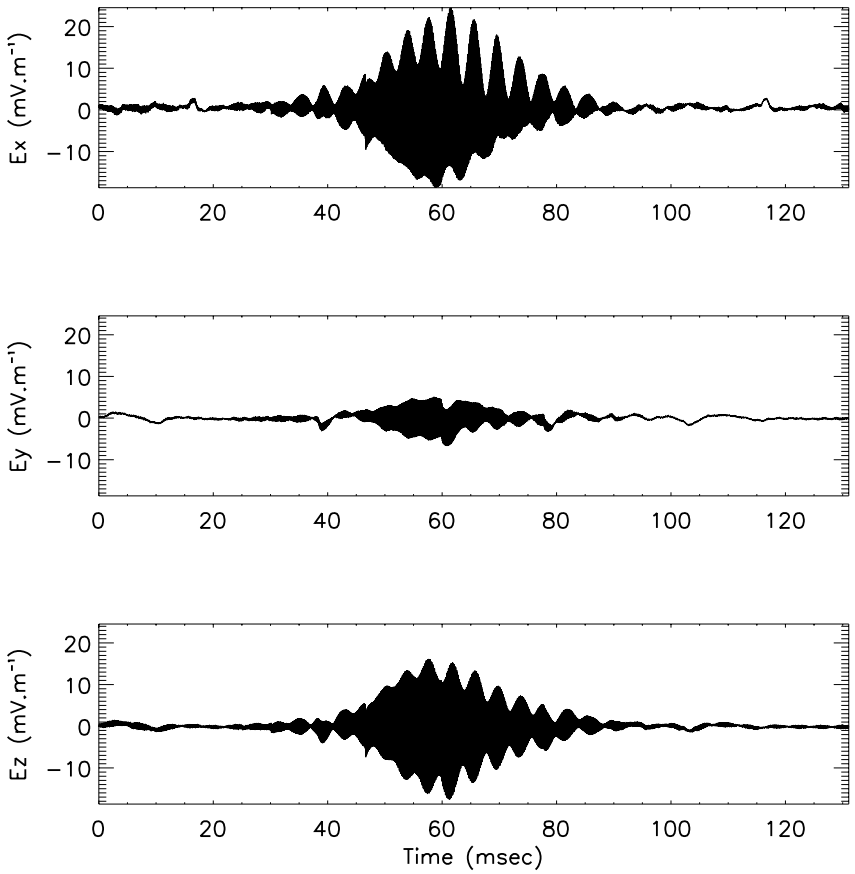

Figure 3. Typical electric field waveform of Langmuir waves recorded by S/WAVES/TDS in spacecraft coordinates, associated with type III.

IAW density fluctuation. From now on, we will work only with the x component electric field, and we consider the density fluctuations as a tracer for IAW electric field.

[25] During the period of strong Langmuir activity, a total of 37 TDS events (19 from STEREO A and 18 from B) were transmitted from the two spacecraft. Among these events, 14 (10 on STEREO A and 4 on B) show two distinguishable Langmuir wave peaks together with an IAW. Figure 5 displays for each event the relation between the frequency difference Δf_L between the two Langmuir waves and the frequency f_{IA} of the IAW for the two spacecraft. The resonant relation $\Delta f_L = f_{IA}$ is very well satisfied for all 14 events. This relation between frequencies observed in the spacecraft frame is compatible with the conservation of momentum and energy that must be satisfied in case of three-wave coupling (equation 5) and strongly suggests the possibility of such a nonlinear wave coupling. In order to confirm this three-wave coupling, we use two different analyses: a wavelet analyses (section 3.2) and a bicoherence analyses (section 3.3) are now considered on these selected TDS events.

3.2. Wavelet Analyses

[26] The wavelet transform is a powerful method to study a signal composed of nonstationary waves [*Daubechies*, 1990; *Farge*, 1992].

[27] Consider a time series E_n with time step δt, the wavelet transform of the time series is defined as the convolution of the signal with a "mother" wavelet function ψ normalized, translated, and scaled (s being the scale):

$$W_n(s) = \sum_{n'=0}^{N-1} E_{n'} \frac{1}{\sqrt{s}} \psi^* \left(\frac{(n'-n)\delta t}{s} \right)$$

where ψ* stands for the complex conjugate of ψ. Among various wavelets, we choose the Morlet wavelet Ψ_0, consisting of a plane wave modulated by a gaussian envelope:

$$\Psi_0(\eta) = \pi^{-1/4} e^{i2\pi\eta} e^{-\eta^2/2}$$

With this definition, the Morlet wavelet scale factor s is equal to the inverse of the Fourier frequency, which simplifies the interpretation of the wavelet analyses. The Morlet wavelet is known to provide a good compromise between time and frequency resolution (reviews on wavelet analyses can be found in the work by *Torrence and Compo* [1998] and *van den Berg* [1999]).

[28] Figure 6 displays the modulus of the wavelet transform applied to the waveform displayed in Figure 3 (top). The resolution in frequency of the Morlet wavelet transform

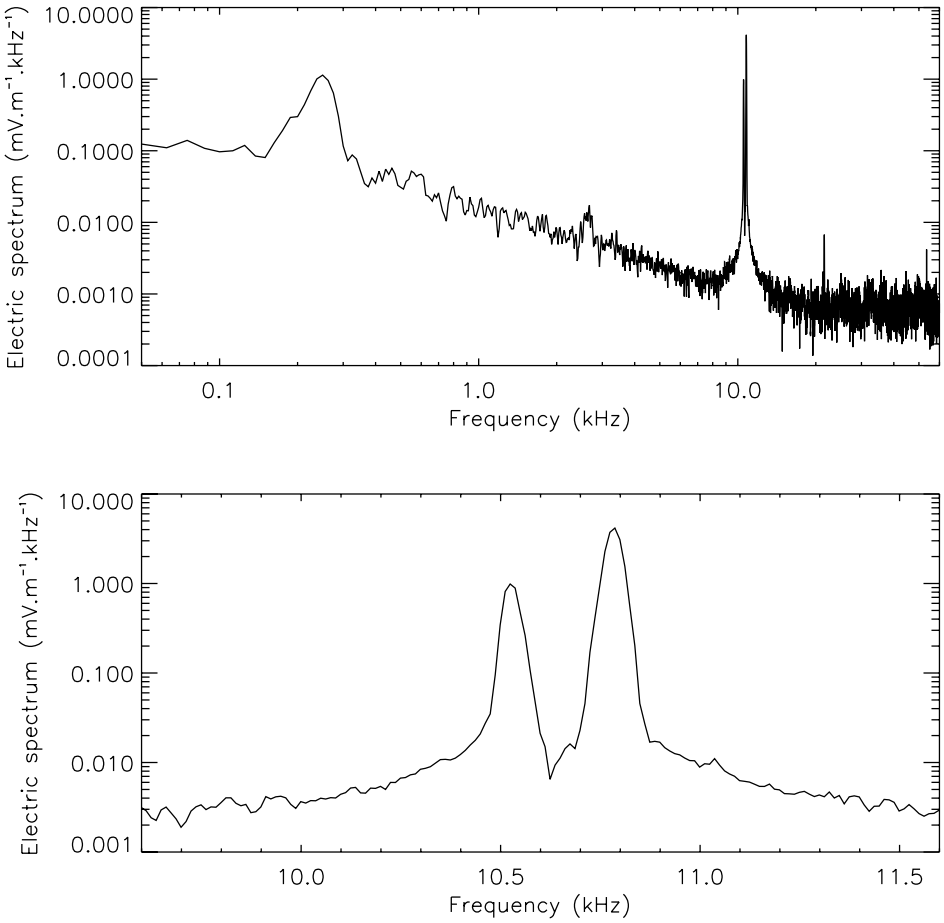

Figure 4. Fourier spectrum of the x component electric field from Figure 3. (top) Whole frequency range. (bottom) Zoom centered on the high-frequency double feature at 10 kHz.

is not sufficient to separate the two high frequencies at about 10 kHz. Instead it shows a signal, at the average of these two frequencies, modulated by the beating frequency. The IAW at 0.25 kHz is maximum at 60 ms when the maximum of the Langmuir waves occurs.

[29] This is a general feature: a systematic wavelet analyses on the 14 events reported in Figure 5 shows indeed that the IAW and the Langmuir signals always occur simultaneously. Knowing the electron temperature, the ion sound speed is estimated to be $C_s \simeq 30$ km.s^{-1}. Since the solar wind speed $V_{SW} \simeq 315$ km.s^{-1}, the IAW packets are mainly advected by the solar wind flow. From the average duration of the IAW packets, the spatial length of the IAW packet is estimated to be $\sim 18 \pm 5$ km. Note that the 3 kHz signal is present during all the event, but is not correlated with the two Langmuir waves, neither with the IAW.

3.3. Bicoherence Analyses

[30] Up to now, we have focused on the simultaneous occurrence of three waves, with frequencies consistent with a three-wave nonlinear coupling. But coupling requires also phase coherence between the waves. Such phase relations can only be checked from waveform data.

[31] The bicoherence is used as an estimator of quadratic phase coupling, characteristic of three-wave coherent interactions. *Lagoutte et al.* [1989] give a methodological introduction to bicoherence analyses based on a Fourier approach. Although studies of bicoherence have been reported in the ionosphere [*Pecseli et al.*, 1993], the bow shock [*Dudok de Wit and Krasnosel'Skikh*, 1995] and the solar wind near the foreshock edge [*Bale et al.*, 1996], to our knowledge, the present analyses represents the first time that bicoherence is used to study three-wave coupling in the solar wind during a type III.

[32] In the case of three-wave coupling, the relative phase $\Phi_1 + \Phi_2 - \Phi_3$ between the three phases $\Phi_{i=1,3}$ associated to the three frequencies $f_{i=1,3}$ linked by the relation $f_1 + f_2 = f_3$ should remain constant. Bicoherence measures statistically the degree of stationarity of this relative phase.

[33] To optimize the time resolution, and diminish the bias introduced by the method, the wavelet bicoherence [*Van Milligen et al.*, 1995; *Dudok de Wit and Krasnosel'Skikh*, 1995] is here preferred to the Fourier bicoherence. For convenience, the wavelet transform will thereafter be expressed in terms of frequencies, instead of scales. The wavelet cross bispectrum is defined in frequency space as

$$B(f_1,f_2) = < W(f_1)W(f_2)W^*(f_1+f_2) > \qquad (6)$$

where $< >$ stands for the average over the samples, and W^* for the complex conjugate of W (recall that $W(n\delta t, F = 1/s)$ is a function of both time and frequency).

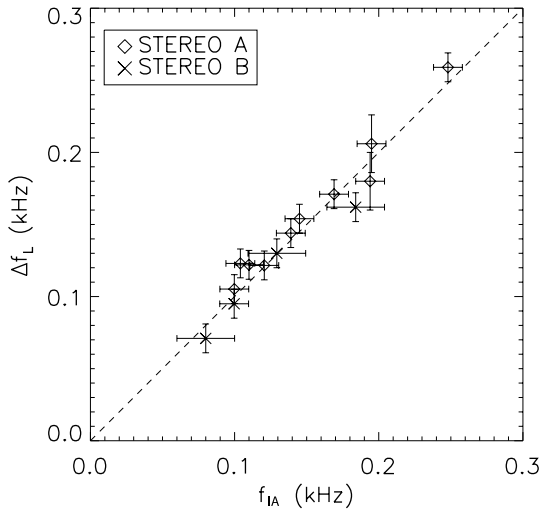

Figure 5. Difference between the two Langmuir frequencies (Δf_L) as a function of the ion acoustic wave frequency (f_{IA}) on 14 different events on STEREO A and B. Each point represents a different Time Domain Sampler (TDS) event during the type III. Only events showing an ion acoustic mode and two Langmuir waves are displayed. The dotted line is not a fit but shows the expected identity $\Delta f_L = f_{IA}$.

[34] To take into account phase effects only, in other words to avoid amplitude effects, the wavelet cross bispectrum is normalized. The wavelet normalized cross bispectrum, also called wavelet bicoherence, is thus defined as

$$b(f_1,f_2) = \frac{< W(f_1)W(f_2)W^*(f_1+f_2) >}{< |W(f_1)W(f_2)W^*(f_1+f_2)| >}$$

For a stationary signal, the bicoherence vanishes when the phase relation is random, and maximal (1 for the chosen normalization) when the phase relation remains constant. A nonzero bicoherence value $b(f_1, f_2)$ is thus the signature of phase locking between three waves with frequencies f_1, f_2, and $f_1 + f_2$.

[35] When using a wavelet basis, the bicoherence is computed by averaging on overlapping samples. But as stressed by *Soucek et al.* [2003], the statistical validation of bicoherence requires to use independent samples. The duration of an independent sample can be evaluated from the time of coherence of the waves, which is about the duration of the wave packet. It means that each TDS event should be considered as an independent sample and that the bicoherence computed with only one event can be meaningless.

[36] Bicoherence is very sensitive to the nonstationarity of frequencies and to the presence of discontinuities in the data set. The nonstationarity of frequencies involved in a three-wave coupling spreads the bicoherence signal and thus decreases the wavelet bicoherence value at all involved frequencies. This is a consequence of the intrinsic frequency accuracy of the Morlet wavelet. Indeed, the time-frequency finite resolution of the chosen wavelet implies that the uncertainty on the frequencies is $\Delta F \simeq 1/4f$, with Δf the resolution at 3 dB. Discontinuities in the waveform, such as spikes, appears through spectral analyses as a large spectrum of coupled frequencies (for instance Dirac's function is a white noise with correlated phases). This implies an increase of the bicoherence signal, without physical significance, and thus reduces the signal-to-noise ratio of the bicoherence. To avoid both effects, only events with an IAW in the frequency range (100 Hz, 200 Hz), and free of spikes are considered, reducing the number of useful samples to 10. The signal analyzed for the study of bicoherence resulted from the concatenation of these 10 "independent"

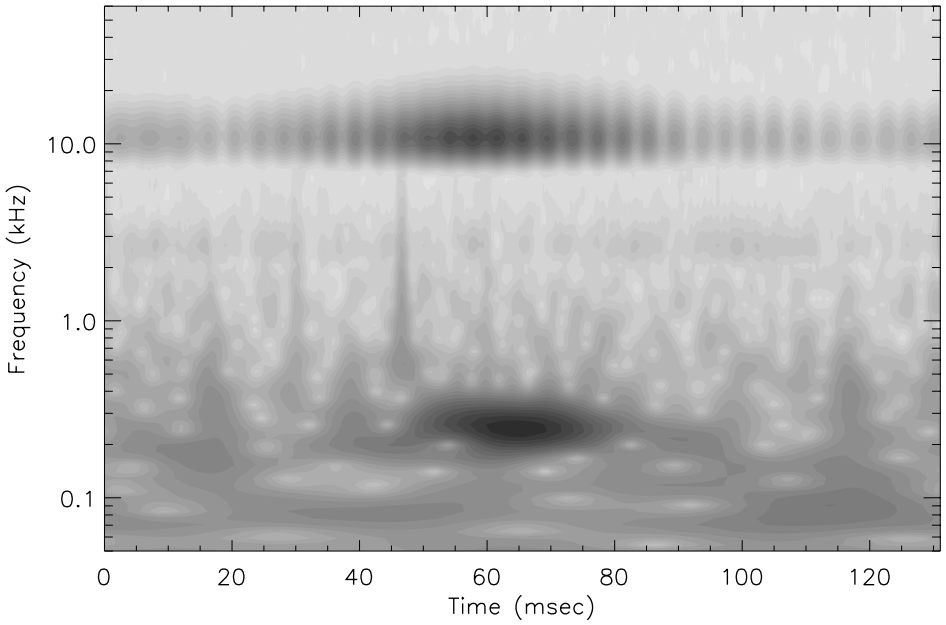

Figure 6. Modulus of the Morlet wavelet transform of the event displayed in Figure 3 (top).

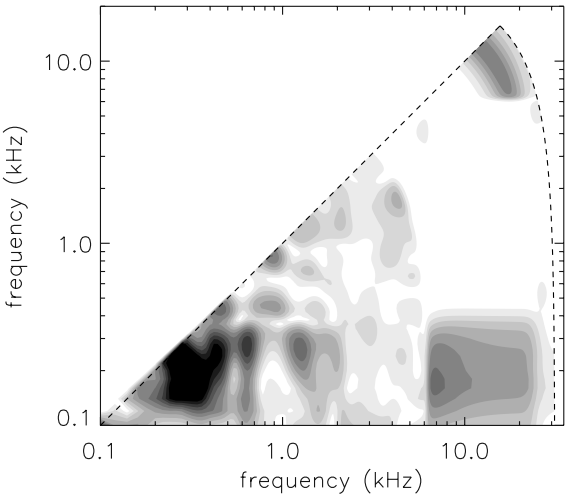

Figure 7. Wavelet bicoherence of three-wave TDS events computed for frequencies from 100 Hz to 30 kHz (inside the dotted line). Minimum value in white for bicoherence $b = 0$, maximum value in black for bicoherence $b = 0.6$. Note three main signatures at $(f_{IA}, f_{IA}) \simeq$ (0.2 kHz, 0.2 kHz); $(f_L, f_L) \simeq$ (10 kHz, 10 kHz) and $(f_L, f_{IA}) \simeq$ (10 kHz, 0.2 kHz).

samples, the averages appearing in equation (6) being replaced by averages over the points of the concatenated signal.

[37] Note that the density fluctuation of the IAW is in phase quadrature with its associated electric field, which does not affect the bicoherence study because bicoherence is not sensitive to constant dephasing.

[38] Figure 7 shows the results of the bicoherence analyses computed in this way. Three main signatures linked to the three waves discussed above arise at $(f_{IA}, f_{IA}) \simeq$ (0.2 kHz, 0.2 kHz); $(f_L, f_L) \simeq$ (10 kHz, 10 kHz); $(f_L, f_{IA}) \simeq$ (10 kHz, 0.2 kHz). The evaluation of the statistical significance of the bicoherence, discussed bellow, shows that the multiple signatures at frequencies lower than 6 kHz are significant. However, it is not linked to the three-wave process discussed in this paper and will described in a future work. We limit the present discussion to the following results.

[39] First, at low frequencies, the phase resonance between low-frequency modes at $(f_{IA}, f_{IA}) \simeq$ (0.2 kHz, 0.2 kHz) can be interpreted as the generation of harmonics of the IAW. It could also be linked to the multiple bicoherence signatures present in this frequency range. However, no obvious peak at twice the IAW frequency is seen in the Fourier spectrums.

[40] Second, the bicoherence shows a phase locking that involves waves at about 10 kHz. This could be interpreted as the generation of the transverse EM mode at $2f_p^-$ generated during the type III. However, the conversion of Langmuir waves into EM waves $L + L' \rightarrow T$ should be hard to detect because of the low sensitivity of the antennas to local EM waves. The observed bicoherence signature is more likely due to the generation of the Langmuir harmonics at twice the plasma frequency. The bicoherence value is $b(f_L, f_L) = 0.34$.

[41] Third, the main result of this bicoherence analyses is the evidence for a bicoherence signal that involves a high-frequency mode $f_L \simeq 10$ kHz and a low-frequency mode $f_{IA} \simeq 0.1-0.2$ kHz, with a value of $b(f_L, f_{IA}) = 0.37$. Indeed, this implies that the three waves described in sections 3.1 and 3.2 remain phase locked from one event to the other. It is the signature of the expected phase coupling between the IAW and the two Langmuir waves. This is a strong evidence in favor of three-wave interaction in agreement with the hypothesis suggested by Fourier and wavelet analyses.

[42] To validate the bicoherence study, one can evaluate the statistical threshold above which the bicoherence applied to the original signal is considered significant, by computing the bicoherence on phase randomized surrogate data. Surrogate data are generated from the original data set by keeping the power spectrum unchanged and redistributing the phases randomly, in order to destroy the nonlinear dynamics in the data. See *Koga and Hada* [2003] and *Siu et al.* [2008] for details on the method. Bicoherence computed on 30 phase randomized surrogates (a good compromise between statistics and computing time) shows in the frequency domain of interest a mean bicoherence response $\bar{b} < 0.04$, with a standard deviation $\sigma_b < 0.03$. Bicoherence computed on the original data with response above $\bar{b} + 3\sigma_b \simeq 0.1$ are thus considered significant. This result clearly confirms the validity of our bicoherence analyses, thus demonstrating the three-wave coupling.

4. Discussions

[43] We have shown that the data obtained on 14 January 2007 by the waveform analyzer of the S/WAVES instrument onboard STEREO, show strong evidence for a nonlinear coupling between two Langmuir waves and an IAW in the range 80–250 Hz. The IAW observed frequency is dominated by the Doppler shift; its wavelength is estimated between 1 and 3 km for the different events. From conservation of momentum, the wavelengths of the Langmuir waves are about twice this value. Considering that the spatial length of the coupling region is of the order of the length of the advected ion acoustic wave packet, we estimate the average spatial length L_c of the coupling region to be $L_c \sim 18 \pm 5$ km (about 2.10^3 λ_D). As a result, the length of the coupling zone, as discussed in section 3.2, is quite short since it only covers a few Langmuir wavelengths. We shall now come to discuss the nature of the coupling as well as the consequences for the understanding of the physics of type III bursts.

4.1. Electrostatic Coupling

[44] The bicoherence analysis shows a phase resonance between the three waves. Therefore, we interpret the observed coupling between electrostatic waves in term of a parametric instability rather than the weak turbulence approach.

[45] The observed electrostatic three-wave coupling can be explained via two kinds of parametric coupling. The first one concerns the parametric decay of a finite-amplitude Langmuir wave (L) into an IAW (S) and a backscattered daughter Langmuir wave (L'):

$$L \rightarrow S + L'$$

The second one concerns the scattering of a beam excited mother Langmuir wave by preexistent IAW into a backscatter Langmuir wave:

$$L + S \rightarrow L'$$

[46] In the case of parametric decay, the IAW is expected to be generated by the ponderomotive force created by the two beating Langmuir waves. The electric pressure is thus expected to compensate the thermal pressure. To test this possibility, the ratio of electric energy to thermal energy is

$$\frac{\epsilon_0 E^2}{n k_B T} \simeq 6.10^{-4}$$

using the following values: $E \simeq 10$ mV.m^{-1} the observed electric field for the Langmuir waves, $T \simeq 10^5$ K the electron temperature and $n \simeq 10^6$ m^{-3} the electron density. The threshold for parametric decay of the pump Langmuir wave into a daughter Langmuir wave and an IAW is [*Nishikawa*, 1968; *Bardwell and Goldman*, 1976]

$$\frac{\epsilon_0 E^2}{n k_B T} > 8 \frac{\gamma_{IA}}{\omega_{IA}} \frac{\gamma_{L'}}{\omega_{L'}}$$

with ω and γ the angular frequency and Landau damping of the IAW and daughter Langmuir waves. The threshold for electrostatic decay has been estimated for typical solar wind parameters to be $\frac{\varepsilon_0 E^2}{n k_B T} \geq 2.5\ 10^{-5}$ [*Lin et al.*, 1986]. The observed ratio is much higher than this threshold, which allows the development of parametric decay. Since the parametric decay is far more efficient than the parametric scattering, we conclude in favor of the decay.

[47] To take into account the limited size of the wave packets, we shall now estimate whether the daughter waves have enough time to be generated via the decay process before leaving the region of the pump Langmuir wave packet. We compare the characteristic growth rate for the parametric decay to the available interaction time before the daughter wave packets leave the coupling region.

[48] First, the efficiency of the coupling requires that the ion acoustic speed matches the Langmuir wave group velocity. The IAW packets travel at the ion sound speed $C_s \simeq 30$ km.s^{-1}, and the Langmuir wave packets travel at its group velocity V_g^L, given by $V_g^L = \partial\omega/\partial k \simeq 3k\lambda_D v_e^{th}$ evaluated to $V_g^L \simeq 30$ to 100 km.s^{-1} for Langmuir wavelength $\lambda_L \simeq 2$ to 6 km. Thus both the beam-driven Langmuir wave and the ion acoustic wave packets travel at comparable speed, enabling energy transfer between the waves providing that the growth rate for the decay is large enough.

[49] Then, the available interaction time τ_I for the three waves to resonate is estimated by considering the time for which the pump Langmuir wave packet L and the backscatter Langmuir daughter wave packet L' remain inside the same region of length L_c:

$$\tau_I \sim L_c / V_g^L \sim 1\ s$$

This available interaction time for coupling is then compared to the characteristic growth time of the daughter waves. The growth rate v for electrostatic decay in the case of monochromatic waves in an homogeneous background is [*Sagdeev and Galeev*, 1969]

$$\nu \simeq k_{IA} C_s \left(\frac{\epsilon_0 E^2}{n k_B T} \frac{m_p}{m_e} \right)^{1/4} \sim 200\ \mathrm{s}^{-1}$$

The growth rate for electrostatic decay is evaluated to 200 s^{-1}, which is about the ion acoustic time. The available interaction time for coupling is far larger than the evaluated growth time of the daughter waves

$$\tau_I >> 1/\nu,$$

which enable the decay to develop before the daughter wave packets leave the region of coupling. The growth rate for electrostatic decay has been evaluated for infinite waves in a homogeneous medium, and gives a first order of magnitude, but the nonmonochromatic nature of the wave packets should be taken into account. Let us now describe the electrostatic coupling in the context of the type III burst.

4.2. Three-Wave Coupling and Type III Burst

[50] The main picture is the following: during a type III, electron beams generate the mother Langmuir wave through beam instability. It then decays into a backscattered daughter Langmuir wave and an IAW with proper wave numbers and frequencies given by momentum and energy conservation (equations (3) and (4)).

[51] If this Langmuir mother wave couples to a second Langmuir wave and the IAW, the relation between the frequency f_{IA} of the IAW and the speed of the electron beam is given to a good approximation by *Cairns and Robinson* [1992] and *Hospodarsky and Gurnett,* [1995]

$$V_b \approx \frac{2 f_p V_{SW} |\cos\theta|}{f_{IA}} \tag{7}$$

The beam speed for the fastest electrons involved in the coupling and observed by the TDS can be estimated from the minimum IAW frequency observed at 80 Hz at the beginning of the type III on STEREO B, together with equation (7):

$$V_b \simeq 4\ 10^5\ \mathrm{km.s}^{-1} \simeq 0.13\ c$$

which is consistent with the estimation in section 2 from the dynamic diagram of type III (Figure 2).

[52] Simple time-of-flight arguments on the type III electron beam predict that at a given position, the beam speed V_b vary inversely with time (fast electrons cross the spacecraft first, the slower ones come after):

$$V_b \simeq D/(t - t_0) \tag{8}$$

with D the distance between the generation of the beam at t_0 and the fixed observer. *Lin et al.* [1981] observed this drift and explained how it controls the frequency drift of the beam-generated Langmuir wave. With equation (7) the IAW frequency (equal to the difference of frequency

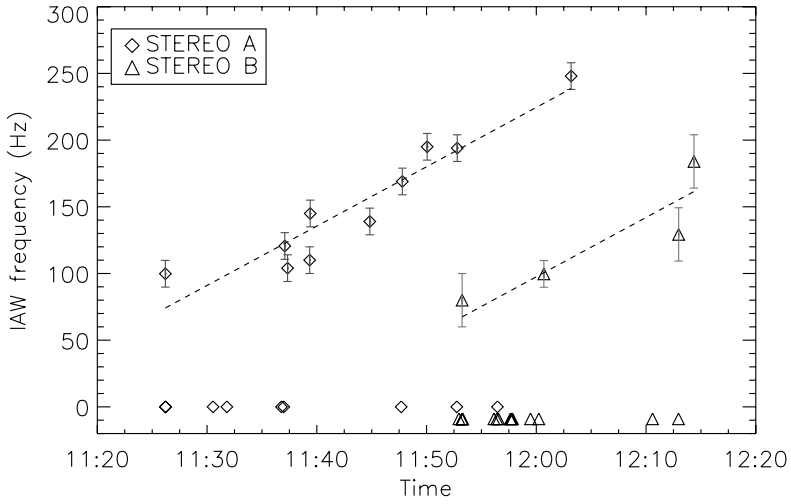

Figure 8. Ion acoustic wave frequency (f_{IA}) versus time of the event (UT). Each single event is represented by a diamond for STEREO A and a triangle for STEREO B, together with their respective error bars. The dashed line displays the least squares fit. Points at bottom ($f_{IA} \simeq 0$) show events without coupling. (For sake of clarity, STEREO B events have been shifted downward. In these last cases no IAW is reported.)

between the two Langmuir waves) is expected to vary linearly with time:

$$f_{IA} = \Delta f_L \approx \frac{2 f_p V_{SW} |\cos\theta|}{D} (t - t_0) \tag{9}$$

[53] *Cairns and Robinson* [1992] and *Hospodarsky and Gurnett* [1995] used electron distribution function measurements on different type III observed at 1 AU and derived values for the drift of the IAW frequency of 100 to 300 Hz.h^{-1} depending on the plasma parameters. Distribution functions are not yet available on STEREO and we cannot fit the beam speed drift by equation (7), so that the distance parameter D is still unknown. But a crude estimation of D $\approx$ 1 AU can be made, to get an order of magnitude of about 100 Hz.h^{-1} for the expected frequency drift.

[54] The observed IAW frequency are considered for each single event, and then plotted against the time of the event on Figure 8. Over the 14 three-wave events, the observed time variation, from one event to another, of the IAW frequency is well represented by a linear drift of 260 $\pm$ 30 Hz.h^{-1}, consistent with the time evolution of an IAW coupled with the beam-driven Langmuir wave. Since $\Delta f_L = f_{AI}$, at the same time, the two Langmuir peaks have frequencies that move away one from the other, with the same drift (not shown in the paper). This frequency drift of the IAW together with the separation in frequency of the Langmuir waves is another evidence for wave coupling in the context of the type III.

[55] Previous observations of electron distribution functions during type III also allowed the derivation of the beam velocity and the beam temperature. From these measurements *Cairns and Robinson* [1995] predicted a relative bandwidth for IAW $\Delta f_{IA}/f_{IA}$ ranging from 5% to 40%, but had not the frequency resolution to check it. Fourier analyses of the S/WAVES/TDS waveforms enables to measure it directly: $\Delta f_{AI}/f_{AI} \simeq 20\%$, which is compatible with previous observations of type III electron beams. These two last results should however be checked in the future from STEREO distribution function observations, when available.

[56] Finally, the eventual coalescence of the two Langmuir waves into a transverse wave T

$$L + L' \rightarrow T_{2f_p}$$

could then explain the generation of the type III radio harmonic emission at twice the plasma frequency observed on Figure 2 [*Ginzburg and Zheleznyakov*, 1958]. However, this mechanism was not detected in this study because of the presence of electrostatic harmonic Langmuir waves at twice the plasma frequency that prevent the direct detection of less intense transverse electromagnetic waves from *in situ* measurements.

5. Conclusion

[57] This paper shows for the first time, to our knowledge, a complete set of direct evidence of the coherent coupling between Langmuir waves and ion acoustic waves during a type III emission. The work is based on three independent methods: Fourier, wavelet, and bicoherence analyses of the S/WAVES waveform data (TDS observation mode).

[58] More than a third of the electric field data shows beam-driven Langmuir waves coupled with a second Langmuir wave and an ion acoustic wave. (1) The Doppler-shifted frequencies of the three waves satisfy the resonant relations expected for three-wave coupling. (2) The relative phase between the three waves remains constant from one waveform to another, consistent with a coherent wave-coupling mechanism. (3) The coupling regions are spatially localized with size of about 20 km, corresponding to about 2000 Debye lengths. (4) The electric field of the beam-

driven Langmuir wave is above the threshold for parametric decay. (5) By defining the interaction time as the time before interacting wave packets separate, we found that the interaction time is long enough when compared to the inverse of the excited mode growth rate. (6) The frequency of the ion acoustic waves drifts in time during the whole type III, as consistent with the expected evolution of the type III electron beam speed. This confirms the interpretation of the data in terms of the parametric electrostatic decay of the beam-driven Langmuir waves.

[59] Waveform data of S/WAVES give access to both phase information and high-frequency resolution which cannot be obtained by spectral instruments. It is worth noting that, for the first time in solar wind observations, long time series of waveform data are available. This allows us first to observe low frequencies (around 100 Hz), and second to resolve the entire coupling region. Finally, the possibility to compute time-frequency analyses with high temporal and spectral resolution enable to discriminate among the observed waves which ones are actually involved in the coupling process. For instance the 3 kHz IAW (Figure 3), frequently seen in our waveforms during the observed time of interest, but totally independent to the observed coupling, could have been thought to participate to the coupling through spectral observations only.

[60] Important questions still remain open. For example: why do the beam-driven Langmuir fluctuations appears as short isolated wave packets? *Ergun et al.* [2008] have recently shown that gaussian-shaped and modulated solar wind Langmuir waves commonly recorded in the solar wind can be interpreted trapped eigenmodes in density structures. The trapping of beam-driven Langmuir waves in density cavities, not observed but not excluded in the events studied here, could explain their spatial shape. An other possible approach could be that of beam-plasma interaction in an inhomogeneous media [*Krasnoselskikh et al.*, 2007].

[61] Another related question concerns the efficiency of the parametric decay for a nonmonochromatic pump wave. What is the evolution for the parametric decay for a short isolated Langmuir wave packet? Therefore, our model of monochromatic wave in an homogeneous media must be considered as a first step in the line of interpreting observational type III data. Numerical simulations are expected to be of great help in elucidating this nonlinear, inhomogeneous problem.

[62] The present study is based on a single type III burst, for which radio electromagnetic waves were detected from remote sensing measurements together with electrostatic Langmuir waves detected by in situ measurements. A statistical analysis will certainly be possible during the growing phase of the current solar cycle, when more events are observed, to offer more observational constraints on the theory.

[63] **Acknowledgments.** The authors thank S. Hoang for his work on the type III dynamic diagram and the evaluation of the beam speed. The authors also thank the referees for their useful comments. The STEREO/WAVES investigation is a collaboration of the Observatoire de Paris, the University of Minnesota, the University of California Berkeley, and NASA/GSFC. The French contribution to this project is supported by the CNES and CNRS.

[64] Amitava Bhattacharjee thanks Peter Yoon and another reviewer for their assistance in evaluating this paper.

References

Acuña, M. H., D. Curtis, J. L. Scheifele, C. T. Russell, P. Schroeder, A. Szabo, and J. G. Luhmann (2007), The STEREO/IMPACT magnetic field experiment, *Space Sci. Rev.*, *136*, 203.

Bale, S. D., D. Burgess, P. J. Kellogg, K. Goetz, R. L. Howard, and S. J. Monson (1996), Phase coupling in Langmuir wave packets: Possible evidence of three-wave interactions in the upstream solar wind, *Geophys. Res. Lett.*, *23*, 109.

Bale, S. D., et al. (2008), The electric antennas for the STEREO/WAVES experiment, *Space Sci. Rev.*, *136*, 529.

Bardwell, S., and M. V. Goldman (1976), Three-dimensional Langmuir wave instabilities in type III solar radio bursts, *Astrophys. J.*, *209*, 912.

Bougeret, J. L., et al. (2007), S/WAVES: The radio and plasma wave investigation on the STEREO mission, *Space Sci. Rev.*, *136*, 487.

Budden, K. G. (1985), *The Propagation of Radio Waves: The Theory of Radio Waves of Low Power in the Ionosphere and Magnetosphere*, Cambridge Univ. Press, New York.

Cairns, I. H., and P. A. Robinson (1992), Theory for low-frequency modulated Langmuir wave packets, *Geophys. Res. Lett.*, *19*, 2187.

Cairns, I. H., and P. A. Robinson (1995), Ion acoustic wave frequencies and onset times during type III solar radio bursts, *Astrophys. J.*, *453*, 959.

Daubechies, I. (1990), The wavelet transform time-frequency localization and signal analysis, *IEEE Trans. Inf. Theory*, *36*, 961.

Dudok de Wit, T., and V. V. Krasnosel'Skikh (1995), Wavelet bicoherence analysis of strong plasma turbulence at the Earth's quasiparallel bow shock, *Phys. Plasmas*, *2*, 4307.

Ergun, R. E., et al. (2008), Eigenmode structure in solar-wind Langmuir waves, *Phys. Rev. Lett.*, *101*(5), doi:10.1103/PhysRevLett.101.051101.

Farge, M. (1992), Wavelet transforms and their applications to turbulence, *Annu. Rev. Fluid Mech.*, *24*, 395.

Ginzburg, V. L., and V. V. Zheleznyakov (1958), On the possible mechanisms of sporadic solar radio emission (radiation in an isotropic plasma), *Sov. Astron., Engl. Transl.*, *2*, 653.

Gurnett, D. A., G. B. Hospodarsky, W. S. Kurth, D. J. Williams, and S. J. Bolton (1993), Fine structure of Langmuir waves produced by a solar electron event, *J. Geophys. Res.*, *98*, 5631.

Hoang, S., G. A. Dulk, and Y. Leblanc (1994), Interplanetary type 3 radio bursts that approach the plasma frequency: ULYSSES observations, *Astron. Astrophys.*, *289*, 957.

Hospodarsky, G. B., and D. A. Gurnett (1995), Beat-type Langmuir wave emissions associated with a type III solar radio burst: Evidence of parametric decay, *Geophys. Res. Lett.*, *22*, 1161.

Kellogg, P. J., K. Goetz, N. Lin, S. J. Monson, A. Balogh, R. J. Forsyth, and R. G. Stone (1992), Low frequency magnetic signals associated with Langmuir waves, *Geophys. Res. Lett.*, *19*, 1299.

Kellogg, P. J., K. Goetz, S. J. Monson, S. D. Bale, and M. Maksimovic (2007), Electric field and density measurements with STEREO-Swaves, *Eos Trans. AGU*, *88*(52), *Fall Meet. Suppl.*, Abstract SH33A-1098.

Kennel, C. F., F. V. Coroniti, F. L. Scarf, R. W. Fredricks, D. A. Gurnett, and E. J. Smith (1980), Correlated whistler and electron plasma oscillation bursts detected on ISEE-3, *Geophys. Res. Lett.*, *7*, 129.

Koga, D., and T. Hada (2003), Phase coherence of foreshock MHD waves: Wavelet analysis, *Space Sci. Rev.*, *107*, 495.

Krasnoselskikh, V. V., V. V. Lobzin, K. Musatenko, J. Soucek, J. S. Pickett, and I. H. Cairns (2007), Beam-plasma interaction in randomly inhomogeneous plasmas and statistical properties of small-amplitude Langmuir waves in the solar wind and electron foreshock, *J. Geophys. Res.*, *112*, A10109, doi:10.1029/2006JA012212.

Lagoutte, D., F. Lefeuvre, and J. Hanasz (1989), Application of bicoherence analysis in study of wave interactions in space plasma, *J. Geophys. Res.*, *94*, 435.

Lepping, R. P., et al. (1995), The wind magnetic field investigation, *Space Sci. Rev.*, *71*, 207.

Li, B., P. A. Robinson, and I. H. Cairns (2006), Numerical simulations of type-III solar radio bursts, *Phys. Rev. Lett.*, *96*, 14,5005.

Lin, R. P., D. W. Potter, D. A. Gurnett, and F. L. Scarf (1981), Energetic electrons and plasma waves associated with a solar type III radio burst, *Astrophys. J.*, *251*, 364.

Lin, R. P., W. K. Levedahl, W. Lotko, D. A. Gurnett, and F. L. Scarf (1986), Evidence for nonlinear wave-wave interactions in solar type III radio bursts, *Astrophys. J.*, *308*, 954.

Lin, R. P., et al. (1995), A three-dimensional plasma and energetic particle investigation for the wind spacecraft, *Space Sci. Rev.*, *71*, 125.

Nishikawa, K. (1968), Parametric excitation of coupled waves: II. Parametric plasmon-photon interaction, *J. Phys. Soc. Jpn.*, *24*, 1152.

Pecseli, H. L., J. Trulsen, A. Bahnsen, and F. Primdahl (1993), Propagation and nonlinear interaction of low-frequency electrostatic waves in the polar cap E region, *J. Geophys. Res.*, *98*, 1603.

Robinson, P. A. (1993), Stochastic-growth theory of Langmuir growth-rate fluctuations in type III solar radio sources, *Solar Phys.*, *146*, 357.

Robinson, P. A., A. J. Willes, and I. H. Cairns (1993), Dynamics of Langmuir and ion-sound waves in type III solar radio sources, *Astrophys. J.*, *408*, 720.

Sagdeev, R. Z., and A. A. Galeev (1969), *Nonlinear Plasma Theory*, Benjamin, New York.

Siu, K., J. Ann, J. Kihwan, L. Myoungho, S. Kunsoo, and K. Chon (2008), Statistical approach to quantify the presence of phase coupling using the bispectrum, *IEEE Trans. Biomed. Eng.*, *55*, 1512.

Smith, D. F. (1970), Towards a theory for type III solar radio bursts: I. Nature of the exciting agency, *Solar Phys.*, *15*, 202.

Soucek, J., T. Dudok de Wit, V. Krasnoselskikh, and A. Volokitin (2003), Statistical analysis of nonlinear wave interactions in simulated Langmuir turbulence data, *Ann. Geophys.*, *21*, 681.

Sturrock, P.A. (1964), Type III solar radio bursts, in *Proceedings of a Symposium Held at the Goddard Space Flight Center, Greenbelt, Maryland, October 28–30, 1963*, edited by W. N. Hess, p. 357, NASA, Washington, D. C.

Thejappa, G., and R. J. MacDowall (1998), Evidence for strong and weak turbulence processes in the source region of a local type III radio burst, *Astrophys. J.*, *498*, 465.

Thejappa, G., D. Lengyel-Frey, R. G. Stone, and M. L. Goldstein (1993), Evaluation of emission mechanisms at omega P E using ULYSSES observations of type III bursts, *Astrophys. J.*, *416*, 831.

Thejappa, G., D. G. Wentzel, and R. G. Stone (1995), Low-frequency waves associated with Langmuir waves in solar wind, *J. Geophys. Res.*, *100*, 3417.

Thejappa, G., R. J. MacDowall, E. E. Scime, and J. E. Littleton (2003), Evidence for electrostatic decay in the solar wind at 5.2 AU, *J. Geophys. Res.*, *108*(A3), 1139, doi:10.1029/2002JA009290.

Torrence, C., and G. P. Compo (1998), A practical guide to wavelet analysis, *Bull. Am. Meteorol. Soc.*, *79*, 61.

van den Berg, J. C. (Ed.) (1999), *Wavelets in Physics*, Cambridge Univ. Press, New York.

Van Milligen, B. P., E. Sánchez, T. Estrada, C. Hidalgo, B. Brañas, B. Carreras, and L. García (1995), Wavelet bicoherence: A new turbulence analysis tool, *Phys. Plasmas*, *2*, 3017.

Wild, J. P. (1950), Observations of the spectrum of high-intensity solar radiation at metre wavelengths: III. Isolated bursts, *Aust. J. Sci. Res., Ser. A*, *3*, 541.

Willes, A. J., and I. H. Cairns (2001), Mode conversion and reflection of Langmuir waves in an inhomogeneous solar wind, *Publ. Astron. Soc. Aust.*, *18*, 355.

Willes, A. J., S. D. Bale, and I. H. Cairns (2002), Evidence for Langmuir wave tunneling in the inhomogeneous solar wind, *J. Geophys. Res.*, *107*(A10), 1320, doi:10.1029/2002JA009259.

S. D. Bale, Physics Department and Space Sciences Laboratory, University of California, Berkeley, CA 94720, USA.

C. Briand, F. Califano, P. Henri, and A. Mangeney, LESIA, Observatoire de Paris, Université Paris Diderot, CNRS, UPMC, 5 Place Jules Hansen, F-92190 Meudon, France. (pierre.henri@obspm.fr)

K. Goetz, School of Physics and Astronomy, University of Minnesota, Minneapolis, MN 55455, USA.

M. Kaiser, NASA Goddard Space Flight Center, Code 674, Greenbelt, MD 20771, USA.

Henri et al. (2010)
Proceedings of Solar Wind 12 Conference, 288

Vlasov simulations of Langmuir Electrostatic Decay and consequences for Type III observations.

P. Henri[*,†], F. Califano[†,*], C. Briand[*] and A. Mangeney[*]

[*]*LESIA, Observatoire de Paris, CNRS, UPMC, Université Paris Diderot; 5 Place Jules Janssen, 92190 Meudon, France*

[†]*Dip. Fisica, Università di Pisa, Largo Pontecorvo n.3, 56100 Pisa, Italy*

Abstract. The electrostatic decay enables energy transfer from a finite amplitude Langmuir to a backscattered daughter Langmuir wave and ion acoustic density fluctuations. This mechanism is thought to be a first step for the generation of type III solar radio emissions at twice the plasma frequency. The electrostatic decay is here investigated through Vlasov-Poisson simulations by considering Langmuir localized wave packets in the case $T_e = T_p$. Simulation results are found to be in good agreement with recently reported observations from the STEREO mission of the electrostatic decay of beam-driven Langmuir waves during a type III burst.

Keywords: Type III, parametric instability, Langmuir waves
PACS: 96.50.Tf, 96.60.tg

INTRODUCTION

Solar Type III radio emissions are one of the most prominent features of the meter-decameter ranges of frequency. The emissions show a pronounced drift with time towards lower frequencies. Since the early work of Wild [1] and Ginzburg and Zheleznyakov [2], the generally accepted model for such emission is as summarized below. During a flare, high energy electrons (1-100 keV) are expelled from the solar corona and travel along the interplanetary magnetic field lines. The supra-thermal electrons produce a bump on the local electron distribution function generating Langmuir waves via the so-called "bump-on-tail instability". Then, nonlinear wave couplings generate electromagnetic waves at f_p^- (the local electron plasma frequency) or $2f_p^-$. The plasma frequency decreases with the heliocentric distance due to the decrease of the electron density: this is the origin of the time frequency drift characteristic of the Type III emissions.
Type III electromagnetic emissions are thought to be produced via two different nonlinear wave-wave couplings. Through electromagnetic coupling, a mother Langmuir wave L decays into a low frequency LF waves and a transverse electromagnetic wave $T_{f_p^-}$ at the local plasma frequency, observed as Type III fundamental emission:

$$L \rightarrow T_{f_p^-} + LF$$

Through electrostatic coupling, known as Langmuir Electrostatic Decay (hereafter LED), the mother Langmuir wave L decays into a low frequency ion acoustic wave S and a daughter Langmuir wave L', which can further non linearly couple with the pump wave to generate a transverse electromagnetic wave $T_{2f_p^-}$ at twice the local plasma frequency, observed as Type III harmonic emission:

$$L \rightarrow L' + S \quad \text{then} \quad L' + L \rightarrow T_{2f_p^-}$$

We hereafter concentrate on the LED.
Henri et al. [3] recently reported direct observations of Langmuir waves decaying into secondary Langmuir waves and acoustic waves during a Type III solar event, from STEREO/WAVES data. They found that:

- the Doppler-shifted frequencies of the three observed waves satisfy the resonant relations of momentum and energy conservation expected for three-wave coupling

$$\omega_L = \omega_{L'} + \omega_S \qquad \vec{k}_L = \vec{k}_{L'} + \vec{k}_S \qquad (1)$$

- a bicoherence analysis confirms the phase coherence of the three waves;
- the coupling regions are spatially localized with size of about 2000 Debye lengths.

In this former work, the LED threshold and the growth rate of IAW density fluctuations generated by LED were both evaluated from analytical solutions involving a purely monochromatic three-wave coupling [4]. However, observations show that: (i) the Langmuir waves are isolated wave packets with a packet width of the order of a few wavelengths; (ii) proton and electron temperatures are known to be close in the solar wind so that IAW associated with the LED should be strongly Landau-damped, this would limit the development of the IAW and thus the LED.

CP1216, *Twelfth International Solar Wind Conference,*
edited by M. Maksimovic, K. Issautier, N. Meyer-Vernet, M. Moncuquet, and F. Pantellini

The goal of this paper is to study the dynamic of the LED through 1D-1V Vlasov-Poisson simulations by considering an initial localized Langmuir wave packet, for equal electron and ion temperature. For a better comparison with observed waveform during Type III bursts, the simulation results are also presented as they would appear if observed by spacecraft instruments.

DESCRIPTION OF THE MODEL

LED is here investigated through 1D-1V Vlasov-Poisson simulations in the electrostatic approximation. The description of the code and the numerical scheme can be found in Mangeney et al. [5].

The Vlasov-Poisson system is solved for the 1D-1V electron and proton distribution function, $f_e(x,v,t)$ and $f_p(x,u,t)$. The equations are normalized by using the following characteristic electron quantities: the charge e, the electron mass m_e, the electron density n_e, the plasma (angular) frequency $\omega_{pe} = \sqrt{4\pi n_e e^2/m_e}$, the Debye length $\lambda_D = \sqrt{T_e/4\pi n_e e^2}$, the electron thermal velocity $v_{th,e} = \lambda_D \omega_{pe} = \sqrt{T_e/m_e}$ and an electric field $\tilde{E} = m_e v_{th,e} \omega_{pe}/e$. Then, the dimensionless equations for each species read:

$$\frac{\partial f_e}{\partial t} + v\frac{\partial f_e}{\partial x} - (E + E_{ext})\frac{\partial f_e}{\partial v} = 0 \qquad (2)$$

$$\frac{\partial f_p}{\partial t} + u\frac{\partial f_p}{\partial x} + \frac{1}{\mu}(E + E_{ext})\frac{\partial f_p}{\partial u} = 0 \qquad (3)$$

$$\frac{\partial^2 \phi}{\partial x^2} = \int f_e dv - \int f_p du \; ; E = -\frac{\partial \phi}{\partial x} \qquad (4)$$

where v (resp. u) is the electron (resp. ion) velocity normalized to the electron thermal velocity. Furthermore $\mu = m_p/m_e = 1836$ is the proton-to-electron mass ratio and ϕ and E are the self-consistent electric potential and electric field generated by the plasma charge density fluctuations according to Poisson equation (Eq. 4). Finally, E_{ext} is an "external" driver added to the Vlasov equation that can be switched on or off during the runs. The electron (resp. ion) distribution function is discretized in space for $0 \leq x < L_x$, with $L_x = 10000\ \lambda_D$ the total box length, for a resolution of $dx = \lambda_D$. The electron velocity grid ranges over $-5 \leq v/v_{th,e} \leq +5$, with a resolution of $dv = 0.04\ v_{th,e}$. (resp. $-5 \leq u/u_{th,i} \leq +5$, with a resolution of $du = 0.04\ u_{th,i}$ for the proton velocity grid, where $u_{th,i} = \sqrt{T_p/m_p}$ is the proton thermal velocity). The temperatures are chosen to be equal $T_p = T_e$.

Periodic boundary conditions are used in the spatial direction. The electron and proton distributions functions are initially Maxwellian with respect of velocity, with a random noise in density.

Finally, the initial Langmuir wave packet with the desired wavelength λ_L and electric field amplitude E_L is generated by an "external" electric field E_{ext}. The pump E_{ext} oscillates at the expected Langmuir frequency $\omega_L = \omega_{pe} + 3/2(2\pi\lambda_D/\lambda_L)^2$, with a phase equal to $\omega_L t - 2\pi x/\lambda_L$, and is spatially localized with a gaussian-shaped envelop. A Langmuir wave packet propagating only in the forward direction is thus excited. The external electric field E_{ext} is switched off when the generated Langmuir wave reaches the desired amplitude E_L, typically at $t \sim 300\ \omega_{pe}^{-1}$, much shorter than the LED timescale. The initial Langmuir wave packet then evolves self-consistently. Further details on the forcing can be found in [9].

LANGMUIR ELECTROSTATIC DECAY OF A LOCALIZED WAVEPACKET

In order to compare the simulations results with observations of electric waveforms during Type III events, Langmuir wavelength and amplitude are set as indicated by solar wind observations. We choose a Langmuir wave packet with wavelengths centered on $\lambda_L = 200\ \lambda_D$, a packet width $\Delta = 2000\ \lambda_D$, and a maximum initial electric field $E_L = 6\ 10^{-2}$. Since the electric field associated with IAW is known to be low, in the following, ion density fluctuations will be used as a tracer for IAW.

LED is observed in Vlasov simulations for a level of Langmuir electric amplitude typical of those observed in the solar wind during type III bursts. The evolution of the Langmuir wave packet is shown in Fig. 1. The electrostatic decay starts at $t \simeq 10^4\ \omega_{pe}^{-1}$. The mother and daughter Langmuir wave packets can be follow in the top left panel that shows the space-time evolution of the electric density energy $E(x,t)^2/2$. The Langmuir mother wave packet propagates towards the right at its group velocity (black plain line) and emits daughter Langmuir wave packets propagating backward at their own group velocity (white dashed line). The bottom left panel shows the temporal evolution of ion density fluctuations during the decay of the Langmuir wave. The fluctuations along the dashed line is a small amplitude artifact of the initial forcing, it does not interact with the electrostatic coupling. Instead, ion density fluctuations generated from the Langmuir mother wave packet (along the black solid line) propagate forward at the ion sound speed (slope of the dashed line) with the expected wavelength for the IAW decay product $\lambda_{IA} \simeq 150\ \lambda_D$. They are the decay product. Note that the IA fluctuations are generated locally where the two Langmuir wave packets beats. Indeed, IAW density fluctuations are heavily Landau damped, since $T_e = T_p$, as soon as the waves escape the area where LED occurs. Therefore, the LED-

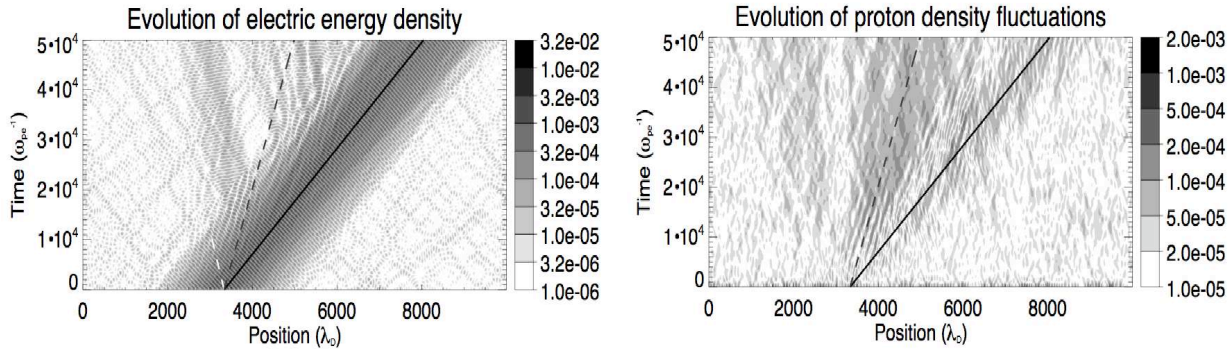

FIGURE 1. Evolution of a localized Langmuir wave packet with initial normalized amplitude $E_L = 6\ 10^{-2}$. Top panel: electric density energy $E(x,t)^2/2$. Bottom panel: proton density fluctuations. The expected group velocity of the mother (resp. daughter) Langmuir wave is shown by the black plain line (resp. white dashed line). The ion sound speed is shown by the black dashed line.

produced IAW is expected to be observed in the solar wind only locally where the mother and daughter Langmuir waves interact.

In order to compare the simulation results with in-situ waveform observations, we mimic the conditions of observation onboard a spacecraft that would record, on monopole antennas, a decaying Langmuir wave. We thus hereafter introduce in the presentation of simulation results (i) a spacecraft floating potential effect, (ii) a Doppler-shift effect.

First, monopole antenna channel are known to be sensitive to both the electric field and the proton density fluctuations, through the fluctuation of the spacecraft potential [6, 7, 8]. This means that the observed signal is a combination of both electric field and proton density fluctuations. To reproduce this effect in the simulation, we consider an "equivalent signal" $s(t) = E(x,t) + \alpha\ n_p(x,t)$, with α the equivalent in the simulation of a calibration parameter that gives in the observations the ratio of the spacecraft floating potential with respect to density fluctuation. This parameter is set to $\alpha = 50$ as an order of magnitude following the prescription of Kellogg et al. [8].

Second, observed waveforms in the spacecraft frame are Doppler-shifted since the plasma is moving at the solar wind speed. A Doppler-shift effect is introduced in the simulation by considering the "equivalent signal" $s(t)$ at position $x(t) = x_0 + V_S t$ where V_S is a constant velocity. We choose here $V_S = v_{th,e}$ as a first approach.

This "equivalent signal" $s(x(t),t)$, obtained from the simulation, represents the signal that would be recorded by a spacecraft crossing such a decaying Langmuir wave packet.

For an easy confrontation with observed waveforms, simulation results are analyzed and presented in Fig. 2 the same way observations have been analyzed and presented by Henri et al. [3]. Both a Doppler-shift effect and the sensitivity to both the electric field and the density fluctuations are taken into account. The top left panel shows the electric field (grey) and proton density (black line) waveforms from the simulation. Both are plotted in normalized units, as described in the simulation model. The left bottom panel shows the wavelet transform of $s(x(t),t)$. The simulations show that (i) beat-like modulation at the plasma frequency would be observed, (ii) the IAW signal would be seen at lower frequency centered where the maximum of the beat-like Langmuir signal is observed. This is in full agreement with the observations. The Fourier spectrum of $s(x(t),t)$ is shown in the right top panel, with a zoom at the plasma frequency in the right bottom panel. The frequency of IAW density fluctuations as well as the separation between the frequency peaks of the two Langmuir waves are essentially a Doppler-shift effect. The full line represents the total Fourier spectrum. Dashed and dotted lines distinguish the contribution of the ion density fluctuations and electric field respectively. The simulation thus proves that the high frequency part of the observed spectrum is dominated by the response of the antenna to the fluctuations of the electric field, whereas the low frequency part is dominated by the response of the spacecraft potential to density fluctuations.

The waveform and spectrum obtained from Vlasov simulations agrees qualitatively well with observations reported in Henri et al. [3]. However, in order to check whether the level of density fluctuations is quantitatively consistent with previsions from Vlasov simulations, a full calibration of the floating potential of the STEREO spacecraft is needed in order to get a better evaluation of α that fully takes into account the geometry and dimension of the spacecraft.

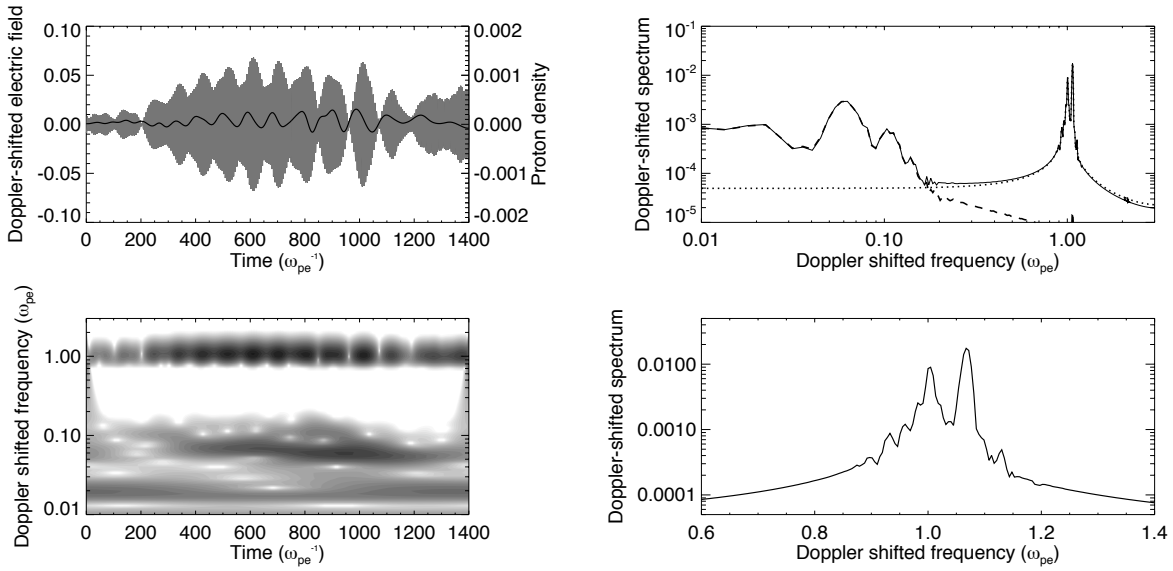

FIGURE 2. Waveform, spectrum and wavelet transform from simulation results, as they would appear when observed by spacecraft instruments when crossing a Langmuir wave under LED. Top left panel: waveform in a moving frame: electric field (grey) and proton density (black). Bottom left panel: Morlet wavelet transform of signal $s(x(t),t)$. Top right panel: corresponding Fourier spectrum (full line) with respective contribution of the density fluctuations (dashed line) and electric field (dotted line). Bottom right panel: zoom on the double peak at the plasma frequency.

CONCLUSION

We have reported 1D-1V Vlasov-Poisson simulations of the Langmuir Electrostatic Decay. The simulations have been done in typical solar wind conditions: (i) equal electron and proton temperature, in order to take into account the strong Landau damping of daughter ion acoustic waves, and (ii) localized wave packets, in order to consider the limited interaction time between the mother and daughter waves, each propagating at its own group velocity.

Vlasov simulations in typical solar wind conditions (i) shows that the observed level of Langmuir electric field during type III burst is high enough for Langmuir Electrostatic Decay to start, (ii) reproduce qualitatively the beat-like Langmuir waveforms as well as the spectrum observed during type III bursts when obtained from monopole antennas.

In order to fully confirm the interpretation of the observed Langmuir waveforms in term of the LED of type III beam-driven Langmuir waves, an effective threshold will be computed from vlasov simulation in typical solar wind conditions [9].

We have study here a first step for the generation of electromagnetic waves like for example Type III emission. Further Vlasov-Maxwell simulations must be performed to study the next step of the process and check the energy transfer from electrostatic to electromagnetic emissions.

ACKNOWLEDGMENTS

The authors thanks Nicole Meyer-Vernet for useful discussions on spacecraft floating potential.

We are grateful to the italian super-computing center CINECA (Bologna) where part of the calculations where performed. We also acknowledge Dr. C. Cavazzoni for discussion on code performance.

REFERENCES

1. J. P. Wild, *Australian Journal of Scientific Research A Physical Sciences* **3**, 541 (1950).
2. V. L. Ginzburg, and V. V. Zheleznyakov, *Soviet Astronomy* **2**, 653 (1958).
3. P. Henri et al., *Journal of Geophysical Research (Space Physics)* **114**, 3103 (2009).
4. R. Z. Sagdeev, and A. A. Galeev, *Nonlinear Plasma Theory*, New York: Benjamin, 1969.
5. A. Mangeney et al., *Journal of Computational Physics* **179**, 495 (2002).
6. A. Pedersen, *Annales Geophysicae* **13**, 118 (1995).
7. N. Meyer-Vernet, *Basics of the Solar Wind*, Cambridge University Press, 2007.
8. P. J. Kellogg, K. Goetz, S. J. Monson, S. D. Bale, M. J. Reiner, and M. Maksimovic, *Journal of Geophysical Research (Space Physics)* **114**, 2107 (2009).
9. P. Henri et al., submitted to *Journal of Geophysical Research (Space Physics)*.

Henri et al. (2010)
JGR-Space Physics, 115, A06106

JOURNAL OF GEOPHYSICAL RESEARCH, VOL. 115, A06106, doi:10.1029/2009JA014969, 2010

Vlasov-Poisson simulations of electrostatic parametric instability for localized Langmuir wave packets in the solar wind

P. Henri,[1,2] F. Califano,[1,2] C. Briand,[3] and A. Mangeney[3]

Received 7 October 2009; revised 2 December 2009; accepted 12 January 2010; published 18 June 2010.

[1] Recent observation of large-amplitude Langmuir waveforms during a type III event in the solar wind has been interpreted as the signature of the electrostatic decay of beam-driven Langmuir waves. This mechanism is thought to be a first step to explain the generation of type III radio emission. The threshold for this parametric instability in the typical solar wind condition has been investigated through 1D-1V Vlasov-Poisson simulations. We show that the amplitude of the observed Langmuir beatlike waveforms is of the order of the effective threshold computed from the simulations. The expected levels of associated ion acoustic density fluctuations have also been computed for comparison with observations.

Citation: Henri, P., F. Califano, C. Briand, and A. Mangeney (2010), Vlasov-Poisson simulations of electrostatic parametric instability for localized Langmuir wave packets in the solar wind, *J. Geophys. Res.*, *115*, A06106, doi:10.1029/2009JA014969.

1. Introduction

[2] During a solar flare, high-energy electrons (1–100 keV) are expelled from the solar corona and travel along the interplanetary magnetic field lines, producing a bump on the local electron distribution function. Langmuir waves then grow via the so-called bump-on-tail instability. Langmuir waves are observed at amplitude large enough ($E^2/(8\pi nT) \simeq 10^{-3}$–$10^{-4}$) to further excite electromagnetic waves through nonlinear processes. These electromagnetic waves are the main signature of type III radio bursts. Wave-wave interaction through parametric instabilities have been shown to be the physical mechanism underlying the non linear evolution of large amplitude Langmuir waves.

[3] Langmuir electrostatic decay (LED), also called Langmuir decay instability (LDI) or parametric decay instability (PDI) in the literature, enables energy transfer from a finite amplitude Langmuir wave L toward a second Langmuir wave L' and an ion acoustic wave (IAW) S through a three-wave resonant interaction:

$$L \rightarrow L' + S.$$

This process is thought to be a first step toward the generation of solar wind type III radio emission at twice the plasma frequency ($T_{2f_{pe}}$), as a result of a coalescence of the two Langmuir waves [*Ginzburg and Zheleznyakov*, 1958]:

$$L + L' \rightarrow T_{2f_{pe}}.$$

[4] Spectral observations of high-frequency intense Langmuir waves and low-frequency ion acoustic waves during type III bursts have been interpreted as a signature of Langmuir electrostatic decay [*Lin et al.*, 1986a]. Furthermore, waveform observations during type III bursts of modulated Langmuir wave packets on one hand [*Cairns and Robinson*, 1992; *Hospodarsky and Gurnett*, 1995; *Bale et al.*, 1996; *Li et al.*, 2003] and of IAW frequency drift associated with type III electron beam velocity drift on the other hand [*Cairns and Robinson*, 1995] have both been interpreted by the Langmuir electrostatic decay.

[5] The LED is a resonant parametric instability. To be resonant, the three-wave coupling requires the fundamental equations of energy and momentum conservation to be satisfied:

$$\omega_L = \omega_{L'} + \omega_S \qquad \vec{k}_L = \vec{k}_{L'} + \vec{k}_S, \tag{1}$$

where ω and $\vec{k}$ are the frequency and wave number of the waves. Moreover, for the LED to develop, the electric field of the mother Langmuir wave has to reach a critical value. The analytical calculation of this threshold has been discussed by *Nishikawa* [1968], *Sagdeev and Galeev* [1969], *Dysthe and Franklin* [1970], *Bardwell and Goldman* [1976], and *Robinson et al.* [1993] by considering three monochromatic waves. The underlying idea is that for the instability to develop, the growth rate γ_{LED} of the two product waves must be higher than their own linear Landau damping rates $\gamma_{L'}$ and γ_S:

$$\gamma_{\mathrm{LED}} > \sqrt{\gamma_{L'}\gamma_S}.$$

[1]Dipartimento Fisica, Università di Pisa, Pisa, Italy.
[2]Also at Laboratoire d'Études Spatiales et d'Instrumentation en Astrophysique, Observatoire de Paris, Université Pierre et Marie Curie, Université Paris Diderot, CNRS, Meudon, France.
[3]Laboratoire d'Études Spatiales et d'Instrumentation en Astrophysique, Observatoire de Paris, Université Pierre et Marie Curie, Université Paris Diderot, CNRS, Meudon, France.

0148-0227/10/2009JA014969

The threshold for parametric decay of the mother Langmuir wave is thus evaluated in term of the electric to kinetic energy ratio [*Bardwell and Goldman*, 1976]:

$$\frac{\epsilon_0 E^2}{n k_B T} > 8 \frac{\gamma_{L'}}{\omega_{L'}} \frac{\gamma_S}{\omega_S},$$

with $\omega_{L'}$, ω_S the angular frequency of the daughter waves. The threshold for electrostatic decay has been estimated for typical solar wind parameters to be $(\epsilon_0 E^2)/(n k_B T) \geq 2.5 \times 10^{-5}$ [*Lin et al.*, 1986b]. To our knowledge, only LED that couples three monochromatic waves have been considered analytically. Indeed, the analytical treatment of resonance becomes complicated when considering a finite frequency bandwidth, in which case a numerical treatment is necessary.

[6] Earlier related works on simulations of LED have been based on the Zakharov equations [*Sprague and Fejer*, 1995; *Gibson et al.*, 1995; *Soucek et al.*, 2003], considering the instability as a fluid mechanism. Recently, kinetic simulations using PIC codes [*Matsukiyo et al.*, 2004; *Huang and Huang*, 2008] and Vlasov codes [*Goldman et al.*, 1996; *Umeda and Ito*, 2008] have shown that the beam-plasma interaction can saturate through LED and have been able to reproduce the modulated shape of Langmuir waves.

[7] If the threshold for LED is commonly thought to be at moderate amplitude, a recent numerical work [*Umeda and Ito*, 2008] claims that no LED would occur until the electric energy is comparable to the plasma kinetic energy. As a result, it would be no more possible to consider the LED as a mechanism for the generation of type III radio emission.

[8] *Henri et al.* [2009] (hereinafter referred to as Paper I) recently reported direct observations of Langmuir waves decaying into secondary Langmuir waves and acoustic waves during a type III solar event, from STEREO/WAVES data. They found that the Doppler-shifted frequencies of the three observed waves satisfy the resonant relations of momentum and energy conservation expected for three-wave coupling. A bicoherence analysis confirmed the phase coherence of the three waves. In this former work, the LED threshold and the growth rate of IAW density fluctuations generated by LED were both evaluated from analytical solutions involving a purely monochromatic three-wave coupling [*Sagdeev and Galeev*, 1969]. However, observations show that (1) the large amplitude Langmuir waves are isolated wave packets with a packet width of the order of a few wavelengths and (2) ion and electron temperatures are close ($0.1 < T_e/T_i < 10$) so that ion acoustic waves associated with the LED should be Landau damped. Thus several questions remain open about the generation and the dynamics of the LED observed in the solar wind: (1) What are the threshold and the growth rate of the LED when electron and ion temperatures are close? What is the effective threshold of LED when the mother Langmuir wave is a localized wave packet? (2) What is the saturation level for IAW density fluctuations in these conditions? What is the expected level of IAW density fluctuations where saturation is not observed? The goal of this paper is to answer these questions by studying the dynamics of the LED through 1D-1V Vlasov-Poisson simulations.

[9] The paper is organized as follows. The Vlasov-Poisson simulation model is described in section 2. The numerical results are presented in section 3, first for a monochromatic mother Langmuir wave (section 3.1), then for a mother Langmuir wave packet (section 3.2). Growth rates, saturation levels for IAW density fluctuations and threshold for LED are studied. The simulation results are finally discussed in section 4 in the context of solar wind observations. Particular attention is paid to the case of equal temperature for electrons and ions, in which case the growth of IAW should be limited by its Landau damping.

2. Full Vlasov-Poisson Simulation Model

[10] In typical solar wind conditions, the ratio between electron and ion temperatures fluctuates around 1. The IAW produced during three-wave coupling should then be suppressed by Landau damping. This would limit the development of the IAW and thus the LED. However, the IAW Landau damping rate in such temperature condition cannot be solved analytically, so that it cannot be included in a fluid code. Kinetic effects due to wave-particle interactions are to be taken into account self-consistently as a possible limitation for the instability to grow. A Vlasov-Poisson approach has thus been used to study LED dynamics. It allows to consider self-consistently the decay of the Langmuir wave together with damping effect on the product waves. Since solar wind electrons are weakly magnetized ($\omega_{ce}/\omega_{pe} \simeq 10^{-2}$), magnetic effects are discarded.

[11] The Vlasov-Poisson system is solved for the electron and ion distribution function, $f_e(x, v, t)$ and $f_i(x, u, t)$, with the numerical scheme described by *Mangeney et al.* [2002], limiting our study to the 1D-1V case. The equations are normalized by using the following characteristic electron quantities: the charge e, the electron mass m_e, the electron density n_e, the plasma (angular) frequency $\omega_{pe} = \sqrt{4\pi n_e e^2/m_e}$, the Debye length $\lambda_D = \sqrt{T_e/4\pi n_e e^2}$, the electron thermal velocity $v_{\mathrm{th},e} = \lambda_D \omega_{pe} = \sqrt{T_e/m_e}$ and an electric field $\overline{E} = m_e v_{\mathrm{th},e} \omega_{pe}/e$. Then, the dimensionless equations for each species read:

$$\frac{\partial f_e}{\partial t} + v \frac{\partial f_e}{\partial x} - (E + E_{\mathrm{ext}}^{\mathrm{init}}) \frac{\partial f_e}{\partial v} = 0, \tag{2}$$

$$\frac{\partial f_i}{\partial t} + u \frac{\partial f_i}{\partial x} + \frac{1}{\mu} (E + E_{\mathrm{ext}}^{\mathrm{noise}}) \frac{\partial f_i}{\partial u} = 0, \tag{3}$$

$$\frac{\partial^2 \phi}{\partial x^2} = \int f_e dv - \int f_i du; \qquad E = -\frac{\partial \phi}{\partial x}, \tag{4}$$

where v (u, respectively) is the electron (ion, respectively) velocity normalized to the electron thermal velocity. Here $\mu = m_i/m_e = 1836$ is the ion-to-electron mass ratio. ϕ and E are the self-consistent electric potential and electric field generated by the plasma charge density fluctuations according to Poisson equation (4). $E_{\mathrm{ext}}^{\mathrm{init}}$ and $E_{\mathrm{ext}}^{\mathrm{noise}}$ are "external" drivers added to the Vlasov equation that can be switched on or off during the run. The electron (ion, respectively) distribution function is discretized in space for $0 \leq x < L_x$, with $L_x = 5000\ \lambda_D$ the total box length, with a resolution of $dx = \lambda_D$. The electron velocity grid ranges over $-5\ v_{\mathrm{th},e} \leq v \leq +5\ v_{\mathrm{th},e}$, with a resolution of $dv = 0.04\ v_{\mathrm{th},e}$. ($-5\ u_{\mathrm{th},i} \leq u \leq +5\ u_{\mathrm{th},i}$, respectively, with a reso-

lution of $du = 0.04\ u_{\mathrm{th},i}$ for the ion velocity grid, where $u_{\mathrm{th},i}$ is the ion thermal velocity). Finally, periodic boundary conditions are used in the spatial direction.

[12] In all the runs the following initial conditions have been taken: electron and ion distributions functions are initially Maxwellian with respect to velocity, with a random noise in density:

$$f_e(x,v) = \frac{e^{-v^2}}{\sqrt{2\pi}}\left[1 + \epsilon \sum_k \cos(kx + \psi_k)\right] \tag{5}$$

$$f_i(x,u) = \frac{\sqrt{\frac{\Theta}{\mu}}e^{-\frac{\Theta}{\mu}u^2}}{\sqrt{2\pi}}\left[1 + \epsilon' \sum_k \cos(kx + \psi'_k)\right], \tag{6}$$

where $\Theta = T_i/T_e$ is the ion-to-electron temperature ratio set to $\Theta = 0.1$ or 1 in the different runs. Variables ψ_k and ψ'_k are random phases with a uniform distribution. The parameter ϵ (ϵ', respectively) is the amplitude of the initial electron (ion, respectively) density level of noise. The parameters (ϵ, ϵ') are chosen so that the development of the instability happens relatively rapidly, as Vlasov codes have a very low level of numerical noise. The influence of the level of initial density fluctuation on the LED has been studied for values $10^{-8} < \epsilon$, $\epsilon' < 10^{-4}$. Neither the growth rate of density fluctuations, nor its saturation level are modified by the choice of the parameters ϵ and ϵ', as long as they remain weak. Only the time needed for the instability to saturate is modified. The chosen values $\epsilon = \epsilon' = 10^{-5}$ are a good compromise to limit the computation time. However, when the electron and proton temperatures are of the same order the initial perturbation on ion density is rapidly damped out and the generation of the IAW starts from the numerical noise. When starting from a monochromatic Langmuir wave (section 3.1), the interaction time between the waves is "infinite." In this case the IAW can grow from the numerical noise to significant values providing we wait for long enough. On the other hand, when starting from a Langmuir wave packet (section 3.2) the interaction time between the waves is now finite. A continuous injection of noise is then needed to seed the instability. This is why an external driver $E_{\mathrm{ext}}^{\mathrm{noise}}$ is added in the Vlasov equation for ions (equation (3)). The aim is to control the generation of a continuous incoherent noise in the proton density. For self-consistency, the driver is used in both cases $\Theta = 0.1$ and $\Theta = 1$. The details of the forcing are described in appendix A. From a physical point of view, IAW grow from the proton density fluctuations background. Note that such density irregularities are observed in the solar wind [*Celnikier et al.*, 1987; *Harvey et al.*, 1988].

[13] In space conditions, the full physical process for the nonlinear evolution of large amplitude Langmuir waves is characterized by two successive steps. The first one is the generation of Langmuir waves from the bump-on-tail instability, the second one the electrostatic decay of these Langmuir waves if their amplitudes reach the LED threshold. Other authors have already studied the generation of beam driven Langmuir wave packets [*Omura et al.*, 1994, 1996; *Silin et al.*, 2007; *Umeda*, 2007]. Among their results, they have shown that the beam-driven Langmuir waves are localized packets. This localization is explained through the mechanism of kinetic localization in the framework of a nonlinear trapping theory [*Muschietti et al.*, 1995, 1996; *Akimoto et al.*, 1996; *Usui et al.*, 2005]. It is has also been shown that the beam-driven Langmuir wave packets are formed on time scales considerably shorter than those of parametric instabilities [*Intrator et al.*, 1984; *Akimoto et al.*, 1996].

[14] Our aim here is to focus the attention on the LED process. Motivated by the fact that the generation and localization of beam-driven Langmuir waves are decoupled from the LED process, we choose not to generate Langmuir waves by a bump-on-tail instability, but to resonantly grow the initial Langmuir wave by means of an electric field $E_{\mathrm{ext}}^{\mathrm{init}}$ added in equation (2). This method enables to have a direct control on the energy and the spectrum of the initial Langmuir wave and avoid other effects due to the non-Maxwellian character of the initial distribution function. Switched on at the beginning of the run, it acts as a driver to resonantly grow the wave with the desired spectrum and electric field amplitude. Details on the external driver $E_{\mathrm{ext}}^{\mathrm{init}}$ are given in Appendix B. The external driver is then switched off and the generated Langmuir wave evolves self-consistently. In section 3.1, a monochromatic Langmuir wave of wavelength λ_L and amplitude E_L is generated by imposing $E_{\mathrm{ext}}^{\mathrm{init}} = E_{\mathrm{ext}}^{(1)}$ (compare equation (B1)). In section 3.2, a Langmuir wave packet of mean wavelength λ_L, packet width Δ and maximum amplitude E_L is generated by imposing $E_{\mathrm{ext}}^{\mathrm{init}} = E_{\mathrm{ext}}^{(2)}$ (compare equation (B2)). The external electric field $E_{\mathrm{ext}}^{\mathrm{init}}$ is switched off when the amplitude (maximum amplitude, respectively) of the generated Langmuir wave (wave packet, respectively) reaches the desired value E_L. This happens typically for time $t < 300\ \omega_{pe}^{-1}$, small compared to the decay time scale. So, the resonant generation of the Langmuir wave (wave packet, respectively) does not interfere with the LED mechanism.

[15] In order to compare the simulation results with observations of electric waveforms during type III events, the Langmuir wavelength and amplitude are set as indicated by solar wind observations. Langmuir waves grow by resonance with an electron beam at phase velocity $v_L^{\Phi} = \omega_L/k_L \simeq V_{\mathrm{beam}}$. Typical electron beams span in the range 0.05–0.2 c [*Dulk et al.*, 1987; *Hoang et al.*, 1994]. Taking into account the Langmuir dispersion relation, we deduce Langmuir wavelengths in the range $\lambda_L = [100\text{–}600]\ \lambda_D$. However, for a temperature ratio $\Theta = 1$ ($\Theta = 0.1$, respectively), the daughter Langmuir wave packet is expected, from equation (1) and respective dispersion relations, to be backscattered for $\lambda_L < 285\ \lambda_D$ ($\lambda_L < 385\ \lambda_D$, respectively), and scattered forward for $\lambda_L > 285\ \lambda_D$ ($\lambda_L > 385\ \lambda_D$, respectively). Thereby, mother and daughter Langmuir Doppler-shifted frequencies are very close and hardly separated on observation. Thus, to be able to compare the simulations with observations, we choose Langmuir wavelengths that allow observations of LED, namely $\lambda_L = 100\ \lambda_D$ for the initial monochromatic Langmuir wave in section 3.1, and $50\ \lambda_D < \lambda_L < 400\ \lambda_D$ for the initial Langmuir wave packet in section 3.2. Since the phase velocities of the two expected Langmuir waves are large enough, their Landau damping can be neglected. Thus the phase velocity of the Langmuir waves do not need to be resolved in the electron distribution function velocity box. On the other hand, the expected IAW travel at the ion-sound speed $c_s = \sqrt{(T_e + T_i)/m_i}$, which is of the order of the ion thermal speed when electron and ion temperature are close,

Table 1. Expected Waves Involved in the Langmuir Electrostatic Decay, Given the Initial Langmuir Wavelength and Using Equations (1) for $\Theta = 0.1$ and $\Theta = 1$[a]

	Waves	Wavelength (λ_D)	Wave Number (λ_D^{-1})	Phase Velocity ($v_{th}^e = \lambda_D \omega_{pe}^{-1}$)	Group Velocity ($v_{th}^e = \lambda_D \omega_{pe}^{-1}$)
$\Theta = 0.1$	L	$\lambda_L = 100$	$k_L = 0.063$	$v_L^\phi = 16$	$v_L^g = 0.189$
	L'	$\lambda_{L'} = 132$	$k_{L'} = (-)\ 0.047$	$v_{L'}^\phi = -21$	$v_{L'}^g = -0.141$
	S	$\lambda_S = 57$	$k_S = 0.110$	$c_s = 0.024$	$c_s = 0.024$
$\Theta = 1$	L	$\lambda_L = 100$	$k_L = 0.063$	$v_L^\phi = 16$	$v_L^g = 0.189$
	L'	$\lambda_{L'} = 154$	$k_{L'} = (-)\ 0.041$	$v_{L'}^\phi = -24.5$	$v_{L'}^g = -0.123$
	S	$\lambda_S = 60$	$k_S = 0.104$	$c_s = 0.033$	$c_s = 0.033$

[a]The table shows for each wave the expected wavelength (in Debye length λ_D) corresponding wave number (in inverse Debye length λ_D^{-1}) used in the paper figures and phase and group velocities (in $\lambda_D \omega_{pe}^{-1}$).

thus leading to a large Landau damping. The ion-sound speed is resolved in the ion distribution function velocity box.

[16] The typical Langmuir waves amplitude is directly given by waveform observations and normalized to the electron temperature:

$$E = \sqrt{\frac{\epsilon_0 E_{\text{obs}}^2/2}{n k_b T_e}}. \tag{7}$$

In Paper I, the typical observed values are $10^{-2} < E_L < 10^{-1}$. We choose several amplitudes in the range $10^{-3} < E_L < 1$.

3. Numerical Results

[17] During the first part of the simulation ($0 < t < t_0$) the external electric pump generates a Langmuir monochromatic wave (wave packet, respectively) at the desired amplitude. At time $t = t_0$, the external pump is switch off when the Langmuir wave (wave packet, respectively) reaches the desired value. For $t > t_0$ the Langmuir wave evolves self-consistently. We consider time $t = t_0$ as the beginning of the numerical experiment.

[18] The typical intensity of the electric field of the IAW generated by LED is much below the level of Langmuir electric noise. In the following, the ion *density* is therefore used as a tracer for IAW.

3.1. Electrostatic Decay of a Monochromatic Langmuir Wave

[19] In this section, we consider the evolution of a monochromatic wave generated by the external pump defined in equation (B1). Table 1 summarizes the expected wavelength, wave numbers, phase velocity and group velocity in the case of three monochromatic resonant waves, as a function of the mother Langmuir wavelength λ_L and the temperature ratio Θ.

[20] A broad spectrum of daughter waves generated by the instability is clearly seen on Figure 1. It shows the electric field and ion density spectrum, black and red lines, respectively, at given times. Dashed vertical lines indicate the expected wave numbers of the LED products as reported in Table 1. In Figure 1 (top left), $t = 10^3\ \omega_{pe}^{-1}$, the spectrum corresponds to the "initial condition" where only the Langmuir wave at $k_L = 0.063\ \lambda_D^{-1}$ and its harmonic at $0.13\ \lambda_D^{-1}$ are present. Then, the growth of the LED produces (1) a daughter Langmuir waves L' at $k_{L'} \simeq 0.04\ \lambda_D^{-1}$ in the electric field spectrum and (2) an IAW at $k_S \simeq 0.10\ \lambda_D^{-1}$ in the ion density spectrum. Both are shown in Figure 1: $t = 5 \times 10^4\ \omega_{pe}^{-1}$ (Figure 1, top right) and $t = 10^5\ \omega_{pe}^{-1}$ (Figure 1, bottom left). Finally, at $t > 10^5$ (Figure 1, bottom right) harmonics of the IAW are produced, low-k fluctuations are generated and the LED saturates. We need to stress here that during the decay phase, even if the Langmuir wave L is monochromatic, the product waves L' and S are both wave packets with wave numbers centered on the expected wave number. This results from the fact that different k channels are available for energy transfer from the Langmuir wave toward its decay products. Indeed Figure 2 shows the linear growth rate versus k for different wave numbers of the daughter Langmuir wave electric field (in black) and IAW density fluctuations (in red) spectrum. Growth rates for both daughter waves are overplotted with k_S axis and $k_{L'}$ axis such that $k_S + k_{L'} = k_L$. As expected, the growth rates are the same for each couple of product waves that verify the wave number resonant condition. The spread in wave number is about $\Delta k_{L'} = \Delta k_S \simeq 0.025$ for both waves, thereby a relative spectral spread of $\Delta k_S / k_S \simeq 0.2$ for the IAW and $\Delta k_{L'}/k_{L'} \simeq 0.6$ for the Langmuir product wave. Note that the generation of a large spectrum of product waves limits the spatial coherence of the interaction. This point is discussed in section 4.2.

[21] We then compute an "integrated" (over space) ion density fluctuations $\langle \delta n \rangle$ generated by LED defined by

$$\langle \delta n \rangle(t) = \sqrt{\frac{1}{L_x} \int_0^{L_x} (n(t,x) - n_0)^2\, dx}, \tag{8}$$

with the mean ion density $n_0 = 1$ in dimensionless units. We define the saturation level δn_{sat} as the maximum value reached by the mean density fluctuations $\langle \delta n \rangle(t)$ during the simulation. The growth rate for average density fluctuation is here $\gamma_{\text{LED}} = 2.3 \times 10^{-5}\ \omega_{pe}$, or $\gamma_{\text{LED}} = 4.1 \times 10^{-2}\ f_S$ when expressed in term of the IAW frequency, defined by $f_S = c_s / \lambda_S = 5.5 \times 10^{-4}$. This means that the characteristic time scale for the density to grow is about 24 IAW periods, in this case. The saturation level $\delta n_{\text{sat}} = 8.7 \times 10^{-5}$, obtained at time $t = 1.4 \times 10^5\ \omega_{pe}^{-1}$, is of the order of the expected saturation level defined by the ratio of electric energy to the thermal energy $\delta n_{\text{sat}}^0 = \frac{1}{2} E_L^2 / (T_e + T_i) = 2.3 \times 10^{-4}$. The simulation has been repeated for several initial Langmuir wave amplitude, with values in the range $10^{-3} < E_L < 1$, and for two temperature ratios $\Theta = 0.1$ and $\Theta = 1$.

[22] We found that the evolution becomes strongly nonlinear when the Langmuir wave electric field is "not small," i.e., when $E_L \gtrsim 0.3$ for $\Theta = 1$ and $E_L \gtrsim 0.2$ for $\Theta = 0.1$. When strong non linear processes take place the evolution is

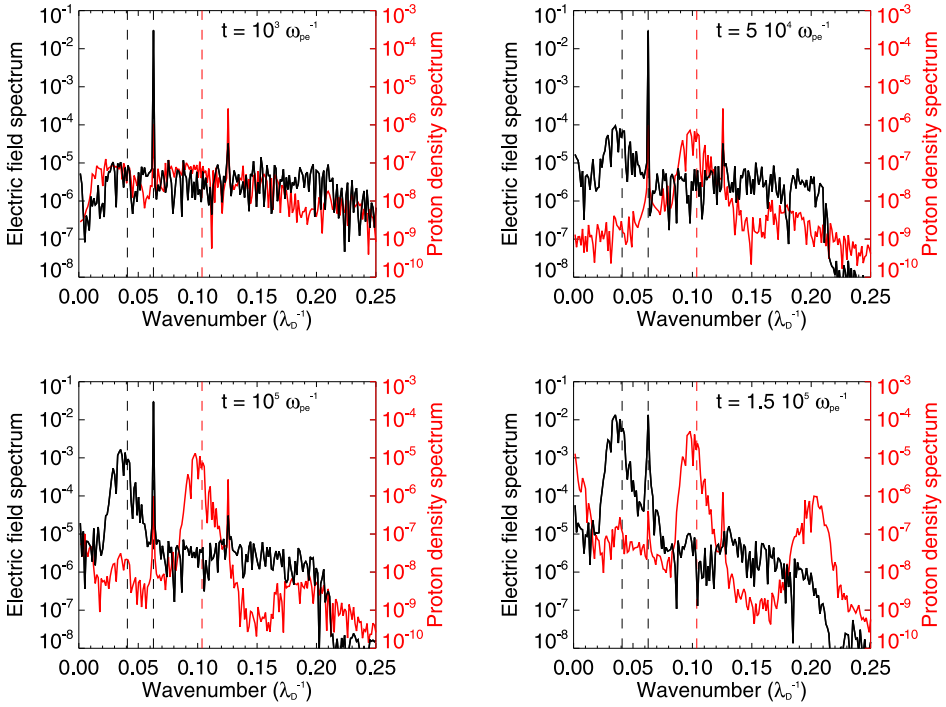

Figure 1. Spectrum of both electric field (in black) and ion density (in red) at four different times from simulation of LED of a monochromatic Langmuir wave with wave number $k_L = 0.063$ and initial electric amplitude $E_L = 3 \times 10^{-2}$. Dashed lines indicate the expected wave numbers of the LED waves. (top left) Initial conditions. (bottom right) Spectrum at saturation. Note the presence of the second harmonic of the IAW in this last case.

not simply driven by the LED mechanism. Conversely, for small values of E_L, the system is mainly driven by the LED process so that we can compute the growth rate for average density fluctuations and the density fluctuations saturation level as previously defined.

[23] The growth rate deduced from simulations γ_{LED} of the average density fluctuations $\langle \delta n \rangle$ deduced from the simulation is displayed in Figure 3 for the two temperature ratios. As shown before, for too high values of the Langmuir amplitude, about $E_L \simeq 0.3$, corresponding to an electric to thermal energy ratio of 0.1, strong nonlinear effects arise before LED. Also, as expected, the growth rates are lower for $\Theta = 1$ than $\Theta = 0.1$, due to the increase of IAW Landau damping in the first case. Contrary to former results [*Umeda and Ito*, 2008], we show here that the LED is observed for initial Langmuir waves with electric energy 5 orders of magnitude lower than the plasma thermal energy.

[24] An analytical effective growth rate $\gamma_{\mathrm{LED}}^{\mathrm{analytical}}$ has been overplotted (dashed lines). It is defined as the difference between the analytical full monochromatic case of undamped monochromatic waves in an homogeneous background $\gamma_{\mathrm{LED}}^{\mathrm{th}}$ [*Sagdeev and Galeev*, 1969] and the IAW Landau damping $\gamma_S^{\mathrm{Landau}}$:

$$\gamma_{\mathrm{LED}}^{\mathrm{analytical}} = \gamma_{\mathrm{LED}}^{\mathrm{th}} - \gamma_S^{\mathrm{Landau}}, \tag{9}$$

where

$$\gamma_{\mathrm{LED}}^{\mathrm{th}} \simeq k_{IA} C_s \left(\frac{\epsilon_0 E^2}{n k_B T} \frac{m_p}{m_e} \right)^{1/4}; \tag{10}$$

$\gamma_{\mathrm{LED}}^{\mathrm{th}}$ is of the order of the IAW frequency with solar wind parameters. The growth rate computed from Vlasov simulations γ_{LED} is 1–2 orders of magnitude lower than $\gamma_{\mathrm{LED}}^{\mathrm{analytical}}$. The discussion concerning the discrepancy

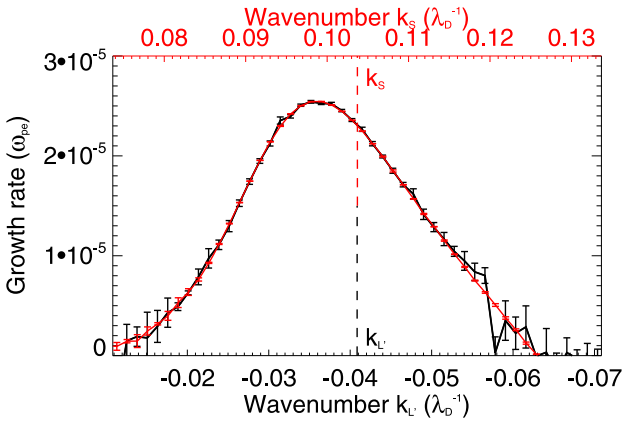

Figure 2. Spectral growth rate for the Langmuir wave L' electric field (in red, $k_{L'}$ axis at the bottom, leftward) and the IAW density fluctuations (in black, k_S-axis at the top, rightward) generated by the LED of a monochromatic Langmuir wave ($E_L = 3 \times 10^{-2}$ and $\Theta = 1$). Both axes are scaled to show the resonant condition in wave numbers: $k_S + k_{L'} = k_L$. Vertical error bars are $1 - \sigma$ error bars for the fitting of the growth rate. The vertical dotted line indicates the expected wave numbers for monochromatic LED products.

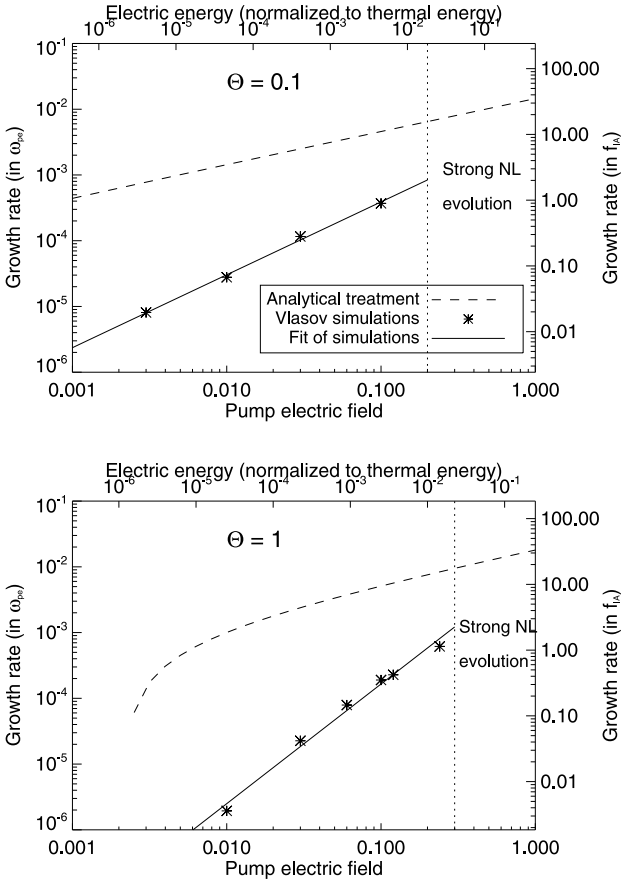

Figure 3. Growth rate for IAW density fluctuations versus Langmuir wave initial electric field amplitude for two temperature ratios. (top) $\Theta = 0.1$. (bottom) $\Theta = 1$. The growth rate is expressed in (left) plasma frequency unit ω_{pe} and in (right) IAW frequency f_{IA}. The full line is a fit of Vlasov simulations (stars). The dashed line shows the analytical growth rate $\gamma_{\mathrm{LED}}^{\mathrm{analytical}}$ from *Sagdeev and Galeev* [1969] when LED-generated IAW remain monochromatic, including the linear Landau damping of IAW. The vertical dotted line sets the limits above which strong nonlinear effects occur before LED starts.

between the analytical monochromatic case and Vlasov simulations is postponed to section 4.2.

[25] We also looked for the dependence of the growth rate with respect to the mother Langmuir wave vector k_L. Finally, the growth rate for density fluctuations generated by LED has been fitted by a power law:

$$\gamma_{\mathrm{LED}} = \Gamma\, E_L^{\alpha} k_L^{\beta}. \tag{11}$$

The fitting parameters Γ, α and β are given in Table 2.

[26] The saturation level of density fluctuation δn_{sat} is summarized in Figure 4 for $\Theta = 0.1$ (Figure 4, top) and $\Theta = 1$ (Figure 4, bottom). The expected saturation level $\langle \delta n_0^{\mathrm{sat}} \rangle$, expressed as the initial Langmuir electric energy to the total kinetic energy ratio,

$$\langle \delta n_0^{\mathrm{sat}} \rangle = \frac{1}{2} E_L^2/(T_e + T_i), \tag{12}$$

is overplotted (dashed lines). The obtained saturation level of density fluctuation is in good agreement with the expected values in both cases.

[27] To summarize, the simulations of the Langmuir electrostatic decay from an initial monochromatic Langmuir wave have shown that (1) the threshold for the instability to grow, expressed in term of the Langmuir wave electric energy, is at least 5 orders of magnitude lower than the plasma thermal energy when $0.1 < \Theta < 1$; (2) the product waves are resonantly generated over a broad range of wave numbers, naturally producing narrow wave packets; (3) growth rates of IAW density fluctuations are 1–2 orders of magnitude lower than the analytical values deduced from the pure monochromatic case; and (4) saturation levels for IAW relative density fluctuations are of the order of the ratio of Langmuir electric energy to the total kinetic energy.

3.2. Electrostatic Decay of a Langmuir Wave Packet

[28] In the following, we consider the evolution of a finite-amplitude Langmuir wave packet, generated by the external electric field pump defined in equation (B2). We recall that, in order to mimic the presence of a low level of small-scale ion acoustic turbulence, we introduce a source term of ion acoustic noise. This forcing generates incoherent proton density fluctuations at a level $\delta n/n \sim 10^{-5}$ much smaller than the expected level of density fluctuations generated by LED.

[29] Figure 5 shows the LED of a Langmuir wave packet with wavelengths centered on $\lambda_L = 200\ \lambda_D$, a packet width $\Delta = 2000\ \lambda_D$, a maximum initial electric field $E_L = 6 \times 10^{-2}$, and the two temperature ratio $\Theta = 0.1$ (Figure 5, left) and $\Theta = 1$ (Figure 5, right). The mother and daughter Langmuir wave packets can be followed in Figure 5 (top) that show the space-time evolution of the electric field density energy $E(x, t)^2/2$. The Langmuir mother wave packet propagates toward the right and emits backscattered Langmuir wave packets. Figure 5 (bottom) shows the temporal evolution of ion density fluctuations during the decay of the Langmuir wave. IAW density fluctuations are generated locally (by ponderomotive force from the two Langmuir wave packets beats) and propagate forward at the ion sound speed (dashed line). When $\Theta = 0.1$ IAW propagate and escape the area where LED develops. Conversely, when $\Theta = 1$, IAW density fluctuations are heavily damped as soon as the waves escape the area where LED occurs. Thereby, the waves can be observed only where the mother Langmuir wave decays. Finally, as for the case of monochromatic Langmuir waves, the LED growth rate is lower for a larger value of Θ.

[30] The simulation has been repeated for different values of E_L and mean wavelength λ_L, with a packet width of $\Delta = 10\ \lambda_L$. Figure 6 summarizes the results for the evolution of the Langmuir wave packet, each point representing a single simulation.

Table 2. Numerical Values for the Fit for the Growth Rate of LED-Driven Density Fluctuations in Equation (11)

	Γ	α	β
$T_p/T_e = 0.1$	0.026	1.11	0.59
$T_p/T_e = 1$	0.025	1.82	0.30

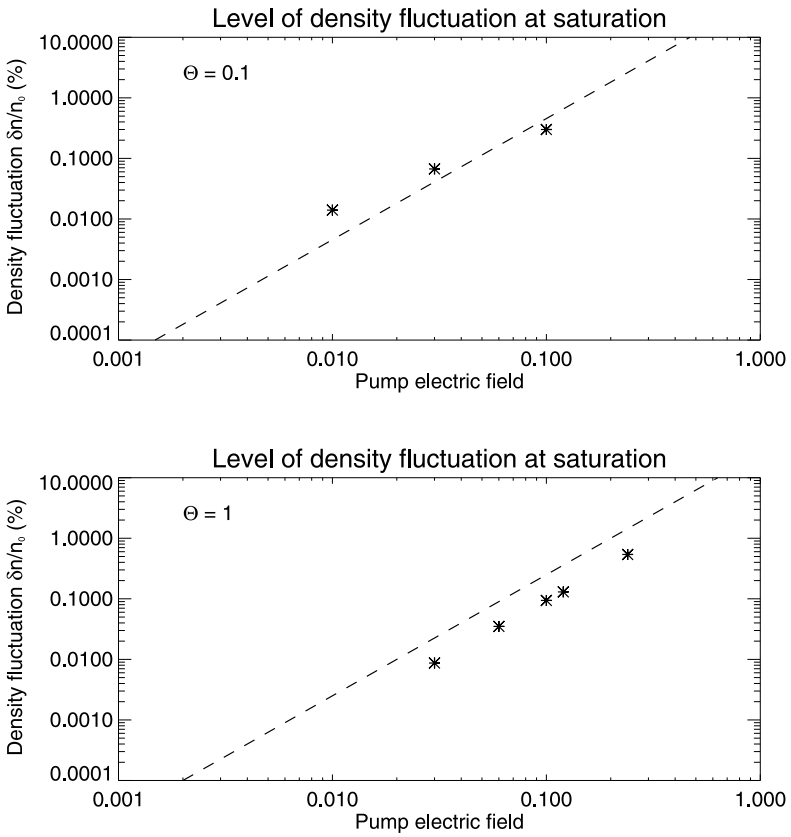

Figure 4. Average density fluctuation at saturation δn_{sat} (expressed in percentage of mean density) for different Langmuir wave initial electric field amplitudes for both (top) $\Theta = 0.1$ and (bottom) $\Theta = 1$. The dashed lines show the expected level of saturation $\delta n_0^{\mathrm{sat}} = (0.5 \times E_L^2)/(T_e + T_i)$ defined as the Langmuir electric energy to the total kinetic energy ratio.

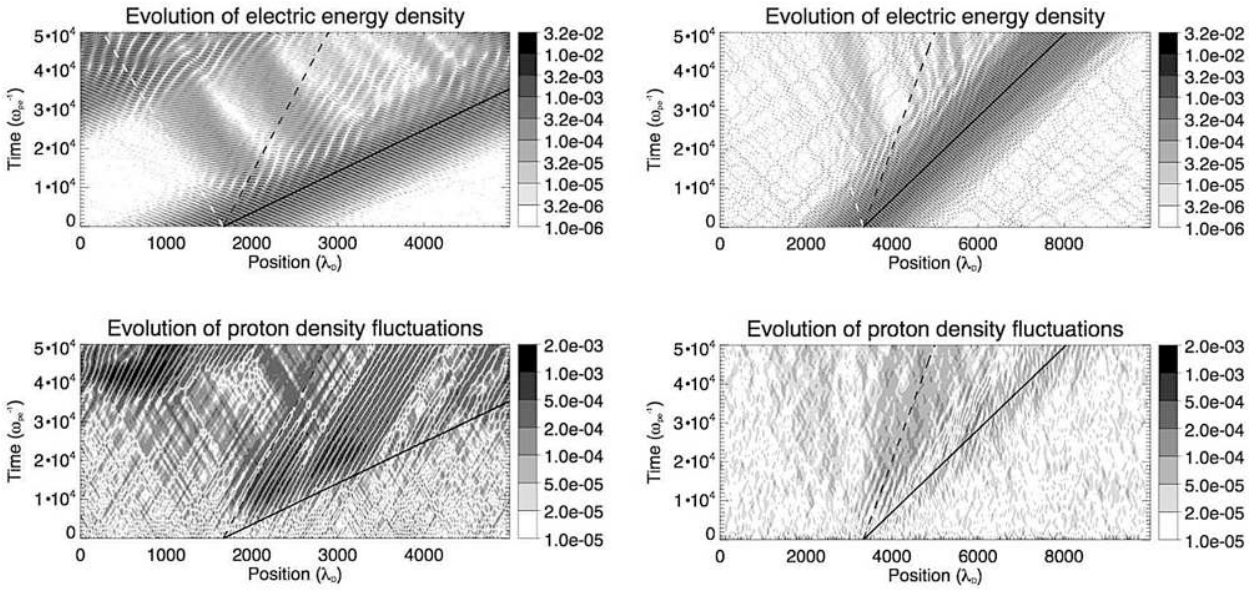

Figure 5. (top) Space-time evolution of the electric energy density. (bottom) Space-time evolution of the ion density fluctuations. (left) $\Theta = 0.1$. (right) $\Theta = 1$. Full lines show the expected group velocities of the Langmuir wave packets, while dashed lines display the ion sound speed.

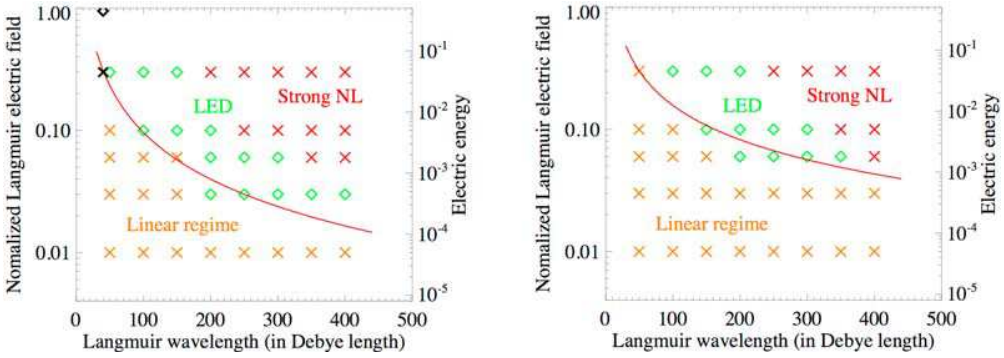

Figure 6. Evolution of a Langmuir wave packet, (bottom) with different wavelengths centered on λ_L but a same packet width of $\Delta = 10\ \lambda_L$ and different initial electric fields E_L (left axis). (left) $\Theta = 0.1$. (right) $\Theta = 1$. In green are simulations where LED is observed; in orange are simulations where the available interaction time between the waves is lower than the LED time scale; in red are simulations where strong NL effects arise before/instead of LED. Previous simulation results from *Umeda* [2007] and *Umeda and Ito* [2008] are overplotted in Figure 6 (left) with black crosses and diamonds, respectively. The red line is the semianalytical threshold expressed in equation (15).

[31] During the decay process, the mother wave packet generates a daughter wave packet traveling at a different group velocity. The region of parameters leading to electrostatic decay is displayed with green squares in Figure 6. Eventually the two wave packets separate thus stopping the LED process. Therefore, LED is efficient only if the interaction time between the two wave packets is longer than the growth time for the daughter waves. The growth time of the instability is controlled by the Langmuir electric field amplitude: the larger the amplitude, the smaller the growth time (Figure 3). The interaction time is controlled by the Langmuir wavelength: the larger the wavelength, the smaller its group velocity and so the larger the interaction time. Thus, for low-amplitude and/or short wavelengths, the Langmuir wave packet propagates at its group velocity without nonlinear interactions. The region of parameters leading to a linear behavior without electrostatic decay is displayed with orange crosses in Figure 6. The efficiency of LED (green) region increases toward the linear (orange) part (i.e., LED is observed for lower λ_L and E_L) if temperature ratio Θ decreases or/and the size Δ of the mother wave packet increases. Finally, strong non linear effects dominate the evolution of high-amplitude and/or large-wavelength Langmuir wave packets, and LED is no more the dominant process. The region of parameters where other non linear effects are dominant is shown with red crosses in Figure 6. These strong non linear effects seem to be the signature of strong turbulence: Langmuir collapse and formation of cavitons. This evolution is out of scope of the present study and will be studied in a future work.

[32] The effective threshold for the electrostatic decay of a Langmuir wave packet can be estimated by imposing that the interaction time τ_{int} is equal to the inverse growth rate of daughter wave packets γ_{LED}. The growth rate for LED γ_{LED} has been obtained from simulations of monochromatic Langmuir waves LED and fitted in equation (11). The interaction time τ_{int} is evaluated from

$$\tau_{int} \simeq \Delta/(v_L^g - v_{L'}^g), \tag{13}$$

where $(v_L^g - v_{L'}^g)$ is the difference of group velocity between the two waves that first separate, here the mother and daughter Langmuir waves, and Δ the packet width of the mother Langmuir wave, which is assumed to be about the length of interaction. Using equation (1) and $k_S \simeq 2\ k_L$, equation (13) can be written in normalized units as

$$\tau_{int} \simeq \Delta/(6\ k_L). \tag{14}$$

Finally, $\tau_{int} = \gamma_{\mathrm{LED}}^{-1}$ gives the effective LED threshold of a Langmuir wave packet with wave vector k_L and a packet width Δ:

$$E_{\mathrm{LED}}^{\mathrm{threshold}} = \left(\frac{6\ k_L^{1-\beta}}{\Delta\Gamma}\right)^{1/\alpha}, \tag{15}$$

expressed in normalized units. The semianalytical threshold is overplotted in Figure 6 (red line) in order to validate its dependency with the mother Langmuir wave vector k_L.

[33] We also performed a series of simulations in order to validate the dependency of $E_{\mathrm{LED}}^{\mathrm{threshold}}$ with Δ. This time the simulation starts with a mother Langmuir wave packet of mean wavelength $\lambda_L = 200$ but with different packet width values in the range $5\ \lambda_L < \Delta < 30\ \lambda_L$, covering the typical range for Langmuir wave packets in the solar wind, and initial amplitude E_L. The results are presented in Figure 7, together with the semianalytical threshold (red line). In both cases, equation (15) is in agreement with simulations of LED of localized Langmuir wave packets.

[34] The threshold decreases when (1) the ion to electron temperature ratio decreases, since the Landau damping of IAW decreases and their effective growth rate increase; (2) the mean Langmuir wavelength increases, since Langmuir wave packets with longer wavelengths propagate at smaller group velocities thus increasing the available interaction time with the ion background; and (3) the width of the Langmuir wave packets increases, since the interaction time between the mother and daughter waves increases. The effective threshold obtained by Vlasov simulations and described in this section is compared to observations of LED in the solar wind in the next section.

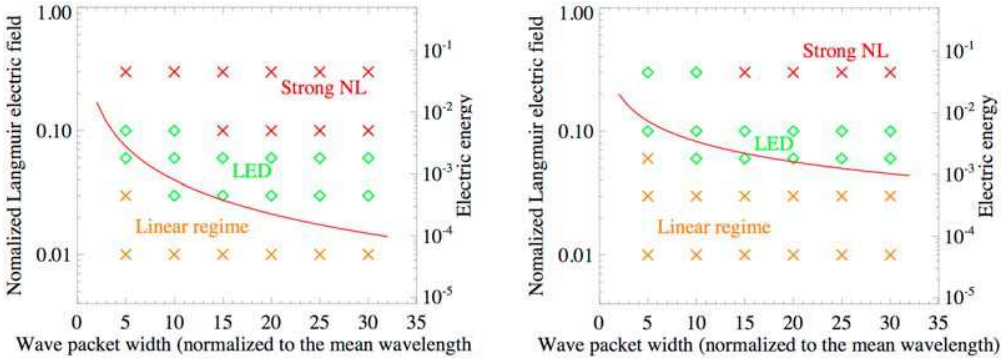

Figure 7. Evolution of a Langmuir wave packet with a mean wavelength $\lambda_L = 200$ but different packet widths Δ (bottom axis, normalized to λ_L) and different initial electric fields E_L (left axis). (left) $\Theta = 0.1$. (right) $\Theta = 1$. In green are simulations where LED is observed; in orange are simulations where the available interaction time between the waves is lower than the LED time scale; in red are simulations where strong NL effects arise before/instead of LED. The red line is the semianalytical threshold expressed in equation (15).

[35] Finally, in two recent works of 1D-1V Vlasov simulations, *Umeda* [2007] and *Umeda and Ito* [2008] reported the evolution of beam-excited Langmuir waves. Their simulation parameters are $\Theta = 0.1$, a beam speed $v_{\text{beam}} = 8 \times v_{\text{th},e}$ with a beam temperature equals to the electron core temperature and a beam density ratio of 0.1% and 0.5%, respectively. These beams generate Langmuir waves at a phase velocity of about $v_{\text{beam}} - v_{\text{th},e} = 7 \times v_{\text{th},e}$, i.e., a Langmuir wavelength $\lambda_L \simeq 40 \times \lambda_D$. The amplitude of the Langmuir waves reaches $E_L \sim 0.3$ in the first case, $E_L \sim 1$ in the second case. They observed the LED process in the second case only. We have overplotted their results in Figure 6 (black cross and diamond, respectively). These previous simulations agrees with equation (15): for these parameters, the equation predicts that LED of localized Langmuir wave packets should occur for high Langmuir electric energy levels (of the order of unity).

[36] To summarize the simulations of the Langmuir electrostatic decay from an initial Langmuir wave packet: (1) we have illustrated how the localization of Langmuir wave packets is crucial for the evolution of Langmuir decay by limiting the interaction time between mother and daughter waves; (2) we have shown that the ion acoustic waves are generated locally, where the wave packets interact, and then IAW are damped as soon as they escape the region where the mother and daughter Langmuir waves interact when electron and ion temperature are equal or escape this region when the electron temperature is higher than the ion temperature; and (3) we used results from the Langmuir electrostatic decay of a monochromatic Langmuir wave (section 3.1) to compute a semianalytical threshold for the electrostatic decay of Langmuir wave packets (equation (15)); this semianalytical threshold has been shown to be in agreement with simulations of the electrostatic decay of Langmuir wave packets.

4. Discussion

[37] In the following, we discuss, first, the initialization of LED in the case $\Theta = 1$, second, the discrepancy between the LED growth rate obtained from simulations and analytical estimation. LED threshold obtained from simulations is then compared to observations. Finally, we show that the saturation of the instability gives an upper limit to the expected level of observed density fluctuations.

4.1. Initialization of Langmuir Electrostatic Decay

[38] In the case of equal electron and ion temperature, associated with a strong Landau damping of ion acoustic fluctuations, one may wonder whether processes complementary to the resonant interaction of the waves could facilitate the LED. In particular, a decrease (even local) of the IAW Landau damping during the beginning of the LED process could ease the initialization of the instability. Such decrease can happen either through two main processes. (1) Wave-particle interactions due to the trapping of ions in the IAW potential well could modify the ion distribution function by forming a plateau at the ion sound speed which, in turn, could then decrease the Landau damping rate. However, no such plateauing is observed. (2) The beats of the mother and daughter Langmuir waves, could heat the electrons so that the ion-to-electron temperature ratio decrease locally, leading to a partial suppression of the IAW Landau damping. However the temperature ratio during the simulation has too small variations $\Delta\Theta/\Theta < 1\%$ to really modify the IAW Landau damping. This hypothesis is thus also ruled out.

[39] Since no such complementary processes are present in the simulations, the initiation of the LED is likely to be caused by the resonant interaction of the waves, that dominates locally the Landau damping of IAW.

4.2. Growth Rate for Langmuir Electrostatic Decay

[40] We have seen in section 3.1 that a large discrepancy exists between the growth rate of mean density fluctuations obtained from the simulations, γ_{LED}, and the analytical one deduced from three monochromatic waves, $\gamma_{\text{LED}}^{\text{th}}$ [*Sagdeev and Galeev*, 1969]. (The influence of the resolution in velocity has been checked, and the results are unchanged as far as the resolution in velocity is not too low. The results

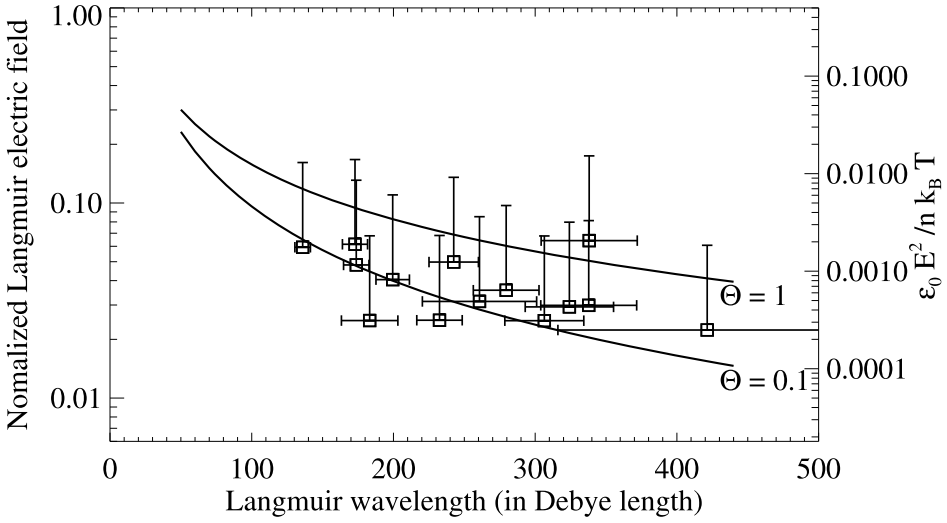

Figure 8. Observed Langmuir electric field amplitude, normalized like the simulations, versus wavelength. The threshold for LED computed from Vlasov simulations is overplotted for two values of the temperature ratio $\Theta = 0.1$ and $\Theta = 1$.

are also independent of the size of the box, as long as the box remains larger than the coherence length of the daughter wave packets.) The existence of a strong IAW Landau damping γ_{Landau}, such that $\gamma_{\text{LED}} = \gamma_{\text{LED}}^{\text{th}} - \gamma_{\text{Landau}}$ could explain this difference. Since Landau damping for IAW cannot be found analytically when electron and temperature are close, we performed complementary simulations and measured an IAW Landau damping of $\gamma_{\text{Landau}} = -1.9 \times 10^{-5}\ \omega_{pe}$ for $\Theta = 0.1$ ($\gamma_{\text{Landau}} = -8.9 \times 10^{-4}\ \omega_{pe}$, respectively, for $\Theta = 1$), much lower than γ_{th}. Thus, the hypothesis that $\gamma_{\text{LED}} = \gamma_{\text{LED}}^{\text{th}} - \gamma_{\text{Landau}}$ is to be ruled out.

[41] Note that the growth rate measured from simulations already takes into account the effect of the Landau damping. Thus, the difference between γ_{LED} and $\gamma_{\text{LED}}^{\text{analytical}}$ should be carried by the evaluation of $\gamma_{\text{LED}}^{\text{th}}$. Actually, the main difference between the analytical treatment of three-wave resonance and Vlasov simulations is that the daughter waves are treated as monochromatic in the first case whereas they are observed to have a non negligible spectral width in the second (see Figures 1 and 2). Simulations have shown that the spectral width of the product waves increases when (1) $\Theta \simeq 1$, in which case the IAW dispersion relation is numerically observed to spread out around the analytical branch; therefore the resonance can occur with (ω, k) values slightly different from the theoretical expectation; and (2) the energy of the Langmuir mother wave increases, in which case the linear approximation for a δ-shaped resonance is no longer valid. The limited spatial coherence of daughter wave packets implies that their growth is localized where mother and daughter wave packets interact, thus strongly limiting their growth rate. This explains why the growth rate deduced from simulations is much lower than the analytical one.

4.3. Threshold of Langmuir Electrostatic Decay and Type III Observations

[42] The TDS observation mode of the S/WAVES experiment on board the STEREO mission [*Bougeret et al.*, 2007] gives access to in situ electric field waveform in 3D with an equivalent spectral resolution up to 60 kHz. In Paper I, we have shown evidence for nonlinear coupling between Langmuir waves at about 10 kHz and ion acoustic waves at about 0.2 kHz. We recall here the global plasma parameters for these observations. The 1-h-average wind speed from WIND/3-DP [*Lin et al.*, 1995] is about $V_{SW} = 315$ km s^{-1}. The electron temperature observed by WIND/3DP is $T_e \simeq 10^5$ *K*, and the electron density in the solar wind, estimated from the plasma frequency, is about $n_e \simeq 10^6$ m^{-3}. From the electron density and temperature, the Debye length is $\lambda_D \simeq 20$ m.

[43] Figure 8 displays the observed value of Langmuir electric field, normalized as described in equation (7), for the whole data set of waveforms where LED has been observed. Their wavelength, not directly measured, is evaluated as follows. By taking into account the Doppler shift caused by the solar wind and noting that the IAW should propagate here antisunward, the ion acoustic wavelength reads:

$$\lambda_S = (V_{SW} + c_s)/f_S^{\text{obs}}$$

where the sound speed c_s is evaluated by

$$c_s = \sqrt{k_B(T_e + T_p)/m_p},$$

where k_B is the Boltzman constant, m_p the proton mass and T_p the proton temperature that remains unknown but is of the order of T_e in the solar wind. The mother Langmuir wavelength λ_L is then about twice the LED-produced ion acoustic wavelength.

[44] However, caution should be taken when directly comparing this threshold value with the observation. Indeed solar wind type III Langmuir wave packets are most probably localized in 3D. The observed waveforms are 1D spatial cuts of the real 3D structures and thus only give a lower limit on the width of the wave packet, as well as its

maximum amplitude. We assume that the Langmuir wave packets have a 3D gaussian shape, and that the spacecraft crosses it somewhere within a distance from the center of the 3D structure of the order of the full width at half maximum. Therefore a realistic range for the maximum electric field E_L^{real} reached by the 3D wave packet is calculated as: $E_L^{obs} \lessapprox E_L^{real} \lessapprox e\, E_L^{obs}$, where E_L^{obs} is the observed level of Langmuir electric field. Data are plotted with such error bars.

[45] The LED threshold expressed in equation (15) is overplotted for two values of the ion to electron temperature ratio $\Theta = 0.1$ and $\Theta = 1$, using computed values from Table 2. The observed electric field amplitudes are of the order of the threshold computed from Vlasov-Poisson simulations, in the case of a localized wave packet and $\Theta \approx 1$, confirming that the development of LED is compatible with the observed events.

4.4. Saturation of LED: Expected Level of Observed Density Fluctuations

[46] In our simulations, for initial Langmuir wave packets in the range of amplitudes that correspond to observations of Langmuir waves during type III events, the IAW-like density fluctuations associated with the LED do not reach the saturation level. Indeed, the mother and Langmuir wave packets that propagate at different group velocities separate before the saturation stage, thus stopping the growth of the IAW. This is confirmed in the observations, since most of the observed waveforms show (1) mother and daughter Langmuir waves with different energies and (2) IAW with no harmonics. The saturation level $\langle \delta n_0^{sat} \rangle / n_0 = E_L^2/(T_e + T_i)$ should thus be an upper limit on the expected level of density fluctuations on observations of LED during type III.

[47] Density fluctuations at the frequencies considered here can be measured in space from the variations of the floating potential of the spacecraft [*Pedersen*, 1995] when it crosses the region where LED is observed. The voltage signal observed on STEREO/Waves waveforms with monopole antennas channels contains information on the floating potential of the spacecraft. This remains however to be calibrated. Knowing the saturation level of IAW during LED, and given the calibration, we could check whether the observed level of density fluctuations is consistent with our simulations.

5. Conclusion

[48] In order to study the origin of electromagnetic radio emissions during type III bursts, we have reported in this paper 1D-1V Vlasov-Poisson simulations of the Langmuir electrostatic decay. The simulations have been done in typical solar wind conditions: ratio of the electron to ion temperature from 0.1 to 1, mother Langmuir wavelengths typical of those observed during type III events and, most important, by considering localized Langmuir wave packets. The main results are the following.

[49] 1. Langmuir electrostatic decay develops even when the electron and ion temperatures are close. Its threshold, when considering a monochromatic wave, is at least 5 orders of magnitude lower than the plasma thermal energy when $0.1 < \Theta < 1$.

[50] 2. Langmuir electrostatic decay resonantly generates daughter waves over a broad range of wave numbers, naturally leading to narrow wave packets. This limits the length of coherence which is why the growth rate is 1–2 orders of magnitude lower than the analytical values deduced from a pure monochromatic case.

[51] 3. The behavior of daughter ion acoustic waves depends on the temperature ratio. Ion acoustic waves can escape the region where the resonant coupling takes place and propagate when electron temperature is higher than proton temperature. Conversely, they are damped as soon as they escape the resonant coupling area when temperatures are equal.

[52] 4. We confirm that the saturation level for IAW density fluctuations is of the order of the ratio of Langmuir electric energy to the total kinetic energy. However, for the range of amplitudes that correspond to observations, the IAW-like density fluctuations associated with the LED should not reach the saturation level because (1) the mother and Langmuir wave packets that propagate at different group velocities separate before the saturation stage and (2) harmonics of the IAW are seen at saturation in the simulations but, to our knowledge, not in type III observations.

[53] 5. Finally, an effective threshold has been obtained (equation (15)) for localized Langmuir wave packets and compared to STEREO/WAVES observations. The observed Langmuir electric field during type III reported by *Henri et al.* [2009] is in the range of LED effective threshold computed from Vlasov simulations, thus confirming the interpretation of these observed electric field waveforms in term of the LED of type III beam-driven Langmuir waves.

[54] The physical mechanism responsible for the generation of electromagnetic radio waves during type III burst is still under study. The process described by *Ginzburg and Zheleznyakov* [1958] and leading to the generation of type III radio emission at twice the local plasma frequency is a two step process: (1) first the beam-driven Langmuir wave decays through LED, then (2) the mother and daughter Langmuir waves coalesce to generated the electromagnetic wave.

[55] Up to now, observations have shown that resonant coupling between Langmuir waves and ion acoustic waves does occur during a type III burst [*Henri et al.*, 2009]. The present paper also shows that Langmuir electrostatic decay may occur in solar wind conditions and that the threshold is reached by the observed Langmuir electric amplitude. These two complementary studies thus confirms step 1 does occur.

[56] Langmuir electrostatic decay generates two counterpropagating Langmuir waves in opposite direction, but step 2 requires obliquely propagating Langmuir waves for waves to couple and produce the transverse electromagnetic wave. Does the density inhomogeneities scatter the Langmuir waves enough to introduce a significant perpendicular component to their wave vector? An important step would be to study the interaction of Langmuir waves with an inhomogeneous background, in order to check this hypothesis. Finally, the coalescence of counterpropagating Langmuir waves is hard to observe because the signal would be hidden by the generation of the harmonic of the mother Langmuir wave. Simulations of step 2 with input from the observations

could at least show whether the coalescence process could occur in the solar wind.

Appendix A: Generation of the Ion Density Noise

[57] The continuous injection of ion density noise is driven by an external fields $E_{\text{ext}}^{\text{noise}}$ added to the ion dynamics (equation (3)). This driver is defined by

$$E_{\text{ext}}^{\text{noise}}(x,t) = E_{\text{ext}}^{\text{ions,max}} \frac{\sum_\lambda \cos(2\pi x/\lambda)\cos(\omega_\lambda t + \Psi_\lambda''(t))}{|\sum_\lambda \cos(2\pi x/\lambda)\cos(\omega_\lambda t + \Psi_\lambda''(t))|}. \quad \text{(A1)}$$

It introduces a flat spectrum for wavelength over the range $50 < \lambda < 1000$. $E_{\text{ext}}^{\text{noise}}(x, t)$ is normalized in order to have a maximum amplitude of $E_{\text{ext}}^{\text{ions, max}} = 1 \times 10^{-5}$. The frequencies ω_λ are chosen to satisfy the dispersion relation of IAW, $\omega_\lambda = (2\pi/\lambda)c_s$ with $c_s = \sqrt{(1+\Theta)/\mu}$ the ion sound speed. The phases $\psi''_k(t)$ have a steplike variation, constant over a time interval δt. At the end of each interval, they are independently drawn from a uniform distribution. This way, the generation of ion acoustic noise is made of a succession of time coherent forcing for time intervals of duration $\delta t = 500 \times \omega_{pe}^{-1}$ (about 80 plasma oscillations). This means that for an IAW of wavelength $\lambda_{IA} = 100$, the forcing lasts 1/20th of a period, much shorter than the typical IAW oscillation time in order to generate an incoherent noise. This forcing thus generates density fluctuations much smaller than the level of density fluctuations generated by LED in our simulations.

Appendix B: Generation of the Initial Langmuir Wave

[58] In this appendix, we describe the driver $E_{\text{ext}}^{\text{init}}$, added in the Vlasov equation for electrons (equation (2)). This external electric field controls the generation of the initial Langmuir wave. It acts as a driver that resonantly grow a Langmuir wave propagating in only one direction, with the desired spectrum and electric field amplitude. In section 3.1, a monochromatic Langmuir wave of wavelength λ_L and amplitude E_L is resonantly excited by the external electric field pump by defining $E_{\text{ext}}^{\text{init}} = E_{\text{ext}}^{(1)}$:

$$E_{\text{ext}}^{(1)}(x,t) = E_0^{(1)}(t)\ \cos(k_0 x - \omega_0 t). \quad \text{(B1)}$$

In section 3.2, a Langmuir wave packet of mean wavelength λ_L, packet width Δ and maximum amplitude E_L is resonantly excited by defining $E_{\text{ext}}^{\text{init}} = E_{\text{ext}}^{(2)}$.

$$E_{\text{ext}}^{(2)}(x,t) = E_0(t)\ \cos(k_0 x - \omega_0 t)\ \exp\left(-\left(\frac{x - x_0 - v_L^g t}{0.5\Delta}\right)^2\right). \quad \text{(B2)}$$

In both cases, the pump wave vector $k_0 = 2\pi/\lambda_L$ and the frequency $\omega_0 = \sqrt{1 + 3k_0^2}$ are chosen to satisfy the Langmuir dispersion relation, in order to generate a Langmuir wave at the desired wavelength λ_L. The width of the wave packet is set to $\Delta = 10\ \lambda_L$. The pump wave packet moves at the Langmuir group velocity $v_L^g = 3k_0/\omega_0$ from its initial position $x_0 = L_x/3$. The time-dependant external electric field amplitude $E_0(t)$ scales on the desired Langmuir amplitude E_L:

$$E_0^{(1)}(t) = \eta E_L(1 - \exp(-t/\tau)). \quad \text{(B3)}$$

In the monochromatic case (wave packet case, respectively), the parameter τ is set to 30 ω_{pe}^{-1} (100 ω_{pe}^{-1}, respectively) so that the external electric field amplitude smoothly increases during a few Langmuir oscillations, in order to avoid the generation of other plasma waves induced by steplike switch of the pump. The parameter η is set experimentally to 5×10^{-2} (10^{-2}, respectively), so that the characteristic time scale to resonantly grow the Langmuir wave (wave packet, respectively) is large compared to its oscillation time scale, but small compared to the decay time scale. So, the resonant generation of the Langmuir wave (wave packet, respectively) does not interfere with the LED mechanism.

[59] **Acknowledgments.** We are grateful to the Italian supercomputing center CINECA (Bologna), where part of the calculations were performed. We also acknowledge C. Cavazzoni for discussion on code performance.

[60] Philippa Browning thanks Takayuki Umeda and another reviewer for their assistance in evaluating this manuscript.

References

Akimoto, K., Y. Omura, and H. Matsumoto (1996), Rapid generation of Langmuir wave packets during electron beam-plasma instabilities, *Phys. Plasmas*, *3*, 2559.

Bale, S. D., D. Burgess, P. J. Kellogg, K. Goetz, R. L. Howard, and S. J. Monson (1996), Phase coupling in Langmuir wave packets: Possible evidence of three-wave interactions in the upstream solar wind, *Geophys. Res. Lett.*, *23*, 109.

Bardwell, S., and M. V. Goldman (1976), Three-dimensional Langmuir wave instabilities in type III solar radio bursts, *Astrophys. J.*, *209*, 912.

Bougeret, J. L., et al. (2007), S/WAVES: The Radio and Plasma Wave Investigation on the STEREO Mission, *Space Sci. Rev.*, *136*, 487.

Cairns, I. H., and P. A. Robinson (1992), Theory for low-frequency modulated Langmuir wave packets, *Geophys. Res. Lett.*, *19*, 2187.

Cairns, I. H., and P. A. Robinson (1995), Ion acoustic wave frequencies and onset times during type III solar radio bursts, *Astrophys. J.*, *453*, 959.

Celnikier, L. M., L. Muschietti, and M. V. Goldman (1987), Aspects of interplanetary plasma turbulence, *Astron. Astrophys.*, *181*, 138.

Dulk, G. A., M. V. Goldman, J. L. Steinberg, and S. Hoang (1987), The speeds of electrons that excite solar radio bursts of type III, *Astron. Astrophys.*, *173*, 366.

Dysthe, K. B., and R. N. Franklin (1970), Non-linear interactions of coherent electrostatic plasma waves, *Plasma Phys.*, *12*, 705.

Gibson, S. E., D. L. Newman, and M. V. Goldman (1995), Langmuir turbulence and three-wave nonlinear dynamics, *Phys. Rev. E*, *52*, 558.

Ginzburg, V. L., and V. V. Zheleznyakov (1958), On the possible mechanisms of sporadic solar radio emission (radiation in an isotropic plasma), *Soviet Astron.*, *2*, 653.

Goldman, M. V., D. L. Newman, J. G. Wang, and L. Muschietti (1996), Langmuir turbulence in space plasmas, *Phys. Scripta*, *63*, 28.

Harvey, C. C., L. Celnikier, and D. Hubert (1988), Results from the ISEE propagation density experiment, *Adv. Space Res.*, *8*, 185.

Henri, P., C. Briand, A. Mangeney, S. D. Bale, F. Califano, K. Goetz, and M. Kaiser (2009), Evidence for wave coupling in type III emissions, *J. Geophys. Res.*, *114*, A03103, doi:10.1029/2008JA013738.

Hoang, S., G. A. Dulk, and Y. Leblanc (1994), Interplanetary type 3 radio bursts that approach the plasma frequency: ULYSSES observations, *Astron. Astrophys.*, *289*, 957.

Hospodarsky, G. B., and D. A. Gurnett (1995), Beat-type Langmuir wave emissions associated with a type III solar radio burst: Evidence of parametric decay, *Geophys. Res. Lett.*, *22*, 1161.

Huang, Y., and G.-L. Huang (2008), Solar type III bursts and the generation of backward Langmuir wave, *Chin. Astron. Astrophys.*, *32*, 178.

Intrator, T., C. Chan, N. Hershkowitz, and D. Diebold (1984), Nonlinear self-contraction of electron waves, *Phys. Rev. Lett.*, *53*, 1233.

Henri et al. (2010)
submitted to PRL

Low energy Langmuir cavitons or the asymptotic limit of weak turbulence

P. Henri* and F. Califano†
Dip. Fisica, Università di Pisa; Largo Pontecorvo 3, 56127 Pisa, Italy and
LESIA, Observatoire de Paris, CNRS, UPMC, Université Paris Diderot; 5 Place Jules Janssen, 92190 Meudon, France

C. Briand‡ and A. Mangeney§
LESIA, Observatoire de Paris, CNRS, UPMC, Université Paris Diderot; 5 Place Jules Janssen, 92190 Meudon, France
(Dated: March 17, 2010)

Langmuir cavitons are coherent structures in equilibrium between the total kinetic pressure force and the ponderomotive force created by the high frequency Langmuir oscillations. They are characteristic of strong Langmuir turbulence and are widely thought to be generated at high energy and to saturate when the Langmuir energy is of the the order of the background plasma thermal energy. By using 1D-1V Vlasov-Poisson simulations, we show, first, that the long time evolution of Langmuir weak turbulence self-consistently generates ion cavitons, thus illustrating the breakdown of long time evolution Langmuir weak turbulence; second, such cavitons saturate at low energy (with an electric to kinetic energy ratio as low as three orders of magnitude), unlike the wide-spread belief that such structures saturate at higher energy ratios. This gives evidence that "large" and "shallow" stable cavitons also exist. Finally we show that Langmuir coherent structures much larger than the Debye length are generated by an initial "low" level of Langmuir turbulence.

PACS numbers: 52.35.Fp,52.25.Dg,52.35.Ra,52.65.-y

The transition between weak and strong turbulence regime is governed by the amplitude level of the fluctuations as well as the width of the spectrum [1–3]. At finite but small energy, the non linear dynamics of the waves is well described by three-waves or four-waves interactions in the random phase approximation through the kinetic wave equations, whereas at higher energies intermittency dominate the dynamics, through the apparition of coherent structures. Moreover, some range of scales may be described by the theory of weak turbulence while other ranges display the properties of strong turbulence. Since the coherent structures are regions where enhanced wave dissipation occurs, it could be expected that the asymptotic long time evolution of plasma turbulence be described by the weak turbulence theory.

In this letter we show that, contrary to this naive expectation, in the simple case of one dimensional Langmuir turbulence, an archetype of wave turbulence in plasma physics, the long time evolution of weak turbulence breaks out toward strong turbulence. Moreover, we show that the characteristic coherent structures of Langmuir strong turbulence, called cavitons, may saturate at "low" energy and remain relatively stable with electric energy three orders of magnitude lower than the thermal energy of the plasma, an energy range considered to belong to the weak Langmuir turbulence regime.

Langmuir cavitons are localized electric fields oscillating at the plasma frequency selfconsistently associated to density cavities [4]. The density depression is known to be in the range $0.01 < \delta n/n < 0.80$ [5]. They have been observed in several plasma experiments starting from Kim, Stenzel and Wong [6] and in ionospheric experiments [7]. However, the occurrence of strong Langmuir turbulence in natural space plasma environment has been ruled out because the coherent structures called cavitons are thought to saturate with electric energies of the order of the thermal energy and lengthscale of about $20-30\lambda_{_D}$. Cavitons at "high" energies have also been intensively studied through numerical experiments with Zakharov codes [8–11] and Vlasov codes [12–14]. For moderate forcing, it has been shown that weak turbulence and strong turbulence features can coexist [8].

We concentrate in this letter on low energy cavitons. We show that even in the "small" forcing regime weak turbulence can fully develop and break out on long time evolution toward strong turbulence behaviour through the formation of low energy cavitons, independently of the initial level of coherence of Langmuir oscillations. A power law governing the relation between the length scale of the structure and its energy is obtained, which could be directly tested on space plasma data. The depth of Langmuir cavitons scales as the electric to thermal energy ratio, as expected.

Long time Langmuir turbulence is here investigated through 1D-1V Vlasov-Poisson simulations in the electrostatic approximation. The Vlasov-Poisson system is solved for the 1D-1V electron and proton distribution function, $f_e(x,v,t)$, $f_p(x,u,t)$ and the self-consistent electric potential and electric field, ϕ and E. The equations are normalized by using the following characteristic electron quantities: the charge e, the electron mass m_e, the electron density n_e, the plasma (angular) frequency $\omega_{pe} = \sqrt{4\pi n_e e^2/m_e}$, the Debye length $\lambda_{_D} = \sqrt{T_e/4\pi n_e e^2}$, the electron thermal velocity $v_{th,e} = \lambda_{_D}\omega_{pe} = \sqrt{T_e/m_e}$ and an electric field $\bar{E} = m_e v_{th,e}\omega_{pe}/e$. The electric energy density (normalized to the electron kinetic energy), will be denoted by

$W_L = 0.5 \times E^2$. Then, the dimensionless equations for each species read:

$$\frac{\partial f_e}{\partial t} + v\frac{\partial f_e}{\partial x} - (E + E_{ext})\frac{\partial f_e}{\partial v} = 0 \quad (1)$$

$$\frac{\partial f_p}{\partial t} + u\frac{\partial f_p}{\partial x} + \frac{1}{\mu}E\frac{\partial f_p}{\partial u} = 0 \quad (2)$$

$$\frac{\partial^2 \phi}{\partial x^2} = \int f_e dv - \int f_p du \;\; ; \;\; E = -\frac{\partial \phi}{\partial x} \quad (3)$$

where v (resp. u) is the electron (resp. ion) velocity normalized to the electron thermal velocity, $\mu = m_p/m_e = 1836$ is the proton-to-electron mass ratio and E_{ext} an "external" driver added to the Vlasov equation that can be switched on or off during the runs.

We shall use a numerical box of length $L_x = 5000\ \lambda_D$, and a velocity range $-5 \leq v/v_{th,e} \leq +5$ (resp. $-5 \leq u/u_{th,i} \leq +5$) for the electrons (resp. protons). The spatial mesh grid spacing is $dx = \lambda_D$, while the velocity resolution is $dv = 0.04\ v_{th,e}$ (resp. $du = 0.04\ u_{th,i}$) for the electrons (resp. protons), $u_{th,i} = \sqrt{T_p/m_p}$ being the proton thermal velocity). Periodic boundary conditions are used in the spatial direction. The electron and proton velocity distribution functions are initially Maxwellian, with equal temperatures, $T_p = T_e$, so that ion acoustic fluctuations are very efficiently damped out. Note in particular that no electron beam is assumed to be present at $t = 0$. An initial random noise in density in the wavelength range $30 < \lambda < 500$ is also added.

Two different initial conditions are considered, (i) coherent and (ii) incoherent initial Langmuir waves. In both cases, the initial electric energy is $10^{-4} \lesssim W \lesssim 10^{-2}$, corresponding to the transition between weak and strong turbulence regime. In case (i), we generate a monochromatic Langmuir wave propagating in one direction only with a wavelength λ_L by resonance by introducing an "external" electric field E_{ext} in Eq 1 oscillating at the plasma frequency with the wavelength λ_L. The forcing is switched off when E reaches the amplitude E_L. The initial wave then evolves self consistently according to the Vlasov-Poisson system. The details of our external forcing for the generation of a Langmuir wave is given in Henri et al. [15, Appendix 1]. The amplitude of the Langmuir wave generated by the forcing is $2\times10^{-2} < E_L < 1.2\times10^{-1}$, corresponding to a Langmuir energy $2 \times 10^{-4} < W < 7.2 \times 10^{-3}$. This is a typical energy range of weak Langmuir turbulence regime. Finally, the initial random noise in density is $\delta n/n = 10^{-5}$. In case (ii), no initial coherent Langmuir wave is generated ($E_{ext} = 0$). Instead the system evolves starting with a relatively high level of random noise in electron density corresponding to a flat spectrum in the electric field. The r.m.s. electron density perturbation amplitude range is $10^{-3} \lesssim \delta n_e/n_e \lesssim 10^{-2}$, corresponding to a r.m.s. electric field $10^{-2} \lesssim E \lesssim 10^{-1}$.

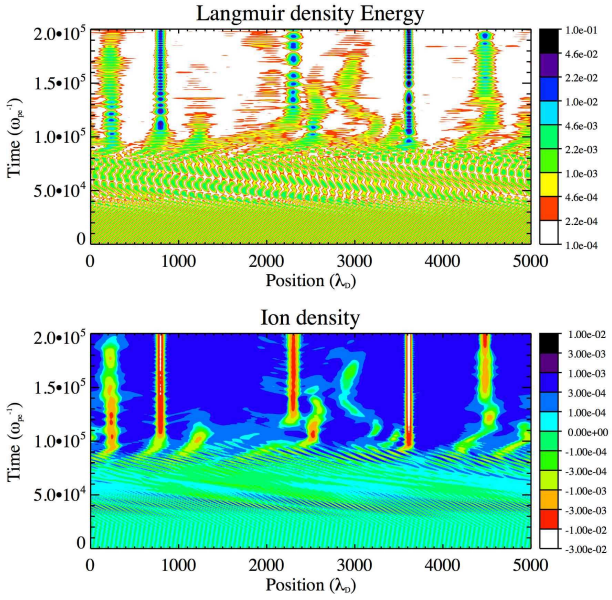

FIG. 1: Long time evolution of electric energy W_L (top panel) and ion density $\delta n/n$ (bottom panel), starting from a monochromatic Langmuir wave. Note in the ion density fluctuations the generation of (i) ion acoustic waves from the Langmuir electrostatic decay between $3 \times 10^4 < t < 6 \times 10^4$; (ii) ion cavities filled with electric energy for $t > 10^5$.

We first discuss the results of a simulation from the first series of numerical experiments, starting with a monochromatic Langmuir wave with $E_L = 0.06$ and $\lambda_L = 100\ \lambda_D$. The time evolution of both electric energy and ion density fluctuations are shown in Fig. 1. The initial Langmuir wave first undergoes electrostatic parametric instability (Langmuir electrostatic decay) during the period $3 \times 10^4 < t < 6 \times 10^4$. In the mean time,

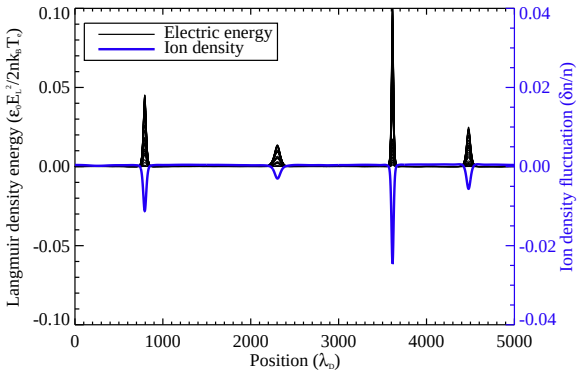

FIG. 2: Ion cavitons. Blue line: mean ion density fluctuations. Black lines: oscillations of trapped Langmuir waves, expressed in normalized electric energy W_L.

as expected, we observe the generation of associated ion acoustic fluctuations (bottom panel). Then, ion cavities start to form at $t \simeq 10^5$. The cavities are filled with electric energy (top panel) in the form of an electrostatic field oscillating at the plasma frequency, i.e. in the form of Langmuir waves. In Fig. 2 we show the spatial profile of these ion cavities. The blue line shows the ion density fluctuation $\delta n/n$ and the black lines show the profile of trapped Langmuir energy $W_{_L}$ for $t > 1.5 \times 10^5$. Ion cavities are shown in Fig. 3 to be in equilibrium between the total kinetic pressure force and the ponderomotive force created by the high frequency Langmuir oscillations. The ponderomotive force (red line) is defined as

$$F_{pond} = -\frac{e^2}{4m_i\omega_L^2}\frac{\partial E^2}{\partial x}$$

and the opposite of the total kinetic pressure force (black line) is defined by

$$F_{pressure} = -\nabla(P_e + P_i)$$

where the electron and ion pressure, P_e and P_i, are directly calculated from the distribution functions:

$$P_\alpha = \int_{-v_{max}}^{v_{max}} f_\alpha \times (v - \bar{v})^2 dv$$

for each species α. These coherent structures are thus identified as the so-called "cavitons", characteristic of strong Langmuir turbulence.

We have performed several simulations with different initial forcings, the initial Langmuir amplitude in case (i), and different values of the initial random noise in density in case (ii). In both cases, we let the system freely evolve until it eventually reaches the timescale for strong turbulence for which we observe the formation of Langmuir cavitons. We observe that the formation of cavitons does not need a high level of Langmuir waves, as soon as the system evolves for "long enough" times. In case (i) parametric decay occurs first and saturates in the first part of the simulation. Then cavitons are formed and remain stable until the end of the simulation $t = 10^5$. In case (ii) the initial electron density fluctuation rapidly self-organise into a large spectrum of Langmuir noise. The "sea" of Langmuir waves that fills the simulation box, then collapses toward stable low energy cavitons. In both cases the non linear structures are similar, which indicates that the asymptotic behavior of Langmuir turbulence is independent from the initial level of coherence of Langmuir oscillations. As expected, regardless of the initialization of the turbulence (i.e. in both (i) and (ii) cases), we find that the larger the initial Langmuir waves, the sooner Langmuir cavitons are generated. For each simulation, we isolate the cavitons, and measure the depth of the ion density hole $\delta n/n$, the length of the structure L (defined as the width of the ion cavity at the height of $1/e$ the maximum depth) and the maximum Langmuir electric energy $W_{_L}$ that sustains the density hole. Results are reported in Fig. 4 where each point represents a single caviton. Langmuir cavitons are observed with maximum Langmuir energy ranging over three decades. It is worth noticing that Langmuir cavitons are observed also at relatively low electric energy values, $W_{_L} \sim 10^{-3}$. The depth of the ion cavity, expressed in relative density $\delta n/n$, is of the order of the Langmuir electric density energy (as expected for high energy cavitons) over three decades:

$$\delta n/n = (\delta n/n)_{_0}\ W_{_L}^{\alpha} \qquad (4)$$

with $(\delta n/n)_{_0} = 0.28 \pm 0.06$ and $\alpha = 1.13 \pm 0.06$ the fitting parameters. Fit results are given with their respective $3-\sigma$ errors. The width of the cavitons (expressed in Debye length units) also scales on the Langmuir electric density energy:

$$L = L_{_0}\ W_{_L}^{\beta} \qquad (5)$$

with $L_{_0} = 18 \pm 4$ and $\beta = -0.47 \pm 0.05$. As expected, Langmuir cavitons have larger length scale when the Langmuir electric energy is lower. A very important result here is that cavitons of length scale of many hundred of Debye length are generated. As a direct consequence of Eq 4 and 5 we can deduced the power law between the depth and the length of the ion cavities associated with the cavitons:

$$L = L_{_0}\ (\delta n/n)^{\gamma} \qquad (6)$$

with $L_{_0} = 10 \pm 3$ and $\gamma = -0.42 \pm 0.05$.

The typical depth of the ion cavities is of the order of the Langmuir electric energy. This result, well known at higher energy levels, has been extended at lower energy and is verified on three order of magnitude. The length

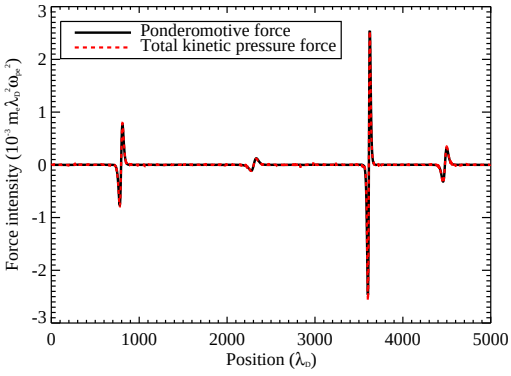

FIG. 3: Equilibrium of Langmuir cavitons. The ponderomotive force (black line) compensates the pressure gradient (red line).

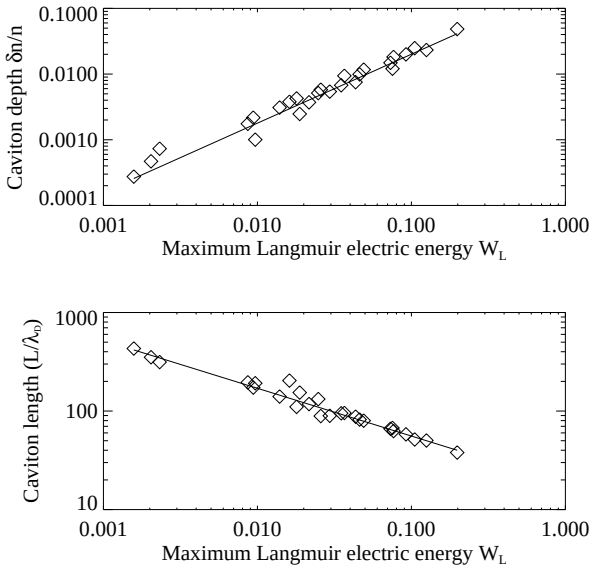

FIG. 4: Depth expressed in relative density $\delta n/n$ (top panel) and width L expressed in Debye length (bottom panel) of cavitons according to their Langmuir energy $W_{_L}$. Each diamond represents a single caviton. The line shows the power law fit.

scale of the Langmuir cavitons is shown to scale as the inverse square root of its electric energy. Interestingly, the scaling laws found for low energy cavitons (Eq. 5, 4, 6) are similar to the scaling laws that describe the depth and length of Langmuir solitons [16]. It is worth to underline that we are studying here the so-called Langmuir cavitons, also called by some authors Langmuir *standing* solitons. The two kinds of coherent structures, Langmuir solitons and Langmuir cavitons, have different equilibria. Langmuir solitons are propagating structures maintaining their shape through the balance between dispersive and nonlinear effects, whereas cavitons are standing structures with electric oscillations that self-consistently sustain the density cavity of which they are eigenmodes.

By using Vlasov simulations, characterized by a very low level of numerical noise even during the non linear regime, we have shown that the coherent structures called Langmuir cavitons, characteristic of strong Langmuir turbulence, also appear during the long time evolution of moderate amplitude Langmuir oscillations. The corresponding energetic range of initial Langmuir perturbations $W_{_L} \sim 10^{-4} - 10^{-3}$, as well as the energy of the largest stable cavitons $W_{_L} \sim 10^{-3}$, are typically considered to belong to the so-called weak Langmuir turbulence regime. The distinction between weak and strong turbulence thus loose part of its signification on long time evolution of moderate amplitude Langmuir oscillations. This result is independent from the initial level of Langmuir waves coherence. The formation of Langmuir cavitons appears to be the asymptotic limits of weak turbulence. We confirm that wave turbulence is expected to breakdown for times larger than the typical non linear time scale [17, 18].

We have shown that electrostatic coherent structures of typical dimension much greater that a few Debye length are produced by the long time evolution of an initial relatively moderate amplitude turbulence. This result can have an important impact on the interpretation of space plasma spacecraft data. We are thus confident that these new insight in Langmuir turbulence may encourage the space physics community to revisit the admitted conclusion that strong turbulent Langmuir structures are formed at too high energy to be relevant in space plasma environments.

We are grateful to the italian super-computing center CINECA (Bologna) where part of the calculations where performed. We also acknowledge Dr. C. Cavazzoni for discussions on code performance.

* pierre.henri@obspm.fr
† califano@df.unipi.it
‡ carine.briand@obspm.fr
§ andre.mangeney@obspm.fr

[1] R. Z. Sagdeev and A. A. Galeev, *Nonlinear Plasma Theory* (New York: Benjamin, 1969).
[2] P. A. Robinson, Reviews of Modern Physics **69**, 507 (1997).
[3] M. V. Goldman, Reviews of Modern Physics **56**, 709 (1984).
[4] V. E. Zakharov, Soviet Journal of Experimental and Theoretical Physics **35**, 908 (1972).
[5] A. Y. Wong, Journal de Physique **38**, 6 (1977).
[6] H. C. Kim, R. L. Stenzel, and A. Y. Wong, Physical Review Letters **33**, 886 (1974).
[7] A. Y. Wong, T. Tanikawa, and A. Kuthi, Physical Review Letters **58**, 1375 (1987).
[8] D. F. Dubois, H. A. Rose, and D. Russell, Physical Review Letters **66**, 1970 (1991).
[9] P. Guio and F. Forme, Physics of Plasmas **13**, 122902 (2006).
[10] B. Eliasson and B. Thidé, Journal of Geophysical Research (Space Physics) **113**, 2313 (2008).
[11] G. D. Doolen, D. F. Dubois, and H. A. Rose, Physical Review Letters **54**, 804 (1985).
[12] J. G. Wang, G. L. Payne, D. F. Dubois, and H. A. Rose, Physics of Plasmas **3**, 111 (1996).
[13] J. G. Wang, D. L. Newman, and M. V. Goldman, Journal of Atmospheric and Solar-Terrestrial Physics **59**, 2461 (1997).
[14] N. J. Sircombe, T. D. Arber, and R. O. Dendy, Physics of Plasmas **12**, 012303 (2005).
[15] P. Henri, F. Califano, C. Briand, and Mangeney, *in press*, Journal of Geophysical Research (Space Physics) (2010).
[16] M. V. Nezlin (Moscow: Energoizdat, 1982).
[17] L. Biven, S. V. Nazarenko, and A. C. Newell, Physics Letters A **280**, 28 (2001).
[18] L. J. Biven, C. Connaughton, and A. C. Newell, Physica D Nonlinear Phenomena **184**, 98 (2003).

Appendices

Appendix A

STEREO Mission

The Solar TErrestrial RElations Observatory (STEREO) mission was launched on October 26, 2006. It is composed of two identical spacecraft (Fig. A.1). Both spacecraft have an heliocentric orbit in the ecliptic plane at nearly 1 Astronomical Unit (AU) [*Kaiser et al.*, 2007]. The "ahead" spacecraft (hereafter STEREO A) being slightly closer from the sun, it has a shorter orbital period than the Earth and hence drifts ahead of the Earth (at an average rate of approximately 22° per year), while the "behind" spacecraft (hereafter STEREO B) is in a slightly larger orbit. As a result, STEREO A travels faster than STEREO B so that, viewed from the Sun, the two spacecraft separates at an average of 45° per year.

The principal mission objective for STEREO is to understand the origin and consequences of Coronal Mass Ejections, the most energetic eruptions on the Sun [*Driesman et al.*, 2007]. In this purpose, the STEREO observatory carries four complementary scientific instruments:

- the Sun-Earth Connection Coronal and Heliospheric Investigation (SECCHI) experiment combines a suite of five optical telescopes that images the Sun and the heliosphere up to Earth orbit. It consists of three types of telescopes: two white light coronagraphs, an extreme ultraviolet imager and two heliospheric white light imagers [*Howard et al.*, 2008].
- the In situ Measurements of PArticles and CME Transients (IMPACT) experiment focuses on in situ observations of energetic particles: it measures in situ solar wind electrons, energetic electrons, protons and heavier ions [*Luhmann et al.*, 2008]. IMPACT also includes a magnetometer to measure the in situ magnetic field strength and direction. [*Acuña et al.*, 2007].
- the PLAsma and SupraThermal Ion Composition (PLASTIC) experiment measures the composition of heavy ions in the ambient plasma as well as protons and alpha particles [*Galvin et al.*, 2008].

- the STEREO/WAVES (S/WAVES) experiment consists of three radio receivers (fixed, high and low frequency receivers) that track electromagnetic disturbances through the heliosphere and a time domain sampler that measures in-situ electric waveforms. It is described in the next section.

The S/WAVES instrument, build by a team led by the Observatoire de Paris and the University of Minnesota, is designed to be an interplanetary radio burst tracker that observes the generation and evolution of traveling radio disturbances from the Sun to the orbit of Earth [*Bougeret et al.*, 2008]. S/WAVES has inherited from the experience gain from WIND/WAVES, a previous similar instrument mounted on the WIND spacecraft (1994). Among the questions regarding the Type II and Type III radio emission listed in *Bougeret et al.* [2008] at the beginning of the STEREO mission, I tackled during my Ph.D. the following ones:

- What is the mechanism of coupling between Langmuir waves and radio waves?
- What are the roles of linear and nonlinear processes in the evolution of Langmuir waves and the production of type II and III radiation?

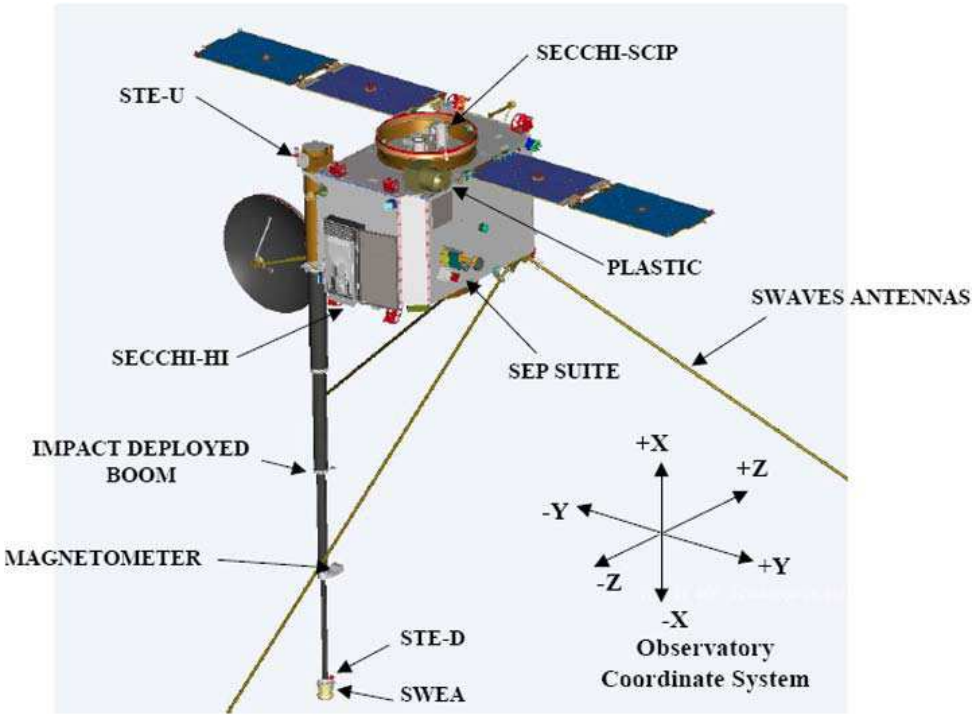

Figure A.1: Illustration of spacecraft B in its deployed configuration. The SECCHI instruments point at the Sun and the IMPACT boom and SWAVES antennas are on the opposite end. For scale, the large vertical boom (IMPACT boom) is approximately 6 m long. Source: *Driesman et al.* [2007]

S/WAVES use three mutually orthogonal wire antenna, each 6 meters long, with an effective length of about 1 meter. Details on the electric antenna system of the S/WAVES instrument can be found in *Bale et al.* [2008]. The S/WAVES instrument is composed of the following receivers:

- Radio receivers (HFR and LFRhi) that measure radio wave intensity, source direction, and angular size in the frequency range of 16 MHz to 40 kHz, corresponding to source distances of about 1 Solar Radius to 1 AU;
- Low Frequency Receivers (LFRlo) that make measurements of radio and plasma waves near the electron plasma frequency at 1 AU (2.5 to 40 kHz);
- a Fixed Frequency Receiver (FFR) that measures radio emissions at 32 - 34 MHz at high time resolution to complement ground-based radio-heliograph measurements;
- a Time Domain Samplers (TDS) that simultaneously make wideband waveform measurements on three electric antennas at one of several commandable sample rates and bandwidths.

Two modes of observation are thus available: (i) remote observation and measurement of radio waves to follow the propagation of the radiosources in the heliosphere with three spectral radio receivers and (ii) *in situ* measurement of electric waveforms with the Time Domain Sampler mode (hereafter TDS).

This last mode produces rapid samples of electric field waveforms and is primarily intended for the study of Langmuir waves. Data from this observation mode are the ones I have principally used to produce this work.

Appendix B

Using the STEREO spacecraft as a density probe.

The measured voltage on an electric filed antenna, used in monopole mode, is the difference between the antenna potential and the spacecraft floating potential. The spacecraft floating potential is usually considered a ground to study electric field oscillations measured on the antenna. We show here how the fluctuation of the spacecraft potential can be used to study density fluctuations[1].
These are the successive steps. After recalling some basics concerning spacecraft charging in the solar wind, I give the explicit dependence of the spacecraft potential on the solar wind plasma density. I then discuss the frequency range for which density fluctuations modify the spacecraft potential, producing a signature on the antenna in monopole mode. Finally, I compute the variation of spacecraft potential associated with a given fluctuation of the solar wind plasma density. I will also show how the nonlinear theory on Langmuir ponderomotive effect can constrain the value of the photoelectron temperature.

Spacecraft charging

In the solar wind, the body of a spacecraft emits and collects charged particles. Its electric potential permanently adjusts to the variation of the ambient plasma parameters, in order to ensure currents balance [*Pedersen*, 1995]. The currents affecting the spacecraft potential result from:

1. The photoelectron current I_{ph}. Photoelectrons emitted from the spacecraft by solar ultraviolet radiation. The average solar ultraviolet radiation at 1 AU is $\sim 10^{-3}\ W.m^2$ corresponds to an average flux of ionising photons $F_\odot \simeq 10^{14}\ m^{-2}sec^{-1}$. On a surface

[1]I acknowledge the help and guidance of Nicole Meyer-Vernet (LESIA, Observatoire de Paris) for this investigation.

at zero potential at 1 AU, the photoemission flux j_{ph} depends on the average surface photoemission efficiency:

$$j_{ph} = \delta \ 10^{14} \ \mathrm{m}^{-2}\mathrm{sec}^{-1}$$

per unit of projected sunlit surface, with $\delta \sim 1 - 4$ for typical spacecraft covers [*Pedersen*, 1995; *Escoubet et al.*, 1997; *Scudder et al.*, 2000; *Pedersen et al.*, 2008]. Photoelectrons escape from the sunlit face of the spacecraft of surface $S_\perp$, so that $I_{ph} = j_{ph} S_\perp$.

2. The collected solar wind electron current I_e. Solar wind electrons have a thermal velocity ($v_{th,e} \simeq 1200$ km.sec^{-1}) larger than the solar wind speed ($v_{th,e} \simeq 300 - 800$ km.sec^{-1}), so that (i) the associated incoming electron flux on a spacecraft at zero potential is the ambient electron random flux:

$$j_e \simeq n_e \sqrt{kT_e/2\pi m_e} < 10^{13} \ \mathrm{m}^{-2}\mathrm{sec}^{-1}$$

where m_e, n_e and T_e are respectively the electron mass, density and temperature; and (ii) solar wind electron are collected on the total surface S_{tot} so that $I_e = j_e S_{tot}$.

3. The collected solar wind proton current I_p. Conversely, solar wind protons have a thermal velocity ($v_{th,p} \simeq 50$ km.sec^{-1}) much smaller than the solar wind speed, so that (i) solar wind protons are collected on one face only, (ii) the associated attachment flux is better estimated from the mean proton flux $j_p \simeq n_p V_{SW} \sim 10^{12}$ m^{-2}sec^{-1}. With $S_{tot} \simeq 6 \ S_{perp}$, the proton current is more than an order of magnitude lower than the proton current $I_p = j_p S_{perp} << j_e S_{tot} = I_e$.

To summarize, the different currents affecting the spacecraft charging in the solar wind are classified as follow:

$$I_{ph} >> I_e >> I_p$$

In the solar wind, the main charging currents are due to the emission of photoelectrons I_{ph}, and to the collection of ambient plasma electrons, I_e. We neglect here the smaller proton current and the secondary emission of electrons.

Since the outward photoelectron current is much greater than the incoming electron current, the surface charges positively, until its positive electric potential Φ binds sufficiently the photoelectrons to make their net outward flux balance the inward flux of solar wind electrons. To do so, the potential must provide the photoelectrons with a potential energy that outweights their typical kinetic energy of a few eV. Hence, the equilibrium potential is a few volts positive. Making the assumption that both solar wind electrons and photoelectrons populations are Maxwellian with temperature T_e and T_{ph} respectively, the ejected photoelectron current I_{ph} and the incoming plasma electron current I_e on a surface at positive potential Φ are respectively given by [*Meyer-Vernet*, 2007, pp. 352-355]:

$$I_{ph} \simeq j_{ph} \ eS_\perp \left(1 + \frac{e\Phi}{k_B T_{ph}}\right)^\alpha \ \exp\left(\frac{-e\Phi}{k_B T_{ph}}\right) \tag{B.1}$$

$$I_e \simeq n_e \Big(\frac{k_B T_e}{2\pi m_e}\Big)^{1/2} eS \left(1 + \frac{e\Phi}{k_B T_e}\right)^{\beta} \tag{B.2}$$

where e is the electron charge, $S_\perp$ and S are respectively the sunlit projected surface and the total surface collecting ambient plasma electrons. α and β are parameters depending on the geometry of the surface relatively to the considered charging process: α and β are both equal to zero, 1/2 and 1 for respectively plan, cylindrical and spherical geometries. We now consider quasi-neutrality of the solar wind plasma, which holds for frequencies much lower than the plasma frequency, so that the electron density n_e is a tracer for the proton density $n_p = n_e$, hereafter called n.

Equilibrium potential

Let us first evaluate the equilibrium potential of the spacecraft surface. Since the length scale of the spacecraft body ($\sim$ 1 m) is larger than the photoelectrons Debye length ($\sim$ 0.1 m), the photoemission process is considered to occur on a plane geometry, so that $\alpha_{SC} = 0$. On the other hand, since the length scale of the spacecraft body is smaller than the solar wind electrons Debye length ($\sim$ 10 m), the plasma electrons are collected in 3D so that $\beta_{SC} = 1$. The current balance condition $I_{ph} = I_e$ applied to Eqs.(B.1)-(B.2) for the spacecraft body then gives the equilibrium spacecraft potential Φ_{SC} solution of:

$$\exp\left(\frac{-e\Phi_{SC}}{k_B T_{ph}}\right) = \frac{n}{N_0}\left(1 + \frac{e\Phi_{SC}}{k_B T_e}\right) \tag{B.3}$$

$$\text{where} \qquad N_0 = j_{ph}\left(\frac{k_B T_e}{2\pi m_e}\right)^{-1/2} \frac{S_\perp^{sp}}{S^{sp}}$$

The previous discussions on surface charging also hold for the equilibrium potential of the antenna, Φ_A, in cylindrical geometry, so that $\alpha_A = \beta_A = 0.5$. Eqs.(B.1)-(B.2) then give Φ_A through:

$$\exp\left(\frac{-e\Phi_A}{k_B T_{ph}}\right) \simeq \frac{n}{N_0^{ant}}\left(\frac{1 + \frac{e\Phi_A}{k_B T_e}}{1 + \frac{e\Phi_A}{k_B T_p h}}\right)^{1/2} \tag{B.4}$$

$$\text{where} \qquad N_0^{ant} = j_{ph}\left(\frac{k_B T_e}{2\pi m_e}\right)^{-1/2} \frac{S_\perp^{ant}}{S^{ant}}$$

Eq (B.4) is a rough approximation because the antenna length is of the order of the Debye length.

Equations (B.3) and (B.4) are solved numerically by considering the following parameters:

- The STEREO spacecraft body has the following dimensions $L_1 \times L_2 \times L_3 = 1.14 \times 1.22 \times 2.03$ meters [*Kaiser et al.*, 2007]. The sunlit surface is $S_{\perp}^{sp} = L_2 \times L_3 \simeq 2.5\, m^{-2}$. Because the electron thermal velocity is higher than the solar wind speed, solar wind electrons can charge the spacecraft from all its surface – except the spacecraft face opposite to the sun that is in the proton wake [2]. The total surface is thus about $S^{sp} \simeq 9.9\ m^{-2}$.
- S/WAVES antennas are approximately 6 m long, with a tip diameter of 15.2 mm and a base diameter of 32 mm, and are inclined by 125^o with respect to the sun-spacecraft direction [*Bale et al.*, 2008]. This gives a sunlit projected surface of about $S_{\perp}^{ant} = 0.12\ m^{-2}$ and a total surface area of about $S_{tot}^{ant} = 0.45\ m^{-2}$.

Solutions of Eqs. (B.3) and (B.4) are especially sensitive to the value of the photoelectron temperature. Various authors have evaluated it in the range $T_{ph} \simeq [1-4] \times 10^4$ K for different spacecraft covers and phases of the solar cycle [*Pedersen*, 1995; *Escoubet et al.*, 1997; *Scudder et al.*, 2000; *Pedersen et al.*, 2008].
I will later show that by applying the current calibration to density fluctuations generated by the non-linear evolution of Langmuir waves in the solar wind, and especially in the foreshock region, I constraint the temperature of photoelectrons emitted by the STEREO spacecraft at $T_{ph} \simeq 3$ eV.
Even though the temperature of the photoelectrons emitted by the STEREO spacecraft cover and its antennas might not to be the same, we will hereafter assume the same value to estimate the charging time scale of the antenna. Anyway, this will not modify our final calibration of $\delta n/n$ in function of $\delta\Phi_{sp}$ (Eq. B.6).

The value of the antenna and spacecraft potential obtained Eqs. (B.3) and (B.4) are shown in Fig. B.1 for $T_e = 10$ eV and $T_{ph} = 3eV$. The spacecraft potential at equilibrium for typical plasma densities $n = [1-10]\ cm^{-3}$ is typically $\Phi_{SC} = [3-8]$ Volts and the antenna potential is in the range $\Phi_A = [5-10]$ Volts.

Charging time scale

These evaluations of the equilibrium potentials hold as long as the solar wind density fluctuates with frequencies lower than the typical charging frequency of the considered object, so that the equilibrium remains quasistatic. Conversely, density fluctuations at frequencies higher than the charging frequency of the object will scarcely modify the potential.
I now concentrate on density fluctuations that produce a quasistatic fluctuation of the spacecraft floating potential *without modifying the antenna potential*, i.e. on density fluctuations observed at frequencies $f_{\delta n}$ such that

$$f_A < f_{\delta n} < f_{SC}$$

[2] The spacecraft face opposite to the sun is thus embedded in an high electric field repelling solar wind electrons of the bulk.

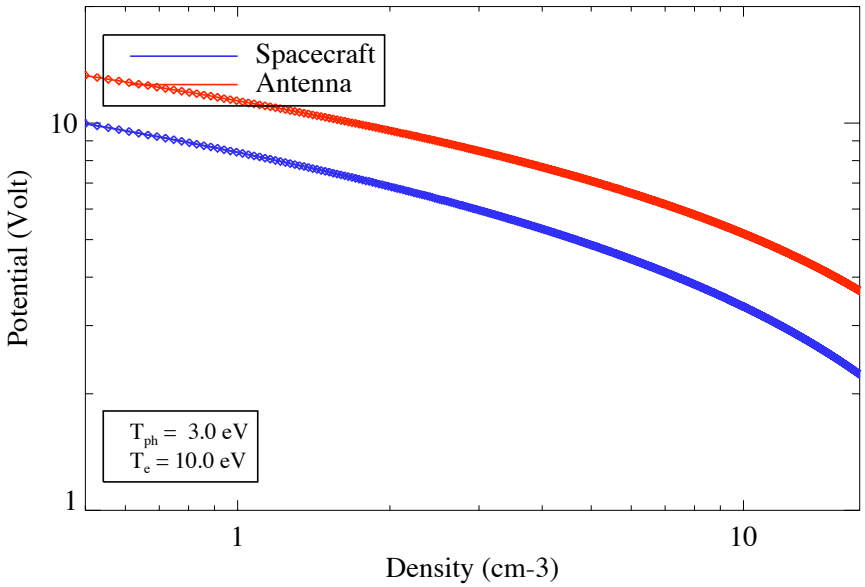

Figure B.1: Values of spacecraft (blue line) and antenna (red line) equilibrium potential for typical solar wind densities $[1-10]$ cm^{-3} at $T_e = 10$ eV and $T_{ph} = 3$ eV.

where $f_{_A}$ (resp. $f_{_{SC}}$) is the charging frequency of the antenna (resp. spacecraft).
I now evaluate these two frequencies by considering the respective charging e-folding times$\tau = RC$, with C the capacitance and R the resistance evaluated as follows.

The typical dimension of the spacecraft $L_{_{SC}}$ and the antenna radius a are both much smaller than the ambient Debye length λ_D, so that the electric field surrounding them can be considered a Coulomb field in their vicinity, vanishing at distance λ_D. The spacecraft capacitance $C_{_{SC}}$ is evaluated as the capacitance of a spherical conductor of radius $L_{_{SC}} = 1$ m at potential $\Phi_{_{SC}}$ and outer radius $\lambda_{_D}$ at potential zero:

$$C_{_{SC}} \simeq 4\pi\epsilon_0 L_{_{SC}} \simeq 110 \text{ pF}$$

and the antenna capacitance $C_{_A}$ is evaluated as the low frequency capacitance of a cylindrical conductor of length L and radius a in a plasma of Debye length $\lambda_{_D}$ [*Meyer-Vernet and Perche*, 1989]. In the limit $L >> \lambda_{_D}$ the antenna capacitance is:

$$C_{_A} \simeq \frac{2\pi\epsilon_0\ L}{ln(\lambda_{_D}/a)} \simeq 47 \text{ pF}$$

whereas for $L << \lambda_{_D}$ it reduces to:

$$C_{_A} \simeq \frac{2\pi\epsilon_0\ L}{ln(L/a) - 1} \simeq 64 \text{ pF}$$

In the case of STEREO, the low frequency antenna capacitance is between those two values $C_{_A} \simeq 60$ pF.

The resistance $R = 1/(dI/d\Phi)$ simplifies to $R \simeq -1/(dI_{ph}/d\Phi)$, since the photoelectron current is the fastest charging process [*Meyer-Vernet*, 2007]. From Eq. B.1 and the respective parameters α, the spacecraft (resp. antenna) resistance R_{SC} (resp. R_A) read:

$$\begin{aligned} R_{SC}^{-1} &= j_{ph} e S_{\perp}^{sp} \frac{e}{k_B T_{ph}} \exp\left(\frac{-e\Phi_{SC}}{k_B T_{ph}}\right) \\ R_A^{-1} &= j_{ph} e S_{\perp}^{ant} \frac{e}{k_B T_{ph}} \left(1 + \frac{e\Phi_A}{k_B T_{ph}}\right)^{1/2} \\ &\quad \times \left[1 - \frac{1}{2}\left(1 + \frac{e\Phi_A}{k_B T_{ph}}\right)^{-\frac{1}{2}}\right] \exp\left(\frac{-e\Phi_A}{k_B T_{ph}}\right) \end{aligned}$$

The spacecraft (resp. antenna) charging frequency $f_{SC} = 1/(2\pi R_{SC} C_{SC})$ (resp. $f_A = 1/(2\pi R_A C_A)$) are solved numerically. Their value mostly depend on the plasma density, through the dependence in Φ, and the value of the photoelectrons temperature, as seen in Fig.B.2. As explained earlier, the photoelectron temperature will be constrained around 3 eV (vertical dotted line in the third panel).

Density fluctuations with frequencies between ~ 100 Hz and a few kHz produce a change in spacecraft potential but no change in antenna potential; such signal can be observed on an antenna in monopole mode. Signals of much higher frequency vary too fast for changing the floating potential of the spacecraft and antennas. Signals of much smaller frequency change similarly the floating potentials of the spacecraft and antennas, so that the difference barely changes and should not be observed on the monopole antenna.
Note that (i) the previous discussion hold for signals observed on a monopole antenna and created by density fluctuations only, whereas electric field oscillations behave just opposite: the spacecraft potential is a ground and the potential antenna oscillate with

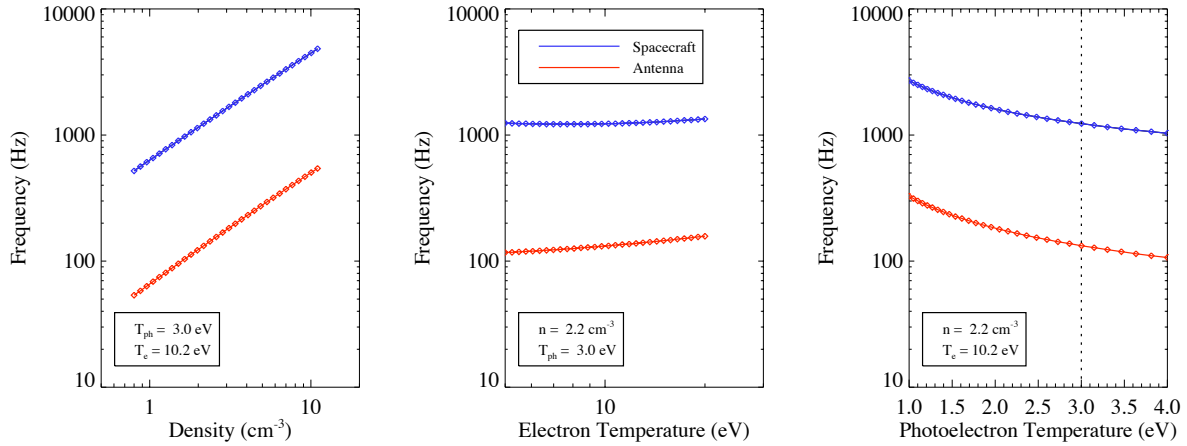

Figure B.2: Frequency transition above which the variation of equilibrium potential of the spacecraft (blue line) and antenna (red line) remains quasistatic. Left to right panels: variations with density, electron temperature and photoelectron temperature. The vertical dotted line in the third panel indicates the photoelectron temperature associated with the STEREO spacecraft $T_{ph} = 3$ eV.

the electric field; (ii) the TDS pass-band filter has its own low frequency cut-off at ~ 100 Hz so that signals of lower frequency should be considered with caution.

Density fluctuations and associated variations of spacecraft potential

A small variation in plasma density δn in the frequency range [100 Hz − 1 KHz] produces a change in spacecraft potential $\delta\Phi_{SC}$ obtained by differentiating Eq. B.3:

$$\delta n/n = -\left(\frac{e}{k_B T_{ph}} + \frac{e}{k_B T_e}\frac{1}{1+\frac{e\Phi_{SC}}{k_B T_e}}\right)\delta\Phi_{SC} \tag{B.5}$$

which contains an implicit dependence on both the plasma density and the spacecraft collecting surfaces in the term Φ_{SC} (Eq. B.3). Since $T_{ph} << T_e$, $\delta n/n$ is mainly determined by the first term in Eq. B.5, so that it is roughly proportional to $\delta\Phi_{SC}$ with a proportional factor determined by T_{ph}. This is confirmed by solving numerically Eq. B.5 to give the density fluctuation $\delta n/n$ associated with a variation $\delta\Phi_{SC}$ of the spacecraft floating potential when varying the mean density, the solar wind electron temperature and the photoelectron temperature, as shown in Fig. B.3. Note that the variation of STEREO spacecraft potential induced when encountering a fluctuation of density hardly depends on the background plasma density (top panel), neither on the electron temperature (medium panel) in the typical range of solar wind plasma parameters. Conversely, this calibration of the level of density fluctuation mostly depend on the value of photoelectrons temperature, we keep this in mind in order to later constrain T_{ph} from observations.

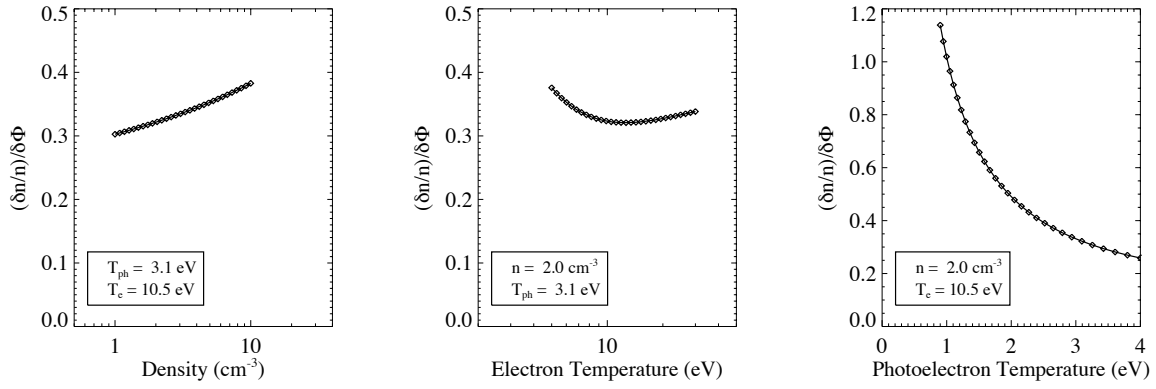

Figure B.3: Ratio of the relative density variation $\delta n/n$ to the variation of spacecraft potential with respect to density, electron temperature and photoelectron temperature (Left to right panels).

Finally, a change in spacecraft potential $\delta\Phi_{SC}$ then corresponds to a variation of the plasma density $\delta n/n$:

$$\boxed{\boldsymbol{\delta n/n \simeq \frac{1}{T_{ph}[eV]}\,\delta\Phi_{SC}[Volt]}} \tag{B.6}$$

which is identically detected on all monopole antenna channels[3].

Validation of the analysis

We now motivate the choice of the photoelectron temperature $T_{ph} = 3\ eV$. The maximum level of spacecraft potential fluctuations and the maximum Langmuir energy is plotted for each waveform in Fig. B.4. We recall that the expected saturation level of density fluctuations generated by non linear Langmuir evolution is $\delta n/n = W_L$ [*Sagdeev and Galeev*, 1969]. The dotted lines shows the level of spacecraft potential fluctuations corresponding to such level of density fluctuations $\delta n/n = W_L$ by using Eq. B.6 with different values of the photoelectron temperature $T_{ph} = 1\ eV$, $3\ eV$ and $5\ eV$. The observed level of spacecraft potential fluctuations is consistent with $T_{ph} = 3\ eV \pm 1\ eV$. This is thus consistent with previously published values, all in the range $T_{ph} = [1 - 3]$ eV, as well as self-consistent with the expected saturation level of density fluctuations generated by non linear Langmuir evolution.

The typical noise level on S/WAVES monopole antenna channel is about 0.1 mV, which means that both (i) Langmuir waves with electric energy $W_L > 10^{-7}$ and (ii) density fluctuation with $\delta n/n > 10^{-4}$ can be observed (3σ above the noise). However, the selection criteria that controls the choice of telemetered events favors the highest voltage events, higher amplitude Langmuir waves will thus be preferentially telemetered.

Finally, we stress that the no correlation is found between the previously described low frequency signals interpreted as fluctuations of the spacecraft potential and the high amplitude Langmuir electric field measured on each separate monopole antenna channel. This important point allows to discard the hypothesis that the low frequency signals observed on STEREO would be generated by either antennas sheath rectification [*Boehm et al.*, 1994; *Stasiewicz et al.*, 1996] or non linear artifacts from the TDS receivers.

[3]Note that Eq. B.3 could have been fairly approximate by $\Phi \simeq (k_B T_{ph}/e)\ \ln[N_0/n]$ when considering that the dependence of Φ_{SC} in the logarithm is negligible. This straightforwardly leads to the variation of spacecraft potential induced by a small variation in electron density:

$$\delta\Phi_{SC} \simeq -(k_B T_{ph}/e)\ (\delta n/n) \simeq -3 \times (\delta n/n) \text{ Volts}$$

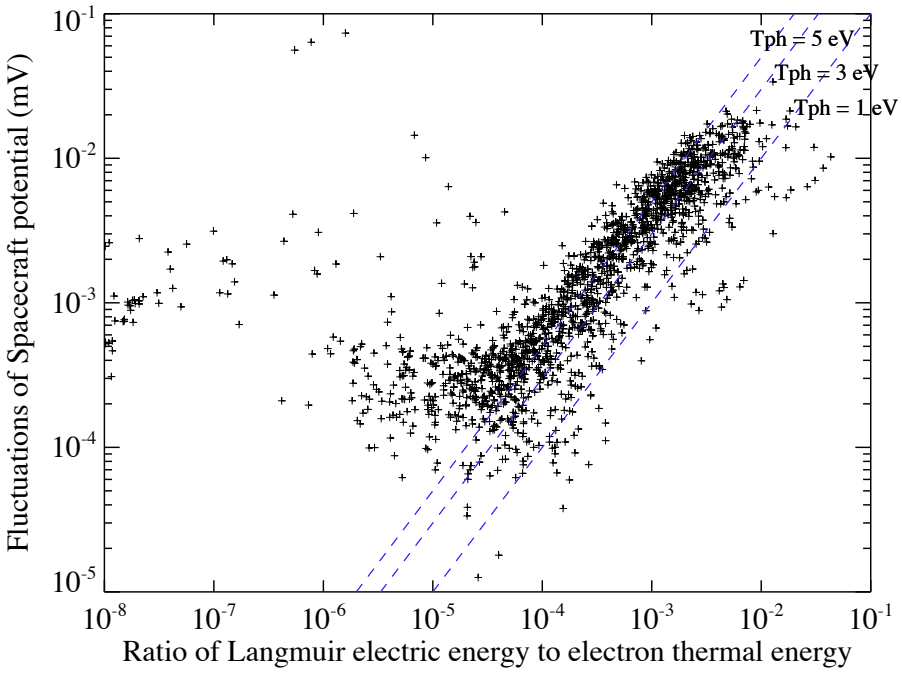

Figure B.4: Level of spacecraft potential fluctuations for different Langmuir energy. Each single point represents a TDS waveform where both Langmuir electric oscillations and spacecraft potential fluctuations are observed. The dotted lines show the expected level of density fluctuations generated by Langmuir ponderomotive effects for different values of the photoelectron temperature T_{ph}.

Appendix C

Identification of waveforms of interest: application to S/WAVES

About 50 to 200 voltage waveforms data from the S/WAVES Time Domain Sampler (TDS) are daily telemetered, depending on the observational mode (Table 2.2, p. 26). The primary goal of the TDS is to observe Langmuir waves. However, other signals of interest are found in these data: signature of dust impact on the spacecraft blanket [*Meyer-Vernet et al.*, 2009], signature of density fluctuations crossing the spacecraft [*Kellogg et al.*, 2009; *Henri et al.*, 2009, 2010c], low frequency waves such as whistler waves [*Cattell et al.*, 2009].

To ease the data analysis, I have classified the TDS waveforms according to the nature of the signals of interest defined and identified as follow. Fig. C.1 show examples of such waveforms.

(1) Langmuir events;

(2) density fluctuations events;

(3) low frequency waves events;

(4) dust events;

(1) Waveform containing signatures of Langmuir waves (Fig. C.1 top left panel) are identified by selecting highly peaked (Typically a spectral peak > 20 times the spectral background with $\Delta f/f_{max} < 5\ 10^{-2}$) high-frequency oscillations in the Langmuir frequency range, typically $\sim$ [5 Hz - 40 KHz].
(2) Density fluctuations affecting the spacecraft floating potential lead to the same low frequency signature on the three monopole antenna channels in a specific range of frequencies, typically $\sim$ [100 Hz - 1 KHz] (section 2.3, p. 28). These events have been identified by selecting events with identical low frequency voltage on the three antennas (top right

panel). The method is the following: a maximum variance analysis is performed on the equivalent 3D voltage signal, selecting events show a clear maximum variance axis directed along the bissectrix of the three antennas.
(3) Waveform containing signatures of low frequency waves (bottom left panel) are simply identified by a low frequency peak seen out of the Langmuir frequency range, i.e. < 5 kHz.
(4) Waveforms characteristic of dust impacts on the spacecraft blanket (bottom right panel) have been isolated by looking for high-derivative and high skewness waveforms (fast growth of antenna charging, long time to reach equilibrium state after the impact).

Signals that do not enter in any of these categories are rejected from the selection algorithm.

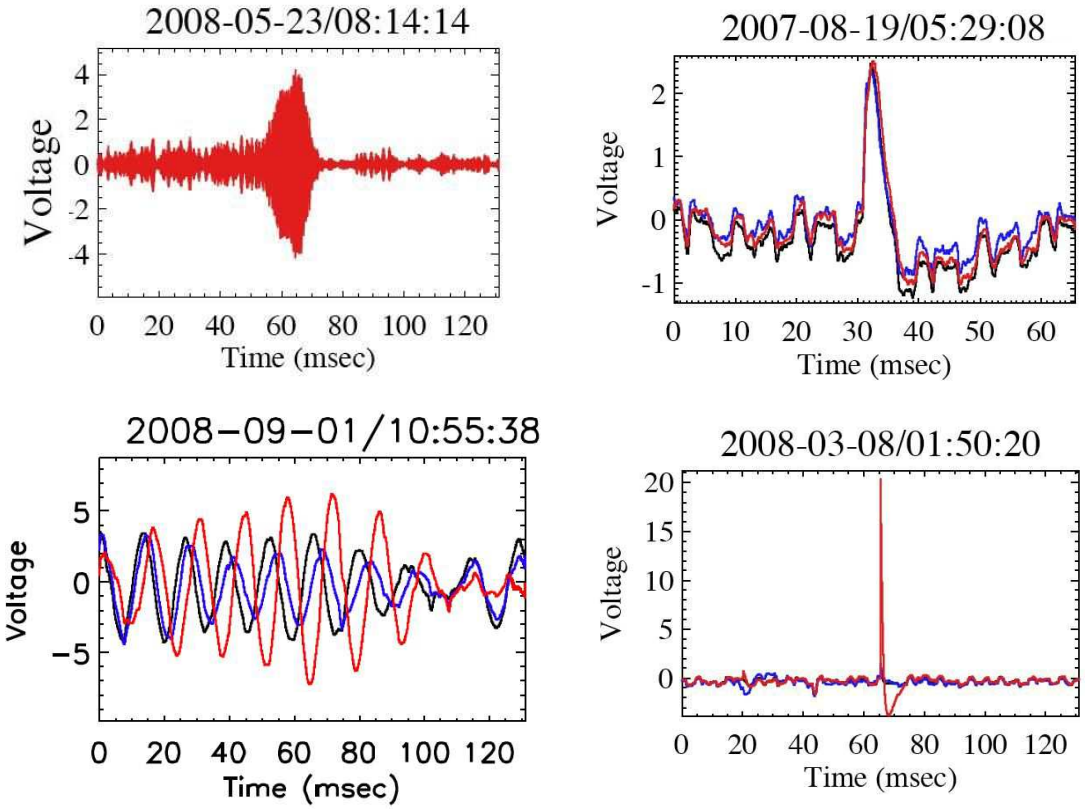

Figure C.1: Classification of signals of interest in TDS waveforms data. The voltage is expressed in mV. Different colors show different antennas voltage. Top left panel: Langmuir wave; bottom left panel: low frequency wave; top right panel: density fluctuations affecting the spacecraft potential; bottom right panel: signature of dust impact on the spacecraft blanket.

Criteria (1), (2) and (3) are independent and can be combined, as illustrated in Fig. C.2. For instance, ion acoustic waves are low frequency density oscillations: criteria (2) and (4). In the case of a waveform showing Langmuir electrostatic decay, both Langmuir oscillations and ion acoustic oscillations are seen: criteria (2), (3) and (4) should be active simultaneously.

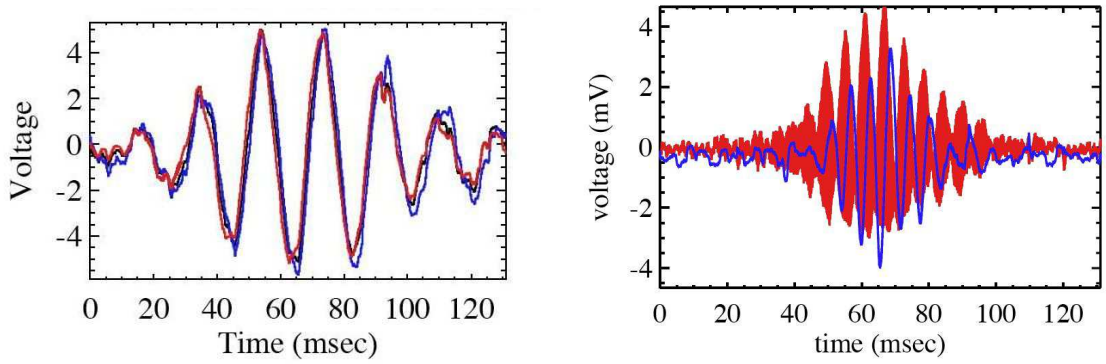

Figure C.2: Example of TDS waveforms. The voltage is expressed in mV. Left panel: ion acoustic oscillation; right panel: Langmuir wave decaying through electrostatic decay.

Application 1: nonlinear evolution of Langmuir waves.

Over all the TDS waveforms from November 2006 to the end of 2009, 49 waveforms (concerning 15 days) are found with a Langmuir electric energy, normalized to the electron thermal energy, greater than 10^{-2}, and 1179 waveforms (concerning a total of 92 days) with Langmuir electric energy greater than 10^{-3}. This set of waveforms offers a good opportunity to study the non linear behaviour of Langmuir waves in the solar wind. First results have been submitted [*Henri et al.*, 2010c].

Application 2: Langmuir waves generated in magnetic holes.

The list of TDS waveforms showing Langmuir oscillations has been used to identify the Langmuir waves associated with magnetic holes (collaboration with C. Briand, LESIA, Meudon, France and I. Soucek, Institute of Atmospheric Physics, Prague, Czech Republic). A paper has been submitted on the properties of these Langmuir waves [*Briand et al.*, 2010].

Application 3: cross-calibration of STEREO/IMPACT electron density measurements

The large number of detection of Langmuir events have enabled to cross-calibrate the electron density measurements from STEREO/IMPACT (collaboration with A. Opitz,

CESR, Toulouse, France). The problem was to calibrate the offset in electron density measurements of the IMPACT experiment. To this purpose, I provided a large number of punctual density estimations obtained from in-situ observations of Langmuir oscillation. I recall that the Langmuir waves oscillate at the electron plasma frequency, which depends on the electron density. This collaboration led to a common submission [*Opitz et al.*, 2009].

The electron density can be obtained from the plasma frequency.
A first method to evaluate the electron plasma frequency is the so-called quasi-thermal noise spectroscopy [*Meyer-Vernet and Perche*, 1989]. It enables to deduce the electron density and temperature from the electric noise generated on the antenna by the thermal motion of the surrounding moving electrons. However, S/WAVES antenna have a high level of shut noise. The electron plasma noise at the plasma frequency is hidden by the shut noise. The electron plasma frequency, and hence the electron density, cannot be deduce from the quasi thermal noise spectroscopy.

A second method, compatible with S/WAVES shut noise level, is too evaluate the plasma frequency directly from the observed Langmuir frequency. The solar wind is a moving medium, the observed frequencies are thus Doppler shifted[1]. The resulting *observed* Langmuir angular frequency is:

$$\begin{aligned} \omega_{_L}^{obs} &= \omega_{_L} + \vec{k}_{_L}.\vec{V}_{_{SW}} \\ &\simeq \omega_{pe}\,(1+\frac{3}{2}k_{_L}^2\lambda_{_D}^2) + k_{_L}V_{_{SW}}\cos\theta_{\vec{B},\vec{V}_{_{SW}}} \end{aligned}$$

where $\vec{V}_{_{SW}}$ is the solar wind speed, and $\theta_{\vec{B},\vec{V}_{_{SW}}}$ the angle between the magnetic field and the solar wind speed directions, recalling that the propagation is parallel to the magnetic field $\vec{k}_{_L} \parallel \vec{B}$.
Uncertainties on the evaluation of the plasma frequency from the Langmuir frequency arise from three effects: (i) the thermal correction $\left(\frac{3}{2}k_{_L}^2\lambda_{_D}^2\right)$, (ii) the Doppler-shift correction and (iii) the shape of the Langmuir wavepackets.

The Doppler shift correction is of the order (foreshock Langmuir waves) or greater (Type III

[1]We here neglect the spacecraft orbital velocity at about 30 km.s^{-1}, orthogonal to the mean flow and small compared to the solar wind speed.

associated Langmuir waves) than the thermal correction:

$$\begin{aligned}
\frac{\text{Thermal correction}}{\text{Doppler correction}} &= \frac{\frac{3}{2}k_L^2\lambda_D^2}{\vec{k}_L.\vec{V}_{SW}/\omega_{pe}} \\
&\simeq \frac{\frac{3}{2}\widetilde{k_L}^2}{\frac{1}{2}\frac{V_{SW}}{v_{th,e}}\widetilde{k_L}} \quad \text{with } \cos\theta_{\vec{B},\vec{V}_{SW}} \simeq 0.5 \\
&\simeq 3\frac{v_{th,e}}{V_{SW}}\widetilde{k_L} \\
&\simeq 10\ \widetilde{k_L} \quad \text{using } v_{th,e} \simeq 3\ V_{SW} \\
&\simeq 10\ \left(\frac{v_b}{v_{th,e}}\right)^{-1}
\end{aligned}$$

where we have written the normalized wavenumber $\widetilde{k_L} = k_L\lambda_D \simeq \frac{v_{th,e}}{v_b}$.
In the typical conditions of the solar wind speed ($\sim 300 - 800$ km.s^{-1}), electron beams in the Earth electron foreshock (resp. associated to Type III bursts) have typical velocities $v_b \simeq 10\ v_{th,e}$ (resp. velocities $v_b \simeq 30 - 40\ v_{th,e}$), and generates Langmuir waves at phase velocity $v_\phi \simeq v_b$, ie at wavelength $\lambda_L \simeq 60\ \lambda_D$ (resp. $\lambda_L \simeq 200 - 300\ \lambda_D$).
The thermal correction to the plasma frequency is $\frac{3}{2}k_L^2\lambda_D^2 \sim 10^{-2}$ for Langmuir waves in the Earth foreshock (resp. $\sim 10^{-3}$ for Type III-associated Langmuir waves), i.e. a few 100 Hz (resp. 10 Hz).
The Doppler shift correction is about 1% of the total observed frequency, i.e. a few 100 Hz: $\vec{k}_L.\vec{V}_{SW}/\omega_{pe} \gtrsim 10^{-2}$ for Langmuir waves in the Earth foreshock (resp. $\lesssim 10^{-2}$ for Type III-associated Langmuir waves). It is worth noticing that two Langmuir waves with similar wavelengths, but propagating in opposite directions, are distinguishable only through the Doppler effect.

I first isolated the S/WAVES "Langmuir oscillations" in-situ electric field waveforms from TDS data. The electron plasma frequency f_{pe} is then estimated from the Langmuir waves frequencies f_L.
A gaussian fit of the Langmuir spectrum gives the mean Langmuir frequency, together with the standard deviation which evaluate mostly the shape of the wavepacket.
The spectral width however hardly exceed 1%, the thermal correction is $\lesssim 1\%$, while the Doppler shift correction is $\lesssim 10\%$. The observed Langmuir frequency thus gives an evaluation of the plasma frequency to about 10%.

The electron density n_e is deduced from the evaluated plasma frequency:

$$n_e[cm^{-3}] = (f_{pe}[kHz]/8.98)^2 \simeq (f_L[kHz]/8.98)^2$$

with an uncertainty $\frac{\delta n_e}{n_e} = 2\frac{\delta f_{pe}}{f_{pe}} \simeq 20\%$. The uncertainty on the plasma frequency evaluation is dominated by the Doppler-shift effect. This correction is however not biased (unlike the thermal correction that is always positive). It can be either positive or negative according to the direction of propagation of the Langmuir wave. Since the objective is to calibrate the *offset* in the electron density measurements from IMPACT, this large uncertainty on the electron density is compensated by the large number of measurements.

Appendix D

Bicoherence: a powerful diagnostic for three-wave interactions

The bicoherence is used as an estimator of quadratic phase coupling, characteristic of three-wave coherent interactions. *Lagoutte et al.* [1989] gives a methodological introduction to bicoherence analyses based on a Fourier approach[1]. Although studies of bicoherence have been reported in the ionosphere [*Pecseli et al.*, 1993], the bow shock [*Dudok de Wit and Krasnosel'Skikh*, 1995] and the solar wind near the foreshock edge[*Bale et al.*, 1996], to our knowledge, *Henri et al.* [2009] is the first bicoherence study of three-wave coupling in the solar wind during a Type III.

In the case of three-wave coupling, the relative phase $\Delta\Phi = \Phi_1 + \Phi_2 - \Phi_3$ between the three phases $\Phi_{i=1,3}$ associated to the three frequencies $f_{i=1,3}$ linked by the relation $f_1 + f_2 = f_3$ should remain constant. Bicoherence measures statistically the degree of stationarity of the relative phase $\Delta\Phi$. The Fourier cross-bispectrum B is defined in a 2D frequency space (f_1, f_2) by

$$B(f_1, f_2) =< F(f_1)F(f_2)F^*(f_1 + f_2) >, \tag{D.1}$$

where F is the Fourier spectrum of a given signal, F^* for the complex conjugate of F and $< >$ stands for the average over different independent samples. The third term $F^*(f_1+f_2)$ means that we consider the correlation between signals at three different frequencies such that the third frequency is equal to the sum of the two others.

To take into account phase effects only, i.e. to avoid amplitude effects, the Fourier cross-bispectrum is normalized. The normalized cross-bispectrum, also called bicoherence, is thus defined as:

$$b(f_1, f_2) = \frac{< F(f_1)F(f_2)F^*(f_1 + f_2) >}{< |F(f_1)F(f_2)F^*(f_1 + f_2)| >} \tag{D.2}$$

[1]Note that high-order spectral statistics are general methods used in a wide range of fields: sonar and radar, interferometry, nonlinear systems, image processing, biomedical signal analysis, etc [*Mendel*, 1991; *Mandel and Wolf*, 1995].

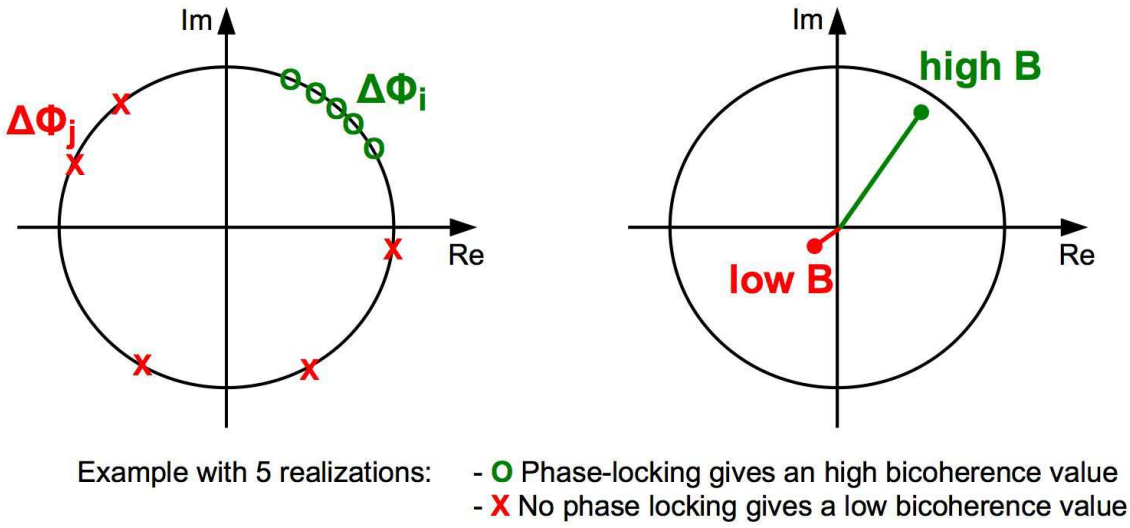

Figure D.1: Illustration of phase locking and bicoherence. Left panel: Relative phases $\Delta\Phi$ in the complex plan for two series of experiments. The first series $\Delta\Phi_j$ (red crosses) is random while the second series $\Delta\Phi_i$ green circles) is almost constant (phase locking). Right panel: the first (resp. second) series is characterized by a low (resp. high) level of bicoherence.

For a stationary signal, the bicoherence vanishes when the phase relation is random, and maximal (1 for the chosen normalization) when the phase relation remains constant. A non-zero bicoherence value $b(f_1, f_2)$ is thus the signature of phase locking between three waves with frequencies f_1, f_2 and $f_1 + f_2$.

To illustrate this property, let us consider two series of experiments where three waves with frequencies f_i (i=1,2,3) such that $f_1 + f_2 = f_3$ are detected. Figure D.1 illustrates how the bicoherence quantifies the phase locking. The left panel shows in the complex plan the relative phases $\Delta\Phi$ for (i) a first series of experiment the relative phases $\Delta\Phi$ between our three waves are different from one experiment to another (red crosses) and (ii) a second series of experiment where $\Delta\Phi$ does not vary to much (green circles), as it would be expected in the case of resonant three-wave interactions. The bicoherence is the norm of the average phase in the complex plan (distance between the average of the complex phases and the origin of the complex plan, represented by colored segment in the right panel). In the first case (red) the bicoherence is almost zero, while in the second case (green) the bicoherence is close to one. In the first case, no resonance is found between the waves, while in the second case bicoherence shows that the three waves stay in phase from one event to another, strongly suggesting that they are resonantly interacting.

To optimize the time resolution, and diminish the bias introduced by the method, the wavelet bicoherence [*Van Milligen et al.*, 1995; *Dudok de Wit and Krasnosel'Skikh*, 1995] has been preferred to the Fourier bicoherence for the observational study of electrostatic

decay *Henri et al.* [2009]. For convenience, the wavelet transform is expressed in terms of frequency f, instead of the wavelet scale $s = 1/f$. The wavelet cross-bispectrum is defined as in Eq. D.1 by replacing the Fourier transform with the wavelet transform W:

$$B(f_1, f_2) =< W(f_1)W(f_2)W^*(f_1 + f_2) >, \tag{D.3}$$

where $< >$ now stands for the time-average over one sample only (I recall that the wavelet $W(t, f)$ is a function of both time and frequency). Wavelet bicoherence is normalized as the Fourier bicoherence (Eq. D.2):

$$b(f_1, f_2) = \frac{< W(f_1)W(f_2)W^*(f_1 + f_2) >}{< |W(f_1)W(f_2)W^*(f_1 + f_2)| >} \tag{D.4}$$

I stress the difference between Fourier and wavelet bicoherence: Fourier bicoherence is computed over different realizations of a same experiment, while the wavelet bicoherence is computed over time for a single experiment. Wavelet bicoherence is thus computed by averaging on overlapping samples. But as stressed by *Soucek et al.* [2003], the statistical validation of bicoherence requires to use *independent* samples. The duration of an independent sample can be evaluated from the time of coherence of the waves, which is about the duration of the wavepacket. It means that each localized waveform can be considered an independent sample. The wavelet bicoherence computed with only one localized waveform would be meaningless. In *Henri et al.* [2009], several TDS waveforms have been first juxtaposed to form a long time series that contains several independent samples. The wavelet bicoherence is then computed on this equivalent signal.

The bicoherence is very sensitive to the non-stationarity of frequencies and to the presence of discontinuities in the data set. The non-stationarity of frequencies involved in a three-wave coupling spreads the bicoherence signal and thus decreases the wavelet bicoherence value at all involved frequencies. This is a consequence of the intrinsic frequency accuracy of the Morlet wavelet. Indeed, the time-frequency finite resolution of the chosen wavelet implies that the uncertainty on the frequencies is $\Delta f \simeq 1/4f$, with Δf the resolution at 3 dB. Discontinuities in the waveform, such as spikes, appears through spectral analyses as a large spectrum of coupled frequencies (for instance Dirac's function is a white noise with correlated phases). This implies an increase of the bicoherence signal, without physical significance, and thus reduces the signal-to-noise ratio of the bicoherence.

Bicoherence analysis has been used on S/WAVES observations [see *Henri et al.*, 2009] and Vlasov simulations of Langmuir electrostatic decay. I describe here the evolution of the bicoherence during a numerical experiment of the electrostatic decay of a monochromatic Langmuir wave.

I use the 1D-1V Vlasov-Poisson model with periodic boundaries described in section 2.4. The ion-to-electron temperature ratio is $T_i/T_e = 1$, the ion-to-electron mass ration is $\mu = 1836$. A monochromatic Langmuir wave with wavenumber $k_{_L} = 0.06$ and electric field amplitude $E_{_L} = 6\ 10^{-2}$ is initially generated by the external forcing E_{ext}.

The evolution of the electric field and the ion density fluctuations are shown in Fig. D.2.

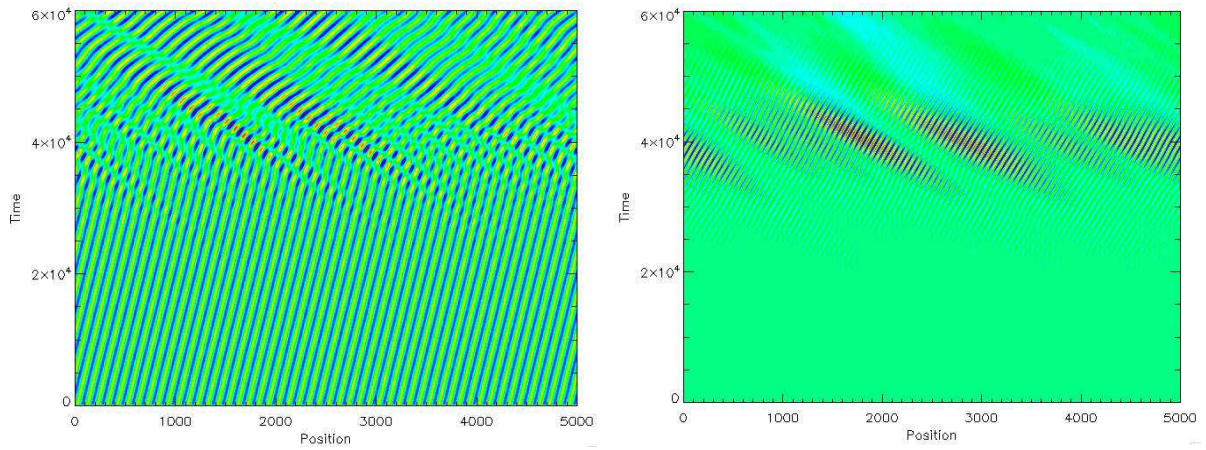

Figure D.2: Time-position evolution of the electric field (left panel) and the proton density fluctuations (right panel). Position is expressed in Debye length unit, time in inverse plasma frequency unit.

The mother Langmuir wave propagate rightward and decays into a backscattered Langmuir wave ($k_{L'} \simeq 0.04$) and an ion acoustic wave ($k_S \simeq 0.1$). The decay product are observed in Fig. D.2 from time $t \simeq 3\ 10^4\ \omega_{pe}^{-1}$.
From the evolution of density fluctuations (right panel), the ion acoustic wave seems to propagate leftward, while the theory predicts that it is emitted in the same direction as the mother Langmuir wave (rightward). In fact, the ion acoustic wave indeed propagate rightward, as seen from the evolution of the wave crests. They are generated where the two Langmuir waves (mother and daughter) beat, but are Landau damped as soon as they escape the beat regions because of the temperature ratio $T_i/T_e = 1$. The leftward-propagating "apparent wavepackets" are only the signature of the beat regions where the ion acoustic waves can exist. Since the mother wave is monochromatic, these leftward-propagating "apparent wavepackets" shows the localization of the daughter Langmuir wavepacket. It can be shown that they follow the expected group velocity of the daughter Langmuir wave. I recall that, as described in *Henri et al.* [2010b], even when considering a monochromatic mother Langmuir wave, both daughter waves are in fact wavepackets.

Let us now look at the three-wave interactions that occur during this run. The Fourier bicoherence is computed in term of wavenumbers to look for phase resonance associated the relation $k_1 + k_2 = k_3$. This means that high bicoherence response at (k_1, k_2) represents a coherent interaction between three waves with wavenumber k_1, k_2 and $k_3 = k_1 + k_2$.
The evolution of the Fourier bicoherence with time during the simulation is shown in Fig. D.3 and D.4 (time evolution from top to bottom). Left panels show the electric field bicoherence, right panels the density bicoherence at the same time. Dotted lines show the expected wavenumbers of the Langmuir and ion acoustic waves associated to the electrostatic decay of the initial Langmuir wave.
When considering the wavenumbers, the Langmuir decay is such that $\vec{k}_L = \vec{k}_{L'} + \vec{k}_S$, but since the Langmuir daughter wave is backscattered, $k_{L'}$ is negative. When expressed in term of the modulus of the wavenumber, the conservation of momentum reads $k_S =$

$k_{L'} + k_L$ (see Fig 1.4 page 12).
At the beginning of the simulation ($0 < t < 10^3\ \omega_{pe}^{-1}$ corresponding to the two top panels of Fig. D.3), the initial large amplitude Langmuir wave is in phase resonance with a wave at $2k_L$ as shown from the maximum electric field bicoherence at $(k_1, k_2) = (k_L, k_L)$. This is most likely the signature of a resonance with a pseudo-mode at $2k_L$, oscillating at $2\omega_L$, as a prelude for the Langmuir nonlinear evolution.
The signature of Langmuir electrostatic decay is then observed, first in the ion density bicoherence[2], then also in the electric field bicoherence at $(k_1, k_2) = (k_{L'}, k_L)$. Note that the decay is observed through the bicoherence before its signature in physical space in Fig. D.2. Again, the bicoherence shows phase resonance and is insensitive to the amplitude of the signal. That is why three-wave coupling is observed with this method at early time, as soon as the decay begins.
At some point, the ion acoustic waves generated by the Langmuir decay are large enough to act themselves as pump waves and generate, first, the harmonic $S^{(2)}$ at $2k_S$ (density bicoherence at (k_S, k_S), as a signature of $S \rightarrow S^{(2)} + S^{(2)}$), then the other harmonics $S^{(n)}$ (density bicoherence at (nk_S, nk_S) in Fig. D.4). This is the ion acoustic cascade.

This example illustrate how the bicoherence analysis allows to identify as well (i) a single three-wave interaction (Langmuir electrostatic decay) and (ii) a full developed weak turbulence based on multiple and simultaneous three-wave interactions (ion acoustic turbulence).

This discussion is based on a poster presented at the 52^{nd} congress of the Società Astronomica Italiana (SAIt), Pisa, Italy, May 2009 (Bicoherence as a diagnostic for non-linear three-wave interactions).

[2]The ion-to-electron mass ratio is finite, a (small) oscillation of the ions is thus also associated to the Langmuir wave. Since the bicoherence is normalized in order to be sensitive to phase coherence, but insensitive to the signal amplitude, it is not surprising to observe signature of the electrostatic decay in the density bicoherence.

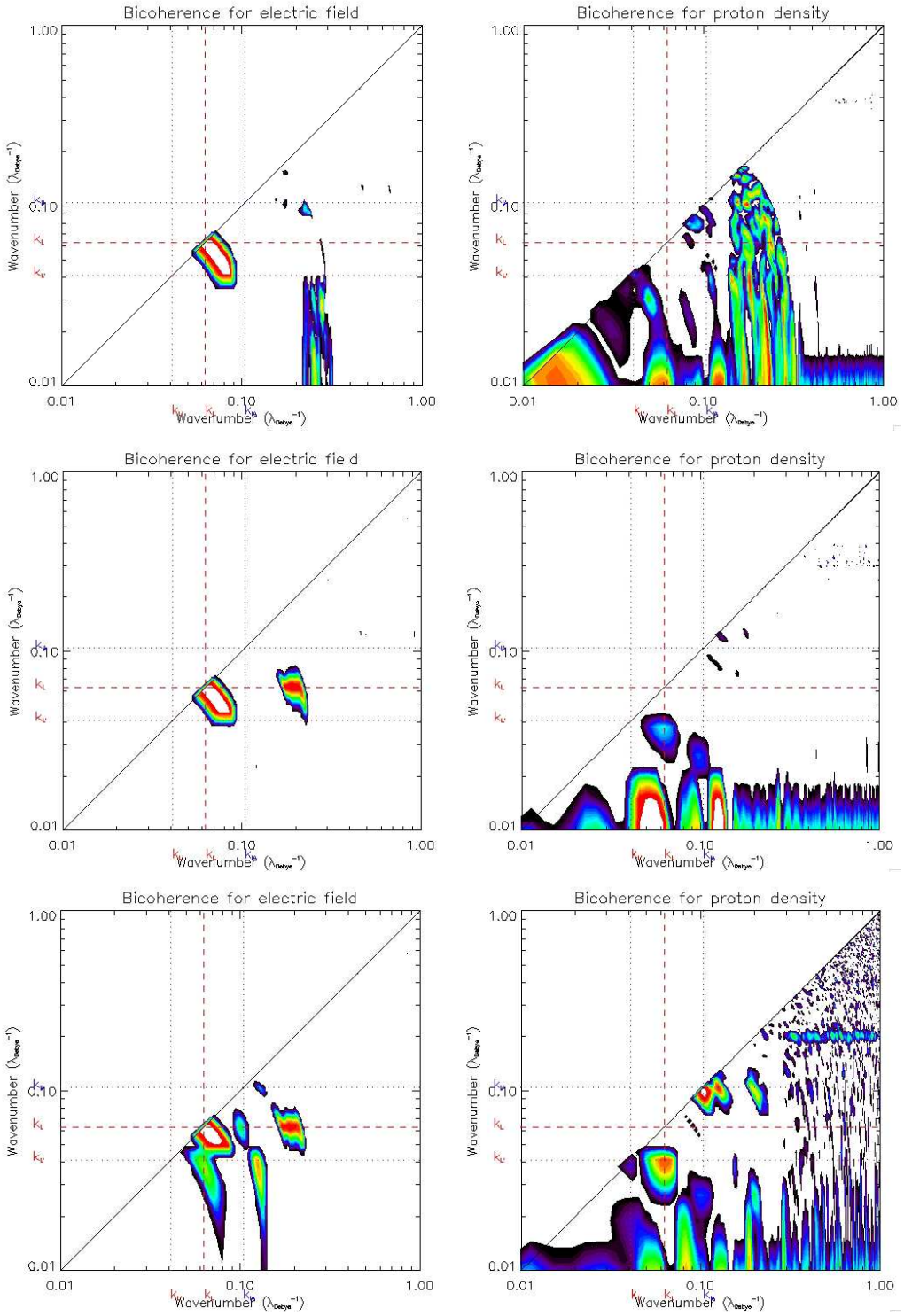

Figure D.3: (First part) Evolution of the Fourier bicoherence computed for both the electric field (left panels) and the ion density (right panels) during the run shown in Fig. D.2. Top panel: $0 < t < 1000\ \omega_{pe}^{-1}$. Medium panel: $1000 < t < 2000\ \omega_{pe}^{-1}$. Bottom panel: $2000 < t < 3000\ \omega_{pe}^{-1}$.

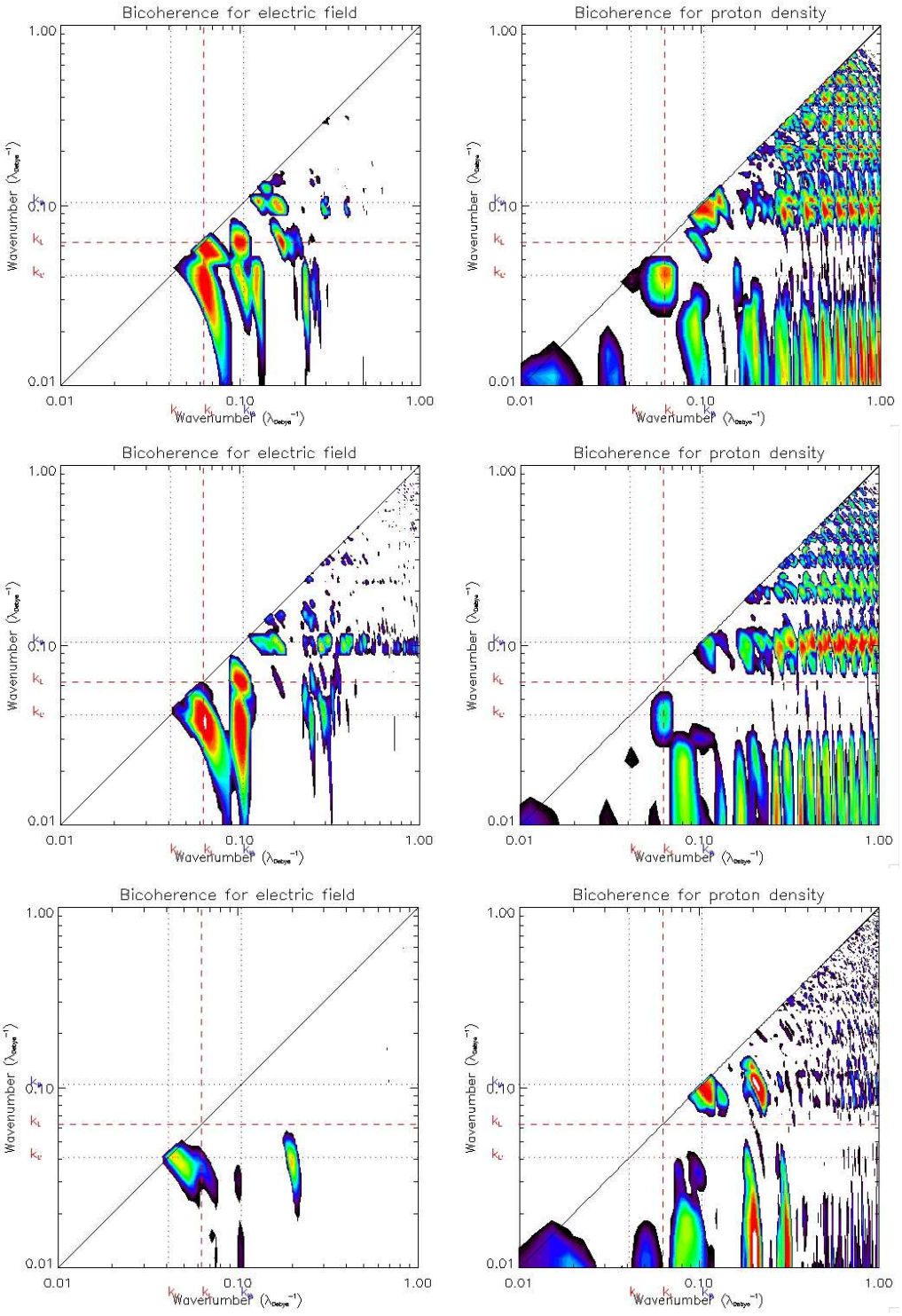

Figure D.4: (Second part) Evolution of the Fourier bicoherence computed for both the electric field (left panels) and the ion density (right panels) during the run shown in Fig. D.2. Top panel: $3000 < t < 4000\ \omega_{pe}^{-1}$. Medium panel: $4000 < t < 5000\ \omega_{pe}^{-1}$. Bottom panel: $5000 < t < 6000\ \omega_{pe}^{-1}$.

Appendix E

Vlasov Code

I summarize in this appendix some numerical work performed on the Vlasov-Poisson code. The simulations discussed in this thesis are 1D and start with an homogeneous medium. In the following, I give the explicit form of the external forcing E_{ext}^{init} and E_{ext}^{noise} added to the Vlasov equation.
Some preliminary simulations have also been performed (i) with considering an initially inhomogeneous plasma, (ii) in 2D configurations. I describe here some complementary investigations to prepare this new step.

Generation of Langmuir waves

To numerically investigate the nonlinear evolution of a Langmuir wave (or wavepacket), I wish to control the amplitude and shape of an initial Langmuir wave. In this purpose, I chose not to generate the Langmuir wave via a bump-on-tail instability, but by directly imposing the desired parameters of the oscillation.

Langmuir waves are oscillations of the electron density on a fixed ion background. An intuitive method could be to generate an initial Langmuir wave by imposing an initial electron density fluctuations in the simulation box. However, imposing an initial electron density fluctuation produces a standing wave, sum of two counter-propagating Langmuir waves.

In order to initially produce a Langmuir wave propagating in a *single* direction, I chose to use an external driver driver E_{ext}^{init}, added in the Vlasov equation for electrons (Eq. 2.4). This 'external' electric field controls the generation of the initial Langmuir wave. It acts as a driver that resonantly grows a Langmuir wave propagating in only one direction, with the desired spectrum and electric field amplitude.

A **monochromatic** Langmuir wave of wavelength λ_L and amplitude E_L is resonantly excited by the external electric field pump by defining $E_{ext}^{init} = E_{ext}^{(1)}$:

$$E_{ext}^{(1)}(x,t) = E_0^{(1)}(t)\ cos(k_0 x - \omega_0 t) \tag{E.1}$$

A Langmuir **wave packet** of mean wavelength λ_L, packet width Δ and maximum amplitude E_L is resonantly excited by defining $E_{ext}^{init} = E_{ext}^{(2)}$:

$$E_{ext}^{(2)}(x,t) = E_0(t)\ cos(k_0 x - \omega_0 t)\ exp\left(- \left(\frac{x - x_0 - v_L^g t}{0.5\Delta} \right)^2 \right) \tag{E.2}$$

In both cases, the pump wavevector $k_0 = 2\pi/\lambda_L$ and the frequency $\omega_0 = \sqrt{1 + 3k_0^2}$ are chosen to satisfy the Langmuir dispersion relation, in order to generate a Langmuir wave at the desired wavelength λ_L. The width of the wave packet is set to $\Delta = 10\ \lambda_L$. The pump wave packet moves at the Langmuir group velocity $v_L^g = 3k_0/\omega_0$ from its initial position $x_0 = L_x/3$. The time-dependant external electric field amplitude $E_0(t)$ scales on the desired Langmuir amplitude E_L:

$$E_0^{(1)}(t) = \eta E_L (1 - exp(-t/\tau)). \tag{E.3}$$

In the monochromatic case (resp. wave packet case), the parameter τ is set to $30\ \omega_{pe}^{-1}$ (resp. $100\ \omega_{pe}^{-1}$) so that the external electric field amplitude smoothly increases during a few Langmuir oscillations. This avoids the generation of other plasma waves induced by step-like switch of the pump. The parameter η is set experimentally to 5×10^{-2} (resp. 10^{-2}), so that the characteristic time scale to resonantly grow the Langmuir wave (resp. wave packet) is large compared to its oscillation time scale, but small compared to the decay time scale. So, the resonant generation of the Langmuir wave (resp. wave packet) does not interfere with the Langmuir electrostatic decay mechanism.

The method is easily transposed to a bi-dimensional description of the wave by simply modifying the phase of the wave and the shape of the envelop.

Generation of ion acoustic noise

A continuous injection of ion density noise can be driven by the external fields E_{ext}^{noise} added to the ion dynamics (Eq 2.5). It may represent the density fluctuations coming through a turbulent cascade, not described in the simulation, from scales larger than the simulation box to smaller scales resolved in the box. This driver is defined by:

$$E_{ext}^{noise}(x,t) = E_{ext}^{ions,max} \frac{\sum_\lambda cos(2\pi x/\lambda) cos(\omega_\lambda t + \Psi_\lambda''(t))}{|\sum_\lambda cos(2\pi x/\lambda) cos(\omega_\lambda t + \Psi_\lambda''(t))|} \tag{E.4}$$

It introduces a flat spectrum for wavelength over the range $50 < \lambda < 1000$. $E_{ext}^{noise}(x,t)$ is normalized in order to have a maximum amplitude of $E_{ext}^{ions,max} = 1 \times 10^{-5}$. The frequencies ω_λ are chosen to satisfy the dispersion relation of IAW, $\omega_\lambda = (2\pi/\lambda)c_s$ with

$c_s = \sqrt{(1+\Theta)/\mu}$ the ion sound speed. The phases $\psi''_k(t)$ have a step-like variation, defined by a piecewise constant function over a time interval δt. At the end of each interval, they are independently drawn from a uniform distribution. This way, the generation of ion acoustic noise is made of a succession of time coherent forcing for time intervals of duration $\delta t = 500 \times \omega_{pe}^{-1}$ (about 80 plasma oscillations). This means that for an IAW of wavelength $\lambda_s = 100$, the forcing lasts $1/20^{th}$ of a period, much shorter than the typical IAW oscillation time in order to generate an incoherent noise. This forcing thus generates density fluctuations much smaller than the level of density fluctuations generated by Langmuir electrostatic decay in our simulations.

Starting with macroscopic inhomogeneities

When setting an initial random density that is different for electrons and ions, charge separation rapidly self-organises into a broad spectrum of Langmuir noise. A "sea" of Langmuir waves then fills the simulation box. This is the way I generate the (small) initial Langmuir random noise needed for the parametric instability to develop.

When setting an initial random density that is identical for electrons and ions, one could expect to generate only ion acoustic fluctuations. This is wrong.
The reason is the following. The ion density fluctuation rapidly self-reorganize into ion-acoustic fluctuations, but ion-acoustic density fluctuations are associated with electric field fluctuations. If the initial charge separation (which controls the initial electric field) is not imposed so that it actually corresponds to the associated ion acoustic initial density fluctuation, then the system self-organize into both ion-acoustic *and Langmuir waves*.

In order for an initial macroscopic density inhomogeneity not to generate Langmuir noise, one must impose an initial charge separation consistent with the ion acoustic fluctuations. The initial ion density fluctuations associated to a pressure gradient $\vec{\nabla} P$ should be compensated by a separation of charges associated through the Poisson equation to an electric field $\vec{E}$ that ensure the initial equilibrium.
A solution is the following. In order to start with density fluctuations that project onto ion acoustic fluctuations only, one imposes an initial Boltzmanian equilibrium for the electrons. By doing so, no Langmuir oscillation is generated by the initial density fluctuation.

In the 1D-1V case, the initial charge separation $n_e - n_i$ corresponds to an electric potential ϕ through Laplace equation:

$$\Delta\phi = \frac{\partial^2 \phi}{\partial x^2} = n_e - n_i$$

We first imposed the electron density inhomogeneity $n_e = n_e(x)$. The ion density $n_i = n_i(x)$ is then calculated by imposing to the electrons to be in Boltzmanian equilibrium:

$$n_e = exp(\phi)$$

The ion density, given by Laplace equation:

$$n_i = n_e - \frac{\partial^2 \phi}{\partial x^2},$$

is expressed in term of the electron density only, by using $\phi = log(n_e)$:

$$n_i = n_e + \Big(\frac{1}{n_e}\frac{\partial n_e}{\partial x}\Big)^2 - \frac{1}{n_e}\frac{\partial^2 n_e}{\partial x^2} \tag{E.5}$$

In the 2D-2V case, Laplace equation becomes:

$$\Delta\phi = \frac{\partial^2 \phi}{\partial x^2} + \frac{\partial^2 \phi}{\partial y^2} = n_e - n_i$$

so that the ion density $n_i = n_i(x, y)$ in equilibrium with the imposed electron density $n_e = n_e(x, y)$ reads:

$$n_i = n_e + \left(\frac{1}{n_e}\Big(\frac{\partial n_e}{\partial x} + \frac{\partial n_e}{\partial y}\Big)\right)^2 - \frac{1}{n_e}\left(\frac{\partial^2 n_e}{\partial x^2} + \frac{\partial^2 n_e}{\partial y^2}\right) \tag{E.6}$$

The spatial grid being periodic, the derivative are calculated in both 1D-1V and 2D-2V cases by Fourier transform.

However, this method does not guarantee to get stable ion fluctuations. Indeed, the initial density fluctuations are modified on ion time scales. It just cancels unwanted Langmuir oscillations by imposing to the initial density fluctuations to reorganize themselves along the ion acoustic branch only. To get a stable ion fluctuation in the Vlasov-Poisson model, one must impose a stabilizing external force on the Vlasov equation for the ions.

In this method, I have imposed the inhomogeneity on the electron density. However, the charge separation for ion acoustic fluctuations is small, so that the ion density inhomogeneity is almost equal to the electron inhomogeneity.

Irrotational initial noise in the 2D-2V electrostatic code

When setting a random noise in density, both rotational and irrotational electric fields are generated. However, the Vlasov-Poisson system does not describe rotational electric fields, filtrated by the resolution of the Poisson equation[1]. We wish to better control the initial noise of the simulation by directly imposing an irrotational initial random electric field, generated by an isotropic initial random density fluctuations. In order to ensure that the electric field is irrotational, we impose a potential $\Phi(x, y)$ define as follow:

$$\Phi(x, y) = \Phi_0 \sum_{i,j=1}^{N_k} \frac{1}{\sqrt{k_i^2 + k_j^2}} \Big(sin\big(k_i x + k_j y + \phi_{i,j}^{(0)}\big) + sin\big(k_i x - k_j y + \phi_{i,j}^{(1)}\big)\Big) \tag{E.7}$$

[1] more exactly through the resolution of Laplace equation!

The associated electric field reads:

$$E_x(x,y) = \Phi_0\, e_x(x,y) \tag{E.8}$$

$$E_y(x,y) = \Phi_0\, e_y(x,y) \tag{E.9}$$

with

$$e_x(x,y) = \sum_{i,j=1}^{N_k} \frac{k_i}{\sqrt{k_i^2+k_j^2}} \left(cos\big(k_i x + k_j y + \phi_{i,j}^{(0)}\big) + cos\big(k_i x - k_j y + \phi_{i,j}^{(1)}\big)\right)$$

$$e_y(x,y) = \sum_{i,j=1}^{N_k} \frac{k_j}{\sqrt{k_i^2+k_j^2}} \left(cos\big(k_i x + k_j y + \phi_{i,j}^{(0)}\big) - cos\big(k_i x - k_j y + \phi_{i,j}^{(1)}\big)\right)$$

The parameter Φ_0 is chosen so that the maximum electric field amplitude is E_{max}:

$$\Phi_0 = E_{max}/\max_{x,y}\left(\sqrt{e_x^2(x,y)+e_y^2(x,y)}\right) \tag{E.10}$$

Then, the divergence of the electric field reads:

$$\begin{aligned}
\vec{\nabla}.\vec{E}(x,y) &= \frac{\partial E_x}{\partial x} + \frac{\partial E_y}{\partial y} \\
&= -\Phi_0 \sum_{i,j=1}^{N_k} \frac{k_i^2}{\sqrt{k_i^2+k_j^2}} \left(sin\big(k_i x + k_j y + \phi_{i,j}^{(0)}\big) + sin\big(k_i x - k_j y + \phi_{i,j}^{(1)}\big)\right) \\
&\quad + \frac{k_j^2}{\sqrt{k_i^2+k_j^2}} \left(sin\big(k_i x + k_j y + \phi_{i,j}^{(0)}\big) + sin\big(k_i x - k_j y + \phi_{i,j}^{(1)}\big)\right)
\end{aligned}$$

where $\phi_{i,j}^{(l)} \in [0, 2\pi]$, $i,j = 1, N_k$ and $l = 0, 3$ are random phases, $k_i = i2\pi/L_x$ and $k_j = j2\pi/L_y$ $(i,j = 1, N_k)$ are the wavevectors.

Finally by considering Poisson equation $\nabla\vec{E} = \rho_p - \rho_e$, the electron and proton initial density fluctuations can be chosen as follow:

1. Fixed ions and fluctuation in the electron density $\rho_e(x,y) = -\nabla\vec{E}(x,y)$
2. Fluctuation of both ion density $\rho_i(x,y) = \alpha\, \nabla\vec{E}(x,y)$ and electron density $\rho_e(x,y) = -(1-\alpha)\, \nabla\vec{E}(x,y)$, with $0 < \alpha < 1$.

Bibliography

Abalde, J. R., F. A. Borotto, and A. C.-L. Chian, Plasma emission mechanism for radio spikes from solar flares, *Advances in Space Research*, *28*, 741, 2001.

Acuña, M. H., D. Curtis, J. L. Scheifele, C. T. Russell, P. Schroeder, A. Szabo, and J. G. Luhmann, The STEREO/IMPACT Magnetic Field Experiment, *Space Science Reviews*, p. 208, 2007.

Alves, M. V., A. Chian, M. A. E. De Moraes, J. R. Abalde, and F. B. Rizzato, A theory of the fundamental plasma emission of type-III solar radio bursts, *Astron. & Astrophys.*, *390*, 351, 2002.

Bale, S. D., D. Burgess, P. J. Kellogg, K. Goetz, R. L. Howard, and S. J. Monson, Phase coupling in Langmuir wave packets: Possible evidence of three-wave interactions in the upstream solar wind, *Geophys. Res. Lett.*, *23*, 109, 1996.

Bale, S. D., et al., The Electric Antennas for the STEREO/WAVES Experiment, *Space Science Reviews*, *136*, 529, 2008.

Bardwell, S., and M. V. Goldman, Three-dimensional Langmuir wave instabilities in type III solar radio bursts, *Astrophys. J.*, *209*, 912, 1976.

Bellan, P. M., *Fundamentals of Plasma Physics*, Cambridge University Press, 2006.

Biven, L., S. V. Nazarenko, and A. C. Newell, Breakdown of wave turbulence and the onset of intermittency, *Physics Letters A*, *280*, 28, 2001.

Biven, L. J., C. Connaughton, and A. C. Newell, Structure functions and breakdown criteria for wave turbulence, *Physica D Nonlinear Phenomena*, *184*, 98, 2003.

Boehm, M. H., C. W. Carlson, J. P. McFadden, J. H. Clemmons, R. E. Ergun, and F. S. Mozer, Wave rectification in plasma sheaths surrounding electric field antennas, *J. Geophys. Res.*, *99*, 21361, 1994.

Bougeret, J. L., et al., S/WAVES: The Radio and Plasma Wave Investigation on the STEREO Mission, *Space Science Reviews*, *136*, 487, 2008.

Briand, C., S. I., H. P., and M. A., Waves at the plasma frequency in solar wind magnetic holes, *J. Geophys. Res.*, 2010, *submitted*.

Cairns, I. H., and P. A. Robinson, Theory for low-frequency modulated Langmuir wave packets, *Geophys. Res. Lett.*, *19*, 2187, 1992.

Cairns, I. H., and P. A. Robinson, Ion Acoustic Wave Frequencies and Onset Times during Type III Solar Radio Bursts, *Astrophys. J.*, *453*, 959, 1995.

Cattell, C., et al., Observations of intense whistler-mode waves and simulations of associated acceleration of electrons, *APS Meeting Abstracts*, p. 6001, 2009.

Cheng, C. Z., and G. Knorr, The integration of the Vlasov equation in configuration space, *Journal of Computational Physics*, *22*, 330, 1976.

Chian, A., E. L. Rempel, and F. A. Borotto, Chaos in magnetospheric radio emissions, *Nonlinear Processes in Geophysics*, *9*, 435, 2002.

Davidson, R. C., *Methods in nonlinear plasma theory*, Academic Press, 1972.

Depierreux, S., J. Fuchs, C. Labaune, A. Michard, H. A. Baldis, D. Pesme, S. Hüller, and G. Laval, First Observation of Ion Acoustic Waves Produced by the Langmuir Decay Instability, *Physical Review Letters*, *84*, 2869, 2000.

Diu, B., C. Guthmann, D. Lederer, and B. Roulet, *Elements de Physique Statistique (2nd edition)*, Collection enseignements des sciences, 37, Hermann Éditeurs, 2001.

Driesman, A., S. Hynes, and G. Cancro, The STEREO Observatory, *Space Science Reviews*, p. 210, 2007.

Dudok de Wit, T., and V. V. Krasnosel'Skikh, Wavelet bicoherence analysis of strong plasma turbulence at the Earth's quasiparallel bow shock, *Physics of Plasmas*, *2*, 4307, 1995.

Dysthe, K. B., and R. N. Franklin, Non-linear interactions of coherent electrostatic plasma waves, *Plasma Physics*, *12*, 705, 1970.

Escoubet, C. P., A. Pedersen, R. Schmidt, and P. A. Lindqvist, Density in the magnetosphere inferred from ISEE 1 spacecraft potential, *J. Geophys. Res.*, *102*, 17595, 1997.

Fitzenreiter, R. J., A. F. Viňas, A. J. Klimas, R. P. Lepping, M. L. Kaiser, and T. G. Onsager, Wind observations of the electron foreshock, *Geophys. Res. Lett.*, *23*, 1235, 1996.

Galvin, A. B., et al., The Plasma and Suprathermal Ion Composition (PLASTIC) Investigation on the STEREO Observatories, *Space Science Reviews*, *136*, 437, 2008.

Ginzburg, V. L., and V. V. Zheleznyakov, On the Possible Mechanisms of Sporadic Solar Radio Emission (Radiation in an Isotropic Plasma), *Soviet Astronomy*, *2*, 653, 1958.

Goldman, M. V., Strong turbulence of plasma waves, *Reviews of Modern Physics*, *56*, 709, 1984.

Gurnett, D. A., and L. A. Frank, Ion acoustic waves in the solar wind, *J. Geophys. Res.*, *83*, 58, 1978.

Gurnett, D. A., G. B. Hospodarsky, W. S. Kurth, D. J. Williams, and S. J. Bolton, Fine structure of Langmuir waves produced by a solar electron event, *J. Geophys. Res.*, *98*, 5631, 1993.

Hammond, C. M., W. C. Feldman, J. L. Phillips, and A. Balogh, ULYSSES observations of double ion beams associated with coronal mass ejections, *Advances in Space Research*, *17*, 303, 1996.

Hasegawa, A., *Plasma instabilities and nonlinear effects*, Physics and Chemistry in Space, Springer, 1975.

Henri, P., C. Briand, A. Mangeney, S. D. Bale, F. Califano, K. Goetz, and M. Kaiser, Evidence for wave coupling in type III emissions, *J. Geophys. Res.*, *114*, 3103, 2009.

Henri, P., F. Califano, C. Briand, and A. Mangeney, Vlasov simulations of langmuir electrostatic decay and consequences for type iii observations, in *Twelfth International Solar Wind Conference*, edited by M. Maksimovic, K. Issautier, N. Meyer-Vernet, M. Moncuquet, and F. Pantellini, vol. 1216, p. 288, AIP, 2010a.

Henri, P., F. Califano, C. Briand, and A. Mangeney, Vlasov-Poisson simulations of electrostatic parametric instability for localized Langmuir wave packets in the solar wind, *J. Geophys. Res.*, *115*, 6106, 2010b.

Henri, P., N. Meyer-Vernet, C. Briand, and S. Donato, Observations of Langmuir ponderomotive effects: using the STEREO spacecraft as a density probe, *Geophys. Res. Lett.*, 2010c, *submitted*.

Henri, P., F. Califano, C. Briand, and A. Mangeney, Low energy Langmuir cavitons: the asymptotic limit of weak turbulence, *prl*, 2010d, *submitted*.

Hospodarsky, G. B., and D. A. Gurnett, Beat-type Langmuir wave emissions associated with a type III solar radio burst: Evidence of parametric decay, *Geophys. Res. Lett.*, *22*, 1161, 1995.

Howard, R. A., et al., Sun Earth Connection Coronal and Heliospheric Investigation (SECCHI), *Space Science Reviews*, *136*, 67, 2008.

Hundhausen, A. J., S. J. Bame, J. R. Asbridge, and S. J. Sydoriak, Solar wind proton properties: Vela 3 observations from July 1965 to June 1967., *J. Geophys. Res.*, *75*, 4643, 1970.

Kaiser, M. L., T. A. Kucera, J. M. Davila, O. C. St. Cyr, M. Guhathakurta, and E. Christian, The STEREO Mission: An Introduction, *Space Science Reviews*, p. 198, 2007.

Kellogg, P. J., K. Goetz, N. Lin, S. J. Monson, A. Balogh, R. J. Forsyth, and R. G. Stone, Low frequency magnetic signals associated with Langmuir waves, *Geophys. Res. Lett.*, *19*, 1299, 1992a.

Kellogg, P. J., K. Goetz, N. Lin, S. J. Monson, A. Balogh, R. J. Forsyth, and R. G. Stone, Low frequency magnetic signals associated with Langmuir waves, *Geophys. Res. Lett.*, *19*, 1299, 1992b.

Kellogg, P. J., K. Goetz, S. J. Monson, S. D. Bale, M. J. Reiner, and M. Maksimovic, Plasma wave measurements with STEREO S/WAVES: Calibration, potential model, and preliminary results, *J. Geophys. Res.*, *114*, 2107, 2009.

Kennel, C. F., F. V. Coroniti, F. L. Scarf, R. W. Fredricks, D. A. Gurnett, and E. J. Smith, Correlated whistler and electron plasma oscillation bursts detected on ISEE-3, *Geophys. Res. Lett.*, *7*, 129, 1980.

Kim, E., I. H. Cairns, and P. A. Robinson, Mode conversion of Langmuir to electromagnetic waves at magnetic field-aligned density inhomogeneities: Simulations, theory, and applications to the solar wind and the corona, *Physics of Plasmas*, *15*, 102,110, 2008.

Koepke, M. E., Interrelated laboratory and space plasma experiments, *Reviews of Geophysics*, *46*, 3001, 2008.

Krall, N. A., and A. W. Trivelpiece, *Principles of plasma physics*, International Student Edition - International Series in Pure and Applied Physics, McGraw-Hill, 1973.

Kurth, W. S., D. A. Gurnett, and F. L. Scarf, High-resolution spectrograms of ion acoustic waves in the solar wind, *J. Geophys. Res.*, *84*, 3413, 1979.

Lagoutte, D., F. Lefeuvre, and J. Hanasz, Application of bicoherence analysis in study of wave interactions in space plasma, *J. Geophys. Res.*, *94*, 435, 1989.

Landau, L. D., On the vibration of the electronic plasma, *J. Phys. USSR*, *10*, 25, 1946, english translation in *JETP 16*, 574.

Li, B., A. J. Willes, P. A. Robinson, and I. H. Cairns, Dynamics of beam-driven Langmuir and ion-acoustic waves including electrostatic decay, *Physics of Plasmas*, *10*, 2748, 2003.

Lin, R. P., D. W. Potter, D. A. Gurnett, and F. L. Scarf, Energetic electrons and plasma waves associated with a solar type III radio burst, *Astrophys. J.*, *251*, 364, 1981.

Lin, R. P., W. K. Levedahl, W. Lotko, D. A. Gurnett, and F. L. Scarf, Evidence for nonlinear wave-wave interactions in solar type III radio bursts, *Astrophys. J.*, *308*, 954, 1986a.

Lin, R. P., W. K. Levedahl, W. Lotko, D. A. Gurnett, and F. L. Scarf, Evidence for nonlinear wave-wave interactions in solar type III radio bursts, *Astrophys. J.*, *308*, 954, 1986b.

Luhmann, J. G., et al., STEREO IMPACT Investigation Goals, Measurements, and Data Products Overview, *Space Science Reviews*, *136*, 117, 2008.

Luo, Q., A. C.-L. Chian, and F. A. Borotto, A broadband theory of Langmuir-whistler events in the solar wind, *Astron. & Astrophys.*, *348*, L13, 1999.

Maksimovic, M., et al., Radial evolution of the electron distribution functions in the fast solar wind between 0.3 and 1.5 AU, *J. Geophys. Res.*, *110*, 9104, 2005.

Malaspina, D. M., I. H. Cairns, and R. E. Ergun, The $2f_p$ radiation from localized Langmuir waves, *J. Geophys. Res.*, *115*, 1101, 2010.

Mandel, L., and E. Wolf, *Optical Coherence and Quantum Optics*, Cambridge University Press, 1995.

Mangeney, A., F. Califano, C. Cavazzoni, and P. Travnicek, A Numerical Scheme for the Integration of the Vlasov-Maxwell System of Equations, *Journal of Computational Physics*, *179*, 495, 2002.

Marsch, E., R. Schwenn, H. Rosenbauer, K.-H. Muehlhaeuser, W. Pilipp, and F. M. Neubauer, Solar wind protons - Three-dimensional velocity distributions and derived plasma parameters measured between 0.3 and 1 AU, *J. Geophys. Res.*, *87*, 52, 1982.

Mendel, J. M., Tutorial on higher-order statistics (spectra) in signal processingand system theory: theoretical results and some applications, *Proceedings of the IEEE*, *79*, 278, 1991.

Meyer-Vernet, N., *Basics of the Solar Wind*, Cambridge University Press, 2007.

Meyer-Vernet, N., and C. Perche, Tool kit for antennae and thermal noise near the plasma frequency, *J. Geophys. Res.*, *94*, 2405, 1989.

Meyer-Vernet, N., et al., Dust Detection by the Wave Instrument on STEREO: Nanoparticles Picked up by the Solar Wind?, *solphys*, *256*, 463, 2009.

Montgomery, M. D., S. J. Bame, and A. J. Hundhausen, Solar Wind Electrons: Vela 4 Measurements, *J. Geophys. Res.*, *73*, 4999, 1968.

Moullard, O., D. Burgess, and S. D. Bale, Whistler waves observed during an in-situ solar type III radio burst, *Astron. & Astrophys.*, *335*, 703, 1998.

Nishikawa, K., Parametric Excitation of Coupled Waves. II. Parametric Plasmon-Photon Interaction, *J. Phys. Soc. Japan*, *24*, 1152, 1968.

Opitz, A., et al., Temporal evolution of the solar wind electron core density at solar minimum by correlating the STEREO A and B SWEA measurements, *solphys*, 2009, *submitted*.

Pecseli, H. L., J. Trulsen, A. Bahnsen, and F. Primdahl, Propagation and nonlinear interaction of low-frequency electrostatic waves in the polar cap E region, *J. Geophys. Res.*, *98*, 1603, 1993.

Pedersen, A., Solar wind and magnetosphere plasma diagnostics by spacecraft electrostatic potential measurements, *Annales Geophysicae*, *13*, 118, 1995.

Pedersen, A., et al., Electron density estimations derived from spacecraft potential measurements on Cluster in tenuous plasma regions, *J. Geophys. Res.*, *113*, 7, 2008.

Pilipp, W. G., K. Muehlhaeuser, H. Miggenrieder, M. D. Montgomery, and H. Rosenbauer, Characteristics of electron velocity distribution functions in the solar wind derived from the HELIOS plasma experiment, *J. Geophys. Res.*, *92*, 1075, 1987.

Robinson, P. A., Stochastic-growth theory of Langmuir growth-rate fluctuations in type III solar radio sources, *solphys*, *146*, 357, 1993.

Robinson, P. A., Nonlinear wave collapse and strong turbulence, *Reviews of Modern Physics*, *69*, 507, 1997.

Robinson, P. A., I. H. Cairns, and D. A. Gurnett, Clumpy Langmuir waves in type III radio sources - Comparison of stochastic-growth theory with observations, *Astrophys. J.*, *407*, 790, 1993a.

Robinson, P. A., A. J. Willes, and I. H. Cairns, Dynamics of Langmuir and ion-sound waves in type III solar radio sources, *Astrophys. J.*, *408*, 720, 1993b.

Sagdeev, R. Z., and A. A. Galeev, *Nonlinear Plasma Theory*, Benjamin, 1969.

Sakai, J. I., T. Kitamoto, and S. Saito, Simulation of Solar Type III Radio Bursts from a Magnetic Reconnection Region, *Astrophys. J.l*, *622*, L157, 2005.

Scudder, J. D., X. Cao, and F. S. Mozer, Photoemission current-spacecraft voltage relation: Key to routine, quantitative low-energy plasma measurements, *J. Geophys. Res.*, *105*, 21,281, 2000.

Soucek, J., T. Dudok de Wit, V. Krasnoselskikh, and A. Volokitin, Statistical analysis of nonlinear wave interactions in simulated Langmuir turbulence data, *Annales Geophysicae*, *21*, 681, 2003.

Soucek, J., V. Krasnoselskikh, T. Dudok de Wit, J. Pickett, and C. Kletzing, Nonlinear decay of foreshock Langmuir waves in the presence of plasma inhomogeneities: Theory and Cluster observations, *J. Geophys. Res.*, *110*, 8102, 2005.

Stasiewicz, K., B. Holback, V. Krasnoselskikh, M. Boehm, R. Boström, and P. M. Kintner, Parametric instabilities of Langmuir waves observed by Freja, *J. Geophys. Res.*, *101*, 21,515, 1996.

Sturrock, P. A., Type III Solar Radio Bursts, in *The Physics of Solar Flares*, edited by W. N. Hess, p. 357, 1964.

Thejappa, G., and R. J. MacDowall, Evidence for Strong and Weak Turbulence Processes in the Source Region of a Local Type III Radio Burst, *Astrophys. J.*, *498*, 465, 1998.

Thejappa, G., D. Lengyel-Frey, R. G. Stone, and M. L. Goldstein, Evaluation of Emission Mechanisms at omega P E Using ULYSSES Observations of Type III Bursts, *Astrophys. J.*, *416*, 831, 1993.

Thejappa, G., D. G. Wentzel, and R. G. Stone, Low-frequency waves associated with Langmuir waves in solar wind, *J. Geophys. Res.*, *100*, 3417, 1995.

Thejappa, G., R. J. MacDowall, E. E. Scime, and J. E. Littleton, Evidence for electrostatic decay in the solar wind at 5.2 AU, *J. Geophys. Res.*, *108*, 1139, 2003.

Thornhill, S. G., and D. ter Haar, Langmuir turbulence and modulational instability, *Physics Reports*, *43*, 43, 1978.

Tsurutani, B. T., and G. S. Lakhina, Some basic concepts of wave-particle interactions in collisionless plasmas, *Reviews of Geophysics*, *35*, 491, 1997.

Tsytovich, V. N., *Nonlinear Effects in Plasma*, New York: Plenum Press, 1970.

Van Milligen, B. P., E. Sánchez, T. Estrada, C. Hidalgo, B. Brañas, B. Carreras, and L. García, Wavelet bicoherence: A new turbulence analysis tool, *Physics of Plasmas*, *2*, 3017, 1995.

Vlasov, A. A., On Vibration Properties of Electron Gas (in Russian), *J. Exp. Theor. Phys.*, *8*, 291, 1938.

Vlasov, A. A., The Vibrational Properties of an Electron Gas, *Soviet Physics Uspekhi*, *10*, 721, 1968.

Voitenko, Y., M. Goossens, O. Sirenko, and A. Chian, Nonlinear excitation of kinetic Alfvén waves and whistler waves by electron beam-driven Langmuir waves in the solar corona, *Astron. & Astrophys.*, *409*, 331, 2003.

Wild, J. P., Observations of the Spectrum of High-Intensity Solar Radiation at Metre Wavelengths. III. Isolated Bursts, *Australian Journal of Scientific Research A Physical Sciences*, *3*, 541, 1950.

Zakharov, V. E., Collapse of Langmuir Waves, *Soviet Journal of Experimental and Theoretical Physics*, *35*, 908, 1972.

Zakharov, V. E., S. L. Musher, and A. M. Rubenchik, Hamiltonian approach to the description of non-linear plasma phenomena, *Physics Reports*, *129*, 285, 1985.